



NUCLEAR MEDICINE IN CANCER DIAGNOSIS

EDITED BY: Francesco Cicone and Philipp Lohmann
PUBLISHED IN: Frontiers in Medicine



frontiers

Frontiers eBook Copyright Statement

The copyright in the text of individual articles in this eBook is the property of their respective authors or their respective institutions or funders. The copyright in graphics and images within each article may be subject to copyright of other parties. In both cases this is subject to a license granted to Frontiers.

The compilation of articles constituting this eBook is the property of Frontiers.

Each article within this eBook, and the eBook itself, are published under the most recent version of the Creative Commons CC-BY licence.

The version current at the date of publication of this eBook is CC-BY 4.0. If the CC-BY licence is updated, the licence granted by Frontiers is automatically updated to the new version.

When exercising any right under the CC-BY licence, Frontiers must be attributed as the original publisher of the article or eBook, as applicable.

Authors have the responsibility of ensuring that any graphics or other materials which are the property of others may be included in the CC-BY licence, but this should be checked before relying on the CC-BY licence to reproduce those materials. Any copyright notices relating to those materials must be complied with.

Copyright and source acknowledgement notices may not be removed and must be displayed in any copy, derivative work or partial copy which includes the elements in question.

All copyright, and all rights therein, are protected by national and international copyright laws. The above represents a summary only. For further information please read Frontiers' Conditions for Website Use and Copyright Statement, and the applicable CC-BY licence.

ISSN 1664-8714

ISBN 978-2-83250-406-2

DOI 10.3389/978-2-83250-406-2

About Frontiers

Frontiers is more than just an open-access publisher of scholarly articles: it is a pioneering approach to the world of academia, radically improving the way scholarly research is managed. The grand vision of Frontiers is a world where all people have an equal opportunity to seek, share and generate knowledge. Frontiers provides immediate and permanent online open access to all its publications, but this alone is not enough to realize our grand goals.

Frontiers Journal Series

The Frontiers Journal Series is a multi-tier and interdisciplinary set of open-access, online journals, promising a paradigm shift from the current review, selection and dissemination processes in academic publishing. All Frontiers journals are driven by researchers for researchers; therefore, they constitute a service to the scholarly community. At the same time, the Frontiers Journal Series operates on a revolutionary invention, the tiered publishing system, initially addressing specific communities of scholars, and gradually climbing up to broader public understanding, thus serving the interests of the lay society, too.

Dedication to Quality

Each Frontiers article is a landmark of the highest quality, thanks to genuinely collaborative interactions between authors and review editors, who include some of the world's best academicians. Research must be certified by peers before entering a stream of knowledge that may eventually reach the public - and shape society; therefore, Frontiers only applies the most rigorous and unbiased reviews. Frontiers revolutionizes research publishing by freely delivering the most outstanding research, evaluated with no bias from both the academic and social point of view. By applying the most advanced information technologies, Frontiers is catapulting scholarly publishing into a new generation.

What are Frontiers Research Topics?

Frontiers Research Topics are very popular trademarks of the Frontiers Journals Series: they are collections of at least ten articles, all centered on a particular subject. With their unique mix of varied contributions from Original Research to Review Articles, Frontiers Research Topics unify the most influential researchers, the latest key findings and historical advances in a hot research area! Find out more on how to host your own Frontiers Research Topic or contribute to one as an author by contacting the Frontiers Editorial Office: frontiersin.org/about/contact

NUCLEAR MEDICINE IN CANCER DIAGNOSIS

Topic Editors:

Francesco Cicone, Magna Græcia University, Italy

Philipp Lohmann, Institute of Neuroscience and Medicine, Research Center
Juelich, Germany

Citation: Cicone, F., Lohmann, P., eds. (2022). Nuclear Medicine in Cancer
Diagnosis. Lausanne: Frontiers Media SA. doi: 10.3389/978-2-83250-406-2

Table of Contents

- 04 Editorial: “Nuclear Medicine in Cancer Diagnosis”**
Francesco Cicone and Philipp Lohmann
- 07 Optimized Application of ^{68}Ga -Prostate-Specific Membrane Antigen-617 Whole-Body PET/CT and Pelvic PET/MR in Prostate Cancer Initial Diagnosis and Staging**
Chunxia Qin, Yongkang Gai, Qingyao Liu, Weiwei Ruan, Fang Liu, Fan Hu, Xiaoping Zhang and Xiaoli Lan
- 18 Development of PET Radioligands Targeting COX-2 for Colorectal Cancer Staging, a Review of in vitro and Preclinical Imaging Studies**
Caroline Dagallier, François Avry, Yann Touchefeu, Frédéric Buron, Sylvain Routier, Michel Chérel and Nicolas Arlicot
- 29 Additive Value of Dynamic FDOPA PET/CT for Glioma Grading**
Antoine Girard, Pierre-Jean Le Reste, Alice Metais, Nibras Chaboub, Anne Devillers, Hervé Saint-Jalmes, Florence Le Jeune and Xavier Palard-Novello
- 37 The Value of ^{18}F -FDG PET/CT in Diagnosing Pancreatic Lesions: Comparison With CA19-9, Enhanced CT or Enhanced MR**
Shengyun Huang, Huanhuan Chong, Xun Sun, Zhijian Wu, Qing Jia, Yongxue Zhang and Xiaoli Lan
- 49 Performance of Ultrasound-Guided Core Biopsy Driven by FDG-avid Supraclavicular Lymph Nodes in Patients With Suspected Lung Cancer**
Tongtong Wang, Junbao Liu, Ningning Lv, Shi Xuan, Lin Bai, Bin Ji and Shi Gao
- 56 Pre-Clinical Study of the [^{18}F]AIF-Labeled HER2 Affibody for Non-Invasive HER2 Detection in Gastric Cancer**
Jingya Han, Yang Chen, Yan Zhao, Xinming Zhao, Jingmian Zhang, Jianfang Wang and Zhaoqi Zhang
- 68 The Impact of Total Variation Regularized Expectation Maximization Reconstruction on ^{68}Ga -DOTA-TATE PET/CT Images in Patients With Neuroendocrine Tumor**
Lin Liu, Hanxiang Liu, Shijie Xu, Shumao Zhang, Yi Tao, Greta S. P. Mok and Yue Chen
- 76 Differentiation Between Malignant and Benign Pulmonary Nodules by Using Automated Three-Dimensional High-Resolution Representation Learning With Fluorodeoxyglucose Positron Emission Tomography-Computed Tomography**
Yung-Chi Lai, Kuo-Chen Wu, Neng-Chuan Tseng, Yi-Jin Chen, Chao-Jen Chang, Kuo-Yang Yen and Chia-Hung Kao
- 86 Prognostic Significance of PD-L1 Expression and Standardized Uptake Values in the Primary Lesions of Stage IV Adenocarcinoma Lung Cancer**
Bui Tien Cong, Pham Cam Phuong, Pham-Van Thai, Vu-Le Thuong, Nguyen Quang Hung, Dong-Thi Hang, Hoang Anh Tuan, Doan Minh Khuy, Pham-Van Tuyen and Nguyen Minh Duc
- 94 ^{18}F -FDG / ^{18}F -Choline Dual-Tracer PET Behavior and Tumor Differentiation in HepatoCellular Carcinoma. A Systematic Review**
Jérôme Ghidaglia, Nicolas Golse, Alina Pascale, Mylène Sebah and Florent L. Besson



OPEN ACCESS

EDITED AND REVIEWED BY

Giorgio Treglia,
Ente Ospedaliero Cantonale
(EOC), Switzerland

*CORRESPONDENCE

Francesco Cicone
cicone@unicz.it

SPECIALTY SECTION

This article was submitted to
Nuclear Medicine,
a section of the journal
Frontiers in Medicine

RECEIVED 03 September 2022

ACCEPTED 09 September 2022

PUBLISHED 21 September 2022

CITATION

Cicone F and Lohmann P (2022)
Editorial: "Nuclear medicine in cancer
diagnosis". *Front. Med.* 9:1035994.
doi: 10.3389/fmed.2022.1035994

COPYRIGHT

© 2022 Cicone and Lohmann. This is
an open-access article distributed
under the terms of the [Creative
Commons Attribution License \(CC BY\)](#).
The use, distribution or reproduction
in other forums is permitted, provided
the original author(s) and the copyright
owner(s) are credited and that the
original publication in this journal is
cited, in accordance with accepted
academic practice. No use, distribution
or reproduction is permitted which
does not comply with these terms.

Editorial: "Nuclear medicine in cancer diagnosis"

Francesco Cicone 1,2,3* and Philipp Lohmann^{4,5}

¹Nuclear Medicine Unit, University Hospital "Mater Domini", Catanzaro, Italy, ²Department of Experimental and Clinical Medicine, "Magna Graecia" University of Catanzaro, Catanzaro, Italy, ³Neuroscience Research Centre, PET/MR Unit, "Magna Graecia" University of Catanzaro, Catanzaro, Italy, ⁴Institute of Neuroscience and Medicine (INM-4), Research Center Juelich (FZJ), Juelich, Germany, ⁵Department of Stereotaxy and Functional Neurosurgery, Faculty of Medicine and University Hospital Cologne, Cologne, Germany

KEYWORDS

diagnostic radiopharmaceuticals, nuclear medicine, radionuclide imaging, molecular imaging, tumor detection, PET

Editorial on the Research Topic Nuclear medicine in cancer diagnosis

In recent years, nuclear medicine had a tremendous impact on the management of patients with cancer, particularly thanks to the widespread use of positron emission tomography (PET) with [¹⁸F]-fluorodeoxyglucose (FDG). Furthermore, additional fluorinated and non-fluorinated radiopharmaceuticals emerged and have now been integrated in current diagnostic guidelines of several tumors. The landscape of diagnostic radiopharmaceuticals is theoretically limitless, given the infinite number of molecules currently under development or that could be radiolabeled to probe any cellular metabolic and functional aspects of tumors and tumor microenvironment. Owing to the rapidly expanding role of nuclear medicine in cancer diagnosis, a focused Research Topic was launched by the section of Nuclear Medicine of *Frontiers in Medicine*. Between May 2021 and July 2022, ten articles were eventually published within the Research Topic, covering clinical and pre-clinical applications of either well-established or novel radiopharmaceuticals for cancer diagnostics.

Four published articles were dedicated to FDG, the most widely used tracer in oncology. Wang et al. investigated the use of FDG findings to drive ultrasound-guided core biopsy of supraclavicular lymph nodes (SLN) in 54 patients with suspected lung cancer. Diagnosis through SLN has a high potential clinical impact despite minimal invasiveness, as it can directly upstage patients with lung cancer indicating an inoperable disease. The biopsy procedure was performed within 2 days after FDG PET/CT and revealed a diagnostic yield of 98.1%, sparing further bronchoscopy, CT-guided lung biopsy or surgery in 38/54 (70%) patients. In the study conducted by Tien Cong et al. in 86 patients with stage IV lung adenocarcinoma, FDG uptake was found to be higher in patients with positive programmed death-ligand 1 (PD-L1) expression than in patients with PD-L1-negative tumors. This study compares with other previous publications, suggesting that FDG PET could help predict response to PD-1/PD-L1 inhibitors.

One of the most frequent applications of FDG is the investigation of incidental pulmonary nodules. [Lai et al.](#) evaluated the potential of a novel deep learning method for an improved differentiation between malignant and benign pulmonary nodules using FDG PET/CT in a group of 112 patients. The authors demonstrated that a deep learning model using high-resolution representation learning might aid in the classification of pulmonary nodules without the need for manual expert annotations. [Huang et al.](#) reported on the diagnostic value of FDG PET in the differential diagnosis of pancreatic lesions as compared with contrast-enhanced CT (CE-CT), contrast-enhanced magnetic resonance imaging (CE-MRI) and serum carbohydrate antigen 19-9 (CA 19-9) in a large retrospective cohort of 467 patients. The study showed that FDG PET/CT has higher specificity than CE-CT and CE-MRI, resulting in a higher overall diagnostic accuracy. In addition, FDG was more sensitive and specific than CA 19-9. The authors conclude that the combination of FDG PET/CT with other diagnostic modalities could enhance the diagnostic efficiency, although medium or well-differentiated pancreatic cancers may show low FDG uptake.

Six published articles were dedicated to non-FDG radiopharmaceuticals. Two of these papers focused on the optimization of imaging acquisition and reconstruction of widely available radiopharmaceuticals, such as 3,4-dihydroxy-6- ^{18}F -fluoro-L-phenylalanine (FDOPA) and ^{68}Ga -DOTA-TATE, respectively. The study by [Girard et al.](#) assessed the value of dynamic FDOPA PET/CT in 14 patients with newly diagnosed glioma and found an additive value of kinetic parameters over conventional static semiquantitative image assessment. Although the results of the study are interesting, the clinical value of kinetic FDOPA uptake parameters in patients with primary brain warrants confirmation in larger cohorts.

Improvements in PET image reconstruction methods that allow for shorter acquisition times or for a reduction of the injected tracer activity while preserving image quality and accurate quantification are of high clinical relevance. This was accomplished by the total variation regularized expectation maximization (TVREM) image reconstruction method evaluated by [Liu et al.](#) in 17 patients with neuroendocrine tumors undergoing ^{68}Ga -DOTA-TATE PET/CT. TVREM could reduce the image noise and increase the signal-to-noise ratio and, hence, seems to be a promising reconstruction algorithm that should be further evaluated for other applications.

Two additional papers reported on novel radiopharmaceuticals, currently at different stages of development. The ability of ^{18}F AIF-NOTA-HER2 to monitor changes of human epidermal growth factor receptor 2 (HER2), an important predictive biomarker in gastric cancer, was demonstrated by [Han et al.](#) in a xenograft mouse model. The radiopharmaceutical could be produced with a high radiochemical yield and demonstrated a good image contrast

and resolution. Consequently, ^{18}F AIF-NOTA-HER2 may be a promising PET probe for the non-invasive whole-body detection of the HER2 status in patients with gastric cancer.

Prostate-specific membrane antigen (PSMA) represents an attractive target for theragnostic applications in patients with prostate cancer (PC). Due to its favorable characteristics, the PSMA-targeting analog PSMA-617 has been mostly used for therapeutic applications following radiolabelling with ^{177}Lu or alpha emitters. In their paper, [Qin et al.](#) made diagnostic use of ^{68}Ga -PSMA-617 in 53 patients with suspected PC, assessing the utility of a delayed PET/MR pelvic acquisition about 3 h following radiopharmaceutical injection, in addition to whole-body PET/CT or PET/MRI. The authors concluded that a delayed acquisition is not necessary in most patients with advanced PC, although it may be interesting to further investigate its role in patients with early-stage disease.

Lastly, the Research Topic features two review papers. [Ghidaglia et al.](#) conducted a systematic review of dual-tracer FDG/ ^{18}F -Choline PET to investigate the level of evidence for a link between tracer uptake and the degree of differentiation of resected hepatocellular carcinoma (HCC). The authors found overlapping uptake behavior between well- and less differentiated HCC, which makes the differentiation based on PET alone challenging. Further studies to improve the usefulness of PET in the clinical management of patients with HCC were recommended.

The inflammatory marker cyclooxygenase-2 (COX-2) was shown to play a role in colon cancer development since the early stages of tumorigenesis. [Dagallier et al.](#) reviewed the results of COX-2-targeting radiopharmaceuticals in preclinical models of colon cancer. Despite promising results *in vitro*, none of the radiopharmaceuticals developed so far demonstrated sufficient targeting efficiency *in vivo* to advance to the clinical stage.

In summary, the articles published in this Research Topic present original works, as well as review papers on a diverse range of nuclear medicine diagnostic applications and developments. We sincerely hope that the readers will enjoy and find useful information for their clinical and research activity.

Author contributions

All authors listed have made a substantial, direct, and intellectual contribution to the work and approved it for publication.

Conflict of interest

The authors declare that the research was conducted in the absence of any commercial or financial relationships that could be construed as a potential conflict of interest.

Publisher's note

All claims expressed in this article are solely those of the authors and do not necessarily represent those of their affiliated

organizations, or those of the publisher, the editors and the reviewers. Any product that may be evaluated in this article, or claim that may be made by its manufacturer, is not guaranteed or endorsed by the publisher.



Optimized Application of ^{68}Ga -Prostate-Specific Membrane Antigen-617 Whole-Body PET/CT and Pelvic PET/MR in Prostate Cancer Initial Diagnosis and Staging

Chunxia Qin^{1,2}, Yongkang Gai^{1,2}, Qingyao Liu^{1,2}, Weiwei Ruan^{1,2}, Fang Liu^{1,2}, Fan Hu^{1,2}, Xiaoping Zhang^{3*} and Xiaoli Lan^{1,2*}

¹ Department of Nuclear Medicine, Union Hospital, Tongji Medical College, Huazhong University of Science and Technology, Wuhan, China, ² Hubei Key Laboratory of Molecular Imaging, Wuhan, China, ³ Department of Urology, Union Hospital, Tongji Medical College, Huazhong University of Science and Technology, Wuhan, China

OPEN ACCESS

Edited by:

Francesco Cicone,
University of Catanzaro, Italy

Reviewed by:

Joseph A. O'Donoghue,
Memorial Sloan Kettering Cancer
Center, United States
Salvatore Annunziata,
Catholic University of the Sacred
Heart, Italy

*Correspondence:

Xiaoli Lan
xiaoli_lan@hust.edu.cn
Xiaoping Zhang
xzhang@hust.edu.cn

Specialty section:

This article was submitted to
Nuclear Medicine,
a section of the journal
Frontiers in Medicine

Received: 23 January 2021

Accepted: 19 April 2021

Published: 13 May 2021

Citation:

Qin C, Gai Y, Liu Q, Ruan W, Liu F,
Hu F, Zhang X and Lan X (2021)
Optimized Application of
 ^{68}Ga -Prostate-Specific Membrane
Antigen-617 Whole-Body PET/CT and
Pelvic PET/MR in Prostate Cancer
Initial Diagnosis and Staging.
Front. Med. 8:657619.
doi: 10.3389/fmed.2021.657619

Purpose: To analyze ^{68}Ga -PSMA-617 PET/CT or PET/MR and delayed PET/MR images in patients diagnosed with or suspicion of prostate cancer, and to explore the optimal use of PET/CT and PET/MR for initial diagnosis and staging in prostate cancer.

Methods: Images from conventional scan by ^{68}Ga -PSMA whole-body PET/CT or PET/MR followed by delayed pelvic PET/MR were retrospectively analyzed. Prostatic ^{68}Ga -PSMA uptake was measured as SUVmax1 (conventional scan 1 h post injection) and SUVmax2 (delayed scan 3 h post injection). Age, PSA levels, and SUVmax were compared between benign and malignant cases. The correlation of SUVmax1 and SUVmax2 was analyzed. Diagnostic performance was evaluated by ROC analysis.

Results: Fifty-six patients with 41 prostate cancers and 15 benign prostate lesions were enrolled. Fifty-three patients had paired conventional and delayed scans. Age, tPSA, fPSA levels, and SUVmax were significantly different between benign and malignant cases. A good correlation was found between SUVmax1 and SUVmax2. There was significant difference between SUVmax1 and SUVmax2 in the malignant group ($p = 0.001$). SUVmax1 had superior diagnostic performance than SUVmax2, SUVmax difference and PSA levels, with a sensitivity of 85.4%, a specificity of 100% and an AUC of 0.956. A combination of SUVmax1 with nodal and/or distant metastases and MR PI-RADS V2 score had a sensitivity and specificity of 100%. Delayed pelvic PET/MR imaging in 33 patients were found to be redundant because these patients had nodal and/or distant metastases which can be easily detected by PET/CT. PET/MR provided incremental value in 8 patients at early-stage prostate cancer based on precise anatomical localization and changes in lesion signal provided by MR.

Conclusion: Combined ^{68}Ga -PSMA whole-body PET/CT and pelvic PET/MR can accurately differentiate benign prostate diseases from prostate cancer and accurately stage prostate cancer. Whole-body PET/CT is sufficient for advanced prostate cancer.

Pelvic PET/MR contributes to diagnosis and accurate staging in early prostate cancer. Imaging at about 1 h after injection is sufficient in most patients.

ClinicalTrials.gov: NCT03756077. Registered 27 November 2018—Retrospectively registered, <https://clinicaltrials.gov/show/NCT03756077>.

Keywords: ^{68}Ga -PSMA, PET/CT, PET/MR, benign prostatic hyperplasia, prostatitis, prostate cancer

INTRODUCTION

Prostate cancer is a common malignancy harmful to health of old males. The incidence ranks second (13.5%) and it is the fifth leading cause of cancer death (6.7%) among males worldwide (1). Accurate diagnosis and staging are very important to choose the most suitable treatment.

Serum prostate-specific antigen (PSA) testing and digital rectal examination (DRE) are the most commonly used initial screening methods for prostate disease (2). The limitations of PSA level as a prostate cancer biomarker are well-known because false positive and false negative results are common, and screening for prostate cancer with PSA is generally no longer recommended (3). The value of DRE is limited in the early stages of the disease. Systematic transrectal ultrasound (TRUS)-guided biopsy is regarded as a standard, but it has frequent false-negative results and underestimates the final Gleason score of the tumor compared with histologic examination after radical prostatectomy (4).

Imaging technologies play an important role in the management of prostate cancer. Conventional imaging modalities, including ultrasound, computed tomography (CT), magnetic resonance imaging (MRI), and bone scan are commonly used in the diagnosis, staging, and restaging of prostate cancer (5). However, these conventional imaging modalities are usually regional imaging, or have limited accuracy in small lymph node metastases and small-volume bone metastases. Molecular imaging is regarded as a promising approach to improve prostate cancer diagnosis and staging (6). Several positron emission tomographic (PET) tracers, like ^{18}F -FDG, ^{18}F -fluorocholine, ^{11}C -choline, and ^{11}C -acetate, have been studied in patients with prostate cancer, but the diagnostic performance of most PET radiotracers has so far remained limited (7, 8).

Prostate-specific membrane antigen (PSMA) is a transmembrane protein which is overexpressed in prostate cancer (9, 10). It becomes a promising target for specific imaging of prostate cancer (11). In recent years, gallium ^{68}Ga has been used to label PSMA ligands for PET imaging (12). Initial experience using ^{68}Ga -PSMA PET/CT indicates that ^{68}Ga -PSMA PET can visualize relapses and metastases of prostate cancer with high contrast through binding to the extracellular domain of PSMA and internalization (13). Studies have described the superior value of ^{68}Ga -PSMA ligand PET imaging to conventional imaging in different clinical scenarios, including differential diagnosis; guiding biopsy, surgery and radiotherapy; initial staging and restaging; recurrence detection

and selecting patients who may benefit from systemic targeted radionuclide therapy (14–16).

PET/MR is a hybrid technology that can provide both biologic and morphologic information. Recently introduced ^{68}Ga -PSMA PET/MR combines multi-parametric MRI (mpMRI) along with molecular information of PSMA expression into a “one-stop shopping” procedure for better anatomic localization and characterization of prostate lesions. Compared with PET/CT, simultaneous PET/MR has the advantages of reduced radiation exposure and inherent higher soft-tissue contrast resolution (17, 18). PSMA PET/MR is particularly important for accurate localization and assessment of the extent of pelvic disease in the initial staging of prostate cancer. Despite the advantages of PSMA PET/MR over PSMA PET/CT, cost, scanning time, and patient comfort should also be considered. Domachevsky et al. (19) demonstrated that although early PET/MR has very good agreement compared to same-day PET/CT, PET/CT, and early PET/MR cannot be used interchangeably. They further demonstrated that pelvic PSMA PET/MR is better than whole-body PSMA PET/CT for detecting extensions of localized disease, and may be useful for initial evaluation of prostate cancer (20).

Some PET centers have both PET/CT and PET/MR. Does every patient need to undergo both PET/CT and PET/MR? How to choose the right scan is a matter of concern. The purpose of this study was to retrospectively analyze the images of whole-body PSMA PET/CT or PET/MR followed by delayed limited pelvic PSMA PET/MR in patients diagnosed with or suspicion of prostate cancer, and to explore how to rationally use PET/CT and PET/MR in prostate diseases.

MATERIALS AND METHODS

Patients

This study was approved by Institutional Review Board. Patient data involved in a study that was registered on ClinicalTrials.gov (NCT03756077) were retrospectively analyzed. Inclusion criteria include all of the following: (a) patients diagnosed with or suspicion of prostate cancer; (b) patients underwent whole-body ^{68}Ga -PSMA PET/CT or PET/MR followed by delayed pelvic PET/MR; (c) patients have pathological results or follow-up results, systemic multi-point biopsy of prostate was performed 1 month prior PET imaging or after PET imaging. Patients with any other malignancies and if they had been pretreated for prostate cancer were excluded. General information and biochemical test results were collected. All the patients were divided into a “malignant group” or a “benign group” according to the histological or follow-up results. Patients with prostate

cancer were staged according to AJCC Prognostic Groups by combination of TNM, PSA level and Gleason score.

Imaging Protocol

^{68}Ga was produced from a $^{68}\text{Ge}/^{68}\text{Ga}$ generator (ITG GmbH, Munich, Germany) by eluting with 0.05N hydrochloric acid. ^{68}Ga -PSMA-617 was synthesized using an ITG manual synthesis module as described previously (21). Briefly, 4 mL of $^{68}\text{GaCl}_3$ was reacted with 20 μg (20 nmol) PSMA-617 ligand (Jiangsu Huayi Technology Company, Changshu, China) in 1 mL of 0.25 M sodium acetate buffer for 5 min at 105°C. The production was purified in a C18 cartridge and collected through a 0.22- μm -pore filter.

All patients were intravenously injected with a dose of 173.53 ± 50.69 MBq (4.69 ± 1.37 mCi) of ^{68}Ga -PSMA-617. Patients were encouraged to drink water after injection and asked to empty their bladder before PET scan. Conventional imaging from vertex to proximal legs were performed using a hybrid PET/CT scanner (Discovery VCT; GE Healthcare, Waukesha WI, USA) or a time-of-flight (TOF) hybrid PET/MR scanner (SIGNA PET/MR; GE Healthcare). Delayed pelvic PET/MR images were acquired using hybrid PET/MR.

PET/CT acquisition followed our standard protocol. A CT scan (120 kV, 110 mAs) was acquired after a scout image with a scanning thickness of 3.75 mm, followed by whole-body emission static PET imaging in a three-dimensional (3D) mode at 3 min per bed position. PET images were attenuation-corrected using CT images, and reconstructed using an ordered-subset expectation maximization (OSEM) iterative reconstruction algorithm (28 subsets and 2 iterations) and co-registered with CT images (Xeleris; GE Healthcare).

For PET/MR, MR attenuation images were acquired using ZTE technology after acquisition of localization images. The PET acquisition of PET/MR was performed in 3D mode for 6 min per bed position (89 sections per bed) in five bed positions. MR imaging of the brain [axial T2-weighted, T1-weighted, and fluid-attenuated inversion recovery (FLAIR)] was performed along with the PET scan, then whole-body imaging (from skull base to midhigh in four bed positions, a high-resolution axial T1-weighted LAVA-Flex sequence and a coronal T2-weighted fast recovery fast spin echo [FRFSE] sequence in two planes were included) were acquired during the PET scan. Next, pelvic dedicated mpMRI images of the prostate [transverse, coronal, and sagittal T2-weighted images and diffusion-weighted spin-echo echo-planar images (b-factor, 0/1,000/1,400 s/mm^2)] were acquired along with a 10 min per bed position PET imaging. Other MR protocols were included when clinically required. The delayed pelvic PET/MR imaging was the same to the previous pelvic PET/MR. All PET data were reconstructed with TOF information, using the system's default 3D OSEM protocol iterative reconstruction algorithms with 2 iterations and 28 subsets and co-registered to MR images on a workstation (AW, GE Healthcare).

Image Analysis

PET/CT and PET/MR images were interpreted by two experienced nuclear medicine physicians using dedicated

software on the AW workstation. Visual assessment was used for characterizing PSMA-avid lesions in axial, coronal and sagittal reconstructions. Lymph nodes, bone lesions and other foci suspected of being distant metastases were evaluated first. Intraprostatic PSMA-avid foci were defined as PSMA uptake greater than the adjacent prostate gland or background on PET/CT or PET/MR, and regions of interest (ROIs) were manually drawn on PSMA-avid area or prostate bed if presented with a diffuse pattern of uptake, and maximum standard uptake value (SUVmax) were measured, the SUVmax in the conventional scan was defined as "SUVmax1," and the SUVmax in the delayed scan was defined as "SUVmax2." Capsular invasion; seminal vesicle, bladder or other adjacent organ involvement; and involvement of small pelvic lymph nodes were identified if PSMA uptake and abnormal MR signal were seen outside the boundaries of the prostate gland or corresponded to sites on PET/MR images. Version 2 of the Prostate Imaging Reporting and Data System (PI-RADS V2) was used to score prostatic regions with abnormal signal on MR images (22).

Statistical Analysis

Independent samples *t*-tests were performed to compare the mean values between the malignant group and the benign group. Paired samples *t*-tests were performed to compare SUVmax1 and SUVmax2. All the correlations were analyzed using Spearman's rank correlation test, and a scatter diagram was drawn with the regression line. Bland-Altman plots were used to assess the agreement between SUVmax1 and SUVmax2. ROC curves were generated to assess the diagnostic performance of each parameter, and to calculate a cutoff value. The sensitivity and specificity were calculated on a per-patient basis imaging diagnosis against the final clinical diagnosis. All statistical analyses were performed using SPSS Statistics, version 22 (IBM, Armonk, NY, USA). A *p* < 0.05 was considered to indicate significant difference.

RESULTS

Scanner Usage, Characteristics of Patients, and Prostatic Features in Benign and Malignant Groups

Of the 56 patients enrolled between May 2018 and January 2020. Conventional imaging began at 70.0 ± 16.9 min (PET/CT) or 74.3 ± 12.5 min (PET/MR) [*p* = 0.357] after injection. Delayed pelvic PET/MR images were acquired at 171.2 ± 37.9 min after injection. Forty patients underwent whole-body PET/CT and delayed pelvic PET/MR, 13 patients underwent whole-body PET/MR and delayed pelvic PET/MR, 3 patients underwent only whole-body PET/MR. Finally, forty-one patients were diagnosed as malignant and 15 were benign. In the malignant group, 32 patients were confirmed by histopathology, including 19 acinar adenocarcinoma, 1 ductal adenocarcinoma, 5 adenocarcinoma, and 7 prostate cancers with undefined pathological type. The other 9 patients were diagnosed by imaging and response of endocrine therapy. The benign group included benign prostatic hyperplasia (BPH) and/or prostatitis, 6 patients had biopsy results, symptoms of all patients eased and PSA level decreased

TABLE 1 | Patient characteristics and prostatic features in benign group and malignant group.

	Benign group	Malignant group	p-value
Age (y)	61.93 ± 7.41 (47–75)	71.02 ± 8.58 (52–91)	$p = 0.001$
tPSA (ng/ml)	15.67 ± 18.43 ($n = 15$)	135.98 ± 232.92 ($n = 37$)*	$p = 0.004$
fPSA (ng/ml)	2.82 ± 4.45 ($n = 14$)	11.18 ± 11.49 ($n = 35$) [#]	$p = 0.001$
fPSA/tPSA	0.164 ± 0.086 ($n = 14$)	0.132 ± 0.840 ($n = 27$)	$p = 0.247$
Prostatic SUVmax1	4.09 ± 0.96	20.31 ± 15.74	$p < 0.001$
Prostatic SUVmax2	4.63 ± 1.34	24.53 ± 16.38	$p < 0.001$
Location of lesion in prostate			
Peripheral zone	7 (46.7%)	12 (29.3%)	$p = 0.006$
Central zone	5 (33.3%)	3 (7.3%)	
Peripheral zone+central zone	3 (20.0%)	26 (63.4%)	

* 6 patients have tPSA >100 ng/ml, 2 >1,000 ng/ml; [#] 5 patients have fPSA >30 ng/ml. The limit values were used in statistics.

after anti-inflammatory or anti-prostatic hyperplasia treatment. The follow-up time was at least 1 year. The patient characteristics are listed in **Table 1**.

The differences in age, total prostate-specific antigen (tPSA), free prostate-specific antigen (fPSA), and prostatic SUVmax between the benign group and the malignant group were statistically significant. Intra-prostatic PSMA-avid foci were found in 6 patients in the benign group (40.0%) and 35 in malignant group (85.4%). In the benign group, three of six presented with symmetrical accumulation in posterior peripheral bands at the base of prostate. In six prostate cancer patients without intra-prostatic PSMA-avid foci, one had bone metastases, two had lymph node metastases, two had both lymph node and bone metastases. Representative images are shown in **Figures 1, 2**. The locations of the lesions in prostate are shown in **Table 1**; most were in the peripheral or central zone in the benign group. In the malignant group, most involved both the peripheral zone and central zone (**Figure 2**).

Characteristics of Prostatic ⁶⁸Ga-PSMA-617 Uptake and Its Correlation With Gleason Score and PSA Level

In the 53 of the 56 patients with paired conventional and delayed scans, ⁶⁸Ga-PSMA-617 uptake in the two phases was compared. In the benign group, the mean prostatic SUVmax values in the conventional and delayed scans were 3.95 ± 0.88 and 4.64 ± 1.34 ($n = 13$), respectively. No significant difference was found between the two phases ($t = -1.642$, $p = 0.127$). In the malignant group, the mean prostatic SUVmax in the conventional and delayed scans were 20.31 ± 15.74 and 24.53 ± 16.38 ($n = 40$), respectively, with a significant difference between the two phases ($t = -3.695$, $p = 0.001$). The scatter diagram of SUVmax from different scanners at different time point is shown in **Figure 3A**. Bland–Altman plots reveal a scatter diagram of the differences plotted against the means of SUVmax values

from conventional whole-body PET/CT or PET/MR with delayed pelvic PET/MR. In the benign group, the mean SUVmax has a narrow range at low levels, and the mean difference is 0.68, with the limits of agreement (LOA) between -2.26 and 3.63 . In the malignant group, mean SUVmax had a wide range, and the mean difference was 4.22, with LOA between -10.32 and 18.75 (**Figure 3B**). Good correlation was found between SUVmax1 and SUVmax2 [$r = 0.932$, $p < 0.001$, **Figure 3C**, $Y(\text{SUVmax1}) = -0.41 + 0.85 \times X(\text{SUVmax2})$]. No significant correlation was found between SUVmax and Gleason score, tPSA, and fPSA. There was a significant negative correlation between SUVmax and fPSA/tPSA ($r = 0.674$, $p = 0.039$). The scatter diagram shown in **Figure 3D** expresses Y (SUVmax1) as the result of $20.45 - 47.99 \times X$ (SUVmax2).

Gleason Score, AJCC Prognostic Stage and Primary Lesion, Involvement of Surrounding Tissues, and Distant Metastases in Patients With Prostate Cancer

Because this was a retrospective study, only 30 patients had available Gleason scores. The numbers of patients with different Gleason scores and AJCC prognostic stage are listed in **Table 2**. No significant differences were found in SUVmax among different groups according to Gleason score and AJCC prognostic stage. The higher Gleason score, the higher incidence of nodal and distant metastases. However, nodal and distant metastases also occurred even in patients with low Gleason score.

Diagnostic Performance

ROC analysis was performed to evaluate the diagnostic performance of tPSA, fPSA, and fPSA/tPSA (**Figure 4A**), SUVmax1, SUVmax2, and the difference between SUVmax1 and SUVmax2 (ΔSUVmax) (**Figure 4B**) for differentiating malignant from benign lesions. Cutoff values, sensitivity, specificity, AUC, 95% confidence interval (CI) and P -values are shown in **Table 3**. SUVmax1 from the conventional PET/CT or PET/MR revealed the best diagnostic performance with an AUC of 0.956, cutoff value of 5.25 (sensitivity, 85.4%; specificity, 100%; $p < 0.001$). So SUVmax1 was used for the following analysis. When combining SUVmax1 with nodal/distant metastases, the sensitivity improved to 95.1%. If we combine SUVmax1, nodal/distant metastases and MR PI-RADS V2, sensitivity and specificity both reached 100%.

Diagnostic Overview of All Patients in This Study

A diagnostic overview of all patients is shown in **Figure 5**. Thirty-three patients at advanced stages were diagnosed and staged by conventional whole-body PET/CT or PET/MR due to detection of bone metastases and involved lymph nodes, so pelvic PET/MR imaging of these patients would be redundant. Among the rest of the patients, delayed pelvic PET/MR was used for further evaluation. Seven had prostatic foci with SUVmax > 5.25 (**Figure 2A**), and 1 had a PI-RADS score ≥ 4 and SUVmax < 5.25 (**Figure 2B**), which were diagnosed as malignant and

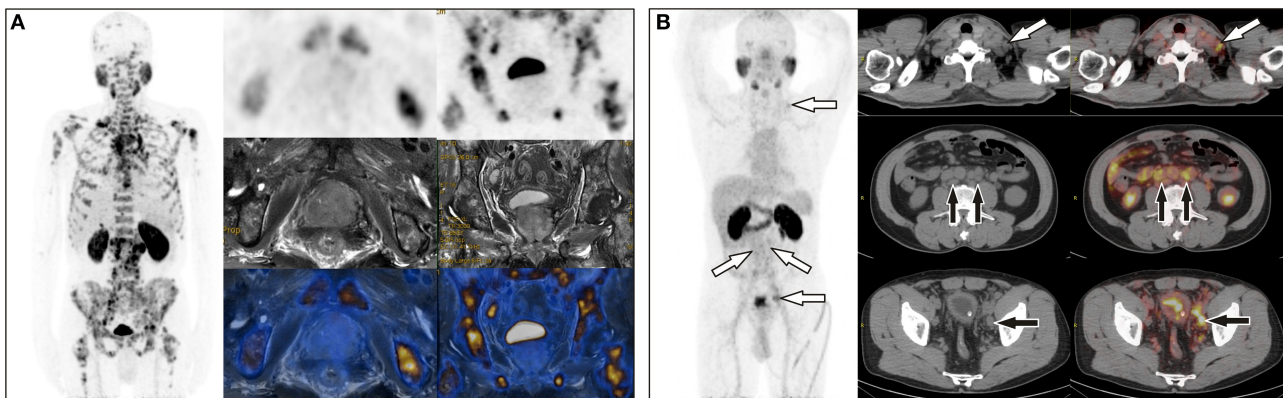


FIGURE 1 | (A) A 65-year-old man with a total PSA level of $> 1,000$ ng/L and free PSA > 30 ng/L underwent ^{68}Ga -PSMA PET/MR, which revealed extensive bone metastases but negative uptake of PSMA in the prostate. **(B)** A 64-year-old man with a total PSA level of 13.9 ng/L and free PSA of 2.15 ng/L underwent ^{68}Ga -PSMA PET/CT, which showed uptake in multiple lymph nodes in the left supraclavicular area, retroperitoneum, and the left iliac chain, but no focal uptake in prostate. Prostate acinar adenocarcinoma with left iliac lymph node metastases (6/6) were histopathologically proved.

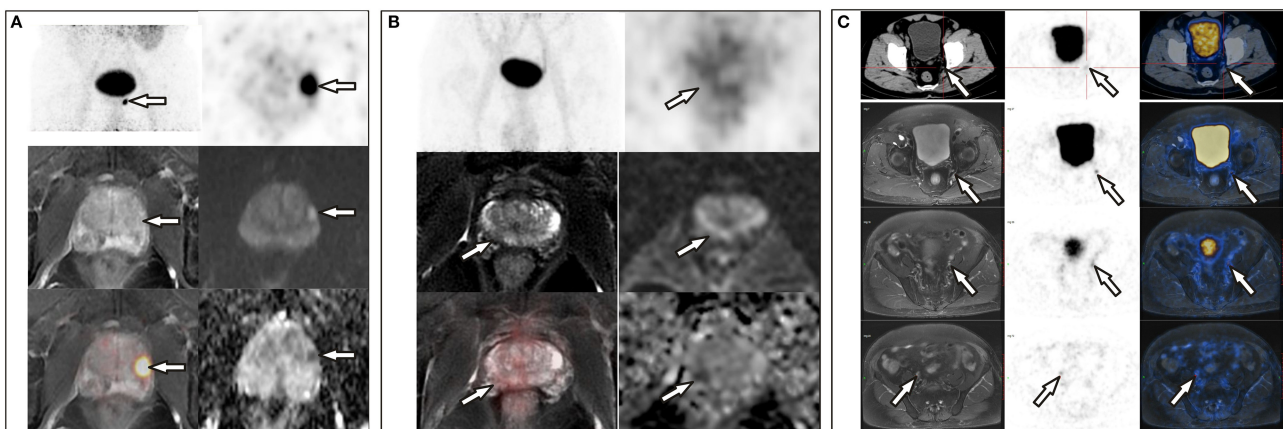


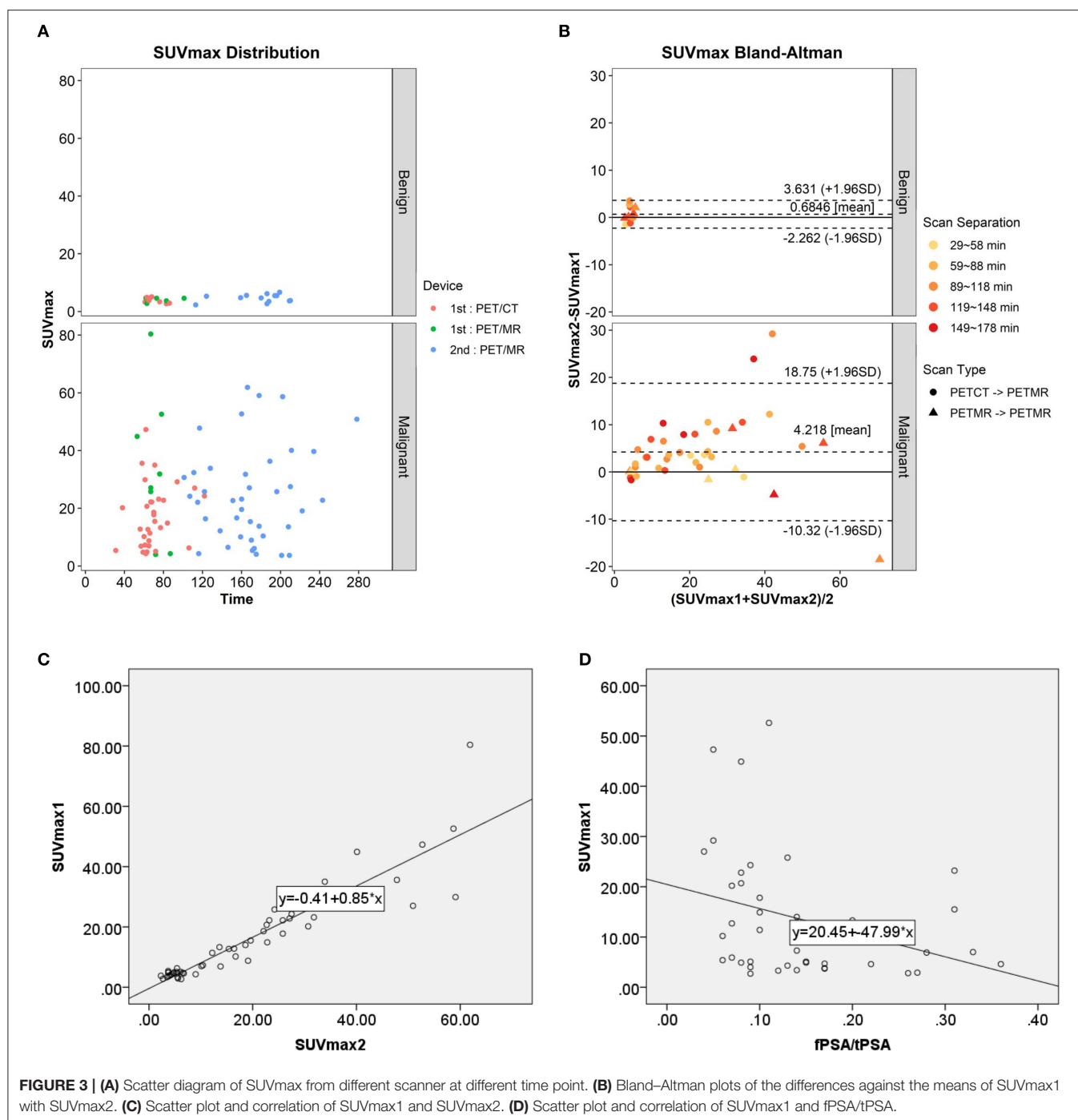
FIGURE 2 | (A) A 72-year-old man with a PSA level of 21.26 ng/L underwent ^{68}Ga -PSMA PET/CT and delayed pelvic PET/MR. Positive PSMA uptake was revealed in the left peripheral zone, consistent with the signal change in mpMR. **(B)** A 68-year-old man with proven prostate cancer in the right lobe underwent PET/MR for staging. Axial T2-weighted image shows an ill-defined hypointense lesion in the right peripheral zone with corresponding hypo-intensity on the apparent diffusion coefficient map. No significant hyperintense signal was observed on DW images ($b = 1,000$ s/mm²). This was assigned a PI-RADS score of 4, but negative PSMA uptake was observed with diffuse ^{68}Ga -PSMA uptake in the prostate (SUVmax, 4.10). **(C)** A 71-year-old man with proven prostate cancer after prostate transurethral resection, ^{68}Ga -PSMA PET/CT and pelvic PET/MR were performed for staging. PET/CT revealed only one small lymph node in the left pelvic cavity, which was revealed more clearly on PET/MR, and more lesions were revealed on PET/MR, which were proved to be metastases after surgery.

accurate staging was identified by invasion of the capsule and/or surrounding tissue provided by MR. The remaining 15 patients were diagnosed with benign disease.

DISCUSSION

This retrospective study confirmed the value of PSMA PET/CT and PET/MR in prostate disease diagnosing and staging. In this study, whole-body PET/CT (PET/MR) and delayed pelvic PET/MR accurately diagnosed and staged all of the patients. When the SUVmax from a conventional scan was used as the only criterion, sensitivity and specificity reached 85.4% and 100%, respectively. Our optimal cutoff value is 5.25, which

is close to literature reports of 5.94 (23). However, PSMA uptake in the prostate is not significantly elevated in some patients; fortunately, nodal or bone metastases were observed on PET/CT or PET/MR imaging (Figure 1), so combination of SUVmax with nodal or bone metastases further improved the sensitivity to 95.1%. There are still a few cases with neither bone, nodal metastasis nor positive prostatic PSMA uptake. In this situation, mpMRI may improve detection (Figure 2B). Combination use of nodal metastases, bone metastases, SUVmax of primary lesions, and MR PI-RADS score from whole-body PET/CT and PET/MR made the sensitivity and specificity reach 100% for prostate diseases diagnosis in this study.



Because it has been proven that the FDG SUV measured by PET/CT and PET/MR has clinically acceptable repeatability (24, 25), our PET/CT and PET/MR scanner are calibrated to ensure the accuracy of the measurements. We ignored the influence of SUV from different devices for statistics. Our results showed that SUVmax values from delayed scans were significantly higher than those from conventional scans in patients with prostate cancer, indicating tracer accumulation

increased overtime. Park, S. Y. reported similar results (26). Our results revealed SUVmax values from conventional scanning at about 1 h post injection and those from delayed scan at about 3 h are linearly correlated, which is consistent with the results reported by Ringheim et al. (27). However, they also found a mean 20% difference between PET/CT than on PET/MR (higher on PET/CT), which cannot be used interchangeably in follow-up (27). The difference between

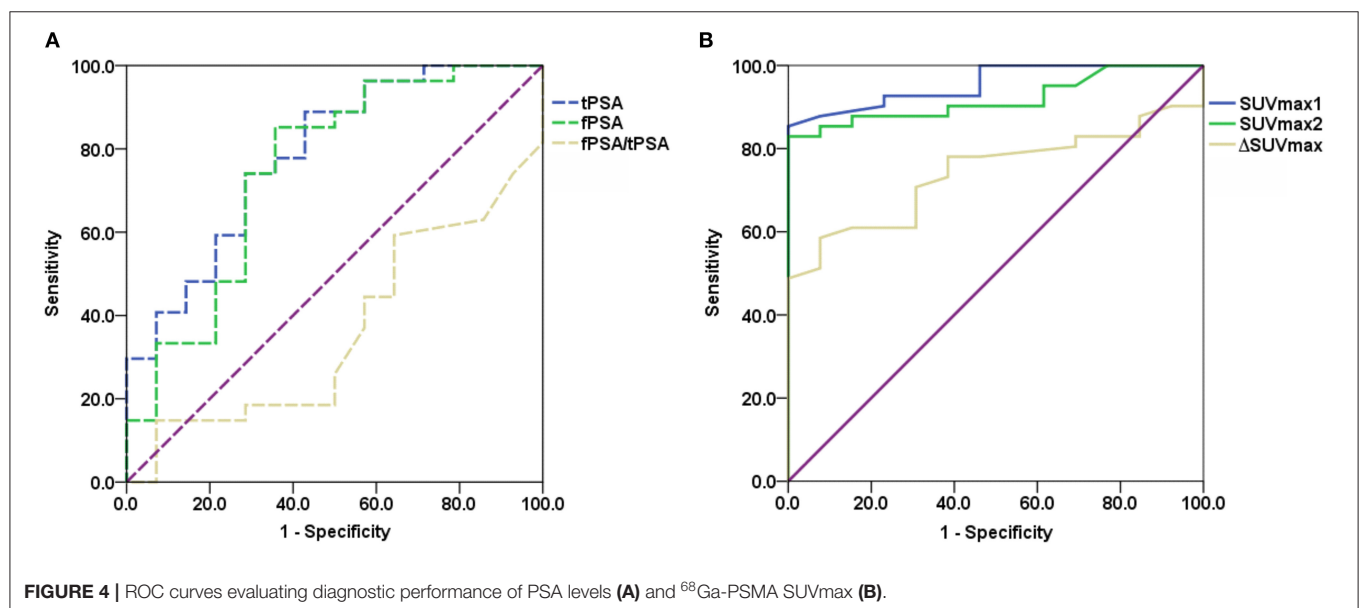
TABLE 2 | Clinical and imaging characteristics in patients with prostate cancer.

Characteristic	No.	Prostatic SUVmax	Seminal vesicle involvement	Other adjacent organ involvement*	Lymph node metastasis	Bone metastasis	Other metastases [#]
Gleason score	30	$p = 0.550$	16	8	23	13	4
1 (≤ 6)	4		0	1 (12.5%)	2 (8.7%)	3 (23.1%)	2 (50%)
2 (3 + 4 = 7)	3	24.3 ± 22.6	2 (12.5%)	0	2 (8.7%)	2 (15.4%)	1 (25%)
3 (4 + 3 = 7)	2	(GS ≤ 7)	0	0	0	0	0
4 (4 + 4 = 8)	9	17.3 ± 12.4	6 (37.5%)	4 (50%)	8 (34.8%)	2 (15.4%)	0
5 (9 or 10)	12	21.3 ± 15.9	8 (50%)	3 (37.5%)	11 (47.8%)	6 (46.2%)	1 (25%)
AJCC prognostic stage	41	$p = 0.700$	23	11	29	19	7
2A	5	20.1 ± 14.8	0	0	0	0	0
2B	3		0	0	0	0	0
4A	14	19.3 ± 12.1	10 (43.5%)	3 (37.5%)	14 (48.3%)	0	0
4B	19	21.1 ± 18.9	13 (56.5%)	8 (62.5%)	15 (51.7%)	19 (100%)	7 (100%)

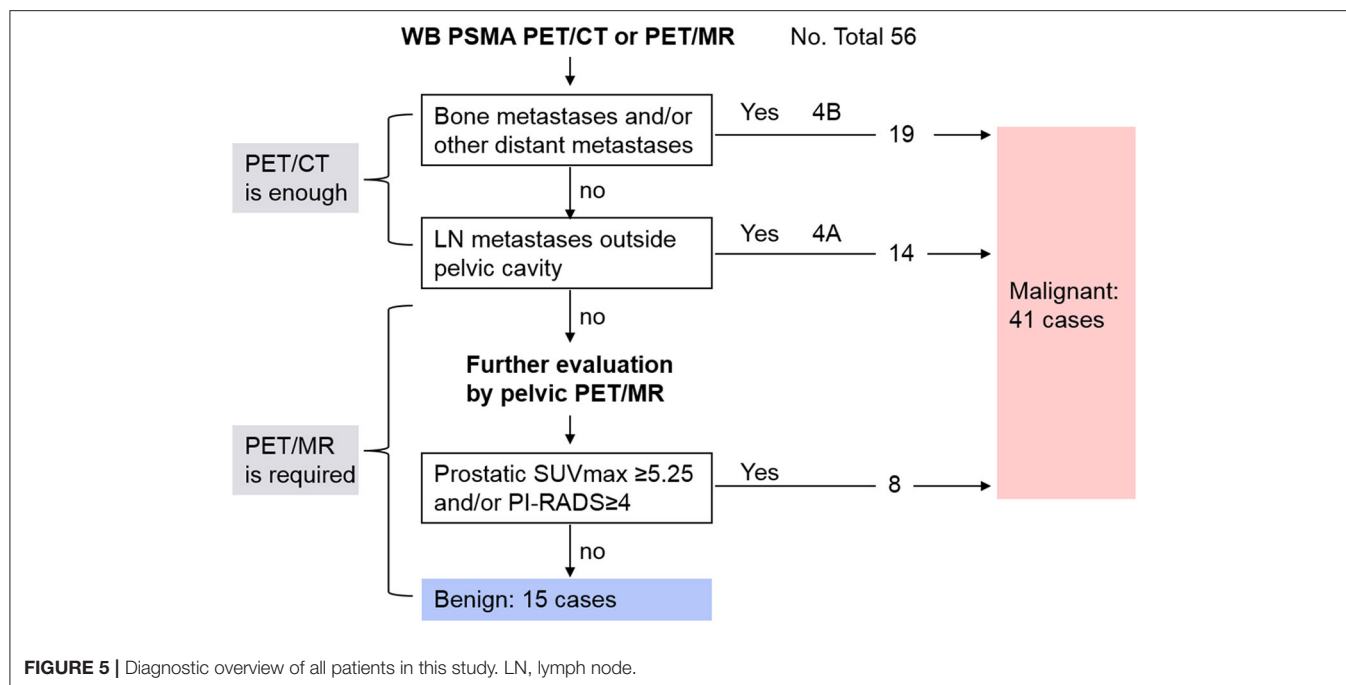
*Other adjacent organ involvement include 11 bladder involvement, 1 combined with urethra and corpus spongiosum penis involvement, 1 right ureter and rectum involvement, 1 right ureter involvement, and 1 rectum involvement.

[#]Other distant metastases include 4 patients with bilateral lung metastases, 1 patients with bilateral lung metastases and liver metastases, 2 patients with muscle metastases (1 right obturator, 1 right psoas major).

GS: Gleason score.

**FIGURE 4** | ROC curves evaluating diagnostic performance of PSA levels (A) and ⁶⁸Ga-PSMA SUVmax (B).**TABLE 3** | Diagnostic performance of several indices and its combination.

	Cut-off	sensitivity	specificity	AUC	95% CI	P
tPSA	7.73	88.9%	57.1%	0.786	0.637–0.934	0.003
fPSA	1.58	85.2%	64.3%	0.751	0.583–0.920	0.009
SUVmax1	5.25	85.4%	100%	0.956	0.907–1.000	<0.001
SUVmax2	7.85	82.9%	100%	0.919	0.848–0.991	<0.001
ΔSUVmax	0.90	70.7%	69.2%	0.742	0.614–0.870	0.009
LN/Distant metastases + SUVmax1		95.1%	100%			
LN/Distant metastases + SUVmax1+mpMR		100%	100%			



PET/CT and PET/MR devices may affect image quality and SUV measurement, therefore, a more detailed study is needed to evaluate the quantitative accuracy of PET/MR and the factors governing it.

As for the optimal timing for prostate PSMA imaging, ROC analysis shows that SUVmax1 from conventional imaging has relatively good diagnostic performance compared with delayed imaging, so we believe that conventional imaging at about 1 h is sufficient for most patients. Delayed imaging takes up time, increases patient anxiety, and may make patients with urinary retention uncomfortable, so it is not necessary on a routine basis. However, for those patients who are difficult to diagnose and whose pelvic images were affected by urine in the bladder, it is necessary to perform delayed imaging after drinking plenty of water and urinating. Some studies have analyzed multiple time-point ^{68}Ga -PSMA imaging, including early dynamic images, static scans after 60 min (conventional scan) and 180 min (delayed scan) post-injection. Kabasakal et al. (28) and Uprimny et al. (29) demonstrated that early PET/CT pelvic imaging has better lesion detectability of lesions in the pelvis than in late images because of the low incidence of halo artifact in the bladder. Another study showed that PET/MR early acquisition has high lesion contrast with very good agreement for lesion detectability with same-day whole-body PET/CT. However, 95% LOAs in SUVpeak and Metabolic Tumor Volume (MTV) are far beyond the clinically acceptable range. Therefore, they suggested whole-body PET/CT and early PET/MR should not be used interchangeably (19). Some studies compared conventional and delayed scans, and reported that detection rates were the same between 60 and 180 min, although improved contrast and an additional cancer focus was found, they concluded that delayed imaging has limited impact (26, 30).

However, Afshar-Oromieh et al. (31) reported different results: compared with 1 h after injection, 3-h images revealed higher detection rates and more lesions, but these PET-positive lesions were not confirmed by histopathology.

PSA has a certain value for the identification of benign and malignant prostate lesions (3). This study showed that the difference of fPSA/tPSA between benign and malignant groups is not statistically significant, while the differences of tPSA and fPSA between the two groups are statistically significant, but there are false positive and false negative results and the sensitivity and specificity are not as good as PSMA PET imaging. One study confirmed that SUVmax correlated significantly with PSA level (26). However, our results detected no correlation between tPSA, fPSA and SUVmax, while fPSA/tPSA was negatively correlated with SUVmax. Incomplete data maybe one reason and further study is needed.

Gleason score is a commonly used grading method for prostate cancer. However, we could not find any correlation between SUVmax of primary tumor and Gleason scores. The same results were also reported in two studies, due to inherent bias of the limited range of Gleason scores (23, 32). Our results also showed lymph node and distant metastases presented in patients with low Gleason scores, so Gleason score cannot reflect clinical stage, the possible reason may due to underestimate of the actual Gleason score from biopsy in some patients. These results suggest that imaging techniques have better performance in the detection of prostate cancer than screening techniques such as PSA, DRE, and TRUS-guided biopsy.

Despite many studies reporting the advantages of PET/MR (26, 33–35), its limitations include high expense, a relatively long whole-body scanning time, low visibility of lung lesions, and challenges in patients with claustrophobia and metal

implants. For 33 patients with advanced prostate cancer, PET/CT is enough because these patients have nodal and/or distant metastases which can be easily diagnosed by PET/CT only, and PET/CT is better for lung lesion detection, and more time-saving and economic than PET/MR, so pelvic PET/MR had no incremental value. However, to accurately stage those patients without obvious lymph node or bone involvement, to differentiate BPH or prostatitis from early stage or PSMA-negative prostate cancer, pelvic PET/MR is required mainly because of the high soft tissue resolution of MR (20). For 7 patients with $SUV_{max} \geq 5.25$, PET/MR identified whether there is invasion of the capsule and surrounding tissue, which defined T stages of disease precisely. For the 16 patients with $SUV_{max} < 5.25$, PET/MR identified one patient with PI-RADS ≥ 4 and diagnosed as prostate cancer, playing a decisive role. In the other 15 patients with benign disease, MR-based PI-RADS crosschecked with PET results to enhance diagnostic confidence. Thus, PET/MR actually played role in 43.4% (23/53) of the patients in this study. As reported, PI-RADS 3 lesions are difficult to diagnose by MR only; PET/MR improves the detection of these patients through PET (36). Therefore, whole-body PET/CT with or without pelvic PET/MR would be a sufficient, time-saving method for initial diagnosis and accurate staging of prostate cancer, rational use of pelvic PET/MR for proper patients is important. In centers with both PET/CT and PET/MR, we recommend that all patients undergo PET/CT scanning first, and if lymph node and/or bone metastases are found, the patient can be diagnosed as advanced prostate cancer and PET/MR is unnecessary. Otherwise, according to whether the image quality and prostatic lesion detectability were affected by activity of ^{68}Ga -PSMA from urine in bladder, pelvic PET/MR should be performed subsequently or at about 3 h post injection to further evaluate the prostate, surrounding tissue involvement, and small lymph nodes (Figure 2C), if the patient has no contraindications. Undoubtedly, PET/MR provides superior diagnostic performance in local prostate cancer recurrence, especially biochemical failure, compared with ^{68}Ga -PSMA-617 PET/CT (37–39).

There are some limitations to the present study. First, the number of cases, especially the patients without disseminated disease, is relatively limited. Second, due to it being a retrospective study, some patients did not have a histopathology confirmation and Gleason score, they were diagnosed through comprehensive clinical evaluation and follow-up after treatment. Third, some data are not suitable for statistical analysis, such as the results of $t\text{PSA} > 100 \text{ ng/L}$, $f\text{PSA} > 30 \text{ ng/L}$ in some patients. Fourth, the high proportion of advanced prostate cancer in this study may have affected the final results. Therefore, larger

sample-sized study with early-stage patients should be included to further evaluate the incremental value of PET/MR.

CONCLUSION

This study confirmed that a combination application of PSMA whole-body PET/CT and pelvic PET/MR can accurately distinguish BPH/prostatitis from prostate cancer and accurately stage prostate cancer. Whole-body PET/CT is sufficient to diagnose advanced prostate cancer. The value of pelvic PET/MR is for the diagnosis and accurate staging of early prostate cancer. Conventional imaging at about 1 h is recommended with no need to perform delayed imaging for most patients. Further study with more early-stage prostate cancer patients and a prospective design is needed.

DATA AVAILABILITY STATEMENT

The raw data supporting the conclusions of this article will be made available by the authors, without undue reservation.

ETHICS STATEMENT

The studies involving human participants were reviewed and approved by Human Ethics Committee of Union hospital, Tongji Medical College, Huazhong University of Science and Technology. The patients/participants provided their written informed consent to participate in this study.

AUTHOR CONTRIBUTIONS

CQ conducted the analyses and was a major contributor in writing the manuscript. YG and QL synthesized the radiopharmaceuticals and performed quality control. WR and FH acquired PET/CT and PET/MR images. FL analyzed the images. XZ provided clinical information of all patients and contributed to revision. XL conceived the idea and contributed to analysis and revision. All authors read and approved the final manuscript.

FUNDING

This work was supported by the National Natural Science Foundation of China (Grant Nos. 81873906 and 81401444).

ACKNOWLEDGMENTS

We thank Tingfan Wu from GE healthcare, Shanghai, China for providing advice about statistics.

REFERENCES

- Bray F, Ferlay J, Soerjomataram I, Siegel RL, Torre LA, Jemal A. Global cancer statistics 2018: GLOBOCAN estimates of incidence and mortality worldwide for 36 cancers in 185 countries. *CA: Cancer J Clin.* (2018) 68:394–424. doi: 10.3322/caac.21492
- Issa MM, Zasada W, Ward K, Hall JA, Petros JA, Ritenour CW, et al. The value of digital rectal examination as a predictor of prostate cancer diagnosis among United States Veterans referred for prostate biopsy. *Cancer Detect Prevent.* (2006) 30:269–75. doi: 10.1016/j.cdp.2006.04.007
- Ilic D, Djulbegovic M, Jung JH, Hwang EC, Zhou Q, Cleves A, et al. Prostate cancer screening with prostate-specific antigen (PSA) test: a systematic review and meta-analysis. *BMJ.* (2018) 362:k3519. doi: 10.1136/bmj.k3519

4. Rajinikanth A, Manoharan M, Soloway CT, Civantos FJ, Soloway MS. Trends in Gleason score: concordance between biopsy and prostatectomy over 15 years. *Urology*. (2008) 72:177–82. doi: 10.1016/j.urology.2007.10.022
5. Mohler JL, Antonarakis ES, Armstrong AJ, D'Amico AV, Davis BJ, Dorff T, et al. Prostate cancer, version 2.2019, NCCN clinical practice guidelines in oncology. *J Natl Compr Clin Oncol*. (2019) 17:479–505. doi: 10.6004/jnccn.2019.0023
6. Boustani AM, Pucar D, Saperstein L. Molecular imaging of prostate cancer. *Br J Radiol*. (2018) 91:20170736. doi: 10.1259/bjr.20170736
7. Jadvar H. Prostate cancer: PET with 18F-FDG, 18F- or 11C-acetate, and 18F- or 11C-choline. *J Nuclear Med*. (2011) 52:81–9. doi: 10.2967/jnumed.110.077941
8. Oyama N, Akino H, Suzuki Y, Kanamaru H, Sadato N, Yonekura Y, et al. The increased accumulation of [18F]fluorodeoxyglucose in untreated prostate cancer. *Japan J Clin Oncol*. (1999) 29:623–9. doi: 10.1093/jjco/29.12.623
9. Bostwick DG, Pacelli A, Blute M, Roche P, Murphy GP. Prostate specific membrane antigen expression in prostatic intraepithelial neoplasia and adenocarcinoma: a study of 184 cases. *Cancer*. (1998) 82:2256–61. doi: 10.1002/(SICI)1097-0142(19980601)82:11<2256::AID-CNCR22>3.0.CO;2-S
10. Sweat SD, Pacelli A, Murphy GP, Bostwick DG. Prostate-specific membrane antigen expression is greatest in prostate adenocarcinoma and lymph node metastases. *Urology*. (1998) 52:637–40. doi: 10.1016/S0090-4295(98)00278-7
11. Eder M, Eisenhut M, Babich J, Haberkorn U. PSMA as a target for radiolabelled small molecules. *Eur J Nuclear Med Mol Imag*. (2013) 40:819–23. doi: 10.1007/s00259-013-2374-2
12. Hillier SM, Maresca KP, Femia FJ, Marquis JC, Foss CA, Nguyen N, et al. Preclinical evaluation of novel glutamate-urea-lysine analogues that target prostate-specific membrane antigen as molecular imaging pharmaceuticals for prostate cancer. *Cancer Res*. (2009) 69:6932–40. doi: 10.1158/0008-5472.CAN-09-1682
13. Afshar-Oromieh A, Malcher A, Eder M, Eisenhut M, Linhart HG, Hadaschik BA, et al. PET imaging with a [68Ga]gallium-labelled PSMA ligand for the diagnosis of prostate cancer: biodistribution in humans and first evaluation of tumour lesions. *Eur J Nucl Med Mol Imaging*. (2013) 40:486–95. doi: 10.1007/s00259-012-2298-2
14. Maurer T, Gschwend JE, Rauscher I, Souvatzoglou M, Haller B, Weirich G, et al. Diagnostic efficacy of (68)Gallium-PSMA positron emission tomography compared to conventional imaging for lymph node staging of 130 consecutive patients with intermediate to high risk prostate cancer. *J Urol*. (2016) 195:1436–43. doi: 10.1016/j.juro.2015.12.025
15. Pyka T, Okamoto S, Dahlbender M, Tauber R, Retz M, Heck M, et al. Comparison of bone scintigraphy and (68)Ga-PSMA PET for skeletal staging in prostate cancer. *Eur J Nucl Med Mol Imaging*. (2016) 43:2114–21. doi: 10.1007/s00259-016-3435-0
16. Lenzo NP, Meyrick D, Turner JH. Review of gallium-68 PSMA PET/CT imaging in the management of prostate cancer. *Diagnostics*. (2018) 8:16. doi: 10.3390/diagnostics8010016
17. Antoch G, Bockisch A. Combined PET/MRI: a new dimension in whole-body oncology imaging? *Eur J Nucl Med Mol Imag*. (2009) 36(Suppl. 1):S113–20. doi: 10.1007/s00259-008-0951-6
18. Bouchelouche K, Choyke PL. Prostate-specific membrane antigen positron emission tomography in prostate cancer: a step toward personalized medicine. *Curr Opin Oncol*. (2016) 28:216–21. doi: 10.1097/CCO.0000000000000277
19. Domachevsky L, Bernstine H, Goldberg N, Nidam M, Stern D, Sosna J, et al. Early (68)Ga-PSMA PET/MRI acquisition: assessment of lesion detectability and PET metrics in patients with prostate cancer undergoing same-day late PET/CT. *Clin Radiol*. (2017) 72:944–50. doi: 10.1016/j.crad.2017.06.116
20. Domachevsky L, Bernstine H, Goldberg N, Nidam M, Catalano OA, Groshar D. Comparison between pelvic PSMA-PET/MR and whole-body PSMA-PET/CT for the initial evaluation of prostate cancer: a proof of concept study. *Eur Radiol*. (2020) 30:328–36. doi: 10.1007/s00330-019-06353-y
21. Nanabala R, Anees MK, Sasikumar A, Joy A, Pillai MR. Preparation of [(68)Ga]PSMA-11 for PET-CT imaging using a manual synthesis module and organic matrix based (68)Ge/(68)Ga generator. *Nucl Med Biol*. (2016) 43:463–9. doi: 10.1016/j.nucmedbio.2016.05.006
22. Weinreb JC, Barentsz JO, Choyke PL, Cornud F, Haider MA, Macura KJ, et al. PI-RADS prostate imaging - reporting and data system: 2015 version 2. *Eur Urol*. (2016) 69:16–40. doi: 10.1016/j.eururo.2015.08.052
23. Taneja S, Jena A, Taneja R, Singh A, Ahuja A. Effect of combined (68)Ga-PSMAHBED-CC uptake pattern and multiparametric MRI derived with simultaneous PET/MRI in the diagnosis of primary prostate cancer: initial experience. *AJR Am J Roentgenol*. (2018) 210:1338–45. doi: 10.2214/AJR.17.18881
24. Rasmussen JH, Fischer BM, Aznar MC, Hansen AE, Vogelius IR, Löfgren J, et al. Reproducibility of (18)F-FDG PET uptake measurements in head and neck squamous cell carcinoma on both PET/CT and PET/MR. *Br J Radiol*. (2015) 88:20140655. doi: 10.1259/bjr.20140655
25. Groshar D, Bernstine H, Goldberg N, Nidam M, Stein D, Abadi-Korek I, et al. Reproducibility and repeatability of same-day two sequential FDG PET/MR and PET/CT. *Cancer Imag*. (2017) 17:11. doi: 10.1186/s40644-017-0113-9
26. Park SY, Zacharias C, Harrison C, Fan RE, Kunder C, Hatami N, et al. Gallium 68 PSMA-11 PET/MR imaging in patients with intermediate- or high-risk prostate cancer. *Radiology*. (2018) 288:495–505. doi: 10.1148/radiol.2018172232
27. Ringheim A, Campos Neto GC, Martins KM, Vitor T, da Cunha ML, Baroni RH. Reproducibility of standardized uptake values of same-day randomized (68)Ga-PSMA-11 PET/CT and PET/MR scans in recurrent prostate cancer patients. *Ann Nucl Med*. (2018) 32:523–31. doi: 10.1007/s12149-018-1275-7
28. Kabasakal L, Demirci E, Ocak M, Akyl R, Nematyazar J, Aygun A, et al. Evaluation of PSMA PET/CT imaging using a 68Ga-HBED-CC ligand in patients with prostate cancer and the value of early pelvic imaging. *Nucl Med Commun*. (2015) 36:582–7. doi: 10.1097/MNM.0000000000000290
29. Uprimny C, Kroiss AS, Decristoforo C, Fritz J, Warwitz B, Scarpa L, et al. Early dynamic imaging in (68)Ga-PSMA-11 PET/CT allows discrimination of urinary bladder activity and prostate cancer lesions. *Eur J Nucl Med Mol Imag*. (2017) 44:765–75. doi: 10.1007/s00259-016-3578-z
30. Schmuck S, Nordlohne S, von Klot CA, Henkenberens C, Sohns JM, Christiansen H, et al. Comparison of standard and delayed imaging to improve the detection rate of [(68)Ga]PSMA I&T PET/CT in patients with biochemical recurrence or prostate-specific antigen persistence after primary therapy for prostate cancer. *Eur J Nucl Med Mol Imag*. (2017) 44:960–8. doi: 10.1007/s00259-017-3669-5
31. Afshar-Oromieh A, Sattler LP, Mier W, Hadaschik BA, Debus J, Holland-Letz T, et al. The clinical impact of additional late PET/CT imaging with (68)Ga-PSMA-11 (HBED-CC) in the diagnosis of prostate cancer. *J Nucl Med*. (2017) 58:750–5. doi: 10.2967/jnumed.116.183483
32. Woythal N, Arsenic R, Kempkensteffen C, Miller K, Janssen JC, Huang K, et al. Immunohistochemical validation of PSMA expression measured by (68)Ga-PSMA PET/CT in primary prostate cancer. *J Nucl Med*. (2018) 59:238–43. doi: 10.2967/jnumed.117.195172
33. Jena A, Taneja R, Taneja S, Singh A, Kumar V, Agarwal A, et al. Improving diagnosis of primary prostate cancer with combined (68)Ga-prostate-specific membrane antigen-HBED-CC simultaneous PET and multiparametric MRI and clinical parameters. *AJR Am J Roentgenol*. (2018) 211:1246–53. doi: 10.2214/AJR.18.19585
34. Eiber M, Weirich G, Holzapfel K, Souvatzoglou M, Haller B, Rauscher I, et al. Simultaneous (68)Ga-PSMA HBED-CC PET/MRI improves the localization of primary prostate cancer. *Eur Urol*. (2016) 70:829–36. doi: 10.1016/j.eururo.2015.12.053
35. Afshar-Oromieh A, Haberkorn U, Schlemmer HP, Fenchel M, Eder M, Eisenhut M, et al. Comparison of PET/CT and PET/MRI hybrid systems using a 68Ga-labelled PSMA ligand for the diagnosis of recurrent prostate cancer: initial experience. *Eur J Nucl Med Mol Imag*. (2014) 41:887–97. doi: 10.1007/s00259-013-2660-z
36. Chen M, Zhang Q, Zhang C, Zhao X, Marra G, Gao J, et al. Combination of (68)Ga-PSMA PET/CT and multiparametric MRI improves the detection of clinically significant prostate cancer: a lesion-by-lesion analysis. *J Nucl Med*. (2019) 60:944–9. doi: 10.2967/jnumed.118.221010
37. Burger IA, Muller J, Donati OF, Ferraro DA, Messerli M, Kranzbühler B, et al. (68)Ga-PSMA-11 PET/MR detects local recurrence occult on mpMRI in prostate cancer patients after HIFU. *J Nucl Med*. (2019) 60:1118–23. doi: 10.2967/jnumed.118.221564

38. Metser U, Chua S, Ho B, Punwani S, Johnston E, Pouliot F, et al. The contribution of multiparametric pelvic and whole-body MRI to interpretation of (18)F-fluoromethylcholine or (68)Ga-HBED-CC PSMA-11 PET/CT in patients with biochemical failure after radical prostatectomy. *J Nucl Med.* (2019) 60:1253–8. doi: 10.2967/jnumed.118.225185
39. Guberina N, Hetkamp P, Ruebben H, Fendler W, Grueneisen J, Suntharalingam S, et al. Whole-body integrated [(68)Ga]PSMA-11-PET/MR imaging in patients with recurrent prostate cancer: comparison with whole-body PET/CT as the standard of reference. *Mol Imag Biol.* (2019) 22:788–96. doi: 10.1007/s11307-019-01424-4

Conflict of Interest: The authors declare that the research was conducted in the absence of any commercial or financial relationships that could be construed as a potential conflict of interest.

Copyright © 2021 Qin, Gai, Liu, Ruan, Liu, Hu, Zhang and Lan. This is an open-access article distributed under the terms of the Creative Commons Attribution License (CC BY). The use, distribution or reproduction in other forums is permitted, provided the original author(s) and the copyright owner(s) are credited and that the original publication in this journal is cited, in accordance with accepted academic practice. No use, distribution or reproduction is permitted which does not comply with these terms.



Development of PET Radioligands Targeting COX-2 for Colorectal Cancer Staging, a Review of *in vitro* and Preclinical Imaging Studies

Caroline Dagallier^{1,2}, François Avry², Yann Touchefeu^{3,4}, Frédéric Buron⁵, Sylvain Routier⁵, Michel Chérel³ and Nicolas Arlicot^{1,2,6*}

¹ Unité de Radiopharmacie, CHRU de Tours, Tours, France, ² Inserm UMR1253, iBrain, Université de Tours, Tours, France, ³ CRCINA, INSERM, CNRS, Nantes University, Nantes, France, ⁴ Institut des Maladies de l'Appareil Digestif, University Hospital, Nantes, France, ⁵ ICOA, Université d'Orléans, UMR CNRS 7311, Orléans, France, ⁶ INSERM CIC 1415, CHRU de Tours, Tours, France

OPEN ACCESS

Edited by:

Anil Kumar Mishra,
Institute of Nuclear Medicine & Allied
Sciences (DRDO), India

Reviewed by:

Linjing Mu,
ETH Zürich, Switzerland
Zhen Cheng,
Stanford University, United States
Neil Vasdev,
Centre for Addiction and Mental
Health (CAMH), Canada

*Correspondence:

Nicolas Arlicot
nicolas.arlicot@univ-tours.fr

Specialty section:

This article was submitted to
Nuclear Medicine,
a section of the journal
Frontiers in Medicine

Received: 02 March 2021

Accepted: 03 May 2021

Published: 08 June 2021

Citation:

Dagallier C, Avry F, Touchefeu Y, Buron F, Routier S, Chérel M and Arlicot N (2021) Development of PET Radioligands Targeting COX-2 for Colorectal Cancer Staging, a Review of *in vitro* and Preclinical Imaging Studies. *Front. Med.* 8:675209. doi: 10.3389/fmed.2021.675209

Colorectal cancer (CRC) is the second most common cause of cancer death, making early diagnosis a major public health challenge. The role of inflammation in tumorigenesis has been extensively explored, and among the identified markers of inflammation, cyclooxygenase-2 (COX-2) expression seems to be linked to lesions with a poor prognosis. Until now, COX-2 expression could only be accessed by invasive methods, mainly by biopsy. Imaging techniques such as functional Positron Emission Tomography (PET) could give access to *in vivo* COX-2 expression. This could make the staging of the disease more accurate and would be of particular interest in the exploration of the first metastatic stages. In this paper, we review recent progress in the development of COX-2 specific PET tracers by comparing the radioligands' characteristics and highlighting the obstacles that remain to be overcome in order to achieve the clinical development of such a radiotracer, and its evaluation in the management of CRC.

Keywords: COX-2, PET, colorectal cancer, radioligands, preclinical model

INTRODUCTION

Colorectal cancer (CRC) is one of the most frequent types of cancer, ranking second in most developed countries, and has the second highest mortality rate (1, 2). This rate is especially high for late diagnosis and advanced stage disease. Thanks to an increase in CRC screening, the incidence rate has been decreasing for the last two decades (2). However, this high mortality rate draws early detection of CRC and prediction of recurrences and metastases as two major public health challenges, in order to initiate the appropriate treatment as early as possible.

Inflammation seems to play a key role in CRC pathophysiology. Among the many known markers of inflammation, cyclooxygenase-2 (COX-2) was identified as having a crucial role from the first stages of tumorigenesis (3, 4). Reviews of over 30 epidemiologic studies showed that regular consumption of non-steroidal anti-inflammatory drugs (NSAID) was associated with a 30–50% reduced incidence of several cancer types, including CRC (5, 6). Interestingly, patients with familial adenomatous polyposis receiving COX-2 inhibitors as a preventive treatment developed fewer adenomas than patients receiving a placebo (7).

COX-2 is an enzyme that intervenes in the first steps of prostaglandin E2 synthesis from arachidonic acid and can be induced by various pro-inflammatory signals. COX-2 overexpression has been identified in different malignant neoplastic tissues, especially in up to 85% of adenocarcinomas (8–10) and is also associated with the potential for progression and recurrences of colorectal tumors. Molecular biology studies on CRC tissue samples concluded that COX-2 expression is significantly correlated with invasive (11) and metastatic phenotypes (12, 13). Moreover, high COX-2 expression in patients treated with radical surgery is a prognostic factor for recurrences, mainly because of undetected metastasis (13, 14). The COX-2 expression level is high in CRC cells. On the contrary, COX-2 has a low basal expression in healthy colon epithelial cells (15), making COX-2 a relevant biomarker for molecular imaging, especially for Positron Emission Tomography (PET).

The correlation of elevated COX-2 expression with the first stages of tumorigenesis and cancer progression suggests that COX-2 could be a target for the early imaging of pre-cancerous colorectal lesions. Since inflammation seems to be a hallmark of malignant CRC, PET imaging could allow the early detection of CRC dissemination and thus spot metastasis. In addition, in other cancerous pathologies (breast, prostate), COX-2 expression increases with the stage of the disease (16, 17). PET-scanning could therefore be a tool for CRC staging. Furthermore, positive therapeutic results in cohorts of patients with different types of solid tumors receiving COX-2 inhibitors in addition to their respective standard chemotherapy (18–20) suggest that COX-2 molecular imaging could provide stratification of the patients, enabling individualized treatment approaches. Notably, it could help to decide whether neoadjuvant chemotherapy is needed or determine whether patients would respond to COX-2 inhibitors therapy.

Up to now, numerous radioligands targeting COX-2 have been developed for SPECT or PET applications. Reviews by Laube et al., de Vries et al., and Pacelli et al., summarized their structures and synthesis methods and highlighted the challenges encountered in the development of COX-2 radiotracers (21–23). In the present review, we explore the recent progress of COX-2 molecular imaging in CRC, by comparing the radioligands' characteristics and highlighting the obstacles that remain to be overcome in order to achieve the clinical development of such a radiotracer.

The PubMed database was screened using pre-defined search dates (January 1995–January 2021). The search terms used were as follows: “colorectal cancer” and “COX-2” or “cyclooxygenase 2” and “PET.” It yielded 78 results. We screened preclinical results performed only on colorectal cancer cell lines. Title-, abstract- or full text-reading led to the exclusion of 70 papers because they did not focus on CRC or did not include *in vivo* PET radioligand evaluation or did not target COX-2. Eight original papers fulfilled these criteria and were thus included in the scope of the present review. Chemical structures of the PET radioligands are presented. The main conditions and results of these PET imaging preclinical studies assessing COX-2 radiotracers in CRC xenograft models are summarized in **Table 1**.

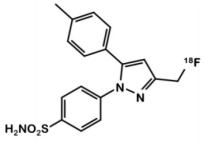
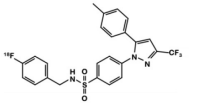
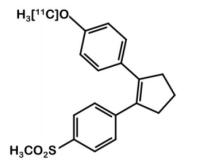
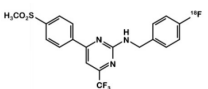
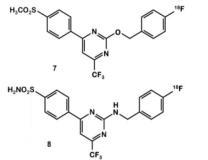
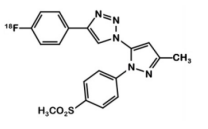
COXIB FAMILY DERIVATIVES

Celecoxib **1** (**Figure 1**) is a well-known COX-2 specific inhibitor used as an anti-inflammatory drug. Its specificity and selectivity for COX-2 over COX-1 makes it a natural candidate for PET applications. In 2005, Prabhakaran et al. synthesized ^{11}C -Celecoxib **2** (**Figure 1**) in 8 efficient steps including a palladium catalyzed radiomethylation (32), but this radioligand has not yet been tested in a CRC preclinical model. A biodistribution study in baboons showed unsatisfactory pharmacokinetic properties. ^{11}C -**2** underwent a fast metabolism (80% after 30 min in plasma samples) and was quickly cleared out of the organism by urinary excretion (33). Therefore, several series of celecoxib derivatives were proposed to work around the limitations of celecoxib. In 2011, Uddin et al. developed a series of celecoxib [^{18}F]-fluorine derivatives (24). Synthesis in 7 steps involving an aliphatic nucleophilic substitution led to the best candidate. Diethylaminosulfurtrifluoride (DAST) mediated fluorination of its alcohol precursor gave the fluoromethyl derivative ^{18}F -**3** (**Figure 2**). In inhibition assays using purified COX-2, ^{18}F -**3** exhibited an IC_{50} of 160 vs. 30 nM for **1**. *In vivo* evaluation was conducted in a Nu-fox1nu mice model bearing human head and neck squamous cell carcinoma cells HNSCC 1483 (COX-2+) or human colorectal carcinoma cells HCT-116 (COX-2-). A biodistribution study gave promising results, with an uptake ratio in COX-2 positive/COX-2 negative tumors of 3, similar to the COX-2+ tumor to muscle ratio (T/M). Blocking experiments with cold celecoxib produced a clear decrease of the radiotracer uptake in the COX-2+ tumor (T/M = 1). However, only the COX-2 negative tumors were CRC cells (HCT-116); the COX-2 positive model was a xenograft of human head and neck squamous cell carcinoma.

In 2015, Kaur et al. synthesized a radiolabeled derivative ^{18}F -**4** from a key sulfonylchlorine and its amination by the prosthetic 4- [^{18}F]fluorobenzylamine scaffold (25) (**Figure 3**). Derivative **4** exhibited interesting *in vitro* properties on human recombinant COX-2 (log P = 3.18; IC_{50} = 360 vs. 40 nM for **1**) but suffered from a lack of specificity. Indeed, cellular uptake experiments in human CRC cells expressing COX-2 (HCA-7) showed an accumulation of the radioligand that could not be inhibited by a celecoxib or rofecoxib pre-treatment. *In vivo*, NIH-III mice xenografted with HCA-7 cells exhibited a maximum tumor to muscle ratio 10 min post injection (p.i.) of 1.4, slowly decreasing over time. Dynamic acquisitions showed a rapid elimination of the radioactivity through the intestinal tract. *In vitro* results were not convincing, and specificity was not investigated *in vivo*.

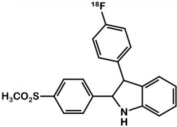
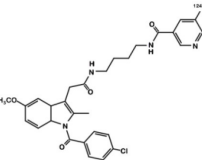
Other teams focused on different coxib-like derivatives. Derivative **5** was first studied by Li et al. and exhibited a very promising COX-2 affinity, with an IC_{50} in the range of the nanomolar concentration (IC_{50} = 5 nM) and a high *in vitro* selectivity for COX-2 over COX-1 (COX-1/COX-2 = 2,000) (34). Wuest et al. synthesized the [^{11}C]methoxy-1,2-diarylcyclopentene ^{11}C -**5** in 4 steps from 2-dibromocyclopentene using a double Suzuki cross coupling and as final step a Williamson type O-methylation with [^{11}C]CH₃I (26) (**Figure 4**). The authors confirmed the specificity of compound **5** for COX-2 with cellular uptake studies (especially in the COX-2+

TABLE 1 | Summary of characterization studies assessing COX-2 PET radiotracers in CRC xenograft models.

Radioligand	Structure	Parent molecule	<i>In vitro</i> models/cell lines	IC ₅₀ (μM)	<i>In vitro</i> results	<i>In vivo</i> model	<i>In vivo</i> results	References
¹⁸F-3 Fluoromethyl-celecoxib		Celecoxib	COX-2-: HCT-116 COX-2+: RAW 264.7*	0.16	Affinity in the range of celecoxib's (IC ₅₀ = 0.03 μM). No blocking experiment available.	NU-Fox1nu mice bearing 1483 or HCT-116 cells	3-fold higher accumulation in the COX-2+ expressing tumor vs. COX-2- or muscle. Accumulation was inhibited by celecoxib pre-treatment	(24)
¹⁸F-4 fluoromethyl-celecoxib derivative		Celecoxib	COX-2+: HCA-7	0.36	Significant uptake after 60 min. No inhibition observed after pre-treatment with celecoxib	NIH-III mice bearing HCA-7 cells	Maximum T/M ratio of 1.4 10 min p.i. High intestinal uptake.	(25)
¹¹C-5 [11C]methoxy-1, 2-diarylcyclopentane		Coxib-like	COX-2-: RAW264.7 COX-2+: HT-29	0.005	High selectivity for COX-2 over COX-1 (x2000). In HT-29 cell cultures, Celecoxib pre-treatment reduced radioactivity uptake by 40% to 60%.	NMRI nu/nu mice bearing HT-29 cells	T/M ratio of 1.7 (60 min p.i.) Poor specificity (no effect of pre-treatment with a non-radioactive competitor). Fast metabolism (98 % eliminated 60 min p.i.). High intestinal and fat tissue uptake	(26)
¹⁸F-6 Pyricoxib		Celecoxib	COX-2-: HCT-116 COX-2+: HCA-7	0.007	Better <i>in vitro</i> affinity and specificity than its parent, celecoxib. Higher uptake in HCA-7 cells than HCT-116 cells. Maximum uptake reduction of 65% when pre-treated with non-radioactive coxib.	NIH-III nude mice bearing HCA-7 xenografts with or without celecoxib pre-treatment. Control group: NIH-III nude mice bearing HCT-116 cells.	50% decrease of radiotracer uptake in COX-2+ tumors after pre-treatment with celecoxib. T/M ratio of 2.25 (4 h p.i.) High intestinal uptake.	(27)
¹⁸F-6-8		Celecoxib	COX-2+: HCA-7	6: 0.007 7: 0.039 8: 0.02	Similar <i>in vitro</i> properties (lipophilicity, affinity, specificity). Higher uptake for compound 6 > 7 > 8.	HCA-7 xenografts administered to NIH-III nude mice	PET acquisitions displayed a substantially higher uptake of [¹⁸F] 6 than 7 and 8, with a T/M ratio of 1.19 (1 h p.i.). High intestinal uptake	(28)
¹⁸F-9 Triacoxib		5-azido-pyrazole	COX-2+: HCA-7	0.09	COX-2/COX-1 selectivity ratio > 1,000. Pre-treatment with celecoxib induced a decrease of 47% in the uptake.	NIH-III mice bearing HCA-7 xenograft	Pre-treatment with celecoxib induced a decrease of 20% of the uptake. T/M ratio of 1.49 (1 h p.i.). Unspecific binding in lipid rich tissues.	(29)

(Continued)

TABLE 1 | Continued

Radioligand	Structure	Parent molecule	<i>In vitro</i> models/cell lines	IC ₅₀ (μM)	<i>In vitro</i> results	<i>In vivo</i> model	<i>In vivo</i> results	References
¹⁸F-10		2,3-diaryl indole based on COX-2 inhibitors	COX-2+: HT-29	1.2	High uptake in COX-2+ cell lines. Pre-treatment with celecoxib induced a decrease of 80% in the uptake. Low specificity (COX-2/COX-1 ratio of 5.5);	NMRI nu/nu mice bearing HT-29 xenografts	No substantial accumulation of the radioligand in COX-2+ xenografts. High intestinal uptake.	(30)
¹²⁵I-12/¹²⁴I-12 indomethacin amide		indomethacin	COX-2 Celecoxib: HCT-116 COX-2+: HT-29, HEK, HUVEC	/	¹²⁵I-12 COX-2+/COX-2- uptake ratio of 7.6 Pre-treatment with celecoxib induced a decrease of 70% in the uptake.	HT-29 and HCT-116 xenografted SCID mice	¹²⁴I-12 Normalized uptake (kBq/g tissue) was approximately 5-fold higher in HT-29 tumors than in HCT-116 tumors. T/M ratio was more than 50-fold higher in HT-29 xenografts compared to HCT-116 xenografts. μPET imaging highlighted a predominantly intestinal uptake (no quantitative results available).	(31)

The table summarizes for each probe: chemical structure, parent molecule, IC₅₀, cell lines used for *in vitro* studies and conclusion of these studies, models used for preclinical studies and conclusions, reference article. Cell lines with high COX-2 expression: HT-29, Human colorectal adenocarcinoma cells; HCA-7, Human colon adenocarcinoma cells; HUVEC, human umbilical vein endothelial cell; HEK, human embryonic kidney. Cell lines with low COX-2 expression: HCT-116, human colorectal carcinoma cells; *RAW264.7, murine macrophage cell line. Low basal COX-2 expression, but that can be induced, for instance with γ-interferon and lipopolysaccharide.

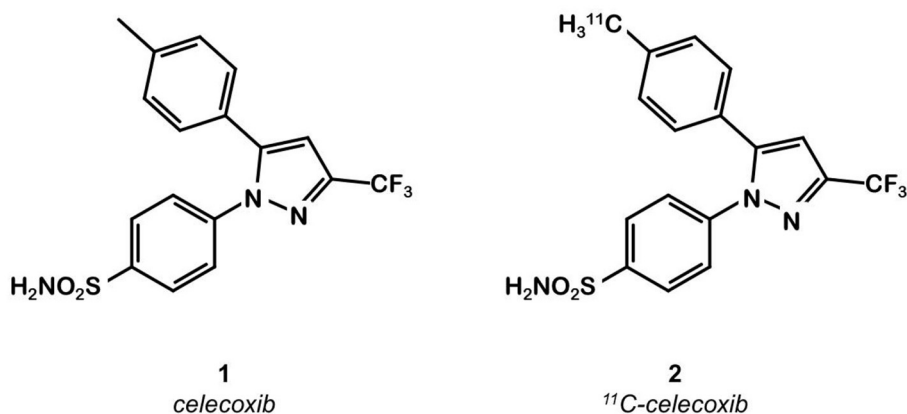


FIGURE 1 | Celecoxib and ^{11}C -celecoxib structures.

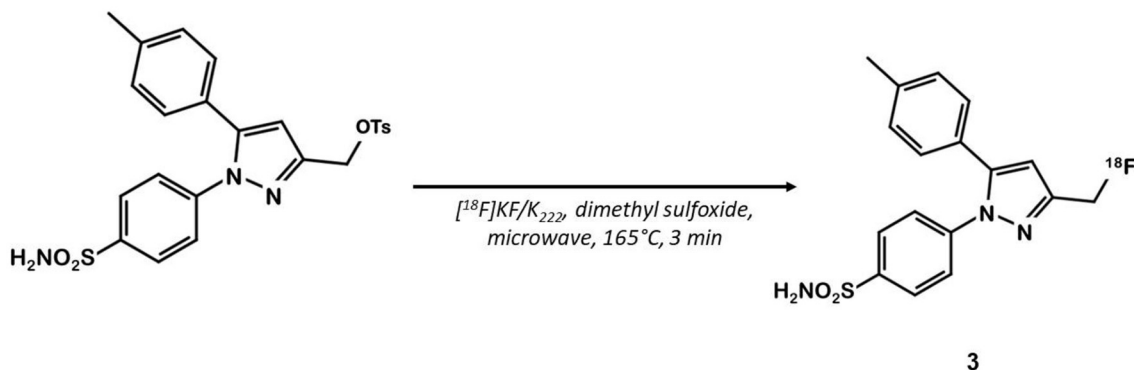


FIGURE 2 | Radiosynthesis of pyrazole derivative ^{18}F -3.

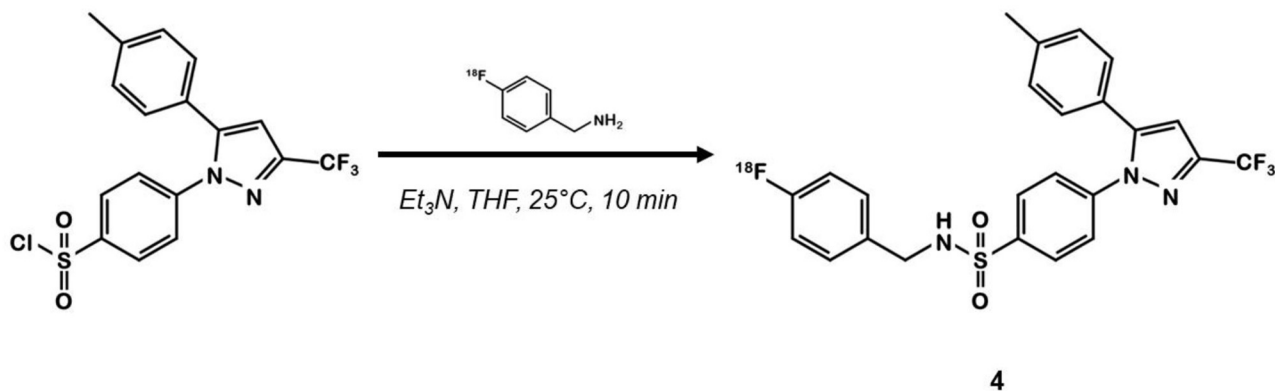


FIGURE 3 | Radiosynthesis of pyrazole derivative ^{18}F -4.

human colorectal adenocarcinoma cell line HT-29 vs. COX-2-RAW264.7). Its lipophilicity of 4.2 enabled it to cross the cell membranes but might be responsible for a lack of specificity *in vivo*. In fact, *in vivo* assays on a preclinical rodent xenograft model of human CRC cells (HT-29 cells, COX-2+) exhibited

an accumulation of the tracer in the tumor, that could not be inhibited in blocking experiments with an excess of non-radioactive competitor. Moreover, this radiotracer was quickly metabolized, with only 17% remaining intact in plasma samples 10 min p.i.

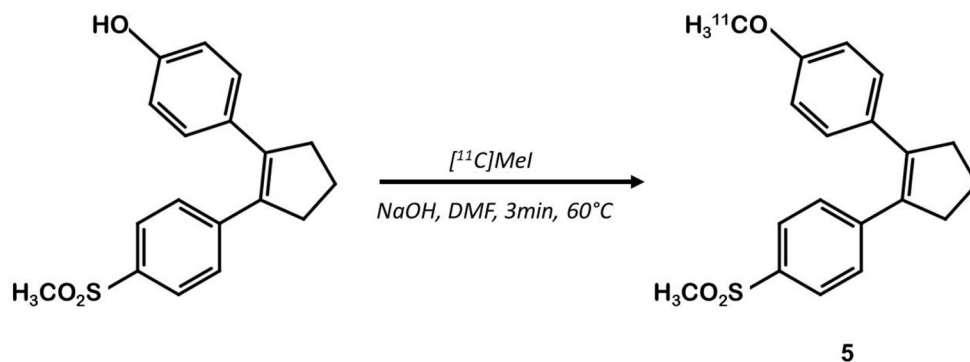


FIGURE 4 | Radiosynthesis of [^{11}C]diaryl cyclopentene 5.

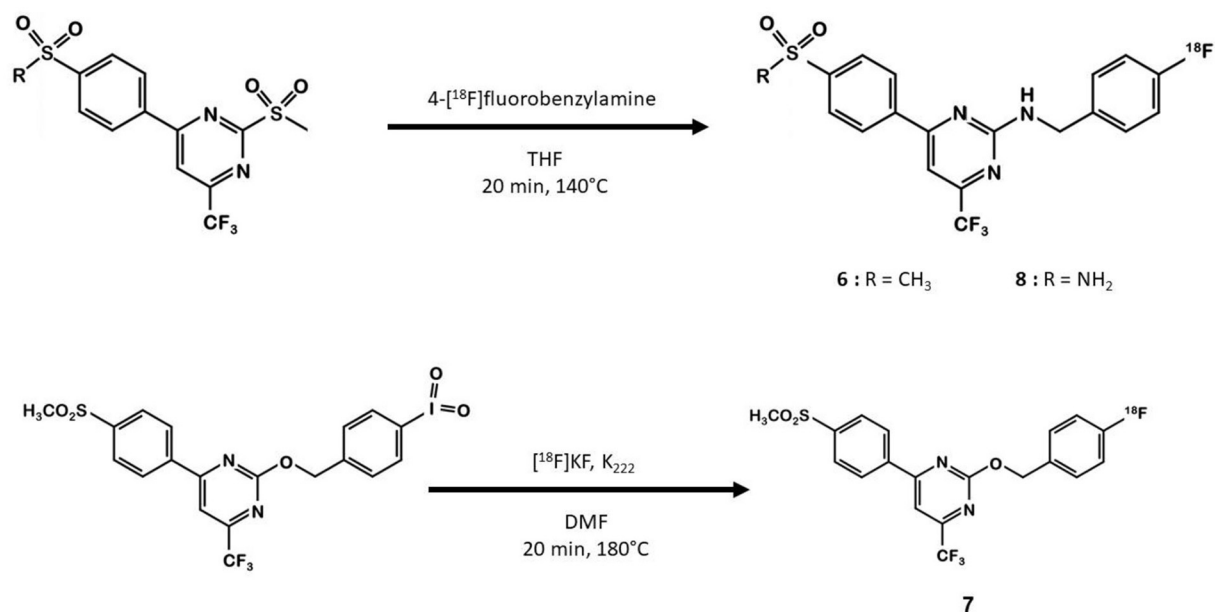
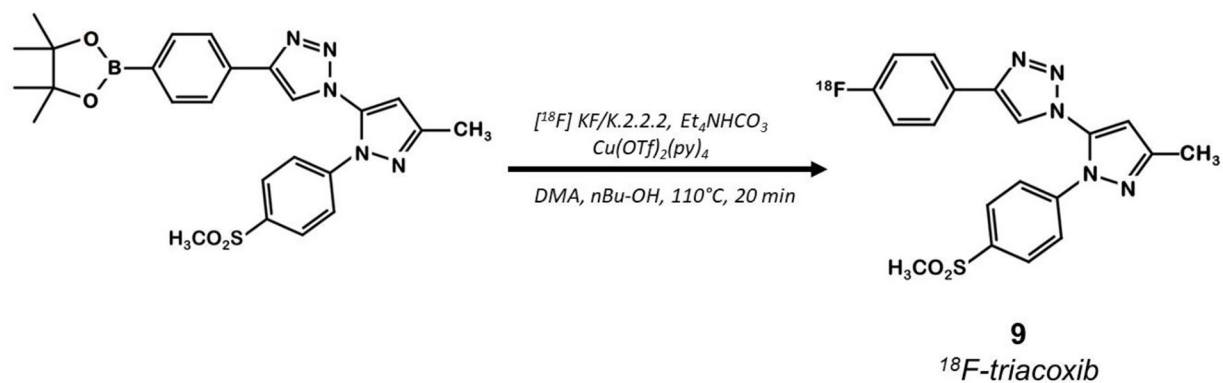
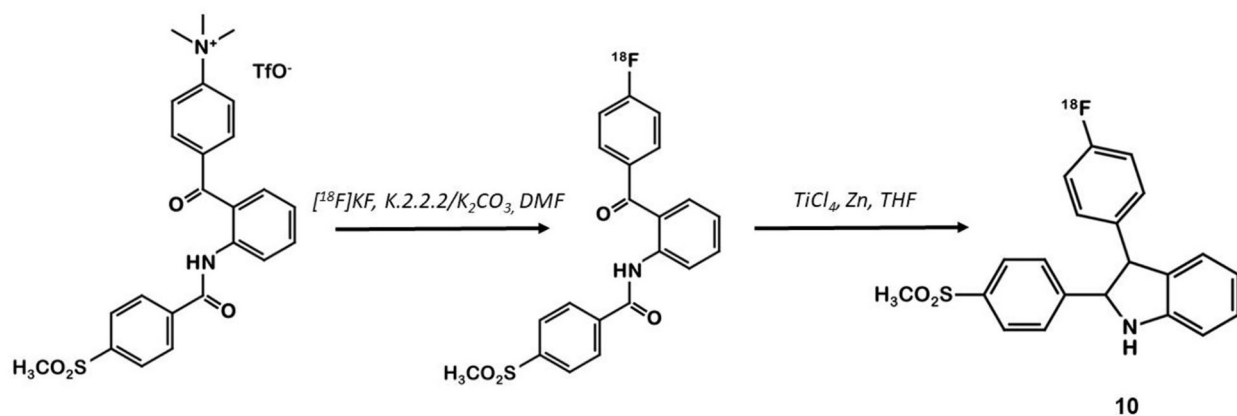
In 2013, Tietz et al. developed ^{18}F -Pyricoxib **6**, designed by replacing the celecoxib pyrazole ring by a pyrazine isoster (35). In 2016, Tietz et al. proved that derivative **6** showed better *in vitro* affinity and specificity than its parent Celecoxib **1** ($\text{IC}_{50} = 7$ vs. 40 nM for **1**) (27). *In vitro* blocking experiments in HCA-7 and HCT-116 cells were promising. Radiotracer uptake in COX-2 positive cells (HCA-7) was significantly higher than in COX-2 negative cells (HCT-116), and pre-treatment with diverse non-radiolabeled COX-2 inhibitors led to a maximum uptake reduction of 65%. *In vivo* experiments were then conducted on NIH-III mice xenografted with either HCA-7 or HCT-116 cells, showing a satisfactory uptake in HCA-7 tumors (T/M ratio of 2.25 after 4 h p.i.). Pre-treatment with 2 mg of Celecoxib **1** (intraperitoneal administration, i.p.) led to a marked decrease in radiotracer uptake in the tumors. Biodistribution results showed a %ID/g of 2.12% in HCA-7 tumors, scaled down to 1.04% after a celecoxib pretreatment. However, radiotracer uptake was similar in HCA-7 and HCT-116 tumors. Expression of COX-2 in HCT-116 tumors was confirmed by immunohistochemistry, highlighting a cell line drift and questioning the relevance of the HCT-116 cell line as a COX-2 negative model. They concluded that ^{18}F -pyricoxib **6** was a very promising candidate for a “first in human” study (27). In 2018, Tietz et al. deepened their understanding of this chemical entity by performing pharmacomodulation experiments (28). For the O-analog ^{18}F -7 the radiolabeling was carried out on a preoxidized iodyl precursor. The authors started from 4-chloro-2-(methylsulphonyl)-6-(trifluoromethyl)pyrimidine after 5 steps including radiolabeling with 4- ^{18}F fluorobenzylamine. ^{18}F -**8** radiosynthesis was similar to that of ^{18}F -pyricoxib **6**, using sulfonyl precursors and a 4- ^{18}F fluorobenzylamine (FBA) as building block (Figure 5). The three tested probes ^{18}F -**6**-**8** exhibited similar *in vitro* properties (lipophilicity, affinity, specificity for COX-2). However, even slight modifications of the structure led to radically different pharmacokinetic, biodistribution and uptake profiles (Table 1). One of the radiotracers was slightly metabolized and excreted *via* the urinary tract but did not accumulate in the tumors, while the other was rapidly eliminated but had a better T/M ratio.

The same team developed a pyricoxib derivative to reduce this unspecific binding previously observed with ^{18}F -pyricoxib

6 (29). They designed ^{18}F -triacoxib **9** which was obtained from the Celecoxib **1** structure by replacing the CF_3 by a CH_3 group and the acidic sulfonylamide by a simple methylsulfonyl. Nevertheless, the best innovation in this series consisted in the insertion of a triazole between the pyrazole and the phenyl ring, which required building an azidopyrazole as key intermediate. Noteworthy, ^{18}F -fluorination was achieved using a pinacol boronic ester (in the presence of a copper catalyst $[\text{Cu}(\text{OTf})_2(\text{py})_4]$) as leaving group (Figure 6). Compound **9** displayed a satisfactory *in vitro* affinity and selectivity for COX-2 ($\text{IC}_{50} = 90$ vs. 70 nM for **1**; IC_{50} COX-1 > 100 μM for both compounds, HCA-7 cells). *In vitro* binding experiments with increasing doses of non-radiolabeled compounds (celecoxib or triacoxib) resulted in an inhibition of the radiotracer uptake by 47 to 63%. *In vivo* experiments on BALB/c mice bearing HCA-7 xenografts suggested an improved stability of ^{18}F -triacoxib **9** compared to ^{18}F -pyricoxib **6** (respectively, 90 vs. 75% intact radiotracer in plasma samples 60 min p.i.). PET acquisitions confirmed a higher uptake in the tumors than in the muscle, within a similar range as ^{18}F -pyricoxib **6** (tumor-to-muscle ratio of 1.49 vs. 1.47, respectively, 60 min p.i.). In Celecoxib **1** pretreated mice, a partial inhibition of ^{18}F -triacoxib **9** uptake was observed (20%). Unspecific binding was also observed in lipid rich tissues. ^{18}F -triacoxib **9** did not seem to be a better candidate than ^{18}F -pyricoxib **6** as a diagnostic tool for CRC.

2,3-DIARYL INDOLES

In 2003, Hu et al. synthesized a large series of original 2,3-diaryl indoles (36). Structure-Activity Relationships (SAR) were established from about thirty derivatives obtained from anthranilic acids in 5 or 6 steps including indole formation by McMurry cyclization (Figure 7). Derivative **10** exhibited high affinity and selectivity for COX-2 ($\text{IC}_{50} = 20$ vs. 520 nM for **1**) over COX-1 ($\text{IC}_{50} > 10$ μM for both compounds), and better anti-inflammatory properties than celecoxib in a rat carrageenan-induced foot pad edema assay. In 2012, Kniess et al. radiolabeled this promising compound using the nucleophilic substitution of a trimethylammonium salt by ^{18}F -fluorine (30). They investigated the determination of PGE2 levels in cell culture supernatants, which is therefore a direct measure of the COX

FIGURE 5 | Radiosynthesis of ^{18}F -6-8 probes.FIGURE 6 | Radiosynthesis of ^{18}F -Triacoxib 9.FIGURE 7 | Radiosynthesis of ^{18}F -10 via McMurry cyclisation.

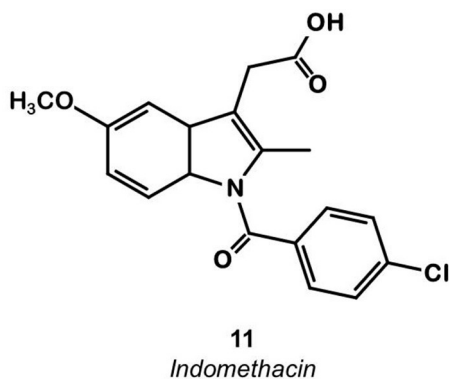


FIGURE 8 | Indomethacin.

activity. The cellular inhibition assay results demonstrated **10** to be a potent cyclooxygenase inhibitor with only low COX-1/COX-2 selectivity. The authors evaluated the selectivity of **10** using an enzymatic competitive inhibition assay with celecoxib as reference. $IC_{50} = 6.6 \mu M$ for COX-1 and $1.2 \mu M$ for COX-2 were determined (IC_{50} COX-1 = 115 and $0.06 \mu M$ for **1**). Pre-incubation of HT-29 cells with cold compound reduced the cellular uptake by almost 80% compared to incubation with the radioactive compound alone. *In vivo* PET imaging of HT-29 xenografted mice showed no accumulation of the tracer in the tumor. Despite a low lipophilicity ($\log D = 1.2$), the tracer was rapidly eliminated through the intestinal tract (half-life: 8 min).

INDOMETHACIN DERIVATIVES

Indomethacin **11** (Figure 8) is a COX ligand that binds to both COX-1 and COX-2. Kalgutar et al. modified its chemical structure by adding an amide group (37). After SAR analysis and the building of nearly twenty analogs, they clearly improved the selectivity of the derivatives for COX-2, which was inhibited in the nanomolar range. Following this work, Morgenroth et al. synthesized radio iodinated analogs from stannyl precursors (31). Derivative ^{125}I -**12** (Figure 9) was found to be the most suitable tracer. *In vitro* studies on CRC cell cultures HT-29 and HCT-116 showed a significantly higher concentration of **12** in COX-2 positive (HT-29) cells (COX-2+/COX-2- ratio of 2.5 and 7.6 for the two tested radiotracers). Blocking experiments were performed on human embryonic kidney (HEK) and human umbilical vein endothelial cell (HUVEC) cell lines, showing a partial decrease of the uptake in cells pre-treated with celecoxib **1**. These affinities and selectivities were confirmed using both *in vivo* microPET and bio-distribution studies. The compound with the highest uptake was radiolabeled with ^{124}I and used for PET imaging of HT-29 and HCT-116 xenografted mice. Due to the lipophilicity of this compound ($\log D = 4.41$), the radioactivity was mainly localized in the liver and the gastrointestinal tract. No tracer uptake was observed in HCT-116 tumors whereas HT-29 tumors displayed a significant uptake. Measurement of

the remaining activity in each organ with a gamma counter confirmed a COX-2+/COX-2- ratio of 5. The T/M ratio was over 50 times higher in HT-29 tumors than in HCT-116 tumors.

In 2011, Uddin et al. also synthesized a series of fluorine-containing indomethacin derivatives. These probes were satisfactory COX-2 inhibitors with an IC_{50} in the range of the nanomolar both in inhibition assays using purified COX-2 and intact cells. However, they could not be successfully radiolabeled due to a lack of stability in the severe reaction conditions required (24).

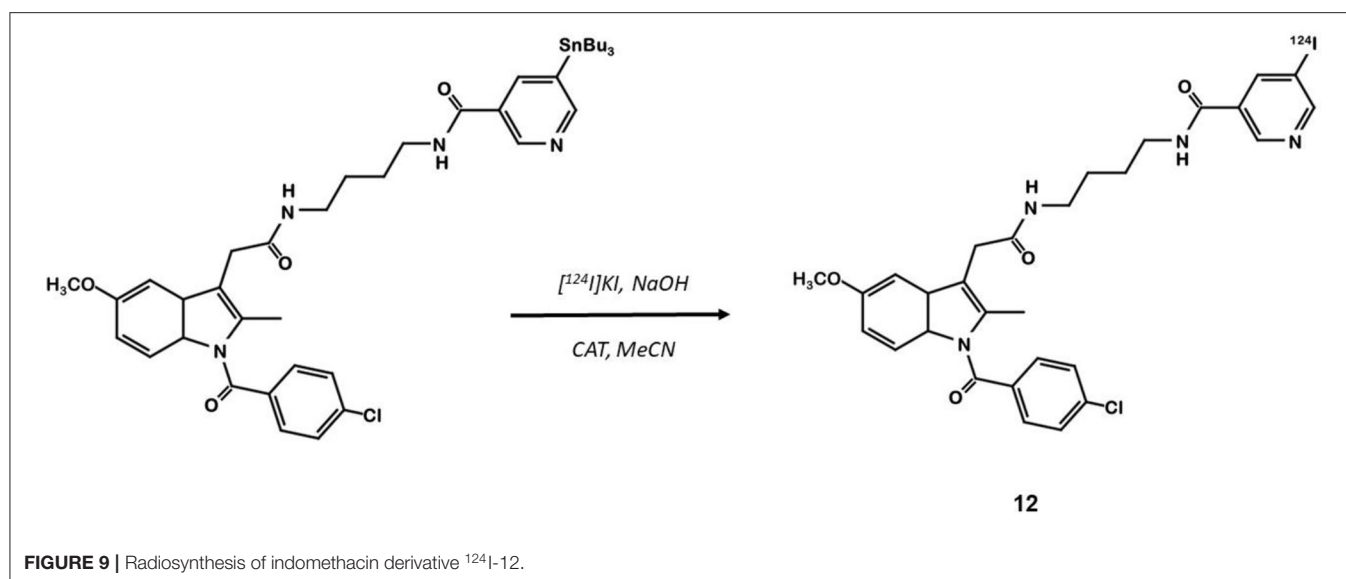
DISCUSSION

This review focuses on COX-2 radiotracers tested in CRC models. Other COX-2 radiotracers have also been developed for other oncologic indications as well as applications in the field of neuroinflammation (22).

These eight studies on CRC xenografts display heterogeneous results. Kaur et al. (25), Wuest et al. (26), and Knies et al. (30) concluded that their radiotracer was not appropriate for further clinical investigation, whereas Uddin et al. (24), Tietz et al. (27, 28), Litchfield et al. (29), and Morgenroth et al. (31) judged their radiotracer to be promising for clinical applications (satisfactory T/M ratio). However, for all the tested compounds, most of the radioactivity uptake was located in the digestive tract. The T/M ratios were deemed satisfactory, ranging from 1.4 to 5.0, but the tumor-to-intestine ratio was not always mentioned in these studies, and, when available, was well above the T/M ratio. The tumors were detectable as xenografts in mice flanks, but these T/M ratios would probably not be sufficient to detect *in situ* CRC tumors (Figure 10). Thus, the challenge to develop the ideal COX-2 radiotracer for CRC staging remains to date. Two areas of work can be explored to achieve this radiotracer development for CRC imaging.

Radiotracer-Linked Properties

All the tested compounds display a high lipophilicity ($\log P$ or $\log D \in [1.7-4.4]$), required to reach their intracellular target COX-2, but also responsible for hepatobiliary excretion that could mask CRC tumors. This assumption questions the relevance of COX-2 as a CRC imaging target and could be tested using *in situ* CRC preclinical models. ^{11}C -celecoxib was deemed unfit for clinical applications but benefited from a renal excretion that would be a serious advantage in CRC imaging. To increase the affinity for COX-2, pharmacomodulations on this parent compound led to more lipophilic molecules. There is still a need to balance affinity and lipophilicity with ideal pharmacokinetic properties. The use of innovative vectors could prove to be the solution to selectively deliver radiolabeled coxib derivatives into cancerous cells. In particular, the use of the RGD sequence (a tripeptide composed of arginine, glycine and aspartic acid) (38), dendrimers (39) or dehydropeptides (40) proved their potential to carry COX inhibitors into inflammatory or cancerous cells. Other pharmacokinetic properties should be taken into account, especially the metabolism rate and the radiotracer half-life. To be used routinely, the ideal radiotracer should be more than 50% intact 1 h p.i. and the half-life of the vector should not



be shorter than 30 min. Other well-known PET tracers, such as ^{18}F -FDG or ^{18}F -FDOPA comply with these requirements (respective renal excretion of 20% 2 h p.i.¹ and 50% 45 min p.i.²).

The second parameter to consider is the radioisotope. Due to its 110 min half-life, the use of ^{18}F is widespread in PET imaging, and most of the COX-2 binders were labeled with ^{18}F . Morgenroth et al. obtained the maximum T/M with a radio-iodinate derivative (31). However, due to both the higher energy of emitted beta particles and the longer half-life of ^{124}I (4.2 days), radio-iodinate derivatives exhibit a poorer dosimetry profile compared to ^{18}F -compounds. On the contrary, the shorter half-life of ^{11}C makes it less accessible for routine use (on-site cyclotron required) but would endow it with a better dosimetry profile.

Finally, pharmacomodulations were performed to increase the specificity for COX-2 compared to COX-1, but other targets are known for coxibs. For instance, celecoxib or valdecoxib bind significantly (IC_{50} in the order of nM) to carbonic anhydrase isoenzymes (CA) (41). In addition, celecoxib is able to bind to PDK1 (42, 43), a cell survival regulation enzyme *via* the Akt/PKB pathway, with an IC_{50} in the range of μ M (44). Likewise, coxibs bind to the transmembrane protein SERCA (45–47), a pump that can induce cellular apoptosis by increasing the intracellular calcium concentration. These different proapoptotic and anti-oncogenic targets have been confirmed by an increasing number of reports indicating that celecoxib does not require the presence of COX-2 to exert its anti-tumoral activity (44, 48, 49). Even more striking, it has been shown that structural analogs close to celecoxib, devoid of any COX-2 inhibitory activity, were able to mimic the anti-tumor properties of celecoxib studied so far, not only *in vitro* but also in

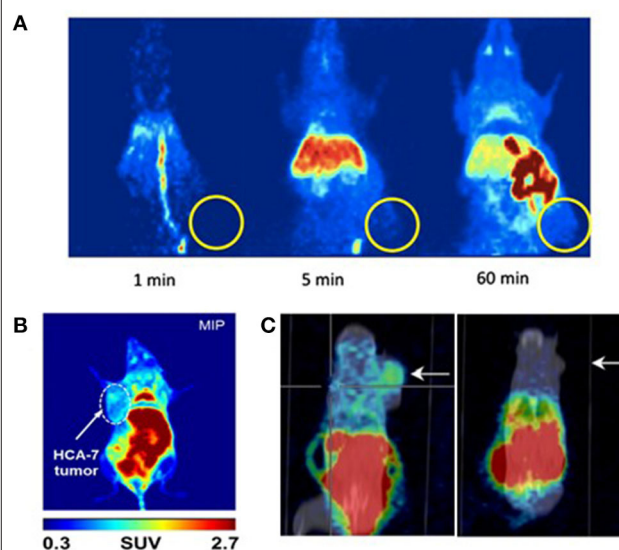


FIGURE 10 | microPET images of mice xenografted with human colorectal cancer cell lines after injection of a COX-2 specific radiotracer. **(A)** Knies et al., 2012 (30): Maximum intensity projection (MIP) images at 1, 5, and 60 min p.i. after a single IV injection of ^{18}F -3 into HT-29 tumor-bearing (right flank) NMRI nu/nu mice. Authors concluded that ^{18}F -3 was not promising. Reprinted from Bioorg Med Chem. 2012 Jun 1;20(11):3410–21, Radiosynthesis of a ^{18}F -labeled 2,3-diarylsubstituted indole via McMurry coupling for functional characterization of cyclooxygenase-2 (COX-2) *in vitro* and *in vivo*. Knies T, Laube M, Bergmann R, Sehn F, Graf F, Steinbach J, et al. Copyright (2012), with permission from Elsevier, license number 5067540791584. **(B)** Litchfield et al. (29): Maximum intensity projection (MIP) images at 60 min p.i. of ^{18}F -9 into HCA-7 tumor-bearing (left flank) BALB/c mice. Authors concluded that ^{18}F -9 was promising. **(C)** Morgenroth et al. (31): $\mu\text{PET}/\text{CT}$ molecular imaging of COX-2 with ^{124}I -12 in HT29 (left panel) and HCT-116 (right panel) xenografted SCID mice at 4 h p.i. Arrows indicate tumor. Authors concluded that ^{124}I -12 was promising.

¹Résumé des Caractéristiques du Produit FDG. Available online at: <http://agence-prd.ansm.sante.fr/php/ecodex/rcp/R0187540.htm> (accessed June 9, 2020).

²Résumé des Caractéristiques du Produit FDOPA. Available online at: <http://agence-prd.ansm.sante.fr/php/ecodex/rcp/R0157439.htm> (accessed October 6, 2020).

various *in vivo* xenograft models (43, 50, 51). These data question the relevance of radiolabeled coxibs as specific COX-2 binders.

In vivo Xenograft Models

Xenografts are known to lead to derangement of the normal tumor architecture and nearby healthy tissues and vasculature, and cause altered drug-sensitivity (52, 53). To address these possible biases, the use of orthotopic xenograft or genetically engineered mice expressing human colorectal cancer genes would mimic *in situ* CRC more accurately (54), easing the evaluation of the impact of unspecific intestinal uptake. Imaging the xenografts with ^{18}F -FDG prior to the radiolabeled COX-2 inhibitor would also inform about the accessibility of tumors for PET radioligands, notably regarding their perfusion.

CONCLUSION

Ultimately, most of these radioligands exhibit promising affinity and specificity *in vitro* but fail to prove their efficiency *in vivo* on xenograft models. Chemical screening and pharmacomodulations have yet to work out the ideal COX-2 radiotracer. The use of innovative vectors should be considered to selectively deliver radiotracers in the tumors. Given the hepatobiliary excretion of most of the known coxib derivatives, *in situ* CRC models should be considered for future explorations. *In vivo* preclinical studies on *in situ* CRC models would be decisive to conclude whether COX-2 is a relevant target in CRC imaging.

REFERENCES

- Lambert R. Épidémiologie du cancer colorectal (CCR). *Cancéro Dig.* (2009) 1:2–6. doi: 10.4267/2042/25061
- Siegel RL, Miller KD, Sauer AG, Fedewa SA, Butterly LF, Anderson JC, et al. Colorectal cancer statistics, 2020. *CA Cancer J Clin.* (2020) 70:145–64. doi: 10.3322/caac.21601
- Wang D, DuBois RN. The role of COX-2 in intestinal inflammation and colorectal cancer. *Oncogene.* (2010) 29:781–8. doi: 10.1038/ncr.2009.421
- Liu Y, Sun H, Hu M, Zhang Y, Chen S, Tighe S, et al. The role of cyclooxygenase-2 in colorectal carcinogenesis. *Clin Colorectal Cancer.* (2017) 16:165–72. doi: 10.1016/j.clcc.2016.09.012
- Thun MJ, Henley SJ, Patrono C. Nonsteroidal anti-inflammatory drugs as anticancer agents: mechanistic, pharmacologic, and clinical issues. *J Natl Cancer Inst.* (2002) 94:252–66. doi: 10.1093/jnci/94.4.252
- Chan AT, Arber N, Burn J, Chia JW-K, Elwood P, Hull MA, et al. Aspirin in the chemoprevention of colorectal neoplasia: an overview. *Cancer Prev Res.* (2012) 5:164–78. doi: 10.1158/1940-6207.CAPR-11-0391
- Phillips RKS, Wallace MH, Lynch PM, Hawk E, Gordon GB, Saunders BP, et al. A randomised, double blind, placebo controlled study of celecoxib, a selective cyclooxygenase 2 inhibitor, on duodenal polyposis in familial adenomatous polyposis. *Gut.* (2002) 50:857–60. doi: 10.1136/gut.50.6.857
- Eberhart CE, Coffey RJ, Radhika A, Giardiello FM, Ferrenbach S, DuBois RN. Up-regulation of cyclooxygenase 2 gene expression in human colorectal adenomas and adenocarcinomas. *Gastroenterology.* (1994) 107:1183–8. doi: 10.1016/0016-5085(94)90246-1
- Gupta RA, DuBois RN. Colorectal cancer prevention and treatment by inhibition of cyclooxygenase-2. *Nat Rev Cancer.* (2001) 1:11–21. doi: 10.1038/35094017
- Marnett LJ, DuBois RN. COX-2: a target for colon cancer prevention. *Annu Rev Pharmacol Toxicol.* (2002) 42:55–80. doi: 10.1146/annurev.pharmtox.42.082301.164620
- Fujita T, Matsui M, Takaku K, Uetake H, Ichikawa W, Taketo MM, et al. Size- and invasion-dependent increase in cyclooxygenase 2 levels in human colorectal carcinomas. *Cancer Res.* (1998) 58:4823–6.
- Cai J, Huang L, Huang J, Kang L, Lin H, Huang P, et al. Associations between the cyclooxygenase-2 expression in circulating tumor cells and the

More conclusive *in vivo* results are required before conducting a “first-in-human” study.

AUTHOR CONTRIBUTIONS

CD wrote the present paper and contributed to the design of the review. FA contributed to the redaction of the manuscript and to the prior bibliographic study. YT contributed to the clinical rational of the work. FB and SR wrote chemical sections of the manuscript. MC contributed to manuscript revision and improvement. NA designed the objectives of the review and supervised its preparation and redaction. All authors have substantially contributed to this work. The manuscript has been re-read and approved by all authors, and they have all contributed to its scientific improvement.

FUNDING

This work was supported by the French National Agency for Research (Investissements d’Avenir No. ANR-11-LABX-0018-01), IRON, by the Site de Recherche Intégrée sur le Cancer Imaging and Longitudinal Investigations to Ameliorate Decision-making SIRIC-ILIAD, and by the Région Centre Val de Loire RTR Motivhealth.

- clinicopathological features of patients with colorectal cancer. *J Cell Biochem.* (2019) 120:4935–41. doi: 10.1002/jcb.27768
- Tomozawa S, Tsuno NH, Sunami E, Hatano K, Kitayama J, Osada T, et al. Cyclooxygenase-2 overexpression correlates with tumour recurrence, especially haematogenous metastasis, of colorectal cancer. *Br J Cancer.* (2000) 83:324–8. doi: 10.1054/bjoc.2000.1270
- Ogino S, Kirkner GJ, Noshio K, Irahara N, Kure S, Shima K, et al. Cyclooxygenase-2 expression is an independent predictor of poor prognosis in colon cancer. *Clin Cancer Res.* (2008) 14:8221–7. doi: 10.1158/1078-0432.CCR-08-1841
- Wasilewicz MP, Kołodziej B, Bojulkó T, Kaczmarszyk M, Sulzyc-Bielicka V, Bielicki D. Expression of cyclooxygenase-2 in colonic polyps. *Pol Arch Med Wewn.* (2010) 120:313–20. doi: 10.20452/pamw.955
- Kerlikowske K, Molinaro AM, Gauthier ML, Berman HK, Waldman F, Bennington J, et al. Biomarker expression and risk of subsequent tumors after initial ductal carcinoma *in situ* diagnosis. *J Natl Cancer Inst.* (2010) 102:627–37. doi: 10.1093/jnci/djq101
- Shao N, Feng N, Wang Y, Mi Y, Li T, Hua L. Systematic review and meta-analysis of COX-2 expression and polymorphisms in prostate cancer. *Mol Biol Rep.* (2012) 39:10997–1004. doi: 10.1007/s11033-012-2001-5
- Edelman MJ, Watson D, Wang X, Morrison C, Kratzke RA, Jewell S, et al. Eicosanoid modulation in advanced lung cancer: cyclooxygenase-2 expression is a positive predictive factor for celecoxib + chemotherapy—cancer and leukemia group B trial 30203. *JCO.* (2008) 26:848–55. doi: 10.1200/JCO.2007.13.8081
- Fabi A, Metro G, Papaldo P, Mottotese M, Melucci E, Carlini P, et al. Impact of celecoxib on capecitabine tolerability and activity in pretreated metastatic breast cancer: results of a phase II study with biomarker evaluation. *Cancer Chemother Pharmacol.* (2008) 62:717–25. doi: 10.1007/s00280-007-0650-1
- Rini BI, Weinberg V, Dunlap S, Elchinoff A, Yu N, Bok R, et al. Maximal COX-2 immunostaining and clinical response to celecoxib and interferon alpha therapy in metastatic renal cell carcinoma. *Cancer.* (2006) 106:566–75. doi: 10.1002/cncr.21661
- Laube M, Kniess T, Pietzsch J. Radiolabeled COX-2 inhibitors for non-invasive visualization of COX-2 expression and activity — a critical update. *Molecules.* (2013) 18:6311–55. doi: 10.3390/molecules18066311

22. de Vries EFJ. Imaging of cyclooxygenase-2 (COX-2) expression: potential use in diagnosis and drug evaluation. *Curr Pharm Des.* (2006) 12:3847–56. doi: 10.2174/138161206778559650
23. Pacelli A, Greenman J, Cawthorne C, Smith G. Imaging COX-2 expression in cancer using PET/SPECT radioligands: current status and future directions. *J Label Comp Radiopharm.* (2014) 57:317–22. doi: 10.1002/jlcr.3160
24. Uddin MdJ, Crews BC, Ghebreselasie K, Huda I, Kingsley PJ, Ansari MS, et al. Fluorinated cyclooxygenase-2 inhibitors as agents in PET imaging of inflammation and cancer. *Cancer Prev Res.* (2011) 4:1536–45. doi: 10.1158/1940-6207.CAPR-11-0120
25. Kaur J, Tietz O, Bhardwaj A, Marshall A, Way J, Wuest M, et al. Design, synthesis, and evaluation of an (18F)-labeled radiotracer based on celecoxib-NBD for positron emission tomography (PET) imaging of cyclooxygenase-2 (COX-2). *ChemMedChem.* (2015) 10:1635–40. doi: 10.1002/cmdc.201500287
26. Wuest F, Knies T, Bergmann R, Pietzsch J. Synthesis and evaluation *in vitro* and *in vivo* of a ¹¹C-labeled cyclooxygenase-2 (COX-2) inhibitor. *Bioorg Med Chem.* (2008) 16:7662–70. doi: 10.1016/j.bmc.2008.07.016
27. Tietz O, Wuest M, Marshall A, Glubrecht D, Hamann I, Wang M, et al. PET imaging of cyclooxygenase-2 (COX-2) in a pre-clinical colorectal cancer model. *EJNMMI Res.* (2016) 6:37. doi: 10.1186/s13550-016-0192-9
28. Tietz O, Marshall A, Bergman C, Wuest M, Wuest F. Impact of structural alterations on the radiopharmacological profile of ¹⁸F-labeled pyrimidines as cyclooxygenase-2 (COX-2) imaging agents. *Nucl Med Biol.* (2018) 62–63:9–17. doi: 10.1016/j.nucmedbio.2018.05.001
29. Litchfield M, Wuest M, Glubrecht D, Wuest F. Radiosynthesis and biological evaluation of [¹⁸F]Triacoxib: a new radiotracer for PET imaging of COX-2. *Mol Pharm.* (2020) 17:251–61. doi: 10.1021/acs.molpharmaceut.9b00986
30. Knies T, Laube M, Bergmann R, Sehn F, Graf F, Steinbach J, et al. Radiosynthesis of a ¹⁸F-labeled 2,3-diarylsubstituted indole via McMurry coupling for functional characterization of cyclooxygenase-2 (COX-2) *in vitro* and *in vivo*. *Bioorg Med Chem.* (2012) 20:3410–21. doi: 10.1016/j.bmc.2012.04.022
31. Morgenroth A, Vogt ATJ, Neumaier B, Mottaghy FM, Zlatopolskiy BD. Radioiodinated indomethacin amide for molecular imaging of cyclooxygenase-2 expressing tumors. *Oncotarget.* (2017) 8:18059–69. doi: 10.18632/oncotarget.15437
32. Prabhakaran J, Majo VJ, Simpson NR, Heertum RLV, Mann JJ, Kumar JSD. Synthesis of [¹¹C]celecoxib: a potential PET probe for imaging COX-2 expression. *J Label Comp Radiopharm.* (2005) 48:887–95. doi: 10.1002/jlcr.1002
33. Kumar JSD, Bai B, Zanderigo F, DeLorenzo C, Prabhakaran J, Parsey RV, et al. *In vivo* brain imaging, biodistribution, and radiation dosimetry estimation of [¹¹C]Celecoxib, a COX-2 PET ligand, in nonhuman primates. *Molecules.* (2018) 23:1929. doi: 10.3390/molecules23081929
34. Li JJ, Anderson GD, Burton EG, Cogburn JN, Collins JT, Garland DJ, et al. 1,2-diarylcyclopentenes as selective cyclooxygenase-2 inhibitors and orally active anti-inflammatory agents. *J Med Chem.* (1995) 38:4570–8. doi: 10.1021/jm00022a023
35. Tietz O, Sharma SK, Kaur J, Way J, Marshall A, Wuest M, et al. Synthesis of three ¹⁸F-labelled cyclooxygenase-2 (COX-2) inhibitors based on a pyrimidine scaffold. *Org Biomol Chem.* (2013) 11:8052–64. doi: 10.1039/c3ob41935e
36. Hu W, Guo Z, Chu F, Bai A, Yi X, Cheng G, et al. Synthesis and biological evaluation of substituted 2-sulfonyl-phenyl-3-phenyl-indoles: a new series of selective COX-2 inhibitors. *Bioorg Med Chem.* (2003) 11:1153–60. doi: 10.1016/S0968-0896(03)00046-4
37. Kalgutkar AS, Crews BC, Rowlinson SW, Marnett AB, Kozak KR, Rummel RP, et al. Biochemically based design of cyclooxygenase-2 (COX-2) inhibitors: facile conversion of nonsteroidal antiinflammatory drugs to potent and highly selective COX-2 inhibitors. *Proc Natl Acad Sci USA.* (2000) 97:925–30. doi: 10.1073/pnas.97.2.925
38. Mohammadi R, Shokri B, Shamshirian D, Zarghi A, Shahhosseini S. Synthesis and biological evaluation of RGD conjugated with Ketoprofen/Naproxen and radiolabeled with [^{99m}Tc] via N4(GGAG) for αVβ3 integrin-targeted drug delivery. *Daru.* (2020) 28:87–96. doi: 10.1007/s40199-019-00318-8
39. Ficker M, Theeuwes MJM, Janaszewska A, Gorzkiewicz M, Svenningsen SW, Klajnert-Maculewicz B, et al. Complexes of indomethacin with 4-carbomethoxy-pyrrolidone PAMAM dendrimers show improved anti-inflammatory properties and temperature-dependent binding and release profile. *Mol Pharm.* (2018) 15:3573–82. doi: 10.1021/acs.molpharmaceut.8b00567
40. Moreira R, Jervis PJ, Carvalho A, Ferreira PMT, Martins JA, Valentão P, et al. Biological evaluation of naproxen–dehydrodiol peptide conjugates with self-hydrogelation capacity as dual LOX/COX inhibitors. *Pharmaceutics.* (2020) 12:122. doi: 10.3390/pharmaceutics12020122
41. Di Fiore A, Pedone C, D'Ambrosio K, Scozzafava A, De Simone G, Supuran CT. Carbonic anhydrase inhibitors: valdecoxib binds to a different active site region of the human isoform II as compared to the structurally related cyclooxygenase II 'selective' inhibitor celecoxib. *Bioorg Med Chem Lett.* (2006) 16:437–42. doi: 10.1016/j.bmcl.2005.09.040
42. Arico S, Patingre S, Bauvy C, Gane P, Barbat A, Codogno P, et al. Celecoxib induces apoptosis by inhibiting 3-phosphoinositide-dependent protein kinase-1 activity in the human colon cancer HT-29 cell line. *J Biol Chem.* (2002) 277:27613–21. doi: 10.1074/jbc.M201119200
43. Kulp SK, Yang Y-T, Hung C-C, Chen K-F, Lai J-P, Tseng P-H, et al. 3-phosphoinositide-dependent protein kinase-1/Akt Signaling represents a major cyclooxygenase-2-independent target for celecoxib in prostate cancer cells. *Cancer Res.* (2004) 64:1444–51. doi: 10.1158/0008-5472.CAN-03-2396
44. Grösch S, Maier TJ, Schiffmann S, Geisslinger G. Cyclooxygenase-2 (COX-2)-independent anticarcinogenic effects of selective COX-2 inhibitors. *J Natl Cancer Inst.* (2006) 98:736–47. doi: 10.1093/jnci/djj206
45. Johnson AJ, Hsu A-L, Lin H-P, Song X, Chen C-S. The cyclo-oxygenase-2 inhibitor celecoxib perturbs intracellular calcium by inhibiting endoplasmic reticulum Ca²⁺-ATPases: a plausible link with its anti-tumour effect and cardiovascular risks. *Biochem J.* (2002) 366:831–7. doi: 10.1042/bj20020279
46. Tanaka K, Tomisato W, Hoshino T, Ishihara T, Namba T, Aburaya M, et al. Involvement of intracellular Ca²⁺ levels in nonsteroidal anti-inflammatory drug-induced apoptosis. *J Biol Chem.* (2005) 280:31059–67. doi: 10.1074/jbc.M502956200
47. Pyrkó P, Kardosh A, Liu Y-T, Soriano N, Xiong W, Chow RH, et al. Calcium-activated endoplasmic reticulum stress as a major component of tumor cell death induced by 2,5-dimethyl-celecoxib, a non-coxib analogue of celecoxib. *Mol Cancer Ther.* (2007) 6:1262–75. doi: 10.1158/1535-7163.MCT-06-0629
48. Kashfi K, Rigas B. Non-COX-2 targets and cancer: expanding the molecular target repertoire of chemoprevention. *Biochem Pharmacol.* (2005) 70:969–86. doi: 10.1016/j.bcp.2005.05.004
49. Schönthal AH. Induction of apoptosis by celecoxib in cell culture: an uncertain role for cyclooxygenase-2. *Cancer Res.* (2007) 67:5575–6. doi: 10.1158/0008-5472.CAN-06-3414
50. Song X, Lin H-P, Johnson AJ, Tseng P-H, Yang Y-T, Kulp SK, et al. Cyclooxygenase-2, player or spectator in cyclooxygenase-2 inhibitor-induced apoptosis in prostate cancer cells. *J Natl Cancer Inst.* (2002) 94:585–91. doi: 10.1093/jnci/94.8.585
51. Schönthal AH. Antitumor properties of dimethyl-celecoxib, a derivative of celecoxib that does not inhibit cyclooxygenase-2: implications for glioma therapy. *Neurosurg Focus.* (2006) 20:E21. doi: 10.3171/foc.2006.20.4.14
52. Frese KK, Tuveson DA. Maximizing mouse cancer models. *Nat Rev Cancer.* (2007) 7:654–8. doi: 10.1038/nrc2192
53. Sikder H, Huso DL, Zhang H, Wang B, Ryu B, Hwang ST, et al. Disruption of Id1 reveals major differences in angiogenesis between transplanted and autochthonous tumors. *Cancer Cell.* (2003) 4:291–9. doi: 10.1016/S1535-6108(03)00245-9
54. Becher OJ, Holland EC. Genetically engineered models have advantages over xenografts for preclinical studies. *Cancer Res.* (2006) 66:3355–8. Discussion 3358–3359. doi: 10.1158/0008-5472.CAN-05-3827

Conflict of Interest: The authors declare that the research was conducted in the absence of any commercial or financial relationships that could be construed as a potential conflict of interest.

Copyright © 2021 Dagallier, Avry, Touchefeu, Buron, Routier, Chérel and Arlicot. This is an open-access article distributed under the terms of the Creative Commons Attribution License (CC BY). The use, distribution or reproduction in other forums is permitted, provided the original author(s) and the copyright owner(s) are credited and that the original publication in this journal is cited, in accordance with accepted academic practice. No use, distribution or reproduction is permitted which does not comply with these terms.



Additive Value of Dynamic FDOPA PET/CT for Glioma Grading

Antoine Girard¹, Pierre-Jean Le Reste², Alice Metais², Nibras Chaboub³, Anne Devillers³, Hervé Saint-Jalmes³, Florence Le Jeune¹ and Xavier Palard-Novello^{3*}

¹ Univ Rennes, CLCC Eugène Marquis, Noyau Gris Centraux EA 4712, Rennes, France, ² CHU Rennes, Rennes, France,

³ Univ Rennes, CLCC Eugène Marquis, INSERM, LTSI – UMR 1099, Rennes, France

OPEN ACCESS

Edited by:

Francesco Cicone,
University of Catanzaro, Italy

Reviewed by:

Vincent Dunet,
University of Lausanne, Switzerland
Philipp Lohmann,
Research Center Juelich, Germany

*Correspondence:

Xavier Palard-Novello
x.palard@rennes.unicancer.fr

Specialty section:

This article was submitted to
Nuclear Medicine,
a section of the journal
Frontiers in Medicine

Received: 06 May 2021

Accepted: 21 June 2021

Published: 09 July 2021

Citation:

Girard A, Le Reste P-J, Metais A,
Chaboub N, Devillers A,
Saint-Jalmes H, Jeune FL and
Palard-Novello X (2021) Additive Value
of Dynamic FDOPA PET/CT for Glioma
Grading. *Front. Med.* 8:705996.
doi: 10.3389/fmed.2021.705996

Purpose: The aim of this study was to assess the value of the FDOPA PET kinetic parameters extracted using full kinetic analysis for tumor grading with neuronavigation-guided biopsies as reference in patients with newly-diagnosed gliomas.

Methods: Fourteen patients with untreated gliomas were investigated. Twenty minutes of dynamic positron-emission tomography (PET) imaging and a 20-min static image 10 min after injection were reconstructed from a 40-min list-mode acquisition immediately after FDOPA injection. Tumors volume-of-interest (VOI) were generated based on the MRI-guided brain biopsies. Static parameters (TBRmax and TBRmean) and kinetic parameters [K1 and k2 using full kinetic analysis with the reversible single-tissue compartment model with blood volume parameter and the time-to-peak (TTP)] were extracted. Performances of each parameter for differentiating low-grade gliomas (LGG) from high-grade gliomas (HGG) were evaluated by receiver-operating characteristic analyses (area under the curve; AUC).

Results: Thirty-two tumoral VOI were analyzed. K1, k2, and TTP were significantly higher for HGG than for LGG (median K1-value = 0.124 vs. 0.074 ml/ccm/min, $p = 0.025$, median k2-value = 0.093 vs. 0.063 min⁻¹, $p = 0.025$, and median TTP-value = 10.0 vs. 15.0 min, $p = 0.025$). No significant difference was observed for the static parameters. The AUC for the kinetic parameters was higher than the AUC for the static parameters (respectively, $AUC_{K1} = 0.787$, $AUC_{k2} = 0.785$, $AUC_{TTP} = 0.775$, $AUC_{TBRmax} = 0.551$, $AUC_{TBRmean} = 0.575$), significantly compared to TBRmax (respectively, $p = 0.001$ for K1, $p = 0.031$ for k2, and $p = 0.029$ for TTP).

Conclusion: The present study suggests an additive value of FDOPA PET/CT kinetic parameters for newly-diagnosed gliomas grading.

Keywords: FDOPA, positron-emission tomography, gliomas grading, dynamic, quantification

INTRODUCTION

Gliomas are the most commonly occurring primary malignant brain tumor in adults (1). Patient outcome and treatment strategy are still mainly defined by tumor grade according to the World Health Organization (WHO) classification (2). Furthermore, the main goal of the gliomas surgical resection is to remove as much of the tumor as safely achievable (2, 3). So, in order to determine

the extent of tumor resection, presurgical identification of high-grade subregions is needed. Currently, magnetic resonance imaging (MRI) with contrast-enhanced (CE), diffusion, and perfusion sequences is the imaging method of reference for gliomas grading (2). However, around one quarter of low-grade gliomas (LGG) present contrast-enhancement (4) and one-third of non-enhancing tumors are high-grade gliomas (HGG) (5). In order to improve gliomas grading, amino-acid (AA) positron-emission tomography (PET) tracers including O-(2-[18F]-fluoroethyl)-L-tyrosine (FET), [11C]-methionine (MET), and 3,4-dihydroxy-6-[18F]fluoro-L-phenylalanine (FDOPA) have been increasingly investigated (6). To date, FET is the most studied AA PET tracer. However, FDOPA is the only AA PET tracer widely available in several countries (7). FDOPA is transported into the cells mainly by L-type amino acid transporter 1 (LAT 1), which is overexpressed in gliomas (6). Regarding performances of FDOPA PET/CT for gliomas grading, previous studies have provided conflicting results (8–18). However, almost all of these studies used static parameters for FDOPA uptake quantification. Advanced pharmacokinetic analysis of time-activity curves (TAC) from dynamic PET scans using compartment models enables the extraction of direct physiological parameters and could add further information concerning tumor aggressiveness for several cancers (19, 20). Positron-emission tomography kinetic analysis has recently increased with newly developed PET systems that offer higher count rate capabilities than previous scanners. For gliomas assessment, studies shown that FET PET kinetic analysis can provide useful information about the tumor characteristics (21, 22), so dynamic analysis has been recommended in recent guidelines (6).

The aim of the present study was to assess the value of the FDOPA PET kinetic parameters extracted using full kinetic analysis for tumor grading with neuronavigation-guided biopsies as reference in patients with newly-diagnosed gliomas.

MATERIALS AND METHODS

Participants

From June 2018 to September 2019, 19 patients with suspected supratentorial diffuse gliomas were prospectively included in the “GLIROPA” clinical trial (NCT03525080). All patients were newly diagnosed for gliomas and selected for resective surgery. Included patients had to be at least 18 years-old and covered by national health insurance; and neither be pregnant, nor in an emergency situation, nor be treated by carbidopa, catechol-O-methyl transferase inhibitor, haloperidol, or reserpine medication. All patients provided their written informed consent. This study has been performed in accordance with the Declaration of Helsinki and approved by an independent national research ethics committee (CPPIDF1-2018-ND27-cat.2).

PET/CT Imaging Protocol

The patients were required to fast at least 4 h before undergoing the imaging protocol. Unenhanced CT (2 mm reconstructed section thickness using iterative method, 512 × 512 matrix;

pitch index, 0.55) was performed with automated tube current modulation (CARE Dose4D) and automated tube voltage selection (CARE kV) followed by a PET acquisition using list-mode acquisition with a single field of view centered on the brain (Siemens Healthcare Biograph mCT Flow, Erlangen, Germany). Hundred and forty-nine MBq (range 122–192) of FDOPA were slowly administered intravenously, without carbidopa premedication. Positron-emission tomography images were reconstructed with attenuation correction, without point-spread function correction, using a fully 3D ordered-subset expectation maximization algorithm (8 iterations and 21 subsets) with a 400 × 400, matrix and 4 mm kernel convolution filter. Voxel size (XYZ) was 1 × 1 × 2 mm³. A 20-min static image 10 min after injection in accordance with current recommendations (23) and an optimal dynamic time sampling of 8 × 15 s—2 × 30 s—2 × 60 s—3 × 300 s from the bolus arrival time (24) were reconstructed from a 40-min list-mode acquisition immediately after FDOPA injection.

Surgical Biopsies

Surgeries were performed under general anesthesia, with the aid of neuronavigation from StealthStation S7 (Medtronic, Dublin, Ireland). Up to three neuronavigation-guided biopsies of 1 cm³ were performed per patient, depending on the tumor size. Biopsy targets were located on 3D-T2 fluid-attenuated inversion recovery (FLAIR) weighted MR imaging, prospectively and previously defined with all of MRI sequences and FDOPA PET/CT imaging. Each resection specimen and biopsy sample was collected, prepared, and analyzed blind to imaging. Samples were prepared using standard histopathological techniques. Diagnosis and grading were performed on formalin-fixed paraffin-embedded tissue sections stained by hematoxylin and eosin, using complementary techniques to detect isocitrate dehydrogenase (IDH) mutation and 1p19q codeletion, in accordance with the World Health Organization (WHO) 2016 Classification of Tumors of the Central Nervous System (25). Each biopsy sample was graded independently. Grade biopsy results were grouped into LGG and HGG, including grade II for LGG, and grade III-IV for HGG, respectively. For each patient, the IDH genotype of the whole specimen was applied for each individual biopsy sample.

Image Analysis

Volume-of-interest (VOI) of 1 cm³ were drawn on each biopsy site using the Syngo.via software (Siemens Healthcare), after registration with the FLAIR weighted images used for the neuronavigation-guided brain biopsies (Figure 1). For each voxel, the standardized uptake value (SUV) was calculated using the following formula: SUV = tissue radioactivity concentration/[injected activity/patient weight]. SUVmax and SUVmean were, respectively, the maximum and the mean of the SUVs of each VOI. A reference area was drawn on one slice including the whole normal contralateral hemisphere at the centrum semiovale level, for the computing of Tumor-to-normal brain (TBR) ratios. Tumor-to-normal brain ratio were computed as SUVmax or SUVmean of the VOI of each biopsy site by the SUVmean of the normal brain (TBRmax

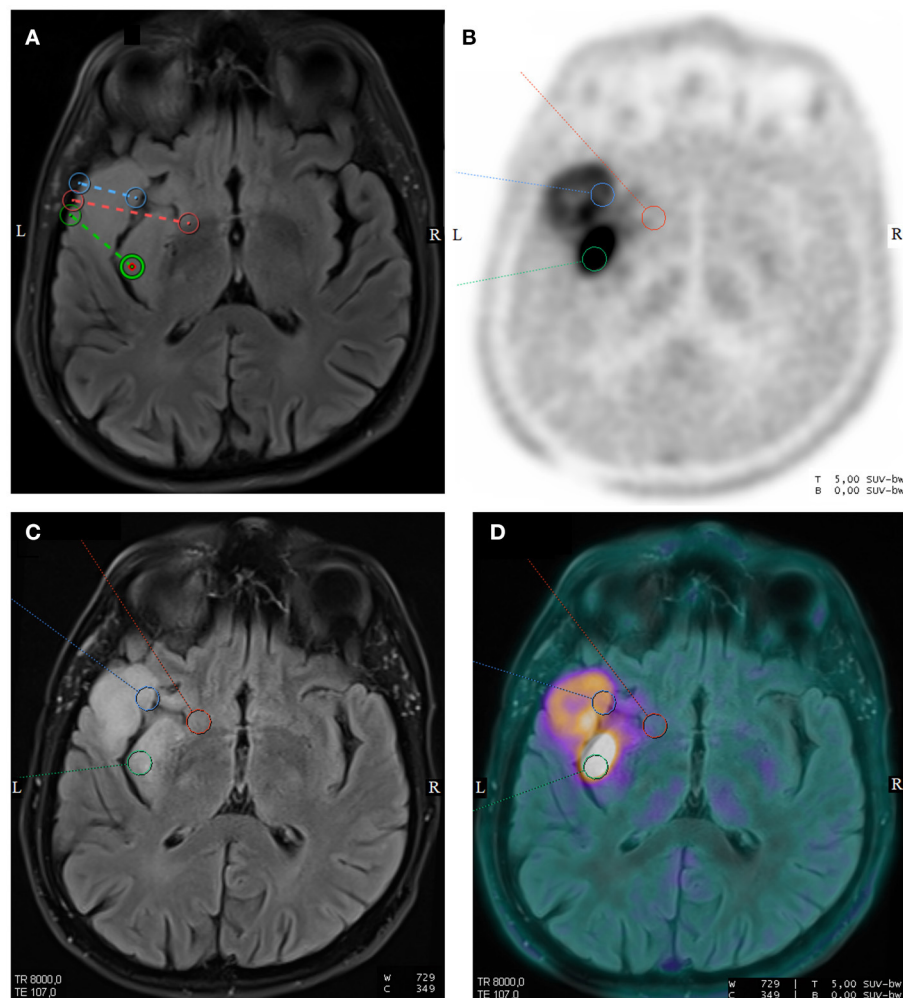


FIGURE 1 | Axial T2-weighted fluid-attenuated inversion recovery (FLAIR) sequence from surgical navigation software with the locations of three neuronavigation-guided biopsies in a 59-year-old man with a left temporal diffuse IDH1-wild-type glioblastoma (A). Corresponding axial images of FDOPA PET (B), T2-weighted FLAIR sequence (C), and fused FDOPA PET/T2-weighted FLAIR sequence (D) are displayed. The pathology grading of the neuronavigation-guided biopsies revealed WHO grade II for the red VOI and WHO grade III for the green and blue VOIs.

and TBRmean). Volume-of-interests of each biopsy site were projected onto each frame of the dynamic reconstruction. Time-to-peak (TTP), corresponding to the delay between the beginning of the acquisition and the timepoint of the maximal mean activity concentration for each VOI. On the early PET image with the maximum blood pool activity, a VOI was manually drawn into the middle cerebral artery to estimate an imaging-derived input function (IDIF). For each patient, FDOPA plasma input function was obtained after corrections for metabolites and hematocrit. Imaging-derived input function was fitted to the measured fractions of metabolites taken from the publication of Huang et al. (26). To extract kinetic parameters (PMOD software version 3.8; PMOD Technologies; Zürich, Switzerland), the reversible single-tissue compartment model with blood volume parameter (1T2k+VB, with K_1 = rate constant from blood to tissue, k_2 = rate constant from the tissue compartment to the arterial blood)

was selected on the basis of the Akaike information criterion for small sample sizes (27).

Statistical Analysis

To compare quantitative kinetic and static FDOPA PET parameters between LGG and HGG, to compare kinetic parameters between CE and non-contrast lesions, and to compare FDOPA PET parameters with gender, a Mann–Whitney U-test was performed. The diagnostic performances of these parameters to discriminate LGG from HGG were assessed by receiver-operator characteristic (ROC) curve analyses using histological grading as reference. The optimal thresholds were defined based on maximization of Youden's index. The area under the ROC curve (AUC) was also determined for each quantitative parameter. Accuracy for grading of the kinetic parameters and CE MRI were compared pairwise with the

TABLE 1 | Summary of patient characteristics and imaging findings.

Characteristic	Value
Age (years), median (range)	40 (23–66)
Gender (<i>N</i> = 14)	
Male	9 (64%)
Female	5 (36%)
Tumor types (<i>N</i> = 14)	
Astrocytomas-IDH mutant	6 (43%)
Oligodendrogliomas/1p19q-codeleted-IDH mutant	2 (14%)
IDH-wild-type glioblastomas	6 (43%)
WHO grading of each biopsy sites (<i>N</i> = 32)	
II	9 (28%)
III	18 (56%)
IV	5 (16%)
K1 (ml/ccm/min), median (range)	0.103 (0.055–0.578)
k2 (min ⁻¹), median (range)	0.082 (0.027–0.180)
TTP (min), median (range)	15.0 (1.25–20.0)
TBR max, median (range)	2.3 (1.4–6.2)
TBRmean, median (range)	1.6 (0.8–5.0)

McNemar *t*-test. A Spearman rank correlation test was used for correlation analysis between FDOPA PET parameters and the age of the participants. A *p*-value < 0.05 with false discovery rate adjustment for multiple comparisons was considered as significant. Statistical analysis was performed using MedCalc® version 12.5.0.0 (Medcalc Software bvba).

RESULTS

Patients

Two patients were excluded because surgeries were performed in other hospitals. Another patient was also excluded because no surgical resection was performed. The dynamic acquisition was unsuccessful for two patients. Thirty-two biopsy sites from 14 patients were finally analyzed. Patient and tumor characteristics are set out in **Table 1**. There were eight men and six women, with a median age of 40 years (range 23–66). The distribution of the 14 cases was as follows: six astrocytomas-IDH-mutant; two oligodendrogliomas/1p19q-codeleted-IDH-mutant; and six IDH-wild-type glioblastomas. The MRI was performed within a median time of 3 days (range 1–23) after FDOPA PET/CT. Surgery was performed within a median time of 14 days (range 6–110) after FDOPA PET/CT.

Among the 32 biopsy samples analyzed, nine (28%) were grade II, eighteen (56%) were grade III, and five (16%) were grade IV. The CE-MR sequence revealed that eight biopsy sites in five participants were CE and 24 biopsy sites in the other nine participants were not CE. Using a tumor-to-brain ratio higher than 1.7, in accordance with previously published data (17), 11 biopsy sites in seven participants were considered as increased FDOPA uptake and 21 biopsy sites in the other seven participants were not considered as FDOPA increased uptake.

TABLE 2 | Comparison of imaging parameters and WHO grade of each biopsy site.

Parameters	WHO Grade		<i>p</i> -value
	LGG (<i>n</i> = 9)	HGG (<i>n</i> = 23)	
median K1 (ml/ccm/min), range	0.074, 0.055–0.131	0.124, 0.056–0.578	0.025*
median k2 (min ⁻¹), range	0.063, 0.027–0.085	0.093, 0.043–0.180	0.025*
median TTP (min), range	15.0, 10.0–20.0	10.0, 1.25–20.0	0.025*
median TBRmax, range	2.2, 1.7–3.7	2.4, 1.4–6.2	0.681
median TBRmean, range	1.7, 1.2–2.7	1.6, 0.8–5.0	0.670

**p*-value < 0.05 with false discovery rate adjustment = statistically significant.

Comparison of Quantitative FDOPA PET/CT Parameters and Gliomas Grading

All quantitative FDOPA PET parameters are given in **Table 1**. K1 and k2 were significantly higher for HGG than for LGG and TTP was significantly lower for HGG than for LGG (**Table 2**). Examples of TAC extracted from a HGG VOI and TAC extracted from a LGG VOI in a 27-year-old man with a left temporal WHO grade III astrocytoma IDH1-mutant are shown in **Figure 2**. The AUC for the kinetic parameters was higher than the AUC for the static parameters, significantly compared to TBRmax ($AUC_{K1} = 0.787$ vs. $AUC_{TBRmax} = 0.551$, $p = 0.001$; $AUC_{k2} = 0.785$ vs. AUC_{TBRmax} , $p = 0.031$ and AUC_{TTP} vs. AUC_{TBRmax} , $p = 0.029$) (**Table 3**). K1, k2, and TBRmax were significantly higher for IDH-wildtype than for IDH-mutant and TTP was significantly lower for IDH-wildtype than for IDH-mutant (**Table 4**). Diagnostic accuracy of k2 was significantly higher than these with CE (accuracy for k2 = 0.63 vs. 0.47 for CE, $p = 0.042$). There was a trend toward greater K1 for CE biopsy sites than for non-CE (median K1-value was, respectively, 0.266 vs. 0.098 ml/ccm/min, $p = 0.06$). TBRmax, TBRmean, K1, and k2 were positively correlated with age (respectively, $r = 0.54$, $p = 0.003$; $r = 0.41$, $p = 0.024$; $r = 0.38$, $p = 0.033$; $r = 0.54$, $p = 0.003$) and TTP was negatively correlated with age (respectively $r = -0.53$, $p = 0.003$). There were no differences in static and kinetic parameters between female and male participants.

DISCUSSION

Parameters extracted from FDOPA PET full kinetic analysis are well-associated with tumoral aggressiveness. To the best of our knowledge, this is the first study comparing FDOPA uptake kinetic parameters and pathology grading with biopsy validation. The characterization of gliomas with full kinetic analysis using compartmental modeling has been reported in two previous studies but serial biopsies were not performed. Schiepers et al. showed that K1 was higher in HGG than LGG in a pilot study including nine patients with newly diagnosed gliomas (18). Nioche et al. also displayed that the use of K1 enables differentiation between LGG and HGG in a study including

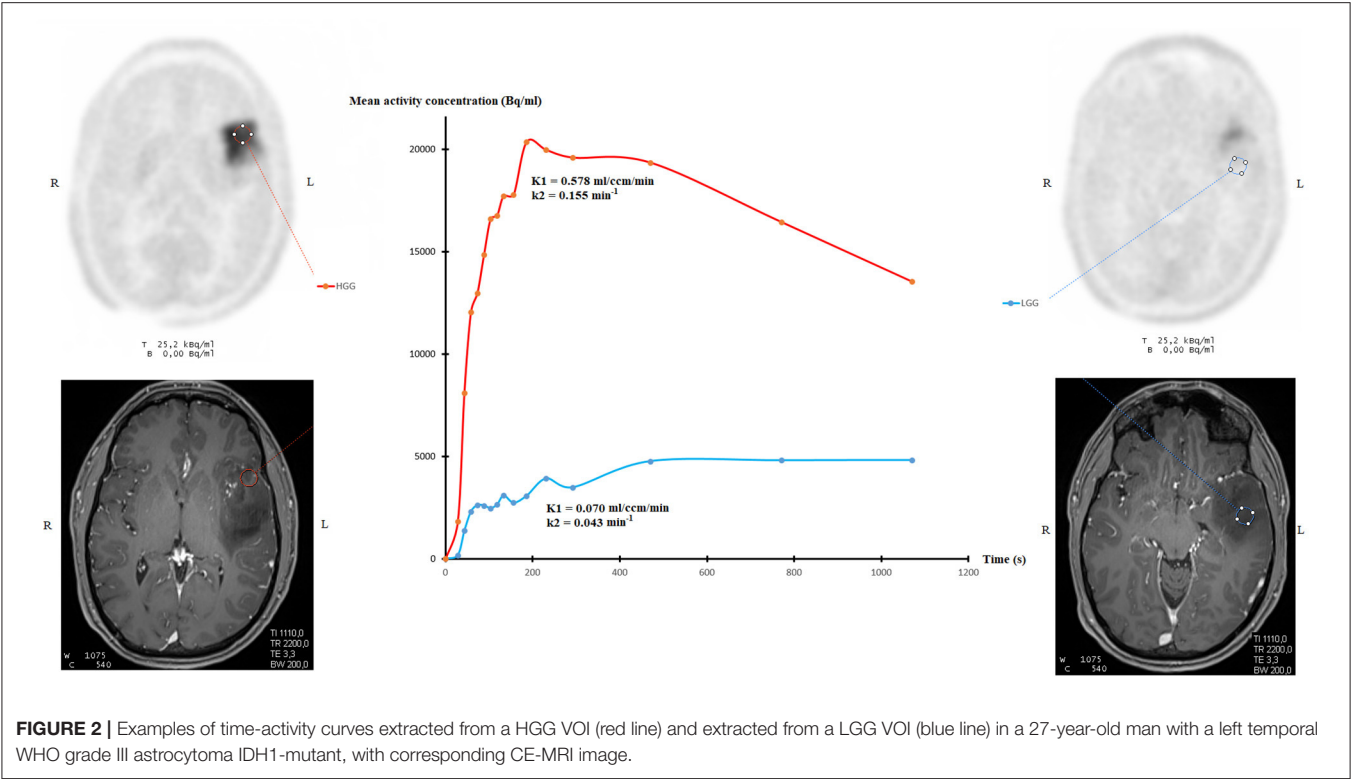


FIGURE 2 | Examples of time-activity curves extracted from a HGG VOI (red line) and extracted from a LGG VOI (blue line) in a 27-year-old man with a left temporal WHO grade III astrocytoma IDH1-mutant, with corresponding CE-MRI image.

TABLE 3 | Diagnostic performances of FDOPA parameters for discrimination of LGG and HGG.

Parameters	AUC (CI 95%)	p-value	Threshold	Youden's index	Sensitivity (CI 95%)	Specificity (CI 95%)	Accuracy (CI 95%)
K1** (ml/ccm/min)	0.787 (0.607–0.911)	0.028*	0.131	0.48	0.48 (0.27–0.69)	1 (0.66–1)	0.63 (0.44–0.79)
k2** (min ⁻¹)	0.785 (0.604–0.910)	0.028*	0.085	0.61	0.61 (0.39–0.80)	1 (0.66–1)	0.72 (0.53–0.86)
TTP** (min)	0.775 (0.594–0.903)	0.028*	13.3	0.50	0.61 (0.39–0.80)	0.89 (0.52–1)	0.69 (0.50–0.84)
TBRmax	0.551 (0.366–0.726)	0.104	2.7	0.32	0.43 (0.20–0.59)	0.89 (0.52–1)	0.56 (0.38–0.74)
TBRmean	0.575 (0.388–0.747)	0.104	2.0	0.19	0.30 (0.13–0.53)	0.89 (0.52–1)	0.47 (0.29–0.65)

*p-value < 0.05 with false discovery rate adjustment = statistically significant for AUC compared to 0.500.
**p-value < 0.05 with false discovery rate adjustment = statistically significant for pairwise comparison of ROC curves with TBRmax.

20 patients with newly diagnosed gliomas (15). The findings of our prospective biopsy-controlled study are consistent with these two previous researches. More recently, using simplified kinetic analysis with determination of SUV at different time points, Ginet et al. showed that IDH-wildtype gliomas, which are associated with a poorer outcome (28), have a shorter TTP than IDH-mutant gliomas (13). In that study, authors also reported that IDH-wildtype gliomas have a higher negative slope (linear regression applied on the 10th to 30th minute interval of SUVmean-based curve) than IDH-mutant gliomas. Our results support that higher FDOPA uptake rate constant and FDOPA clearance rate constant might serve as non-invasive markers of

aggressiveness. Moreover, we found that accuracy for glioma grading of k2 was higher than accuracy of CE sequence. Our findings indicate a trend toward greater K1 for CE biopsy sites than for non-CE biopsy sites. It is known that a higher regional blood volume linked to a higher intratumoral microvessel density due to neoangiogenesis might be responsible for the higher AA PET tracers uptake in HGG compared to LGG (29, 30). Furthermore, the disruption of the blood–brain barrier is the mechanism suggested for the higher FET washout in HGG compared to LGG (31). However, the tumor accumulation of FDOPA in gliomas is also mediated through the specific LAT transport system, a tight bidirectional coupling of influx and

TABLE 4 | Comparison of imaging parameters and IDH mutation status of each biopsy site.

Parameters	IDH mutation status		<i>p</i> -value
	IDH-mutant (<i>n</i> = 16)	IDH-wildtype (<i>n</i> = 16)	
median K1 (ml/ccm/min), range	0.088, 0.055–0.578	0.154, 0.067–0.452	0.049*
median k2 (min ⁻¹), range	0.064, 0.027–0.155	0.091, 0.046–0.180	0.038*
median TTP (min), range	15.0, 3.0–20.0	7.5, 1.25–20.0	0.003*
median TBRmax, range	2.1, 1.4–6.2	3.0, 1.5–5.1	0.049*
median TBRmean, range	1.5, 0.8–5.0	1.7, 1.0–4.0	0.160

**p*-value < 0.05 with false discovery rate adjustment = statistically significant.

efflux with obligatory exchange (32, 33). The estimates for the contribution of blood–brain barrier disruption and the specific LAT transport system contribution to the FDOPA uptake and washout in gliomas are not fully understood (34).

In our study, static parameters did not significantly differ between LGG and HGG. Regarding FDOPA uptake quantification using static parameters, conflicting results have been provided. While some authors found no association between FDOPA uptake and grading (8, 10, 11), others found higher FDOPA uptake values in HGG than in LGG (9, 12, 14, 16–18). Xiao et al. recently exhibited in a meta-analysis a pooled sensitivity of 0.71 and specificity of 0.86 for newly diagnosed gliomas grading using FDOPA PET static parameters (35). Our results confirmed that simplified quantification parameters have high specificity for gliomas grading. However, the current study showed that kinetic analysis provided a higher accuracy compared to static parameters for gliomas grading. These results are consistent with recent studies revealing that kinetic analysis markedly improved diagnostic performances for gliomas grading using FET PET imaging (21, 22), confirming that kinetic parameters provide different metabolic informations from that of static PET parameters. Regarding FET PET/CT, guidelines recently suggested that the standard method should be supplemented by the dynamic approach for non-invasive tumor grading of newly diagnosed gliomas with (23).

Our results showed that static and dynamic parameters were correlated with age. Carideo et al. already exhibited that age has an impact on FDOPA uptake (36).

The current study has several limitations. Only 14 patients were analyzed and only 9/32 samples were classified as LGG. The time range between FDOPA PET/CT and surgery was up to 110

days. However, only two patients had surgery more than 6 weeks after the FDOPA PET/CT and the pathological analysis revealed astrocytoma-IDH mutant for both patients. An IDIF was used for the PET kinetic modeling. However, recent studies also used an IDIF for quantifying FDOPA gliomas uptake (10, 15, 18, 37, 38). The information on dexamethasone or on medications with other steroids at the time of FDOPA PET/CT was not available (39). No partial volume correction was performed for the middle cerebral artery VOI. We compared FDOPA uptake parameters with IDH mutational status applying the IDH genotype of the whole specimen for each individual sample. Finally, the spatial accuracy of the neuronavigation-guided biopsies may have been impacted by brain shift after craniotomy, which could lead to brain shift. However, the biopsies were performed at the beginning of the surgical procedure before durotomy with Sedan needles, thus limiting the consequences of any such shift.

CONCLUSIONS

The present study suggests an additive value of FDOPA PET/CT kinetic parameters for newly-diagnosed gliomas grading.

DATA AVAILABILITY STATEMENT

The original contributions presented in the study are included in the article/supplementary material, further inquiries can be directed to the corresponding author/s.

ETHICS STATEMENT

The studies involving human participants were reviewed and approved by ethics committee of Ile de France 1. The patients/participants provided their written informed consent to participate in this study.

AUTHOR CONTRIBUTIONS

All authors made substantial contributions to the conception of the work, acquisition, interpretation of data, in drafting the work, and approved the submitted version.

ACKNOWLEDGMENTS

The content of this manuscript has been presented at the EANM'20 Annual Congress of the European Association of Nuclear Medicine, European Journal of Nuclear Medicine and Molecular Imaging (2020) 47 (Suppl 1): S1–S753, doi: 10.1007/s00259-020-04988-4.

REFERENCES

- Omuro A, DeAngelis LM. Glioblastoma and other malignant gliomas: a clinical review. *JAMA*. (2013) 310:1842–50. doi: 10.1001/jama.2013.80319
- Weller M, van den Bent M, Tonn JC, Stupp R, Preusser M, Cohen-Jonathan-Moyal E, et al. European Association for Neuro-Oncology (EANO) Task Force on Gliomas. European Association for Neuro-Oncology (EANO) guideline on the diagnosis and treatment of adult astrocytic and oligodendroglial gliomas. *Lancet Oncol*. (2017) 18:e315–29. doi: 10.1016/S1470-2045(17)30194-8

3. Almenawer SA, Badhiwala JH, Alhazzani W, Greenspoon J, Farrokhyar F, Yarascavitch B, et al. Biopsy versus partial versus gross total resection in older patients with high-grade glioma: a systematic review and meta-analysis. *Neuro Oncol.* (2015) 17:868–81. doi: 10.1093/neuonc/nou349
4. Castet F, Alanya E, Vidal N, Izquierdo C, Mesia C, Ducray F, et al. Contrast-enhancement in supratentorial low-grade gliomas: a classic prognostic factor in the molecular age. *J Neurooncol.* (2019) 143:515–23. doi: 10.1007/s11060-019-03183-2
5. Scott JN, Brasher PM, Sevick RJ, Rewcastle NB, Forsyth PA. How often are nonenhancing supratentorial gliomas malignant? A population study. *Neurology.* (2002) 59:947–9. doi: 10.1212/wnl.59.6.947
6. Albert NL, Weller M, Suchorska B, Galldiks N, Soffietti R, Kim MM, et al. Response Assessment in Neuro-Oncology working group and European Association for Neuro-Oncology recommendations for the clinical use of PET imaging in gliomas. *Neuro Oncol.* (2016) 18:1199–208. doi: 10.1093/neuonc/now058
7. Muoio B, Giovannella L, Treglia G. Recent developments of 18F-FET PET in neuro-oncology. *Curr Med Chem.* (2018) 25:3061–73. doi: 10.2174/0929867325666171123202644
8. Becherer A, Karanikas G, Szabó M, Zettinig G, Asenbaum S, Marosi C, et al. Brain tumour imaging with PET: a comparison between [18F]fluorodopa and [11C]methionine. *Eur J Nucl Med Mol Imaging.* (2003) 30:1561–7. doi: 10.1007/s00259-003-1259-1
9. Bund C, Heimburger C, Imperiale A, Lhermitte B, Chenard MP, Lefebvre F, et al. FDOPA PET-CT of nonenhancing brain tumors. *Clin Nucl Med.* (2017) 42:250–7. doi: 10.1097/RLU.0000000000001540
10. Chen W, Silverman DH, Delaloye S, Czernin J, Kamdar N, Pope W, et al. 18F-FDOPA PET imaging of brain tumors: comparison study with 18F-FDG PET and evaluation of diagnostic accuracy. *J Nucl Med.* (2006) 47:904–11. doi: 10.3410/f.30526.487028
11. Cicone F, Carideo L, Scaringi C, Arcella A, Giangaspero F, Scopinaro F, et al. 18F-DOPA uptake does not correlate with IDH mutation status and 1p/19q co-deletion in glioma. *Ann Nucl Med.* (2019) 33:295–302. doi: 10.1007/s12149-018-01328-3
12. Fueger BJ, Czernin J, Cloughesy T, Silverman DH, Geist CL, Walter MA, et al. Correlation of 6-18F-fluoro-L-dopa PET uptake with proliferation and tumor grade in newly diagnosed and recurrent gliomas. *J Nucl Med.* (2010) 51:1532–8. doi: 10.2967/jnumed.110.078592
13. Ginot M, Zaragori T, Marie PY, Roch V, Gauchotte G, Rech F, et al. Integration of dynamic parameters in the analysis of 18F-FDopa PET imaging improves the prediction of molecular features of gliomas. *Eur J Nucl Med Mol Imaging.* (2020) 47:1381–90. doi: 10.1007/s00259-019-04509-y
14. Janvier L, Olivier P, Blonski M, Morel O, Vignaud JM, Karcher G, et al. Correlation of SUV-derived indices with tumoral aggressiveness of gliomas in static 18F-FDOPA PET: use in clinical practice. *Clin Nucl Med.* (2015) 40:e429–35. doi: 10.1097/RLU.00000000000000897
15. Nioche C, Soret M, Gontier E, Lahutte M, Dutertre G, Dulou R, et al. Evaluation of quantitative criteria for glioma grading with static and dynamic 18F-FDopa PET/CT. *Clin Nucl Med.* (2013) 38:81–7. doi: 10.1097/RLU.0b013e318279fd5a
16. Pafundi DH, Laack NN, Youland RS, Parney IF, Lowe VJ, Giannini C, et al. Biopsy validation of 18F-DOPA PET and biodistribution in gliomas for neurosurgical planning and radiotherapy target delineation: results of a prospective pilot study. *Neuro Oncol.* (2013) 15:1058–67. doi: 10.1093/neuonc/not002
17. Patel CB, Fazzari E, Chakhoyan A, Yao J, Raymond C, Nguyen H, et al. 18F-FDOPA PET and MRI characteristics correlate with degree of malignancy and predict survival in treatment-naïve gliomas: a cross-sectional study. *J Neurooncol.* (2018) 139:399–409. doi: 10.1007/s11060-018-2877-6
18. Schiepers C, Chen W, Cloughesy T, Dahlbom M, Huang SC. 18F-FDOPA kinetics in brain tumors. *J Nucl Med.* (2007) 48:1651–61. doi: 10.2967/jnumed.106.039321
19. Palard-Novello X, Blin AL, Bourhis D, Garin E, Salaün PY, Devillers A, et al. Comparison of choline influx from dynamic 18F-Choline PET/CT and clinicopathological parameters in prostate cancer initial assessment. *Ann Nucl Med.* (2018) 32:281–7. doi: 10.1007/s12149-018-1246-z
20. Takesh M. The potential benefit by application of kinetic analysis of PET in the clinical oncology. *ISRN Oncol.* (2012) 2012:349351. doi: 10.5402/2012/349351
21. Pöppel G, Kreth FW, Mehrkens JH, Herms J, Seelos K, Koch W, et al. FET PET for the evaluation of untreated gliomas: correlation of FET uptake and uptake kinetics with tumour grading. *Eur J Nucl Med Mol Imaging.* (2007) 34:1933–42. doi: 10.1007/s00259-007-0534-y
22. Verger A, Stoffels G, Bauer EK, Lohmann P, Blau T, Fink GR, et al. Static and dynamic 18F-FET PET for the characterization of gliomas defined by IDH and 1p/19q status. *Eur J Nucl Med Mol Imaging.* (2018) 45:443–51. doi: 10.1007/s00259-017-3846-6
23. Law I, Albert NL, Arbizu J, Boellaard R, Drzezga A, Galldiks N, et al. Joint EANM/EANO/RANO practice guidelines/SNMMI procedure standards for imaging of gliomas using PET with radiolabelled amino acids and [18F]FDG: version 10. *Eur J Nucl Med Mol Imaging.* (2019) 46:540–57. doi: 10.1007/s00259-018-4207-9
24. Girard A, Saint-Jalmes H, Chaboub N, Le Reste PJ, Metais A, Devillers A, et al. Optimization of time frame binning for FDOPA uptake quantification in glioma. *PLoS ONE.* (2020) 15:e0232141. doi: 10.1371/journal.pone.0232141
25. Wesseling P, Capper D, WHO. (2016). Classification of gliomas. *Neuropathol Appl Neurobiol.* (2018) 44:139–50. doi: 10.1111/nan.12432
26. Huang SC, Barrio JR, Yu DC, Chen B, Grafton S, Melega WP, et al. Modelling approach for separating blood time-activity curves in positron emission tomographic studies. *Phys Med Biol.* (1991) 36:749–61. doi: 10.1088/0031-9155/36/6/004
27. Glatting G, Kletting P, Reske SN, Hohl K, Ring C. Choosing the optimal fit function: comparison of the Akaike information criterion and the F-test. *Med Phys.* (2007) 34:4285–92. doi: 10.1118/1.2794176
28. Cancer Genome Atlas Research Network, Brat DJ, Verhaak RG, Aldape KD, Yung WK, Salama SR, et al. Comprehensive, integrative genomic analysis of diffuse lower-grade gliomas. *N Engl J Med.* (2015). 372:2481–98. doi: 10.1056/NEJMoa1402121
29. Gupta K, Radotra BD, Banerjee AK, Nijhawan R. Quantitation of angiogenesis and its correlation with vascular endothelial growth factor expression in astrocytic tumors. *Anal Quant Cytol Histol.* (2004) 26:223–9.
30. Pöppel G, Kreth FW, Herms J, Koch W, Mehrkens JH, Gildehaus FJ, et al. Analysis of 18F-FET PET for grading of recurrent gliomas: is evaluation of uptake kinetics superior to standard methods? *J Nucl Med.* (2006) 47:393–403.
31. Weckesser M, Langen KJ, Rickert CH, Kloska S, Straeter R, Hamacher K, et al. O-(2-[18F]fluoroethyl)-L-tyrosine PET in the clinical evaluation of primary brain tumours. *Eur J Nucl Med Mol Imaging.* (2005) 32:422–9. doi: 10.1007/s00259-004-1705-8
32. Meier C, Ristic Z, Klauser S, Verrey F. Activation of system L heterodimeric amino acid exchangers by intracellular substrates. *EMBO J.* (2002) 21:580–9. doi: 10.1093/emboj/21.4.580
33. Yee RE, Cheng DW, Huang SC, Namavari M, Satyamurthy N, Barrio JR. Blood-brain barrier and neuronal membrane transport of 6-[18F]fluoro-L-DOPA. *Biochem Pharmacol.* (2001) 62:1409–15. doi: 10.1016/s0006-2952(01)00787-0
34. Dadone-Montaudié B, Ambrosetti D, Dufour M, Darcourt J, Almairac F, Coyne J, et al. [18F] FDOPA standardized uptake values of brain tumors are not exclusively dependent on LAT1 expression. *PLoS ONE.* (2017) 12:e0184625. doi: 10.1371/journal.pone.0184625
35. Xiao J, Jin Y, Nie J, Chen F, Ma X. Diagnostic and grading accuracy of 18F-FDOPA PET and PET/CT in patients with gliomas: a systematic review and meta-analysis. *BMC Cancer.* (2019) 19:767. doi: 10.1186/s12885-019-5938-0

36. Carideo L, Minniti G, Mamede M, Scaringi C, Russo I, Scopinaro E, et al. ^{18}F -DOPA uptake parameters in glioma: effects of patients' characteristics and prior treatment history. *Br J Radiol.* (2018) 91:20170847. doi: 10.1259/bjr.20170847
37. Kratochwil C, Combs SE, Leotta K, Afshar-Oromieh A, Rieken S, Debus J, et al. Intra-individual comparison of ^{18}F -FET and ^{18}F -DOPA in PET imaging of recurrent brain tumors. *Neuro Oncol.* (2014) 16:434–40. doi: 10.1093/neuonc/not199
38. Wardak M, Schiepers C, Cloughesy TF, Dahlbom M, Phelps ME, Huang SC. ^{18}F -FLT and ^{18}F -FDOPA PET kinetics in recurrent brain tumors. *Eur J Nucl Med Mol Imaging.* (2014) 41:1199–209. doi: 10.1007/s00259-013-2678-2
39. Stegmayr C, Stoffels G, Kops ER, Lohmann P, Galldiks N, Shah NJ, et al. Influence of dexamethasone on O-(2-[^{18}F]-fluoroethyl)-L-tyrosine uptake in

the human brain and quantification of tumor uptake. *Mol Imaging Biol.* (2019) 21:168–74. doi: 10.1007/s11307-018-1221-z

Conflict of Interest: The authors declare that the research was conducted in the absence of any commercial or financial relationships that could be construed as a potential conflict of interest.

Copyright © 2021 Girard, Le Reste, Metais, Chaboub, Devillers, Saint-Jalmes, Jeune and Palard-Novello. This is an open-access article distributed under the terms of the Creative Commons Attribution License (CC BY). The use, distribution or reproduction in other forums is permitted, provided the original author(s) and the copyright owner(s) are credited and that the original publication in this journal is cited, in accordance with accepted academic practice. No use, distribution or reproduction is permitted which does not comply with these terms.



The Value of ^{18}F -FDG PET/CT in Diagnosing Pancreatic Lesions: Comparison With CA19-9, Enhanced CT or Enhanced MR

Shengyun Huang^{1,2,3†}, Huanhuan Chong^{1,3,4†}, Xun Sun^{1,3}, Zhijian Wu^{1,3}, Qing Jia^{1,3}, Yongxue Zhang^{1,3} and Xiaoli Lan^{1,3*}

¹ Department of Nuclear Medicine, Union Hospital, Tongji Medical College, Huazhong University of Science and Technology, Wuhan, China, ² Department of Nuclear Medicine, National Cancer Center/National Clinical Research Center for Cancer/Cancer Hospital and Shenzhen Hospital, Chinese Academy of Medical Sciences and Peking Union Medical College, Shenzhen, China, ³ Hubei Key Laboratory of Molecular Imaging, Wuhan, China, ⁴ Department of Radiology, Ruijin Hospital, Shanghai Jiao Tong University School of Medicine, Shanghai, China

OPEN ACCESS

Edited by:

Mike Sathekge,
University of Pretoria, South Africa

Reviewed by:

Natale Quartuccio,
ARNAS Ospedali Civico Di Cristina
Benfratelli, Italy
Salvatore Annunziata,
Fondazione Policlinico Universitario
Agostino Gemelli IRCCS, Italy

*Correspondence:

Xiaoli Lan
xiaoli_lan@hust.edu.cn

[†]These authors share first authorship

Specialty section:

This article was submitted to
Nuclear Medicine,
a section of the journal
Frontiers in Medicine

Received: 17 February 2021

Accepted: 13 September 2021

Published: 08 October 2021

Citation:

Huang S, Chong H, Sun X, Wu Z,
Jia Q, Zhang Y and Lan X (2021) The
Value of ^{18}F -FDG PET/CT in
Diagnosing Pancreatic Lesions:
Comparison With CA19-9, Enhanced
CT or Enhanced MR.
Front. Med. 8:668697.
doi: 10.3389/fmed.2021.668697

Objective: To investigate the value of ^{18}F -FDG PET/CT in diagnosing pancreatic lesions, and compare it with CA19-9, contrast-enhanced CT (CECT), and contrast-enhanced MRI (CEMR).

Methods: Cases of patients with suspected pancreatic lesions examined between January 1, 2011 and June 30, 2017 were retrospectively analyzed. CA19-9, CECT and CEMR within 2 weeks of PET/CT were evaluated. We compared the diagnostic efficacy of PET/CT with CA19-9, CECT and CEMR as well as combined tests.

Results: A total of 467 cases were examined in this study, including 293 males and 174 females, with an average age of 57.79 ± 12.68 y (16–95 y). Cases in the malignant group ($n = 248$) had significantly higher SUVmax (7.34 ± 4.17 vs. 1.70 ± 2.68 , $P < 0.001$) and CA19-9 (663.21 ± 531.98 vs. 87.80 ± 218.47 , $P < 0.001$) than those in the benign group ($n = 219$). The sensitivity, specificity and accuracy of PET/CT were 91.9, 96.3, and 94.0%, respectively. Those for CECT were 83.6, 77.8, 81.2%, respectively; and 91.2, 75.0, 81.7% were for CEMR. PET/CT corrected 14.7% (28/191) CECT diagnoses and 12.2% (10/82) CEMR diagnoses. Although the diagnostic efficiency of CA19-9 was acceptable (80.0, 69.0, 74.9% respectively), the joint application of PET/CT and CA19-9 could significantly enhance the diagnostic efficiency compared with PET/CT alone (sen 97.4 vs. 90.5%, $P = 0.0003$; spe 100.0 vs. 95.2%, $P = 0.0047$).

Conclusions: PET/CT has sensitivity similar to CECT, CEMR and significantly higher specificity and accuracy, helping reduce false diagnoses of morphological images. Combining PET/CT with CA19-9 could enhance diagnostic efficiency.

Keywords: ^{18}F -FDG PET/CT, pancreatic lesions, serum CA19-9, enhanced CT, enhanced MR, diagnosis

INTRODUCTION

Pancreatic cancer is one of the most fatal tumors in the world with a median survival time of merely 3–6 months. Its incidence and mortality have continued to rise in the past decade (1, 2). Only surgery is curative for patients with pancreatic cancer. Early symptoms of pancreatic cancer (including epigastric and back pain, jaundice, and weight loss) are insidious and non-specific (3). About 60% of pancreatic cancer patients have distant metastases at the time of diagnosis (4). The main challenge in clinical practice for patients with pancreatic cancer is to accurately distinguish malignant lesions from benign ones in early evaluation.

Carbohydrate antigen 19-9 (CA19-9) is the most commonly used tumor marker in the management of pancreatic cancer. But it is frequent false-positive in pancreatitis, cirrhosis, and in other gastrointestinal cancers such as colorectal cancer and cholangiocarcinoma carcinoma, and inevitably false-negative in Lewis antigen-negative subpopulations (5). The standard imaging modality recommended by NCCN guidelines is contrast-enhanced multi-detector computed tomography (CECT) (6). Remarkable advances in CT technology have improved its ability to precisely assess local invasion of primary tumor. However, there are still limitations when suspected lesions are ambiguous on CT or when CECT cannot be obtained. Contrast-enhanced magnetic resonance imaging (CEMR) with superior soft tissue resolution and high sensitivity is particularly helpful in these situations. Yet both CECT and CEMR are still restricted to morphological portrait of tumor, leading to inaccurate diagnosis of certain patients.

The rapid development of positron emission tomography/computed tomography (PET/CT) since the 1990s has enabled a comprehensive assessment of both morphology and metabolic activity of lesions. Overexpression of glucose transporter-1 (GLUT-1) and increased glucose utilization are reported in pancreatic carcinoma (PC), making it possible to detect PC early with ^{18}F -FDG PET (7). However, current guidelines (NCCN and ESMO) do not clearly define the role of PET/CT in pancreatic cancer (6, 8). This study compared PET/CT with other traditional tests (CA19-9, CECT, and CEMR) in the diagnosis of pancreatic lesions. We then further explored whether the diagnostic efficiency could be improved by combining different methods.

MATERIALS AND METHODS

Patients

Cases of patients from January 1, 2011 to June 30, 2017 with suspected pancreatic lesions were retrospectively analyzed in our PET center. Inclusion criteria were as follows: (1) no

pathological diagnosis, or any anticancer therapy including surgery, radiotherapy, or chemotherapy before any examination; (2) serum CA19-9, CECT or CEMR performed within 2 weeks of PET/CT if available; (3) complete medical history and follow-up data (>6 months). Exclusion criteria were: (1) blood glucose >11 mmol/L before injection of ^{18}F -FDG; (2) other malignant tumors in addition to the pancreatic lesions confirmed either before or after PET/CT scan; (3) pancreatic neuroendocrine tumors/cancers (NETs/NECs). The reference standard for diagnosis was based on histology (either biopsy or surgery) and/or clinical outcome assessment. This study was approved by the Institutional Review Board of Union Hospital, Tongji Medical College, Huazhong University of Science and Technology.

PET/CT Protocol

All patients were requested to fast for at least 4–6 h before the PET/CT examination, and their blood glucose levels were ≤ 11 mmol/L before ^{18}F -FDG injection. Patients were intravenously injected with 3.7–5.55 MBq/kg ^{18}F -FDG of $\geq 95\%$ radiochemical purity synthesized by a cyclotron (GE Minitracer[®], GE Healthcare, Milwaukee WI, USA) and synthesizer (TracerLab MX-FDG[®], GE). Patients were required to rest in a quiet, dark room for ~ 60 min and drink 300–500 mL of water before examination. After emptying the bladder, patients were scanned (Discovery LS[®] or VCT PET/CT/CT[®], GE Healthcare, Milwaukee WI, USA). A CT scout view was performed followed by a low-dose CT scan (120 kV, 100 mA, and 3.75 mm slice thickness). Whole-body PET scanning was then performed immediately from the top of skull to the upper thighs at six to eight bed positions (2–3 min per bed position). Delayed abdominal scan (2–3 h after injection) was occasionally required for lesions that were inconspicuous or equivocal in early phase. 3D PET images were reconstructed by an iterative algorithm, using the CT image data for attenuation correction and then transferred to a workstation (Xeleris[®], GE).

Image Analysis

PET/CT, CECT, CEMR and other clinical data were retrieved from hospital databases. Diagnoses of pancreatic lesions were independently made by at least two experienced nuclear medicine or radiology physicians. Final consensus was reached after comprehensive image analysis. Visual and semi-quantitative methodology (maximum standardized uptake value, SUVmax) were applied to PET/CT analysis. Retention index (RI) (9, 10) were used for dual-phase PET/CT. The retention index (RI) was calculated as follows:

$$\text{RI} = \frac{\text{SUV}_2 - \text{SUV}_1}{\text{SUV}_1} \times 100$$

In general, lesions with focal ^{18}F -FDG uptake ($\text{SUV}_{\text{max}} \geq 2.5$ or exceeding normal pancreas uptake) or significantly increased uptake on delay scan, evidence of local invasion, or distant metastasis was considered as suspicious for malignancy. CECT and CEMR diagnosis of pancreatic lesions were assessed

Abbreviations: F-FDG, 2-[^{18}F]fluoro-2-deoxyglucose; PET/CT, Positron emission tomography/computed tomography; CA19-9, Carbohydrate antigen 19-9; CECT, Contrast-enhanced computed tomography; CEMR, Contrast-enhanced magnetic resonance imaging; GLUT-1, Glucose transporter-1; SUVmax, Maximum standardized uptake value; RI, Retention index; ROC, Receiver operating characteristic; AUC, Area under curve; PPV, Positive predictive value; NPV, Negative predictive value; ROI, Region of interest.

TABLE 1 | General characteristics of cases.

	Malignant	Benign	All cases (%)	OR P-value
Total	248	219	467	
Sex				OR = 1.27 P = 0.25
Male	162	131	293 (62.7)	
Female	86	88	174 (37.3)	
Age			57.79 ± 12.68 y	OR = 2.37 P < 0.001
≥70 y	64	28	92 (19.7)	
<70 y	184	191	375 (80.3)	
Location of lesions on pancreas				
Head/neck	102	77	179 (38.3)	
Body/tail	133	71	204 (43.7)	
Whole pancreas	7	42	49 (10.5)	
Diffused/multiple lesions	6	11	17 (3.6)	
Not obvious	0	18	18 (3.9)	
Clinical stage				
I/II	98	—		
III/IV	150	—		

according to the NCCN guidelines and radiology reporting template (6, 11).

Statistical Analysis

The data are presented as mean ± standard deviation. Differences in SUVmax and serum CA19-9 between malignant and benign diagnoses were compared with an independent-samples *t*-test. The optimal cut-off points with maximum Youden Index were calculated by receiver operating characteristic (ROC) analysis. Sensitivity, specificity, accuracy, positive predictive value (PPV), and negative predictive value (NPV) of PET/CT, CA19-9, CECT, and CEMR were calculated. The results from different tests were also analyzed in parallel and in serial, to determine whether combinations of tests might give better performance. For parallel tests, results are defined to be positive as long as any one is positive, or negative when both are negative. For serial tests, positive results are considered only when both tests are positive. The diagnostic efficacies of the different methods were compared using the McNemar's chi-squared test. All statistics were generated using statistical packages from R software (www.rproject.org, Version 3.4; "pROC" and "ggplot2"). A two-tailed test with *P*-value < 0.05 was considered statistically significant.

RESULTS

General Characteristics

General characteristics of all 467 patients are detailed in **Table 1**. The average age was 57.79 ± 12.68 y (range, 16–95 y). Patients ≥ 70 y were 2.37 times more likely to have pancreatic cancer than those <70 y (*P* < 0.001). Cases were divided into malignant (*n* = 248) and benign groups (*n* = 219) by histology (either biopsy or operation) in 142 cases, and clinical outcome assessment (at least 6 months follow-up) in 325 cases. Follow-up was carried out until

December 2017. Median follow-up time was 25.7 months (range, 6.1–76.1 months). For the 142 cases who had histology results, 91 were malignant and 51 were benign (**Table 2**).

The Diagnostic Efficacy of PET/CT and Derived Parameters

In general, the sensitivity, specificity, accuracy, PPV and NPV of PET/CT were 91.9, 96.3, 94.0, 96.6, and 91.3%, respectively. For those cases misdiagnosed by PET/CT (**Table 3**), pancreatitis and tuberculosis were the most important false-positive findings on PET/CT (**Figure 1**), while medium-/well-differentiated pancreatic cancers tend to be negative on PET/CT.

SUVmax of primary lesions were measured for all 467 cases. SUVmax in the malignant group were significantly higher than benign group (7.34 ± 4.17 vs. 1.70 ± 2.68, *P* < 0.001) (**Figure 2A**). According to ROC curves (**Figure 2B**), the areas under the curve (AUC) of SUVmax were 0.917. The best diagnostic performances were achieved when the optimal cut-offs were set at SUVmax = 3.75 (with sensitivity of 92.7% and specificity of 82.2%) compared with the conventional standard cut-off 2.5 (with sensitivity of 96.4% and specificity of 67.7%).

Among 47 patients (47/467, 10.1%) examined with delayed abdominal scan, cases in the malignant group tend to have higher SUV1 (5.90 ± 2.35 vs. 3.52 ± 2.15, *P* = 0.0012), SUV2 (7.90 ± 4.12 vs. 3.49 ± 3.20, *P* < 0.001) and RI (31.80 ± 31.25 vs. −7.58 ± 40.82, *P* = 0.0019) than those in the benign group (**Figures 3A,B**). The optimal cut-off was RI = 2.15 (with sensitivity of 93.3% and specificity of 58.8%) (**Figure 3C**). Increased SUV2 (or RI > 0) is noted in most of malignant lesions (28/30, sen 93.3%), except for 2 malignant cases (1 medium differentiated adenocarcinoma and 1 unspecified adenocarcinoma). As for benign cases, 3 maintained stationary, 7 had decreased SUVmax (10/17, spe 58.8%), and the rest 7 cases revealed an increase in SUVmax (7/17,

TABLE 2 | Histology results of 142 patients.

Malignant cases	91
Pancreatic ductal adenocarcinoma (PDAC)	9
Serous/Mucinous cystadenocarcinoma	2
Intraductal papillary mucinous neoplasm (IPMN) with atypical hyperplasia	2
Tubular adenocarcinoma	10
Adenocarcinoma (unspecified)	44
Solid-pseudopapillary carcinoma (SPT)	2
IPMN-related invasive carcinoma - ductal adenocarcinoma with neuroendocrine microadenomas	1
Undifferentiated carcinoma	1
Found multiple metastasis intraoperatively	18
Limited sample*	2
Benign cases	51
Pancreatitis	
Acute pancreatitis	5
Chronic pancreatitis	14
Chronic lymphoplasmacytic pancreatitis	1
Pancreatic pseudocyst	2
Autoimmune pancreatitis	3
Pancreatic benign tumor	
Serous/Mucinous cystadenoma	7
Giant Pancreatic lipoma	1
Pancreatic tuberculosis	2
Normal pancreatic tissue/no obvious lesion was observed**	16

*Two patients without positive finding due to limited sample of biopsy, but then diagnosed as pancreatic cancer during clinical follow-up.

**Sixteen patients without significant abnormal finding on biopsy or multiple imaging's, and were cured after treatment.

41.2%) including 1 chronic lymphoplasmacytic pancreatitis, 1 autoimmune pancreatitis and 5 pancreatitis.

Diagnostic Efficiency of PET/CT Compared With CA19-9

Cases in the malignant group had significantly higher CA19-9 (663.21 ± 531.98 vs. 87.80 ± 218.47 , $P < 0.001$) than those in the benign group (**Figure 4A**). The sensitivity, specificity, and accuracy of CA19-9 alone were 80.0, 69.0, and 74.9%, respectively.

For the 358 cases which underwent both PET/CT and serum CA19-9 within 2 weeks (including only the latest CA19-9 result from PET/CT if repeatedly assessed), we compared their diagnostic efficiency by ROC curves. The areas under the curves (AUCs) of SUVmax and serum CA19-9 were 0.90 and 0.831, respectively, indicating that the diagnostic efficiency of SUVmax is higher than that of serum CA19-9. The best diagnostic performances were achieved when the optimal cut-offs were set at 3.75 for SUVmax (sen 91.6%, spe 79.8%) and 105.35 for CA19-9 (sen 72.1%, spe 85.1%) (**Figure 4B**).

Diagnostic efficiencies were significantly improved when combined PET/CT with CA19-9 compared to PET/CT alone

TABLE 3 | Misdiagnosed cases of PET/CT.

PET/CT false-positive (FP)	8
Pancreatitis	
Chronic pancreatitis	1
Chronic lymphoplasmacytic pancreatitis	1
Autoimmune pancreatitis	2
Inflammatory lesions	1
Pancreatic tuberculosis	2
Benign mass*	1
PET/CT false-negative (FN)	20
By histology	
Well-differentiated adenocarcinoma	1
Medium-well-differentiated adenocarcinoma	1
Medium-well-differentiated tubular adenocarcinoma	1
Medium differentiated ductal adenocarcinoma	2
Poor differentiated mucinous cystadenocarcinoma	1
Adenocarcinoma (unspecified)	3
Solid-pseudopapillary carcinoma (SPT)	1
Multiple metastasis found during operation	3
By clinical follow-up	7

*1 case refuse to carry out biopsy and was clinically diagnosed as benign by multi-disciplinary consultation, cured after supportive treatment (follow-up >16 months).

(parallel test: sen 97.4 vs. 90.5%, $P = 0.0003$; serial test: spe 100.0 vs. 95.2%, $P = 0.0047$). Moreover, the high NPV of parallel test (95.6%) indicates that negative results of both CA19-9 and PET/CT decrease the odds of a malignant diagnosis. Similarly, positive results of both two tests increase malignance possibility with a PPV of 100.0% for serial test (**Table 4**).

Diagnostic Efficiency of PET/CT Compared With CECT or CEMR

Among 467 cases, 191 underwent CECT, while 82 cases had CEMR. The sensitivity, specificity and accuracy of CECT were 83.6, 77.8, 81.2%, respectively. And those for CEMR were 91.2, 75.0, 81.7%, respectively.

PET/CT had similar sensitivity to CECT (89.1 vs. 83.6%, $P = 0.16$) and CEMR (88.2 vs. 91.2%, $P = 0.56$). But its specificity was significantly better than those of CECT and CEMR (96.3 vs. 77.8%, $P < 0.001$; 93.8 vs. 75.0%, $P = 0.0027$). The accuracy of PET/CT was over 90%.

Combined CECT with PET/CT can enhance diagnostic efficiencies compared to CECT alone (sen 94.5 vs. 83.6% for parallel test; spe 97.5 vs. 77.8% for serial test, both $P < 0.001$). Although CEMR was less specific (75.0%) for diagnosis, it seemed to perform better at detection and excluding malignant lesions with relatively high sensitivity (91.2%) and NPV (92.3%) (**Figure 5**). Furthermore, Combined CEMR with PET/CT can significantly improve specificity compared to CEMR alone (93.8 vs. 75.0%, $P = 0.0027$), but not better than PET/CT (**Table 4**).

Some malignant lesions may lack typical malignant signs on morphology, which makes them harder to diagnose only by CT or MR. In our study, PET/CT corrected 14.7% (28/191) CECT

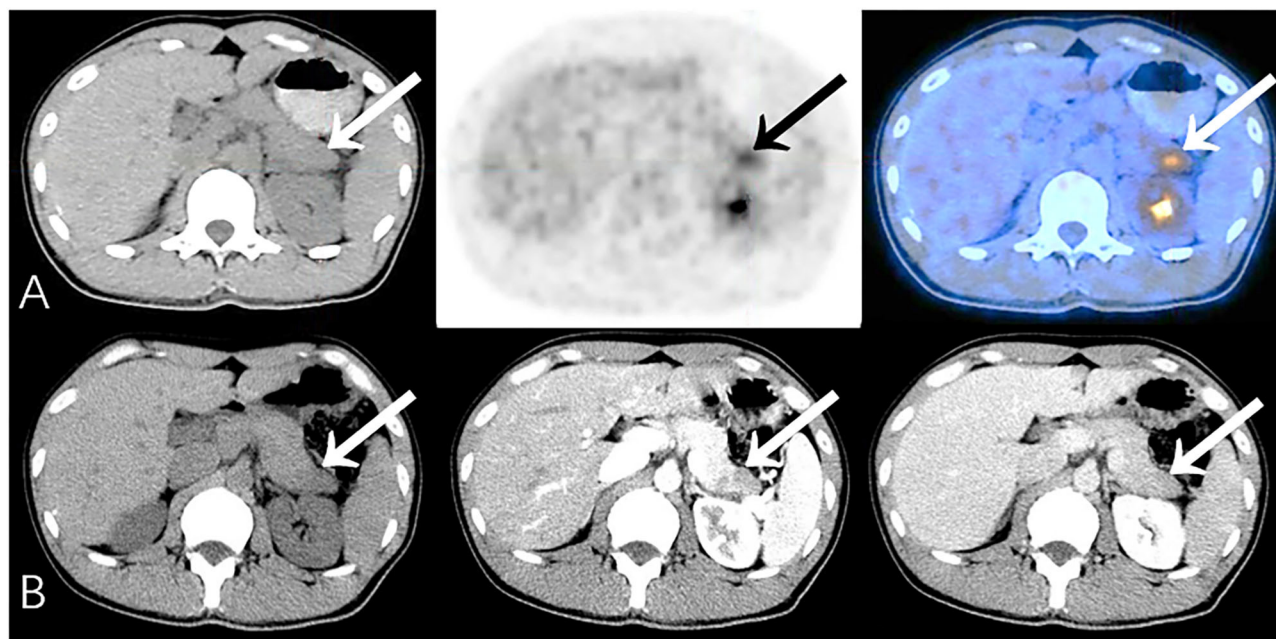


FIGURE 1 | Representative patient on PET/CT (False-Positive) compared to CECT (True-Negative): A 34-year-old male had abdominal pain for 2 months, worsening in the last 10 days. Serum CA19-9 was normal (34.1 U/mL). **(A)** PET/CT showed significantly increased ^{18}F -FDG uptake area in the tail of the pancreas (SUVmax 5.5). The edge of the lesion was indistinct and seemed to be closely related to the stomach wall; it was considered to be malignant. **(B)** Density of the lesion was relatively low at every phase. Fat spaces around the pancreas were clear on CECT (benefits from the higher resolution), suggesting chronic pancreatitis. Patient underwent distal pancreatectomy, and histopathology revealed chronic pancreatitis with small abscesses. No special complaints during follow-up (>23 months).

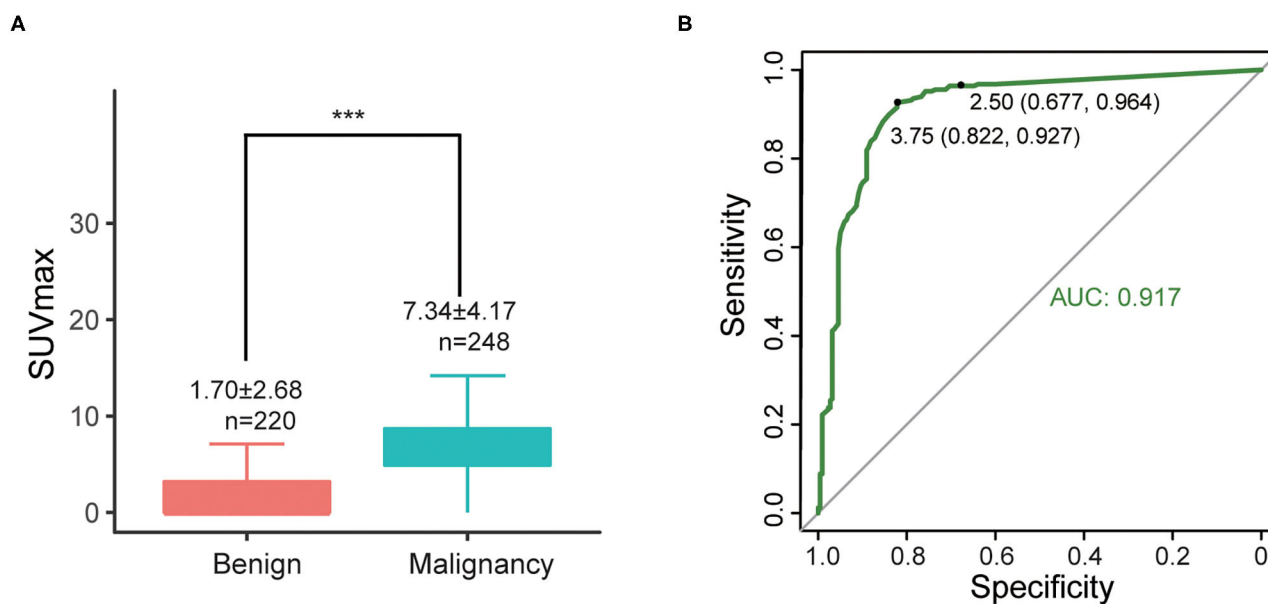
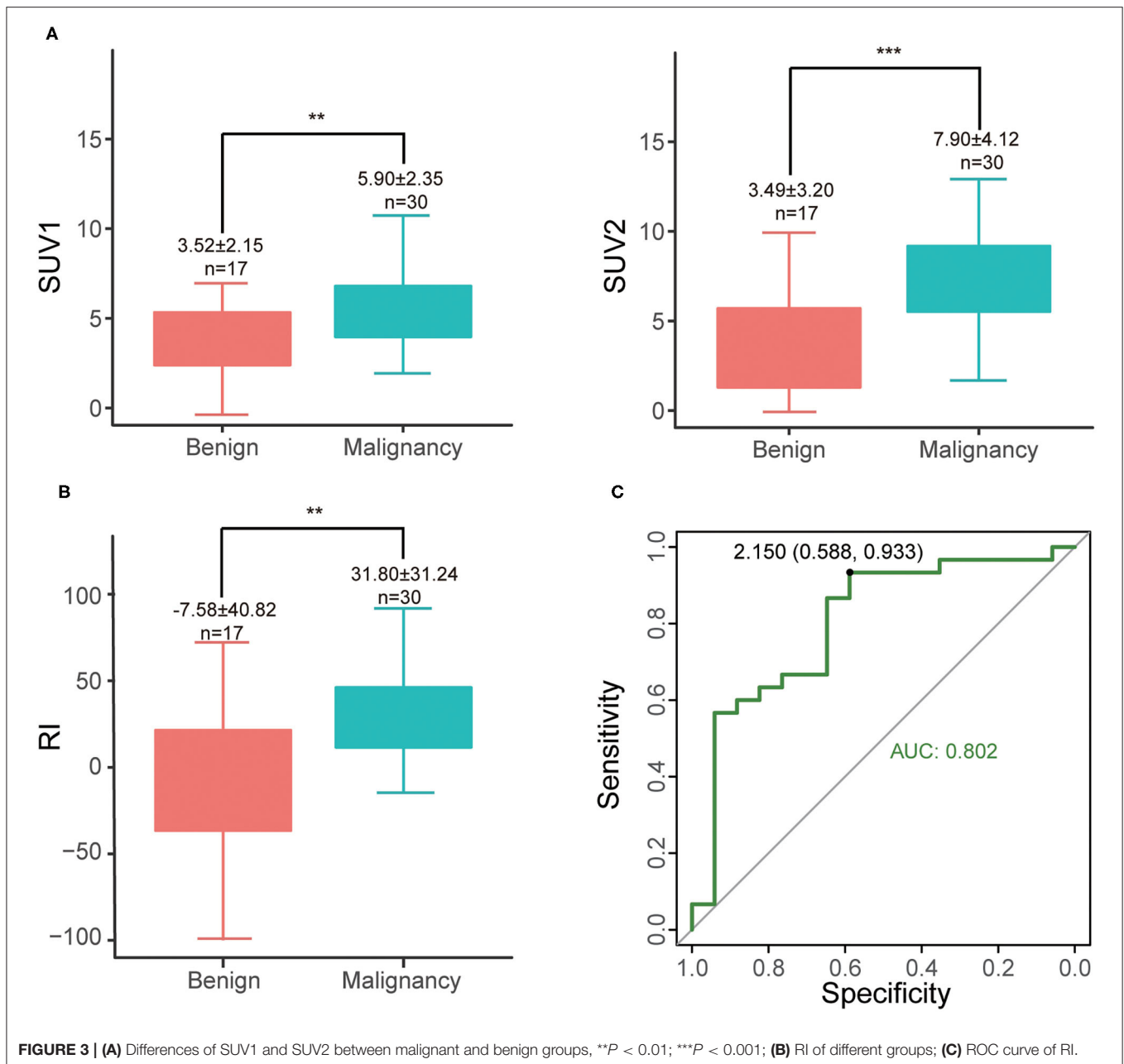


FIGURE 2 | (A) Differences of SUVmax between malignant and benign groups, *** $P < 0.001$; **(B)** ROC curve of SUVmax (all cases).

diagnoses, identifying 12 malignant and 16 benign cases with the opposite diagnosis on CECT, and changed 12.2% (10/82) diagnoses by CEMR (Table 5). Additional metabolic information

provided by PET/CT may lead to an improvement in the diagnostic accuracy of pancreatic lesions and in subsequent management of these patients (Figures 6, 7).



Compare Diagnostic Efficiencies of Other Combinations

CA19-9 could help improve the diagnostic efficiency combined with CECT (sen 95.8 vs. 83.2% for parallel test, $P < 0.001$; spe 97.0 vs. 83.3% for serial test, $P = 0.0027$) or CEMR (spe 97.6 vs. 78.0% for serial test, $P = 0.0047$) compared to the two imaging modalities alone. Given that sensitivity of CEMR is already pretty high, sensitivity of combined diagnosis was not significantly improved (sen 100 vs. 90.0% for parallel test, $P = 0.083$). Although combination of CECT and CEMR showed relatively higher sensitivity and specificity, it had no significant difference compared with CECT alone (sen 100.0 vs. 88.2% for

parallel test, $P = 0.157$; spe 96.4 vs. 85.7% for serial test, $P = 0.083$), which may due to limited cases in this group ($n = 45$) (Table 6).

DISCUSSION

In our study, we retrospectively evaluated a relatively large group of cases with suspected pancreatic lesions examined by PET/CT, CECT, CEMR and CA19-9. We compared not only the independent diagnostic value of ^{18}F -FDG PET/CT, CA19-9, CECT and CEMR, but also the diagnostic efficacy of different combined tests. Our results indicate that ^{18}F -FDG PET/CT

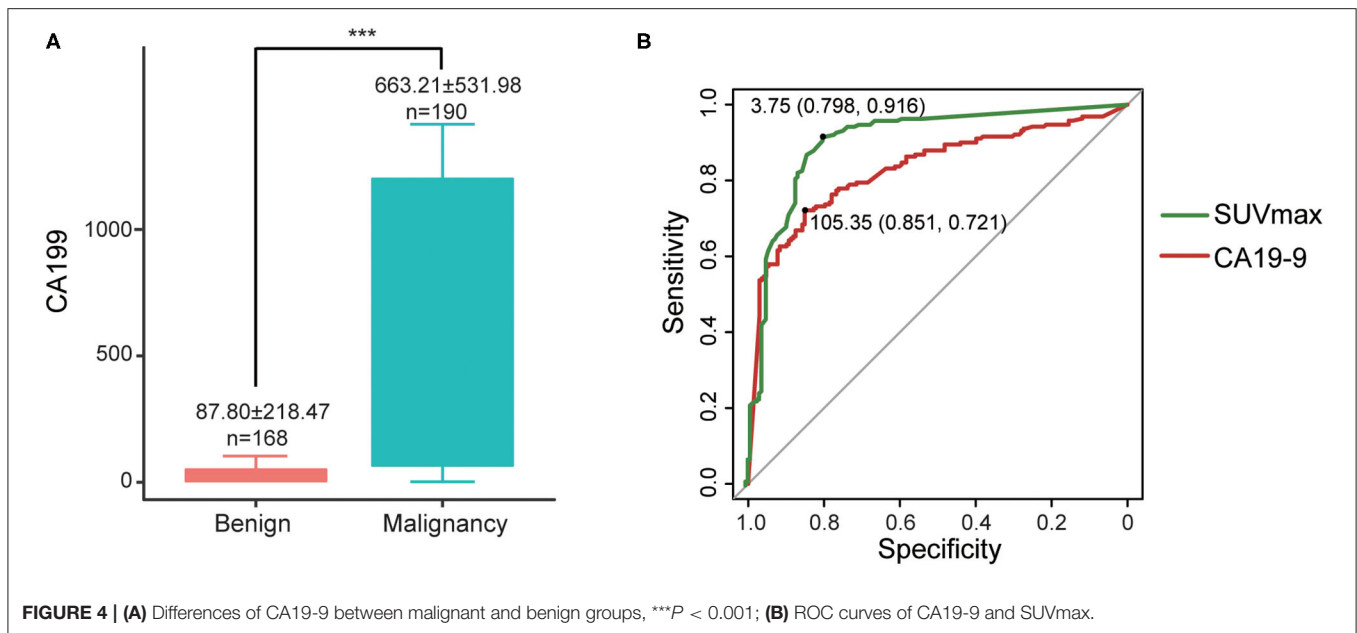


FIGURE 4 | (A) Differences of CA19-9 between malignant and benign groups, *** $P < 0.001$; **(B)** ROC curves of CA19-9 and SUVmax.

performs better than the other three examinations in diagnosis of pancreatic lesions, especially in terms of specificity and accuracy. Moreover, the joint application of PET/CT with other methods could enhance the diagnostic efficiency.

PET/CT has made distinct progress for the diagnosis of tumors since the 1990s. As previously reported, the diagnostic efficacy of ^{18}F -FDG PET/CT in pancreatic lesions varies from 85 to 100% in sensitivity, 61 to 94% in specificity, and 84 to 95% in accuracy (12–17). One of the reasons for the wide variation was the limited sample size. The heterogeneity of imaging technology between early studies may also affect the results. According to our research, ^{18}F -FDG PET/CT has rather high sensitivity, specificity, and accuracy (91.9, 96.3, and 94.0%, respectively). Additional metabolic information provided by PET/CT may lead to an improvement in the diagnostic efficacy. Besides, PET/CT has larger field-of-view, which can help to detect metastasis and confirm the malignant diagnosis. However, tumor heterogeneity may contribute to inconsistent performance of PET/CT. It is important to note that medium- or well-differentiated pancreatic cancers tend to be negative on PET/CT. Higher tumor uptake, evaluated by the tumor SUVmax or the tumor-to-liver SUVmax ratio (SUVmax T/L), seems correlate to increased Ki67 and worse prognosis (18, 19). The overexpression of GLUT-1 play an important role in FDG uptake and accumulation in pancreatic cancer, which was reported to have positive correlations to SUV and histological grade though controversial (20–22). PET/CT may also have a role in the diagnosis of malignant cystic neoplasms (17). It is reported that malignant high-grade IPMN have significantly higher SUVmax (3.5 ± 1.4 , $n = 9$) than the low-grade IPMN group (1.9 ± 1.1 , $n = 9$), but with overlapped range between groups (23). Pancreatic solid pseudopapillary tumor (SPT) is also associated with increased FDG uptake (5.9 ± 5.7 , $n = 10$) which was similar to PDAC (5.8 ± 2.7 , $n = 46$) (24). However, PET/CT may be

false-positive in cases with pancreatitis and tuberculosis. Some benign pancreatic lesions such as chronic lymphoplasmacytic pancreatitis and autoimmune pancreatitis may mimic malignant mass with increased SUVmax (25–28). Researches have been reported that selective use of delayed imaging (usually 2–3 h after injection) is beneficial for differentiating between malignant and benign lesions in pancreas because of the better target non-target ratio (29–31). Our results supported that SUV of malignancies tend to increase over time (or $\text{RI} > 0$) with a high sensitivity of 93.3%, while relatively large variance was observed in benign cases (41.2% increased, 58.8% maintained or decreased). Delayed scan seemed to reduce overlap of SUV obtained in malignant and benign cases and may help improve interpretation confidence especially in benign cases with stable or decreased SUVmax. Future prospective studies are required to better understand the additional value of delayed PET/CT and optimal indication. However, the above parameters were derived from SUV, a semi-quantitative parameter that are known not only as time-dependent values but also as method-dependent ones that can be changed by acquisition conditions, reconstruction methods, region of interest (ROI), plasma glucose level and other factors (32). There are no standard criteria for SUVmax to define an increase in ^{18}F -FDG uptake. Thereby, diagnosis should be made after a comprehensive analysis of the images. With the rapid development of computational biology, extracting advanced image texture features from medical images such as PET/CT could provide a wealth of additional information, which may be promising to improve diagnosis and management of patients (33–35).

Serum CA19-9, CECT, and CEMR have their own merits in diagnosis of pancreatic lesions and have been widely used. Serum CA19-9 is the most useful tumor marker for pancreatic cancer but non-specific. One of the disadvantages of this study is the lack of baseline assessment of serum CA19-9 in some cases (especially

TABLE 4 | Diagnostic efficiency of PET/CT compared with other tests.

	Sensitivity	Specificity	Accuracy	PPV	NPV
PET/CT (<i>n</i> = 467)	91.9%	96.3%	94.0%	96.6%	91.3%
PET/CT^Δ with CA19-9 (<i>n</i> = 358)					
PET/CT	90.5%	95.2%	92.7%	95.6%	89.9%
CA19-9	80.0%**	69.0%***	74.9%	74.5%	75.3%
PET/CT//CA19-9	97.4%***	64.3%***	81.8%	75.5%	95.6%
PET/CT + CA19-9	73.2%***	100.0%**	85.8%	100.0%	76.7%
CECT^Δ with PET/CT (<i>n</i> = 191)					
CECT	83.6%	77.8%	81.2%	83.6%	77.8%
PET/CT	89.1% ^{N.S.}	96.3%***	92.1%	97.0%	86.7%
PET/CT//CECT	94.5%***	76.5% ^{N.S.}	86.9%	84.6%	91.2%
PET/CT + CECT	78.2%*	97.5%***	86.4%	97.7%	76.7%
CEMR^Δ with PET/CT (<i>n</i> = 82)					
CEMR	91.2%	75.0%	81.7%	72.1%	92.3%
PET/CT	88.2% ^{N.S.}	93.8%**	91.5%	90.9%	91.8%
PET/CT // CEMR	94.1% ^{N.S.}	75.0%	82.9%	72.7%	94.7%
PET/CT + CEMR	85.3% ^{N.S.}	93.8%**	90.2%	90.6%	86.5%

Statistical significance compared with test^Δ:****P* < 0.001; ***P* < 0.01; **P* < 0.05; *N.S.* = not significant.

When equal, McNemar test is inapplicable.

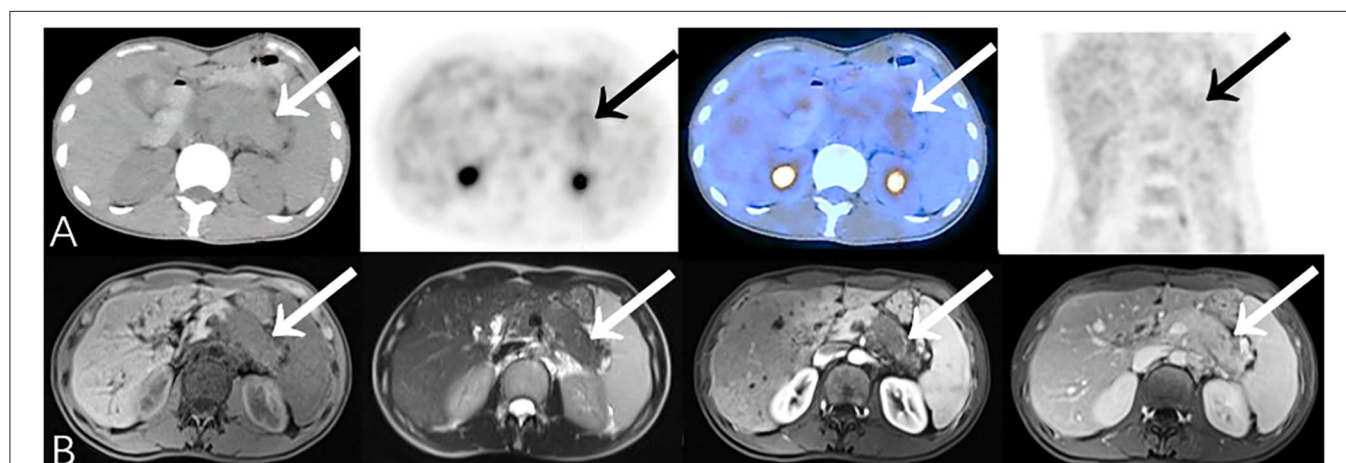


FIGURE 5 | Representative patient on PET/CT (False-Negative) compared to CEMR (True-Positive): A 37-year-old female experienced epigastric pain for 4 months. Serum CA19-9 was elevated (259.4 U/mL). **(A)** The body and tail of pancreas were slightly swollen with slightly increased ¹⁸F-FDG uptake (SUVmax 3.1). There was insufficient evidence of malignancy on PET/CT especially when no other significant abnormality was identified on the rest of the body scan. **(B)** CEMR showed a low-signal area on T1WI with narrowing of the pancreatic duct in the body and tail of pancreas which has no significant density change on PET/CT due to relatively limited resolution. The lesion enclosed retroperitoneal vessels which was suggestive of pancreatic cancer. Biopsy result showed adenocarcinoma (differentiation unspecified). Patient died after 9.2 months.

TABLE 5 | Cross-tabulated diagnosis of PET/CT and CECT, CEMR.

Diagnosis	Malignant		Benign	
	PET/CT positive	PET/CT negative	PET/CT positive	PET/CT negative
CECT positive	86	6	2	16
CECT negative	12	6	1	62
CEMR positive	29	2	3	9
CEMR negative	1	2	0	36

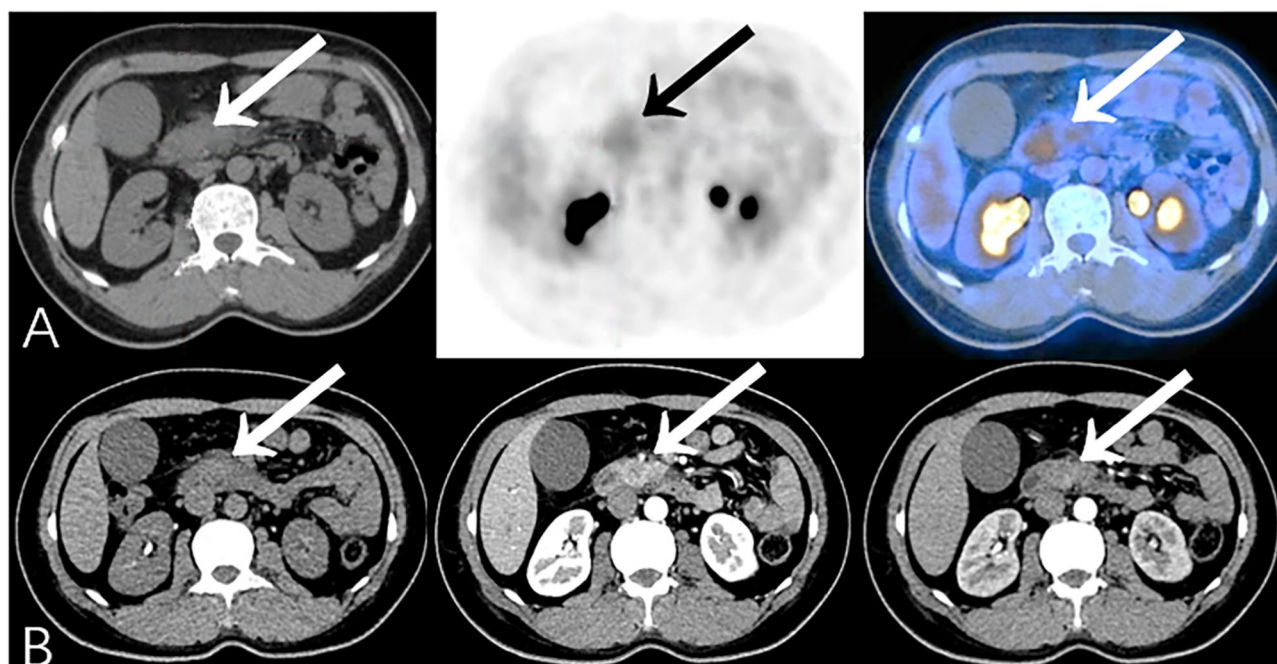


FIGURE 6 | Additional findings on PET/CT (True-Positive) compared to CECT (False-Negative): A 45-year-old female experienced jaundice with abdominal pain for 2 months. Serum CA19-9 was elevated (926.7 U/ml). **(A)** PET/CT showed focal ^{18}F -FDG uptake in the head of the pancreas (SUVmax 3.6). **(B)** CECT only showed obstruction, calcification, and the atrophy of pancreatic parenchyma subsequent to chronic pancreatitis. Patient then underwent pancreaticoduodenectomy, and histopathology revealed moderately-differentiated pancreatic ductal adenocarcinoma complicated with chronic pancreatitis.

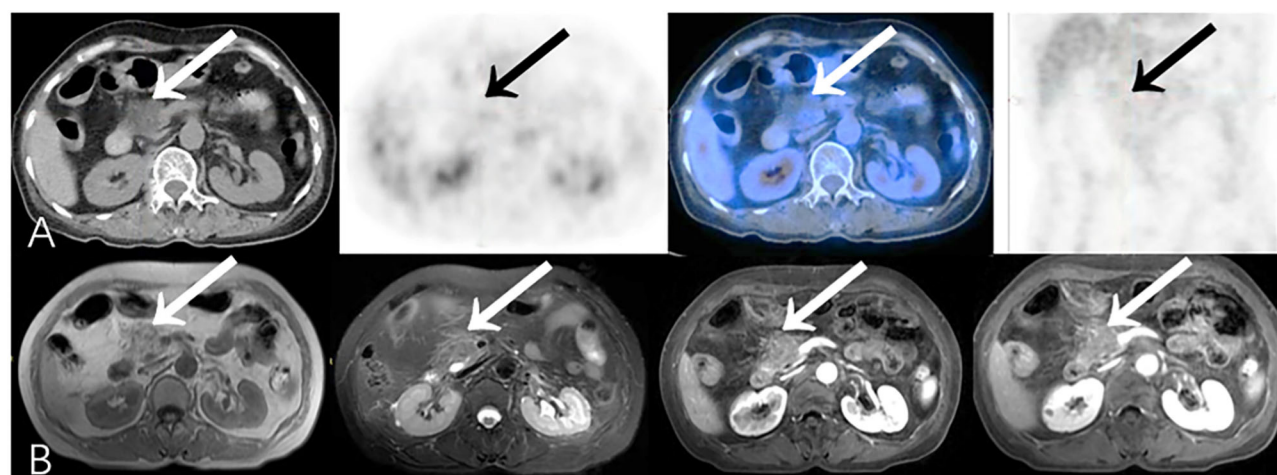


FIGURE 7 | Representative patient on PET/CT (True-Negative) compared to CEMR (False-Positive): A 61-year-old female experienced abdominal pain, nausea and vomiting for 20 days. Serum CA19-9 was normal (12.2 U/ml). **(A)** PET/CT showed hypodense area without obvious increased focal ^{18}F -FDG uptake (SUVmax 1.8) in head of pancreas, which was considered as benign lesion. **(B)** Lesion was inhomogeneously mildly enhanced on CEMR imaging, presumed more likely to be malignancy. Patient refused to undergo biopsy, and improved after symptomatic treatments. During long-term clinical follow-up (>16 months), patient had no complaints of special discomfort.

those with obstructive jaundice or underlying liver conditions), which may explain its relatively lower specificity (69%) than previous reported [80–90% (6)]. Nevertheless, CA19-9 as a more convenient and cheaper blood examination, could significantly improve diagnostic efficiencies when combined with imaging

modalities, with PET/CT in particularly. When the results of PET/CT and CA19-9 are consistent (both positive or negative), the likelihood of supporting or excluding malignant pancreatic lesions increases (with high PPV of 100% for serial test and NPV of 95.6% for parallel test). However, we should also be aware of

TABLE 6 | Diagnostic efficiencies of other combinations.

	Sensitivity	Specificity	Accuracy	PPV	NPV
CECT^A with CA19-9 (n = 161)					
CECT	83.2%	83.3%	83.2%	87.8%	77.5%
CA19-9	74.7% ^{N.S.}	62.1%*	69.6%	74.0%	63.1%
CECT//CA19-9	95.8%***	48.5%***	76.4%	72.8%	88.9%
CECT + CA19-9	62.1%***	97.0%**	76.4%	96.7%	64.0%
CEMR^A with CA19-9 (n = 71)					
CEMR	90.0%	78.0%	83.1%	75.0%	91.4%
CA19-9	86.7% ^{N.S.}	58.5% ^{N.S.}	70.4%	60.5%	85.7%
CEMR//CA19-9	100.0% ^{N.S.}	39.0%***	64.8%	54.5%	100.0%
CEMR + CA19-9	76.7%*	97.6%**	88.7%	95.8%	85.1%
CECT^A with CEMR (n = 45)					
CECT	88.2%	85.7%	86.7%	78.9%	92.3%
CEMR	100.0% ^{N.S.}	85.7% ^{N.S.}	91.1%	81.0%	100.0%
CECT//CEMR	100.0% ^{N.S.}	75.0% ^{N.S.}	84.4%	70.8%	100.0%
CECT + CEMR	88.2%	96.4% ^{N.S.}	93.3%	93.8%	93.1%

Statistical significance compared with test^A: *** $P < 0.001$; ** $P < 0.01$; * $P < 0.05$; N.S. = not significant.

When equal, McNemar test is inapplicable.

that the improved sensitivities of parallel tests are at the cost of lower specificity and PPV, while serial tests were less sensitive and accurate than PET/CT alone. Given that PET/CT performs better than serum CA19-9, the results of PET/CT may be more informative and reliable when the two results are opposite.

CECT is the standard diagnostic method for pancreatic cancer because of its effectiveness and availability. MRI has superior soft tissue resolution and high sensitivity and is often used as a supplementary modality (6). CT or MRI with intravenous contrast allows precise assessment of the relationship of the primary tumor to the vasculature. Yet both CECT and CEMR are still restricted to morphological portrait of tumor. There are small-scaled individual series that have compared PET/CT with traditional tests in diagnosis of pancreatic lesions, suggesting the incremental diagnostic value of PET/CT (13, 16, 36). A recent prospective study in UK have provided evidence for incremental diagnostic benefits of PET/CT compared to CECT, especially for those who are suspected of having pancreatic cancer on MDCT and planned for surgery (17). Our study showed that PET/CT has similar sensitivity to CECT and CEMR, and significantly higher specificity and accuracy than the other two. PET/CT helped reduce false diagnoses of morphological images, specifically 14.7% (28/191) cases for CECT and 12.2% (10/82) for CEMR. Moreover, combined application with PET/CT can enhance diagnostic efficiencies compared to CECT alone, meanwhile improve specificity of CEMR alone. Our study also showed diagnosis improvement of combination CECT with CEMR but had no significant difference compared with CECT alone. However, the small number of cases in this subgroup ($n = 45$) means that a statistical comparison of the diagnostic tests will have a low power to detect small or moderate effects. These results require further verification by larger sample sizes, and prospective methodology research comparing different diagnosis methods.

A major limitation of the current study was the retrospective nature of data collection from a single center, which may lead to selection and recall bias. However, the large sample size, uniform institutional clinical data system and long-term follow-up strengthen the findings of the study. And we also provided comprehensive comparison to diagnosis efficiency of different methods. Secondly, although various types of pancreatic lesions are covered in our study, the cases of certain lesion type, especially with confirmatory pathology results, were too small to provide meaningful statistical results if analyzed as subgroups. Therefore, our study was mainly focused on the general discrimination between malignant and benign pancreatic lesions of different methods. Although current guidelines (NCCN and ESMO) consider that the role of PET/CT in pancreatic cancer remains unclear, NCCN guidelines suggest that functional PET imaging can be used in high-risk patients to detect extra-pancreatic metastases (6, 8). Further systemic analysis comparing PET/CT with standard diagnostic methods, along with prospective, cost-effective analysis are still required to help to address the issues around the widespread utility of PET/CT. Preliminary data suggest that there was a trend for contrast-enhanced PET/CT to be superior to unenhanced PET/CT in detection and assessment of resectability, providing functional information for whole-body staging for surgical and radiotherapeutic planning (12, 37, 38). However, there was also concern about increasing acquisition time, radiation burden, and contrast-related artifacts that may lead to overestimation of SUV in PET/CT with contrast (39). Some researchers suggested that PET/MR can be done without contrast media in some settings where a contrast-enhanced PET/CT is needed to be diagnostic (40). With the increasing installed base of systems, clinical data will be forthcoming and define more clearly its clinical value in pancreatic cancer.

CONCLUSION

¹⁸F-FDG PET/CT has outstanding value in the diagnosis of pancreatic lesions and performs better than serum CA19-9, CECT, and CEMR, especially in terms of specificity and accuracy. The joint application of PET/CT with other methods could enhance diagnostic efficiency in varying degrees by their advantage complementation.

DATA AVAILABILITY STATEMENT

The original contributions presented in the study are included in the article/supplementary material, further inquiries can be directed to the corresponding author/s.

ETHICS STATEMENT

The studies involving human participants were reviewed and approved by Institutional Review Board of Union Hospital, Tongji Medical College, Huazhong University of Science and Technology. Written informed consent from the participants' legal guardian/next of kin was not required to participate in

this study in accordance with the national legislation and the institutional requirements. Written informed consent was not obtained from the individual(s) for the publication of any potentially identifiable images or data included in this article.

AUTHOR CONTRIBUTIONS

SH and HC performed acquisition of data. SH was a major contributor in writing the manuscript. XL substantially contributed to conception and design, drafting the article, and revising it critically for important intellectual content. All authors were involved in the analysis and interpretation of data, read, and approved the final manuscript.

REFERENCES

- Lin QJ, Yang F, Jin C, Fu DL. Current status and progress of pancreatic cancer in China. *World J Gastroenterol.* (2015) 21:7988–8003. doi: 10.3748/wjg.v21.i26.7988
- Quaresma M, Coleman MP, Rachet B. 40-year trends in an index of survival for all cancers combined and survival adjusted for age and sex for each cancer in England and Wales, 1971–2011: a population-based study. *Lancet.* (2015) 385:1206–18. doi: 10.1016/S0140-6736(14)61396-9
- Gobbi PG, Bergonzi M, Comelli M, Villano L, Pozzoli D, Vanoli A, et al. The prognostic role of time to diagnosis and presenting symptoms in patients with pancreatic cancer. *Cancer Epidemiol.* (2013) 37:186–90. doi: 10.1016/j.canep.2012.12.002
- Siegel RL, Miller KD, Jemal A. Cancer statistics, 2020. *CA Cancer J Clin.* (2020) 70:7–30. doi: 10.3322/caac.21590
- Ballehaninna UK, Chamberlain RS. The clinical utility of serum CA 19-9 in the diagnosis, prognosis and management of pancreatic adenocarcinoma: an evidence based appraisal. *J Gastrointest Oncol.* (2012) 3:105–19. doi: 10.3978/j.issn.2078-6891.2011.021
- National Comprehensive Cancer Network. *Clinical Practice Guidelines in Oncology. Pancreatic Adenocarcinoma (Version 1)*. Fort Washington, PA: National Comprehensive Cancer Network (2020).
- Reske SN, Grillenberger KG, Glatting G, Port M, Hildebrandt M, Gansauge F, et al. Overexpression of glucose transporter 1 and increased FDG uptake in pancreatic carcinoma. *J Nucl Med.* (1997) 38:1344–8.
- Seufferlein T, Bachet J, Van Cutsem E, Rougier P, Group EGW. Pancreatic adenocarcinoma: ESMO-ESDO clinical practice guidelines for diagnosis, treatment and follow-up. *Ann Oncol.* (2012) 23(Suppl. 7):vii33–40. doi: 10.1093/annonc/mds224
- Lyshchik A, Higashi T, Nakamoto Y, Fujimoto K, Doi R, Imamura M, et al. Dual-phase 18F-fluoro-2-deoxy-D-glucose positron emission tomography as a prognostic parameter in patients with pancreatic cancer. *Eur J Nucl Med Mol Imaging.* (2005) 32:389–97. doi: 10.1007/s00259-004-1656-0
- Xi Y, Guo R, Hu J, Zhang M, Zhang X, Li B. 18F-fluoro-2-deoxy-D-glucose retention index as a prognostic parameter in patients with pancreatic cancer. *Nucl Med Commun.* (2014) 35:1112–8. doi: 10.1097/MNM.000000000000178
- Al-Hawary MM, Francis IR, Chari ST, Fishman EK, Hough DM, Lu DS, et al. Pancreatic ductal adenocarcinoma radiology reporting template: consensus statement of the Society of Abdominal Radiology and the American Pancreatic Association. *Radiology.* (2014) 270:248–60. doi: 10.1148/radiol.13131184
- Buchs NC, Bühler L, Bucher P, Willi JP, Frossard JL, Roth AD, et al. Value of contrast-enhanced 18F-fluorodeoxyglucose positron emission tomography/computed tomography in detection and presurgical assessment of pancreatic cancer: a prospective study. *J Gastroenterol Hepatol.* (2011) 26:657–62. doi: 10.1111/j.1440-1746.2010.06525.x
- Kauhanen SP, Komar G, Seppänen MP, Dean KI, Minn HR, Kajander SA, et al. A prospective diagnostic accuracy study of 18F-fluorodeoxyglucose

FUNDING

This work was supported by the Key Project of National Natural Science Foundation of China (No. 82030052 and 81630049), Hubei Technical Innovation Major Project (No. 2017ACA182), and the Clinical Research Physician Program of Tongji Medical College, Huazhong University of Science and Technology (No. 5001530008).

ACKNOWLEDGMENTS

We thank Libby Cone, MD, MA, from Edanz Group Japan (www.edanzediting.com/ac) for editing a draft of this manuscript.

- positron emission tomography/computed tomography, multidetector row computed tomography, and magnetic resonance imaging in primary diagnosis and staging of pancreatic cancer. *Ann Surg.* (2009) 250:957–63. doi: 10.1097/SLA.0b013e3181b2fafa
- Santhosh S, Mittal BR, Bhasin D, Srinivasan R, Rana S, Das A, et al. Role of 18F-fluorodeoxyglucose positron emission tomography/computed tomography in the characterization of pancreatic masses: Experience from tropics. *J Gastroenterol Hepatol.* (2013) 28:255–61. doi: 10.1111/jgh.12068
- Zhang J, Zuo CJ, Jia NY, Wang JH, Hu SP, Yu ZF, et al. Cross-modality PET/CT and contrast-enhanced CT imaging for pancreatic cancer. *World J Gastroenterol.* (2015) 21:2988–96. doi: 10.3748/wjg.v21.i10.2988
- Ergul N, Gundogan C, Tozlu M, Toprak H, Kadioglu H, Aydin M, et al. Role of 18F-fluorodeoxyglucose positron emission tomography/computed tomography in diagnosis and management of pancreatic cancer; comparison with multidetector row computed tomography, magnetic resonance imaging and endoscopic ultrasonography. *Rev Esp Med Nucl Imagen Mol.* (2014) 33:159–64. doi: 10.1016/j.remnie.2014.03.016
- Ghaneh P, Hanson R, Titman A, Lancaster G, Plumpton C, Lloyd-Williams H, et al. PET-PANC: multicentre prospective diagnostic accuracy and health economic analysis study of the impact of combined modality 18fluorine-2-fluoro-2-deoxy-d-glucose positron emission tomography with computed tomography scanning in the diagnosis and management of pancreatic cancer. *Health Technol Assess (Winchester, England).* (2018) 22:1–114. doi: 10.3310/hta22070
- Anunziata S, Cuccaro A, Tisi MC, Hohauser S, Rufini V. FDG-PET/CT at the end of immuno-chemotherapy in follicular lymphoma: the prognostic role of the ratio between target lesion and liver SUVmax (rPET). *Ann Nucl Med.* (2018) 32:372–7. doi: 10.1007/s12149-018-1243-2
- de Mestier L, Armani M, Cros J, Hentic O, Rebours V, Cadiot G, et al. Lesion-by-lesion correlation between uptake at FDG PET and the Ki67 proliferation index in resected pancreatic neuroendocrine tumors. *Digest Liver Dis.* (2019) 51:1720–4. doi: 10.1016/j.dld.2019.06.022
- Lu K, Yang J, Li DC, He SB, Zhu DM, Zhang LF, et al. Expression and clinical significance of glucose transporter-1 in pancreatic cancer. *Oncol Lett.* (2016) 12:243–9. doi: 10.3892/ol.2016.4586
- Basturk O, Singh R, Kaygusuz E, Balci S, Dursun N, Culhaci N, et al. GLUT-1 expression in pancreatic neoplasia: implications in pathogenesis, diagnosis, and prognosis. *Pancreas.* (2011) 40:187–92. doi: 10.1097/MPA.0b013e318201c935
- Kaida H, Azuma K, Kawahara A, Yasunaga M, Kitasato Y, Hattori S, et al. The correlation between FDG uptake and biological molecular markers in pancreatic cancer patients. *Eur J Radiol.* (2016) 85:1804–10. doi: 10.1016/j.ejrad.2016.08.007
- Ohta K, Tanada M, Sugawara Y, Teramoto N, Iguchi H. Usefulness of positron emission tomography (PET)/contrast-enhanced computed tomography (CE-CT) in discriminating between malignant and benign intraductal papillary mucinous neoplasms (IPMNs). *Pancreatol.* (2017) 17:911–9. doi: 10.1016/j.pan.2017.09.010

24. Kim YI, Kim SK, Paeng JC, Lee HY. Comparison of F-18-FDG PET/CT findings between pancreatic solid pseudopapillary tumor and pancreatic ductal adenocarcinoma. *Eur J Radiol.* (2014) 83:231–5. doi: 10.1016/j.ejrad.2013.09.031
25. Cheng MF, Guo YL, Yen RF, Chen YC, Ko CL, Tien YW, et al. Clinical utility of FDG PET/CT in patients with autoimmune pancreatitis: a case-control study. *Sci Rep.* (2018) 8:3651–8. doi: 10.1038/s41598-018-21996-5
26. Kamisawa T, Okamoto A. Autoimmune pancreatitis: proposal of IgG4-related sclerosing disease. *J Gastroenterol.* (2006) 41:613–25. doi: 10.1007/s00535-006-1862-6
27. Zheng L, Xing H, Li F, Huo L. Focal autoimmune pancreatitis mimicking pancreatic cancer on FDG PET/CT imaging. *Clin Nucl Med.* (2018) 43:57–9. doi: 10.1097/RLU.0000000000001901
28. Kato K, Nishihashi T, Ikeda M, Abe S, Iwano S, Itoh S, et al. Limited efficacy of 18F-FDG PET-CT for differentiation between metastasis-free pancreatic cancer and mass-forming pancreatitis. *Clin Nucl Med.* (2013) 38:417–21. doi: 10.1097/RLU.0b013e3182817d9d
29. Schillaci O. Use of dual-point fluorodeoxyglucose imaging to enhance sensitivity and specificity. *Semin Nucl Med.* (2012) 42:267–80. doi: 10.1053/j.semnuclmed.2012.02.003
30. Higashi T, Saga T, Nakamoto Y, Ishimori T, Mamede MH, Wada M, et al. Relationship between retention index in dual-phase 18F-FDG PET, and hexokinase-II and glucose transporter-1 expression in pancreatic cancer. *J Nucl Med.* (2002) 43:173–80.
31. Cheng G, Torigian DA, Zhuang H, Alavi A. When should we recommend use of dual time-point and delayed time-point imaging techniques in FDG PET? *Eur J Nucl Med Mol Imaging.* (2013) 40:779–87. doi: 10.1007/s00259-013-2343-9
32. Higashi T, Saga T, Nakamoto Y, Ishimori T, Fujimoto K, Doi R, et al. Diagnosis of pancreatic cancer using fluorine-18 fluorodeoxyglucose positron emission tomography (FDG PET) -Usefulness and limitations in “clinical reality”. *Ann Nucl Med.* (2003) 17:261–79. doi: 10.1007/BF02988521
33. Cui Y, Song J, Pollom E, Alagappan M, Shirato H, Chang DT, et al. Quantitative analysis of 18F-fluorodeoxyglucose positron emission tomography identifies novel prognostic imaging biomarkers in locally advanced pancreatic cancer patients treated with stereotactic body radiation therapy. *Int J Radiat Oncol Biol Phys.* (2016) 96:102–9. doi: 10.1016/j.ijrobp.2016.04.034
34. Hatt M, Majdoub M, Vallières M, Tixier F, Le Rest CC, Groheux D, et al. 18F-FDG PET uptake characterization through texture analysis: investigating the complementary nature of heterogeneity and functional tumor volume in a multi-cancer site patient cohort. *J Nucl Med.* (2015) 56:38–44. doi: 10.2967/jnumed.114.144055
35. Hatt M, Tixier F, Pierce L, Kinahan PE, Le Rest CC, Visvikis D. Characterization of PET/CT images using texture analysis: the past, the present any future? *Eur J Nuclear Med Mol Imaging.* (2017) 44:151–65. doi: 10.1007/s00259-016-3427-0
36. Sun Y, Duan Q, Wang S, Zeng Y, Wu R. Diagnosis of pancreatic cancer using ¹⁸F-FDG PET/CT and CA19-9 with SUVmax association to clinical characteristics. *J BUON.* (2015) 20:452–9.
37. Dibble EH, Karantanis D, Mercier G, Peller PJ, Kachnic LA, Subramaniam RM. PET/CT of cancer patients: part 1, pancreatic neoplasms. *Am J Roentgenol.* (2012) 199:952–67. doi: 10.2214/AJR.11.8182
38. Strobel K, Heinrich S, Bhure U, Soyka J, Veit-Haibach P, Pestalozzi BC, et al. Contrast-enhanced 18F-FDG PET/CT: 1-stop-shop imaging for assessing the resectability of pancreatic cancer. *J Nucl Med.* (2008) 49:1408–13. doi: 10.2967/jnumed.108.051466
39. Dhull VS, Rana N, Nazari AH. Contrast media in PET/computed tomography imaging. *PET Clin.* (2016) 11:85–94. doi: 10.1016/j.cpet.2015.07.007
40. von Schulthess GK, Kuhn FP, Kaufmann P, Veit-Haibach P. Clinical positron emission tomography/magnetic resonance imaging applications. *Semin Nucl Med.* (2013) 43:3–10. doi: 10.1053/j.semnuclmed.2012.08.005

Conflict of Interest: The authors declare that the research was conducted in the absence of any commercial or financial relationships that could be construed as a potential conflict of interest.

Publisher's Note: All claims expressed in this article are solely those of the authors and do not necessarily represent those of their affiliated organizations, or those of the publisher, the editors and the reviewers. Any product that may be evaluated in this article, or claim that may be made by its manufacturer, is not guaranteed or endorsed by the publisher.

Copyright © 2021 Huang, Chong, Sun, Wu, Jia, Zhang and Lan. This is an open-access article distributed under the terms of the Creative Commons Attribution License (CC BY). The use, distribution or reproduction in other forums is permitted, provided the original author(s) and the copyright owner(s) are credited and that the original publication in this journal is cited, in accordance with accepted academic practice. No use, distribution or reproduction is permitted which does not comply with these terms.



Performance of Ultrasound-Guided Core Biopsy Driven by FDG-avid Supraclavicular Lymph Nodes in Patients With Suspected Lung Cancer

Tongtong Wang^{1†}, Junbao Liu^{2†}, Ningning Lv¹, Shi Xuan¹, Lin Bai¹, Bin Ji^{1*} and Shi Gao^{1*}

¹ Department of Nuclear Medicine, China-Japan Union Hospital of Jilin University, Changchun, China, ² Department of Surgery, China-Japan Union Hospital of Jilin University, Changchun, China

OPEN ACCESS

Edited by:

Francesco Cicone,
University of Catanzaro, Italy

Reviewed by:

Angelo Castello,
IRCCS Ca' Granda Foundation
Maggiore Policlinico Hospital, Italy
Marcelo Mamede,
Federal University of Minas
Gerais, Brazil

*Correspondence:

Shi Gao
gaoshi@jlu.edu.cn
Bin Ji
jibin@jlu.edu.cn

[†]These authors have contributed
equally to this work

Specialty section:

This article was submitted to
Nuclear Medicine,
a section of the journal
Frontiers in Medicine

Received: 28 October 2021

Accepted: 24 December 2021

Published: 20 January 2022

Citation:

Wang T, Liu J, Lv N, Xuan S, Bai L,
Ji B and Gao S (2022) Performance of
Ultrasound-Guided Core Biopsy
Driven by FDG-avid Supraclavicular
Lymph Nodes in Patients With
Suspected Lung Cancer.
Front. Med. 8:803500.
doi: 10.3389/fmed.2021.803500

Objectives: Ultrasound-guided core biopsy (UGCB) for supraclavicular lymph nodes (SLNs) represents an attractive procedure to obtain tissues for lung cancer confirmation. The aim of the present study is to evaluate the performance of UGCB driven by FDG-avid SLNs, as performed by nuclear medicine physicians, in patients with suspected lung cancer.

Methods: Institutional database in our hospital was searched for eligible patients between September 2019 and March 2021. A 3-12 MHz linear probe was used to guide the biopsy process and to ensure that the needle tip was being directed at the metabolically active area that had been indicated by side-by-side PET/CT images. Diagnostic yield, malignancy rate, molecular testing results, and complications were reviewed.

Results: Among the 54 patients included in this study, definite pathological diagnosis from UGCB specimens was achieved in 53 patients, reaching a diagnostic yield of 98.1% (53/54) and a malignancy rate of 96.2% (51/53). Among the 50 patients confirmed as lung cancer, thirty-eight were spared from further invasive procedures which had been planned. Molecular analyses were adequately performed on all the 38 specimens obtained from non-small cell lung cancer (NSCLC). The positive rate was 36.8% (14/38) for epidermal growth receptor (EGFR) mutation and 31.6% (12/38) for anaplastic lymphoma kinase (ALK) translocation. 28.9% (11/38) of the patients had a tumor proportion score (TPS) \geq 50% for PD-L1 expression. No complication was observed and the average biopsy time was 15 min.

Conclusions: Nuclear medicine physicians-performed UGCB driven by FDG-avid SLNs in suspected lung cancer patients could produce a high performance in terms of diagnostic yield, malignancy rate, and molecular analysis, which may obviate more invasive interventional procedures and lead to fast decisions on subsequent management.

Keywords: ultrasound-guided core biopsy, supraclavicular lymph nodes, lung cancer-diagnosis, FDG-PET/CT, performance

INTRODUCTION

Ultrasound-guided core biopsy (UGCB) for supraclavicular lymph nodes (SLNs) represents an attractive technique to obtain tissues for lung cancer confirmation (1–3). It is a simple, rapid and minimally invasive choice that could avoid the risk of complications from more costly procedures such as bronchoscopy, CT-guided lung biopsy and diagnostic surgery. Besides, lung cancer confirmation through SLN tissues could directly upstage the patients into stage IIIB disease which would exclude surgical therapeutic options according to guidelines (4, 5).

In recent years, ^{18}F -FDG-PET/CT has been increasingly used in the diagnostic workup of a pulmonary mass to stratify malignancy risk and provide possible staging information (6–8). The PET/CT findings may help to optimize UGCB for SLNs from several aspects. Firstly, it could reveal more suspicious SLNs as compared to initial examinations such as CT (9). This will render more choices in selecting SLNs with easier needle pass routes. Secondly, the PET scan could provide whole-body information of tumor involvement including easy-to-access superficial distant metastases, which may obviate the need for sampling SLNs. Finally, but most importantly, biopsy driven by FDG-avid lesions have demonstrated a high diagnostic yield in various type of changes including thoracic, abdominal, bone, muscle, and breast lesions (10, 11). Because FDG avidness in malignant lesions represents the existence of metabolically active tumor cells, sampling of FDG-avid lesions will be more likely to yield representative material for molecular analysis (12, 13).

Nuclear medicine physicians collect comprehensive patient information and are the first to learn about the PET/CT results. If they become proficient in UGCB, the diagnostic pathway of lung cancer could be significantly optimized. Hence, we hypothesize that UGCB driven by FDG-avid SLNs in suspected lung cancer patients, as performed by nuclear medicine physicians, would produce high performance in terms of diagnostic yield, malignancy rate, molecular testing, and complications. In the present study, we tried to verify this hypothesis by retrospectively reviewing these data within our institution.

MATERIALS AND METHODS

Patient Selection

Since September 2019, we began to routinely implement UGCB upon eligible patients with FDG-avid SLNs by simultaneously consulting side-by-side PET/CT images. Before this time point, WT and LN, which are nuclear medicine physicians in our department, had received over 5 years training for using ultrasound. The following conditions must be fulfilled in order to implement this procedure: (1) suspected lung cancer patients upon initial PET evaluation; (2) an accessible FDG-avid SLN was identified in the absence of other easy-to-access superficial distant metastases, as determined by WT and LN; (3) collective discussions among referring physicians, surgeons and nuclear medicine physicians decided to recommend this procedure to the patients; (4) patients agreed with receiving such an intervention upon recommendation including both the pros (it is simple,

with less pain, and may lead to fast decision on subsequent management) and cons (it may not define the highest disease stage and information from SLN may not replace those of primary tumor in terms of molecular analysis). Between 2019 and March 2021, our department completed 866 PET scans for initial evaluation of suspected lung cancer patients. Among them, a total of 54 patients received nuclear medicine physicians-performed UGCB driven by FDG-avid SLNs.

This retrospective investigation based on institutional database was approved by the ethics committee of our institution.

^{18}F -FDG-PET/CT

All patients underwent ^{18}F -FDG-PET/CT within 2 days before UGCB. The PET/CT scans were acquired by using two dedicated diagnostic PET/CT devices uMI 510 unit and uMI 780 unit (United Imaging, Shanghai, China). All PET-CT acquisitions were performed 40–60 min following intravenous injection of 3.5 MBq/kg of ^{18}F -FDG after a fasting period of at least 6 h. Integrated PET/CT images were corrected for scatter and attenuation based on CT information.

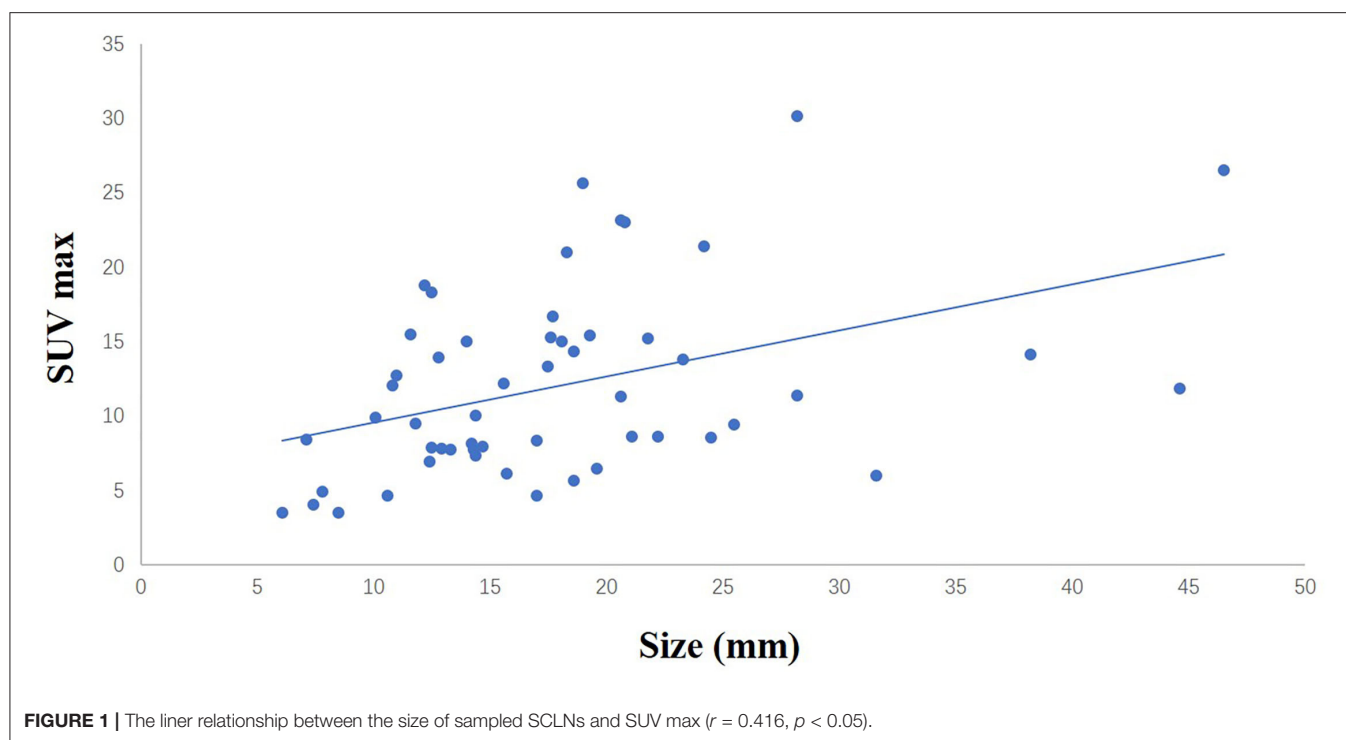
Sampling and Histological Evaluation

All FDG-avid SLNs were detectable on ultrasound. Patients were placed in supine position, with the shoulders raised to fully expose the neck for ultrasound scanning. Ultrasound images were evaluated side by side with the serial transverse PET/CT images (recorded by iPad) to identify the lesion or area of interest. Local anesthesia was achieved by injecting 5 mL of 2% lidocaine hydrochloride. 18-gauge biopsy needles (Argon Medical Devices, USA), with a diameter of 1 mm for the cutting needle and a length of 9 mm for the sampling notch were used to obtain SLN tissue. A 3–12 MHz linear probe (N1500, Neusoft, China) was used to guide the biopsy process and to ensure that the needle tip was being directed at the metabolically active area that had been indicated by the PET/CT images. An average of two to three passes were made to obtain sufficient tissue. PET/CT and ultrasound images in representative patients undergoing UGCB are shown in **Figures 1, 2**.

SLNs samples were subjected to hematoxylin and eosin (HE) staining and immunohistochemical staining for histological evaluation. For patients in whom the tissue diagnosis based on the SLN samples were not metastatic lung cancer, pathological results from the lung lesions were obtained.

Molecular Analysis

When non-squamous cell lung cancer was diagnosed, the SLNs samples were assessed for molecular analysis. The test for epidermal growth receptor (EGFR) mutations was performed using the ADx-ARMS kit (Amplification Refractory Mutation System) that covers exons 18, 19, 20, and 21 (Amoy Diagnostics, Xiamen, China). The analysis for anaplastic lymphoma kinase (ALK) translocation was performed by immunohistochemistry (IHC, clone D5F3, VMSI) on formalin-fixed paraffin-embedded sections. PD-L1 immunohistochemistry was performed using the Dako 22C3 antibody clone (mouse monoclonal primary anti-PDL1 antibody, prediluted, clone 22C3, Dako) according to a previously described protocol (14). The level of PD-L1



expression was based on a tumor proportion score (TPS) which was defined as the percentage of viable tumor cells showing partial or complete membrane labeling regardless of intensity or completeness.

RESULTS

A total of 54 suspected lung cancer patients who have underwent UGCB driven by FDG-positive SLNs and were included in this retrospective study. **Table 1** shows the clinical characteristics of our patient population. The median of age was 63 (range, 47–77) years. Thirty patients (55.6%) were males and 40 (74.1%) had a smoking history. The median of the size of sampled SLNs was 12.5 mm (range, 4.9–32.0 mm) in their short axis and 17.0 mm (range, 6.1–46.5 mm) in their long axis. The median of maximum standard uptake value (SUVmax) was 10.7 (range, 3.5–30.2). **Figure 1** showed the linear relationship between the size of sampled SLNs and SUVmax ($r = 0.416$, $p < 0.05$). The most common histopathological diagnoses were adenocarcinoma (42, 77.8%).

The diagnostic yield was 98.1% (53/54). There was only one non-diagnostic patient who was established as lung adenocarcinoma by subsequent guided bronchoscopy toward the lung lesion. The malignancy rate was 96.2% (51/53). The two benign SLNs revealed by UGCB were tuberculosis and hyperplasia. There is also one SLN of lymphoma and pathological results from the lung lesion confirmed this diagnosis.

Fifty patients were confirmed as lung cancer by UGCB. The suspected stage and metastatic sites of these patients were summarized in **Table 2**. Among them, 38 were spared from

further bronchoscopy, CT-guided lung biopsy and diagnostic surgery which had already been planned.

There were 45 patients with non-small cell lung cancer (NSCLC) in the present study. Thirty-eight of them received molecular analyses for SLNs specimens and they were all adequately performed. The positive rate was 36.8% (14/38) for EGFR mutation and 31.6% (12/38) for ALK translocation. In all these specimens, PDL1 testing was also successfully carried out, with PDL1 not expressed in 13/38 (34.2%), PDL1 >1% and < 50% in 36.8% (14/38), and PDL1 > 50% in 11/38 (28.9%).

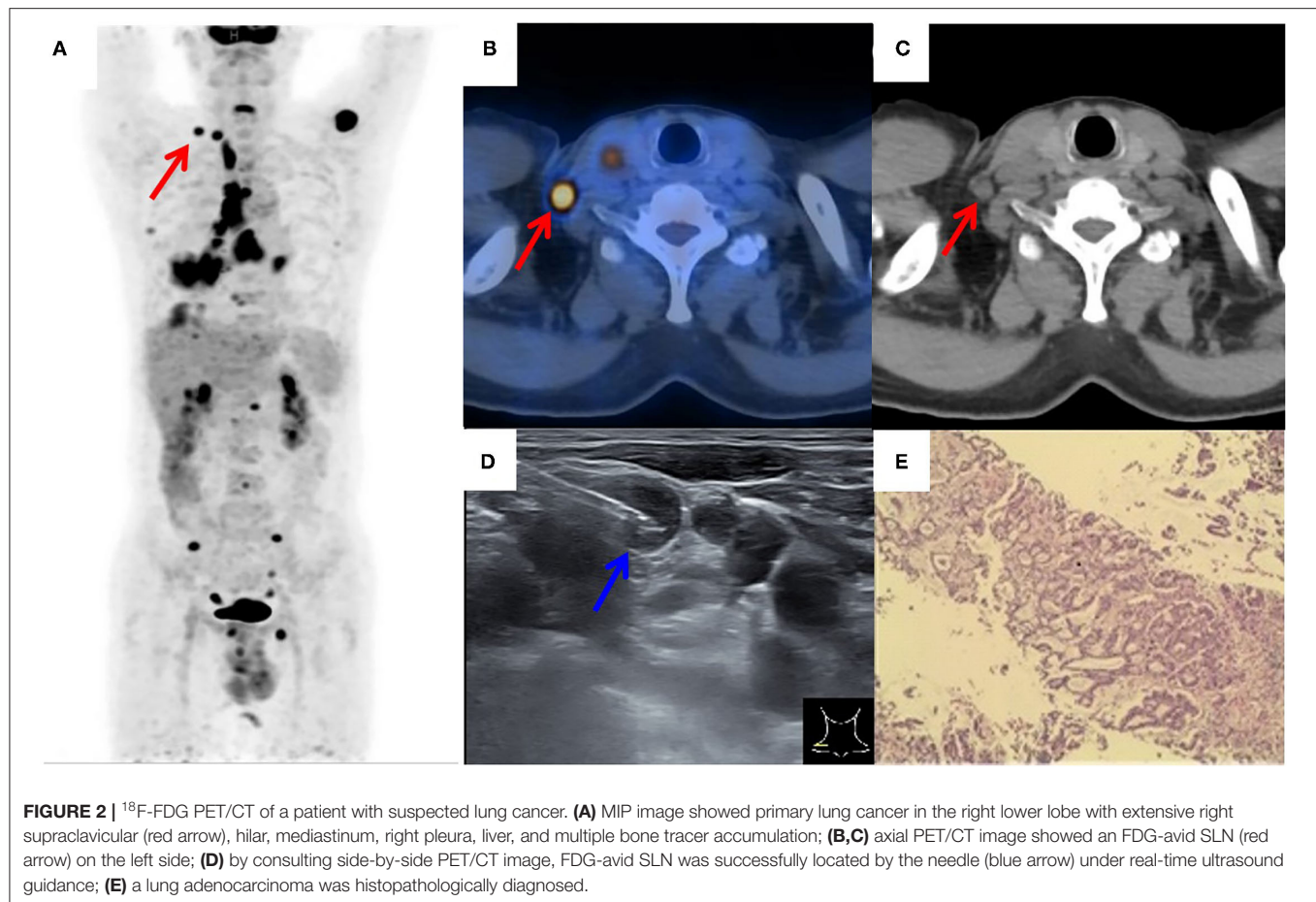
No complication was recorded in the present patient cohort. The average biopsy time was 15 min.

Figures 2, 3 showed the examples of two suspected lung cancer patients who had successfully completed UGCB driven by FDG-avid SLNs.

DISCUSSION

Our retrospective analysis demonstrated a diagnostic yield of 98.1% (53/54) and a malignancy rate of 96.2% (51/53) for UGCB driven by FDG-avid SLNs in a cohort of patients with suspected lung cancer. Due to the superficial location, precise ultrasound guidance as well as the side-by-side PET/CT information, large SLNs specimens can be easily acquired by nuclear medicine physicians without complications.

The performance was higher than that of a previous report, in which pulmonologists-performed UGCB obtained a diagnostic yield of 95.7% (71/74) and a malignancy rate of 90.1% (64/71). However, among the 67 SLNs biopsied in their study, only 44 were FDG-driven and no specified method was described as



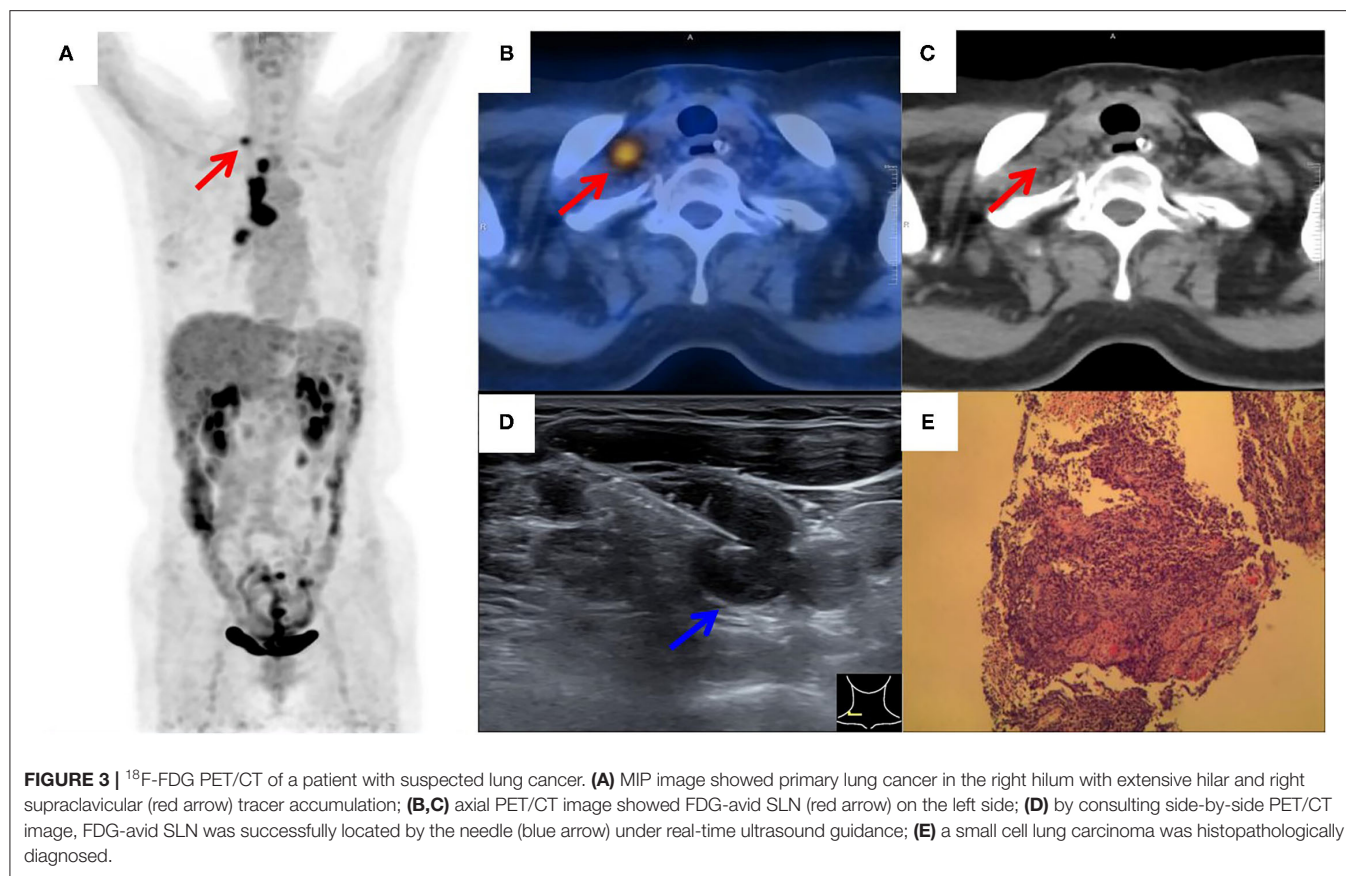
to how PET/CT information was utilized during the sampling process (15). Two reasons might be considered to explain the higher performance in our study. Firstly, although both studies lacked well-defined criteria for SLNs selection, nuclear medicine physicians, who have more experience in PET/CT image interpretation, are more likely to choose SLNs with a high pre-test probability of success and malignancy. This might lead to a higher post-test diagnostic yield and malignant rate. Secondly, nuclear medicine physicians may be more focused on ensuring the needle placement toward the metabolically active area during the process of UGCB, thus pronouncing the benefit of FDG avidity in terms of diagnostic yield.

All 54 patients underwent UGCB with the aim of pathological diagnosis in the present study. Among them, fifty were confirmed as lung cancer by UGCB. In 28 patients, the confirmation of lung cancer in SLNs could define the disease stage (IIIB). For the remaining 22 patients, due to the existence of not-easy-to-access suspicious distant metastases on PET/CT (patients with easy-to-access suspicious distant metastases were excluded), exact pathological disease stage still could not be established. Although the guidelines recommended sampling of the lesions that would establish the highest stage of lung cancer, some patients may be more readily to accept a fast, simple and less painful procedure such as UGCB, which serves with high performance in

pathological diagnosis and proving a non-resectable tumor stage (4, 5). In our department, the determination of the biopsy site was made considering multiple factors such as accessibility, risks involved with the procedures, and patients' preference.

Molecular analysis including EGFR mutation, ALK translocation and PD-L1 expression was adequately performed on the specimens obtained in the present study. Importantly, two SLNs samples with a diameter smaller than 10 mm successfully yield molecular testing results. This may indicate the powerful yield of UGCB in small lesions when PET/CT information was combined. In the patients tested for PD-L1 expression, 28.9% had a TPS of $\geq 50\%$, which was an indication for first-line immunotherapy in metastatic NSCLC (16). However, it should be noted that further studies are still needed to ultimately validate the guiding value of molecular information derived from metastatic SLNs on the survival benefits of NSCLC patients. For example, PD-L1 expression has been found to vary between different regions even within the same tumor, and previous studies found that PD-L1 expression in lymph nodes may not be a biomarker for treatment efficacy (17, 18).

Logistic advantages to the diagnostic pathway of suspected lung cancer patients can be expected from this technique. In our study, as a first-step after the PET/CT scan, UGCB driven by FDG-avid SLNs obviated further interventional procedures

**TABLE 1 |** Patients' characteristic.

Characteristic	Value
Year	63 (47–77)
Sex	
Female	24 (44.4%)
Male	30 (55.6%)
SLN diameter on CT (mm)	
Long axis	17.9 (6.1–46.5)
Short axis	12.9 (4.9–32.0)
Smoking history	
Current	35 (64.8%)
Former	5 (9.3%)
Never	14 (25.9%)
Metastatic site	
Supraclavicular lymph node	52
Neck lymph node	21
Bone	18
Pleura	13
Liver	11
Brain	6

TABLE 2 | Results of tissue diagnosis.

Tissue diagnosis	Number
Adenocarcinoma	42 (77.7%)
Squamous cell carcinoma	3 (5.5%)
Small-cell lung cancer	5 (9.2%)
Lymphoma	1 (1.9%)
Tuberculosis	1 (1.9%)
Hyperplasia	1 (1.9%)
Non-diagnostic	1 (1.9%)

in 38 patients in whom bronchoscopy, CT-guided lung biopsy, and diagnostic surgery had been planned. This may optimize the diagnostic process, especially in older patients who are with poor overall status and often have difficulties in complying with more complex and invasive diagnostic procedures. Moreover, the presentation of a PET/CT report, together with a pathological confirmation of stage IIIB disease, could swiftly exclude the patients from surgical therapeutic options and transfer them to oncology department. In this way, patients could have ample time to prepare for anti-tumor drugs while waiting for the molecular testing results if requested.

Several researchers reported that routine US evaluation of supraclavicular region and US-guided biopsy of suspicious SLNs

in suspected lung cancer patients also have a high performance both for pathological confirmation and staging (19–21). In the present study, the US was solely used for guidance and localization, but not for selection of targeted SLNs, because we believed that FDG-avid SLNs would have a high probability for lung cancer metastases. To date, most of the investigations focusing on the performance of these two strategies were with small sample size and there exist no direct comparison studies as far as we know. Nevertheless, the high performance yielded from the present study verified our hypothesis and may initially justify the routine implementation of this PET-based selection strategy in suspected lung cancer patients who have already underwent ^{18}F -FDG-PET/CT.

Major limitations including retrospective design, single center, small sample size and the lack of well-defined inclusion criteria may limit external validity of our findings. In this regard, well-designed studies are still needed to confirmed the high performance as well as the real added value of PET/CT information to this procedure.

CONCLUSION

Nuclear medicine physicians-performed UGCB driven by FDG-avid SLNs in suspected lung cancer patients could produce a high performance in terms of diagnostic yield, malignancy rate, and molecular analysis, which may obviate more invasive interventional procedures and lead to fast decisions on subsequent management.

REFERENCES

1. Stigt JA, Boers JE, Boomsma MF. Ultrasound-guided tissue core biopsies in supraclavicular lymph nodes in patients with suspected thoracic malignancies. *Respiration*. (2015) 90:412–5. doi: 10.1159/000441301
2. Choe J, Kim MY, Baek JH, Choi CM, Kim HJ. Ultrasonography-guided core biopsy of supraclavicular lymph nodes for diagnosis of metastasis and identification of Epidermal Growth Factor Receptor (EGFR) mutation in advanced lung cancer. *Medicine*. (2015) 94:e1209. doi: 10.1097/MD.0000000000001209
3. Werner L, Keller FA, Bhure U, Roos JE, Tornquist K, Del Sol Pérez-Lago M, et al. The value of ultrasound-guided biopsy of fluorodeoxy-glucose positron emission tomography (FDG-PET)-positive supraclavicular lymph nodes in patients with suspected lung cancer. *BMC Med Imaging*. (2017) 17:41. doi: 10.1186/s12880-017-0214-8
4. Rivera MP, Mehta AC, Wahidi MM. Establishing the diagnosis of lung cancer: diagnosis and management of lung cancer, 3rd ed: American College of Chest Physicians evidence-based clinical practice guidelines. *Chest*. (2013) 143(5 Suppl.):e142S–e65S. doi: 10.1378/chest.12-2353
5. Ettinger DS, Wood DE, Aisner DL, Akerley W, Bauman J, Chirieac LR, et al. Non-small cell lung cancer, version 5.2017, NCCN clinical practice guidelines in oncology. journal of the national comprehensive cancer network: JNCCN. *J Natl Compr Canc Netw*. (2017) 15:504–35. doi: 10.6004/jnccn.2017.0050
6. Kitajima K, Doi H, Kanda T, Yamane T, Tsujikawa T, Kaida H, et al. Present and future roles of FDG-PET/CT imaging in the management of lung cancer. *Jpn J Radiol*. (2016) 34:387–99. doi: 10.1007/s11604-016-0546-2
7. Volpi S, Ali JM, Tasker A, Peryt A, Aresu G, Coonar AS. The role of positron emission tomography in the diagnosis, staging and response assessment of non-small cell lung cancer. *Ann Transl Med*. (2018) 6:95. doi: 10.21037/atm.2018.01.25

DATA AVAILABILITY STATEMENT

The raw data supporting the conclusions of this article will be made available by the authors, without undue reservation.

ETHICS STATEMENT

The studies involving human participants were reviewed and approved by the Ethics Committee of China-Japan Union Hospital of Jilin University. The patients/participants provided their written informed consent to participate in this study.

AUTHOR CONTRIBUTIONS

SG and BJ conceived and design the study, which were proofed by SG. TW, JL, NL, SX, and LB collected and analyzed the data. TW and JL wrote the manuscript. All authors read and approved the manuscript.

FUNDING

This research was supported by Research Fund of Science and Technology Department of Jilin Province (No. 20200201414JC) and Hygiene Specific Subjects of Jilin Province (Nos. 2019SCZ016, 2020SCZ12, and 2021SCZ05).

8. Hou DH, Zhao SJ, Shi JF, Wang L, Wang DB, Huang YC, et al. Lung cancer imaging methods in China from 2005 to 2014: a national, multicenter study. *Thoracic Cancer*. (2019) 10:708–14. doi: 10.1111/1759-7714.12988
9. Sung YM, Lee KS, Kim BT, Kim S, Kwon OJ, Choi JY, et al. Nonpalpable supraclavicular lymph nodes in lung cancer patients: preoperative characterization with ^{18}F -FDG PET/CT. *Am J Roentgenol*. (2008) 190:246–52. doi: 10.2214/AJR.07.2508
10. Klaeser B, Mueller MD, Schmid RA, Guevara C, Krause T, Wiskirchen J. PET-CT-guided interventions in the management of FDG-positive lesions in patients suffering from solid malignancies: initial experiences. *Eur Radiol*. (2009) 19:1780–5. doi: 10.1007/s00330-009-1338-1
11. Bitencourt AG, Tyng CJ, Pinto PN, Almeida MF, Meyrellis LC, Pinheiro RP, et al. Percutaneous biopsy based on PET/CT findings in cancer patients: technique, indications, and results. *Clin Nucl Med*. (2012) 37:e95–7. doi: 10.1097/RLU.0b013e3182443b78
12. Guo W, Hao B, Chen HJ, Zhao L, Luo ZM, Wu H, et al. PET/CT-guided percutaneous biopsy of FDG-avid metastatic bone lesions in patients with advanced lung cancer: a safe and effective technique. *Eur J Nucl Med Mol Imaging*. (2017) 44:25–32. doi: 10.1007/s00259-016-3455-9
13. Broccoli A, Nanni C, Cappelli A, Bacci F, Gasbarrini A, Tabacchi E, et al. Diagnostic accuracy of positron emission tomography/computed tomography-driven biopsy for the diagnosis of lymphoma. *Eur J Nucl Med Mol Imaging*. (2020) 47:3058–65. doi: 10.1007/s00259-020-04913-9
14. Ilie M, Khambata-Ford S, Copie-Bergman C, Huang L, Juco J, Hofman V, et al. Use of the 22C3 anti-PD-L1 antibody to determine PD-L1 expression

- in multiple automated immunohistochemistry platforms. *PLoS ONE*. (2017) 12:e0183023. doi: 10.1371/journal.pone.0183023
15. Stigt JA, Oostdijk AH, Boers JE, van den Berg JW, Groen HJ. Percutaneous ultrasound-guided biopsies in the evaluation of thoracic tumours after PET-CT: a prospective diagnostic study. *Respiration*. (2012) 83:45–52. doi: 10.1159/000330018
 16. Reck M, Rodríguez-Abreu D, Robinson AG, Hui R, Csoszi T, Fülöp A, et al. Pembrolizumab versus Chemotherapy for PD-L1-Positive Non-Small-Cell Lung Cancer. *N Engl J Med*. (2016) 375:1823–33. doi: 10.1056/NEJMoa1606774
 17. Yang H, Hall SRR, Yao F. The value of PD-L1 expression in metastatic lymph nodes of advanced non-small cell lung cancer. *Chest*. (2020) 158:1785–7. doi: 10.1016/j.chest.2020.06.077
 18. Hong L, Negrao MV, Dibaj SS, Chen R, Reuben A, Bohac JM, et al. Programmed death-ligand 1 heterogeneity and its impact on benefit from immune checkpoint inhibitors in NSCLC. *J Thorac Oncol*. (2020) 15:1449–59. doi: 10.1016/j.jtho.2020.04.026
 19. Kumaran M, Benamore RE, Vaidhyanath R, Muller S, Richards CJ, Peake MD, et al. Ultrasound guided cytological aspiration of supraclavicular lymph nodes in patients with suspected lung cancer. *Thorax*. (2005) 60:229–33. doi: 10.1136/thx.2004.029223
 20. Prosch H, Strasser G, Sonka C, Oschatz E, Mashaal S, Mohn-Staudner A, et al. Cervical ultrasound (US) and US-guided lymph node biopsy as a routine procedure for staging of lung cancer. *Ultraschall in der Medizin* (Stuttgart, Germany: 1980). *Ultraschall Med*. (2007) 28:598–603. doi: 10.1055/s-2007-963215
 21. Biswas N, Sangma MA, Dhar D. Association of ultrasound in evaluation of impalpable supraclavicular lymph nodes in patients with suspected lung cancer. *Mymensingh Med J*. (2019) 28:76–84.

Conflict of Interest: The authors declare that the research was conducted in the absence of any commercial or financial relationships that could be construed as a potential conflict of interest.

Publisher's Note: All claims expressed in this article are solely those of the authors and do not necessarily represent those of their affiliated organizations, or those of the publisher, the editors and the reviewers. Any product that may be evaluated in this article, or claim that may be made by its manufacturer, is not guaranteed or endorsed by the publisher.

Copyright © 2022 Wang, Liu, Lv, Xuan, Bai, Ji and Gao. This is an open-access article distributed under the terms of the Creative Commons Attribution License (CC BY). The use, distribution or reproduction in other forums is permitted, provided the original author(s) and the copyright owner(s) are credited and that the original publication in this journal is cited, in accordance with accepted academic practice. No use, distribution or reproduction is permitted which does not comply with these terms.



Pre-Clinical Study of the [^{18}F]AIF-Labeled HER2 Affibody for Non-Invasive HER2 Detection in Gastric Cancer

Jingya Han¹, Yang Chen¹, Yan Zhao², Xinming Zhao^{1,3*}, Jingmian Zhang¹, Jianfang Wang¹ and Zhaoqi Zhang¹

¹ Department of Nuclear Medicine, The Fourth Hospital of Hebei Medical University, Shijiazhuang, China, ² Department of Oncology, The Fourth Hospital of Hebei Medical University, Shijiazhuang, China, ³ Hebei Provincial Key Laboratory of Tumor Microenvironment and Drug Resistance, Shijiazhuang, China

OPEN ACCESS

Edited by:

Philipp Lohmann,
Institute of Neuroscience and
Medicine, Germany

Reviewed by:

Kun Zheng,
Peking Union Medical College
Hospital (CAMS), China
Alberto Miceli,
Università di Genova, Italy

*Correspondence:

Xinming Zhao
xinm_zhao@163.com

Specialty section:

This article was submitted to
Nuclear Medicine,
a section of the journal
Frontiers in Medicine

Received: 16 December 2021

Accepted: 18 January 2022

Published: 16 February 2022

Citation:

Han J, Chen Y, Zhao Y, Zhao X,
Zhang J, Wang J and Zhang Z (2022)
Pre-Clinical Study of the
[^{18}F]AIF-Labeled HER2 Affibody for
Non-Invasive HER2 Detection in
Gastric Cancer.
Front. Med. 9:803005.
doi: 10.3389/fmed.2022.803005

Human epidermal growth factor receptor 2 (HER2) is an important biomarker in gastric cancer (GC) and directly influences the therapeutic effect. Fluorine is firmly bound to Al^{3+} forming [^{18}F]AIF-1,4,7-triazacyclononanetriacetic acid (NOTA)-HER2 affibody is a promising radiolabeled tracer that can monitor the changes of HER2 expression combining the advantages of simple preparation and the properties of ^{18}F . The aim of this study was to develop a quick method for the synthesis of [^{18}F]AIF-NOTA-HER2 affibody and evaluate its utility for HER2+ GC imaging in mouse models. Moreover, ^{68}Ga -NOTA-HER2 affibody imaging was also performed to highlight the superiority of [^{18}F]AIF-NOTA-HER2 affibody imaging in resolution. The HER2 affibody was conjugated with NOTA and labeled using ^{18}F based on the complexation of [^{18}F]AIF by NOTA. Its quality control and stability were performed by high-pressure liquid chromatography (HPLC). The molecular specificity and binding affinity of the novel radiotracer were evaluated in the GC cell line with HER2 overexpression (NCI-N87) and negative expression (MKN74). Distribution studies and PET/CT imaging were performed in mouse models. ^{68}Ga -NOTA-HER2 affibody PET/CT imaging was also performed. [^{18}F]AIF-NOTA-HER2 affibody was efficiently prepared within 30 min with a non-decay-corrected maximum yield of 32.69% and a radiochemical purity of more than 98%. [^{18}F]AIF-NOTA-HER2 affibody was highly stable in incubation medium for 4 h *in vitro* and in the blood of nude mice at 30 min post-injection (p.i.). *In vitro* studies revealed specific binding and high binding affinity of the probe in NCI-N87 cells, while no binding was seen in MKN74 cells. PET imaging showed that NCI-N87 xenografts were differentiated from MKN74 xenografts with excellent contrast and low abdominal background, which was confirmed by the distribution results. High-level accumulation of the [^{18}F]AIF-NOTA-HER2 affibody in HER2+ tumors was blocked by excess unlabeled NOTA-HER2 affibody. [^{18}F]AIF-NOTA-HER2 affibody has a higher image resolution than that of ^{68}Ga -NOTA-HER2 affibody. [^{18}F]AIF-NOTA-HER2 affibody could be produced facilely with high radiochemical yield and may serve as a novel molecular probe with tremendous clinical potential for the non-invasive whole-body detection of the HER2

status in GC with good image contrast and resolution. This method could provide an *in vivo* understanding of GC biology that will ultimately guide the accurate diagnosis and treatment of GC.

Keywords: human epidermal growth factor receptor (HER2), affibody, gastric cancer, molecular imaging, molecular probe

INTRODUCTION

Gastric cancer (GC) ranks fifth in terms of malignancy incidence and third in cancer-related deaths worldwide (1). In China, GC is one of the three most common cancers, and over 70% of patients with GC are diagnosed at an unresectable or metastatic stage (2). Moreover, primary or acquisition cytotoxic chemotherapy resistance renders GC with a very poor prognosis, and the median overall survival (OS) is 10–12 months (3). This finding emphasizes the urgency to identify new therapeutic targets to improve the prognosis.

Approximately 17–20% of patients with GC tested positive for the human epidermal growth factor receptor 2 (HER2) (4). The recommendation in the updated National Comprehensive Cancer Network (NCCN) and European Society for Medical Oncology (ESMO) guidelines suggested that all patients with unresectable, recurrent, or metastatic advanced gastric cancer (AGC) should be screened for HER2 positivity, and those with HER2+ tumors are eligible for first-line trastuzumab in combination with chemotherapy (3). Essentially, accurate monitoring of the HER2 status *in vivo* is critical for effective treatment. Gastroscopic biopsies are spatiotemporally limited due to the high heterogeneity of HER2 expression (5). HER2 heterogeneity may exist between primary tumors and recurrent focus, primary tumors and metastases, among different metastases, and even in the same lesion before and after treatment (6–11). Thus, accurate assessment of the HER2 status is critical in patients with metastatic or recurrent GC, even if the primary lesion is HER2– (12). Furthermore, a repeated biopsy is necessary to evaluate the efficacy of anti-HER2 agents during treatment because treatment resistance eventually develops in some patients with GC. The invasive biopsies are difficult to accurately reflect systemic lesions, monitor HER2 levels in real-time, and measure heterogeneity of tumors. Moreover, repeated invasive biopsies are not feasible in clinical practice considering the tolerance of patients. These limitations have contributed to the development of HER2-targeted molecular imaging and HER2 liquid biopsy technologies [ctDNA sequencing, ctRNA sequencing, circulating tumor cells (CTCs) detection, etc.] (13, 14). Thus, a whole-body, real-time, and non-invasive HER2-targeted molecular imaging method may be a potential alternative to biopsy-based methods for identifying patients suitable for HER2-targeted therapy and monitoring the therapeutic efficacy to improve the management of GC.

Many promising PET radionuclides with long half-lives and decay times, such as ⁶⁴Cu, ⁸⁹Zr, and ¹²⁴I-labeled trastuzumab, have been screened to monitor HER2 levels in malignancies in preclinical studies (15–18). Although these probes showed

good imaging properties, their slow tumor penetration and blood clearance results in imaging were performed several days after injection, which preclude clinical applications. Additionally, because of the long biological half-lives of ⁸⁹Zr-trastuzumab and ¹²⁴I-trastuzumab, the radiation-absorbed doses were calculated to be 0.5 mSv/MBq and 0.3011 ± 0.005 mSv/MBq, respectively, in patients, which were higher than those of ¹⁸F-FDG (0.019 mSv/MBq) (16, 17). As early as 2009, Orlova suggested that the use of the radionuclide-labeled affibody provides much better contrast in HER2 imaging than antibody due to the more rapid clearance from the blood and normal organs (19). The Z_{HER2:342} affibody is one of the most widely studied HER2 affibody molecules and is suitable for HER2 binding since it does not interfere with HER2-targeted therapy due to the use of different HER2 binding domains in the receptors (20). Several derivatives of Z_{HER2:342} have been developed and evaluated in preclinical and clinical Single photon emission CT (SPECT) and PET studies. ¹⁸F is preferred for clinical use due to its good imaging properties and commercial availability (21). [¹⁸F]AIF is rapidly expanding as an ¹⁸F labeling technique that allows convenient ¹⁸F labeling in less time and under milder conditions that can also be combined with a kit (22, 23).

Preclinical studies have shown that [¹⁸F]AIF-NOTA-MAL-MZ_{HER2:342} is a promising tracer for *in vivo* detecting HER2 status (24). Although 9.3% radiochemical yield is greatly improved on the previous ¹⁸F labeled Z_{HER2:342}, it still has some limitations for clinical translation. It results in a high concentration of ¹⁸F to be used in radiosynthesis, which increases radiation exposure of technicians. So exploring improved derivatives of Z_{HER2:342} and effective labeling methods to increase the labeling yield deserves further study.

Thus, we hypothesized that the HER2 affibody molecules with the amino acid sequence apoptosis-enhancing nuclease (AEN)-at the N-terminus and NOTA-based chelators labeled with ¹⁸F using the new one-step labeling method, with preserved binding specificity to HER2, would yield a low abdominal background and would possess more favorable *in vivo* pharmacokinetic performance (25). The aim of the present study was to determine whether the [¹⁸F]AIF-NOTA-HER2 affibody is a promising imaging candidate for HER2 detection in GC.

MATERIALS AND METHODS

Synthesis and Radiolabeling

All chemicals used in this study were purchased commercially. The HER2 affibody (AENKFNKEMRNAYWEIALLPNLNNQQ KRAFIRSLYDDPSQSANLLA EAKKLNDQAQ) was synthesized using manual solid-phase peptide synthesis. NOTA was coupled

to the N-terminus of the HER2 affibody. The synthetic NOTA-HER2 affibody was obtained from China Peptides Company (China). Electrospray ionization-mass spectrometry (ESI-MS) was performed to analyze the identity of the final product. (HPLC) was used to analyze the purity of NOAT-HER2 affibody conjugate.

A QMA cartridge carrying ¹⁸F[−] was pretreated with NaHCO₃ (0.5 M, 10 ml). Then, ¹⁸F[−] was eluted from the cartridge using 0.4 ml of saline. ¹⁸F[−] in saline (0.1 ml, 111 MBq-962 MBq), potassium hydrogen phthalate (KHP) buffer (13 μl, 0.5 M), and AlCl₃·6H₂O (6 μl, 2 mM) in KHP buffer (0.05 M) were mixed and incubated at room temperature for 5 min. Then, 14 μl of HER2 affibody (20 nM) was added to the mixture and heated at 110°C for 15 min. After cooling to room temperature, the mixture was passed through a Sep-Pak C18-Light Cartridge that was activated with 10 ml of EtOH and H₂O. The Sep-Pak C18-Light Cartridge was washed with 10 ml of H₂O and extracted with 0.5 ml of 80% EtOH to obtain the final product.

***In vitro* and *in vivo* Stability**

The *in vitro* stability of the [¹⁸F]AIF-NOTA-HER2 affibody was determined in 5% human serum albumin (HSA) and physiological saline at 37°C. After 0, 1, 2, and 4 h, 20 μl of the mixture were analyzed using HPLC.

For the analysis of *in vivo* stability, 200 μl of [¹⁸F]AIF-NOTA-HER2 affibody (7.4 MBq) were intravenously injected into the caudal region of BALB/c nude mice. After 30 min, blood was collected and centrifuged, and the supernatant was analyzed using HPLC.

Cell Culture

The NCI-N87 cell line derived from human gastric adenocarcinoma with high expression of HER2 was kindly provided by the Stem Cell Bank, Chinese Academy of Sciences. Adherent cells were cultured in RPMI 1640 Medium (Thermo Fisher Scientific, Boston, MA, USA) supplemented with 1% sodium pyruvate 100 mM solution and 10% fetal bovine serum (FBS) (BI, Kibbutz Beit-Haemek, Israel) at 37°C in an atmosphere containing 5% CO₂. The GC cell line MKN74 (HER2-negative) was obtained from Otwo Biotech (Guangzhou, China) and cultured in RPMI-1640 medium supplemented with 10% FBS.

Cellular Uptake, Retention Kinetics, and Blocking Studies

NCI-N87 and MKN74 cell lines were cultured in 24-well plates at a density of 1 × 10⁵ cells/well-overnight, and the fresh culture medium containing was replaced. Subsequently, the cells were incubated with the [¹⁸F]AIF-NOTA-HER2 affibody (111 KBq/well). After 5, 30, 60, and 120 min, the supernatants were collected, and the cells were washed twice using PBS. Radioactivity was measured using a γ-counter. The radioactive medium and PBS were defined as C_{out}. Finally, the cells were harvested with trypsin and flushed again with PBS twice. Radioactivity counts of lysates and PBS were considered C_{in}. The cellular uptake rate was calculated using the formula C_{in}/(C_{in} + C_{out}).

Cellular retention studies were performed in NCI-N87 and MKN74 cells. The cells were incubated with the [¹⁸F]AIF-NOTA-HER2 affibody (111 KBq/well) at 37°C for 1 h, and the culture medium was replaced by a fresh culture medium. After 5, 30, 60, and 120 min, the supernatants were collected, and the wells were washed with PBS. Counts containing radioactive supernatants and PBS were designated as C_{out}. Then the cells were harvested with trypsin and flushed again with PBS twice. Radioactivity counts of lysis solution and PBS were defined as C_{in}. The cellular retention ratio was calculated using the formula C_{in}/(C_{in} + C_{out}).

For the blocking assay, NCI-N87 cells were incubated with the [¹⁸F]AIF-NOTA-HER2 affibody in the presence of 6- and 35-fold excess unlabeled HER2 affibody for 60 min. The supernatant and precipitate were collected and analyzed as mentioned above.

Saturation Binding Assay

The K_d value was studied by adding increasing concentrations (1.625–240 nM) of [¹⁸F]AIF-NOTA-HER2 to NCI-N87 cells. Excess unlabeled HER2 affibody (1,900 nM/well) was used as a blocking agent to determine the non-specific binding in another 48-well plate under the same treatment conditions. After removing the medium after 1 h of incubation, the cells were washed twice with PBS and detached with trypsin. The radioactivity of cells was measured and the K_d value was estimated using GraphPad Prism 5.

Animal Model

All animal experiments were approved by the Principles of Ethical Committee of the Fourth Hospital Hebei Medical University (2018MEC123). Female BALB/c nude mice, 4 weeks old, were housed in ventilated filter-topped cages under specific pathogen-free (SPF) conditions with free access to a standard diet and water. Approximately 2 × 10⁷ gastric tumor cells (in 150 μl of Roswell Park Memorial Institute [RPMI] 1640 medium without FBS) were inoculated subcutaneously into the right forelimb to establish the tumor models.

Biodistribution Studies

Female BALB/c mice-bearing NCI-N87 or MNK74 tumor xenografts were injected with the diluted [¹⁸F]AIF-NOTA-HER2 affibody (200 μl, 2.96 MBq) via the tail vein. The mice were sacrificed and dissected in groups (n = 3) at 30, 60, and 120 min postinjection (p.i.). Tumor, blood, and normal tissues were collected immediately after cleaning, weighed, and measured for radioactivity using a γ-counter after decay correction. The results are reported as the percentage of the injected dose per gram of tissue (%ID/g).

Molecular Imaging Procedure

Mice-bearing NCI-N87 or MKN74 tumors (n = 6) were intravenously injected with the diluted [¹⁸F]AIF-NOTA-HER2 affibody (200 μl, 7.4 MBq). For blocking, 500 μg of cold NOTA-HER2 affibody were coinjected into each mouse bearing NCI-N87 tumors (n = 3). The images in mice-bearing NCI-N87 and MKN74 tumors were acquired at 30, 60, and 120 min p.i., and a blocking study was performed on NCI-N87 xenograft tumor-bearing mice. Imaging was performed using a digital

Vereos PET/CT Scanner (PHILIPS, The Netherlands) acquired with 200 mm diameter Transaxial field of view (FOV) and ordered subsets expectation maximization (OSEM) + filtered back-projection (FBP) + time-of-flight (TOF) reconstruction algorithms. The images were digitally stored in a 1,024 × 1,024 matrix. The SUV_{max} values of the region of interest (ROI) over the tumor and muscle were collected.

At the same time, mice-bearing NCI-N87 tumors (*n* = 3) were intravenously injected with the diluted [¹⁸F]AIF-NOTA-HER2 affibody (200 μl, 7.4 MBq) and imaged by micro-PET/CT at 30, 60, and 120 min p.i. Another group of mice-bearing NCI-N87 tumors (*n* = 3) was intravenously injected with ⁶⁸Ga-NOTA-HER2 affibody (200 μl, 7.4 MBq; *n* = 3) and imaged by micro-PET/CT at 30 and 60 min p.i.

Statistical Analysis

All statistical analyses were completed using SPSS 22.0 software. Variable data are presented as the mean ± SD ($\bar{X} \pm SD$). The significance of differences in comparisons between two datasets was analyzed using Student's *t*-test. When three groups were compared, a one-way ANOVA was applied. A rank-sum test was also performed. A *p* < 0.05 was considered statistically significant.

RESULTS

Synthetic Chemistry and Radiochemistry

Alanine at the N-terminus of the HER2 affibody was subjected to a condensation reaction with -orcarboxylic acid (COOH) of NOTA [serving as a chelator for [¹⁸F]AIF labeling] (Figure 1).

The purity of the obtained NOTA-modified affibody molecules was 97.80%. The MS spectrum indicated a molecular weight of 6680.51, which is consistent with its theoretical molecular weight.

The [¹⁸F]AIF-NOTA-HER2 affibody molecular probe was manually prepared within 30 min. The maximum nondecayed corrected yield of the [¹⁸F]AIF-NOTA-HER2 affibody molecular probe was 32.69% with a radiochemical purity >98%, as analyzed by HPLC with a retention time of 8.5 min (Figure 2A).

Stability

The radiochemical purity of the [¹⁸F]AIF-NOTA-HER2 affibody *in vitro* following an incubation with physiological saline or 5% half-normal saline (HAS; 37°C, 4 h) was maintained at >90% (Figure 2B), and a single peak was observed without free ¹⁸F[−] (Figure 2B). The radiotracer was injected into mice, and a single peak was observed in blood at 30 min p.i. using HPLC, with a radiochemical purity >90% (Figure 2D). The results indicated that the [¹⁸F]AIF-NOTA-HER2 affibody was stable *in vitro* and *in vivo* over the period tested.

Cellular Uptake, Retention, and Blocking Assay *in vitro*

The [¹⁸F]AIF-NOTA-HER2 affibody showed higher cellular uptake and retention in NCI-N87 cells than in MKN74 cells at all time points tested (Figures 3A,B). Radioactivity accumulated rapidly in NCI-N87 cells, peaked at 60 min (6.28 ± 0.47%), and decreased slightly over time. Additionally, HER2-negative MKN74 cells did not show any significant uptake of the [¹⁸F]AIF-NOTA-HER2 affibody, suggesting the specific HER2-mediated uptake of the molecular probe in HER2+ cells.

The uptake of the [¹⁸F]AIF-NOTA-HER2 affibody in NCI-N87 cells was 6.28 ± 0.47% and was reduced to 0.53 ± 0.03% and

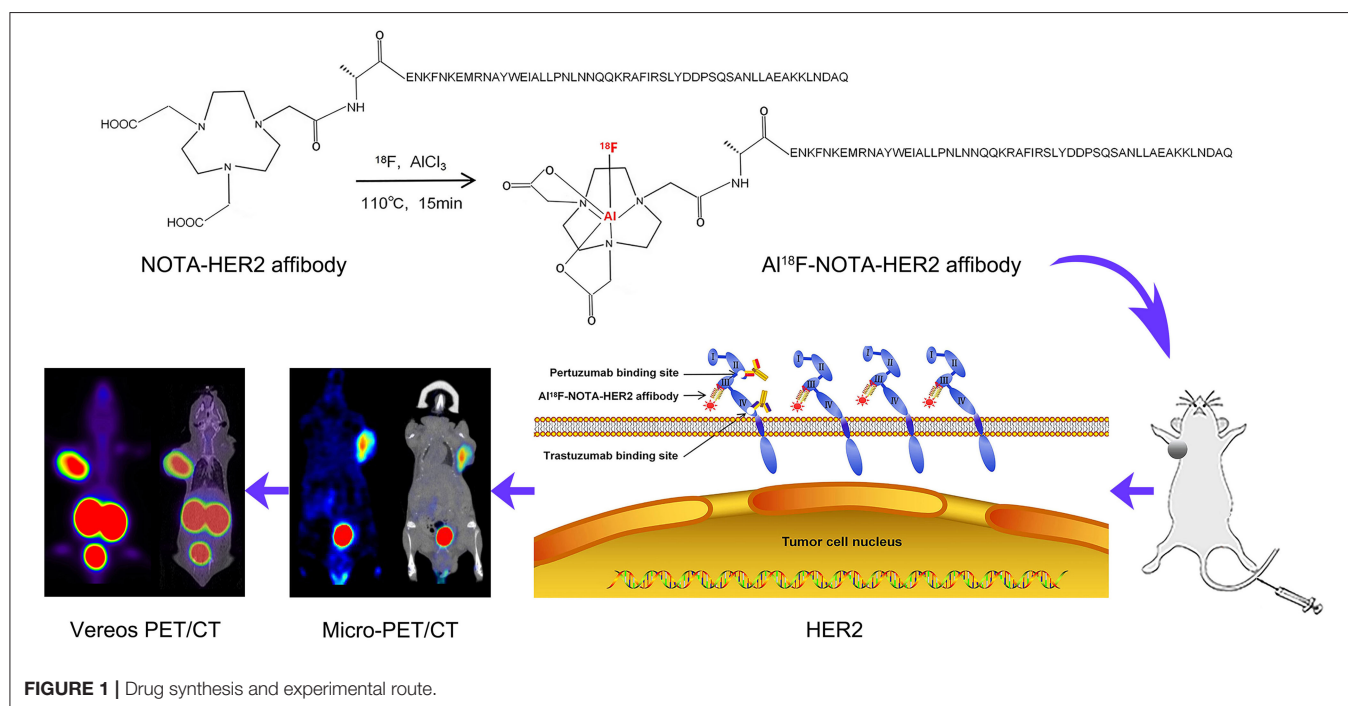
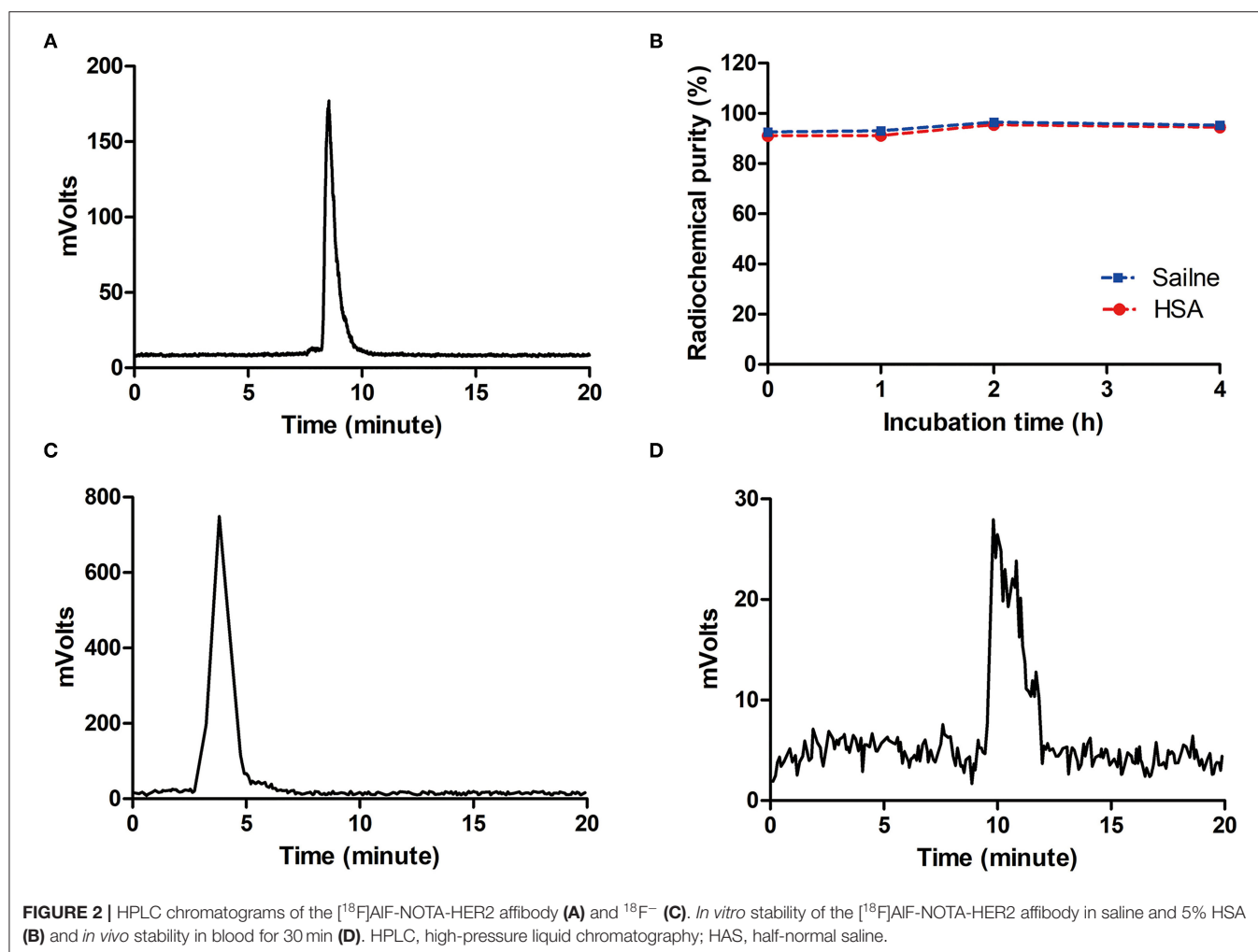


FIGURE 1 | Drug synthesis and experimental route.



0.44 ± 0.05% by 6- and 35-fold excesses of cold HER2 affibody at 60 min, respectively (Figure 3C). The amount of [¹⁸F]AIF-NOTA-HER2 affibody taken up by NCI-N87 cells was decreased by more than 90% after an incubation with an excess of cold HER2 affibody, indicating that the uptake of the molecular probe in NCI-N87 cells was HER2 specific.

Saturation Binding *in vitro*

The saturation binding curve of the K_d determination is shown in Figure 3D. The K_d value of the [¹⁸F]AIF-NOTA-HER2 affibody to HER2 in NCI-N87 cells was 52.25 ± 3.68 nM, indicating that the radiolabeled tracer binds to HER2 with high affinity and specificity.

Ex vivo Distribution

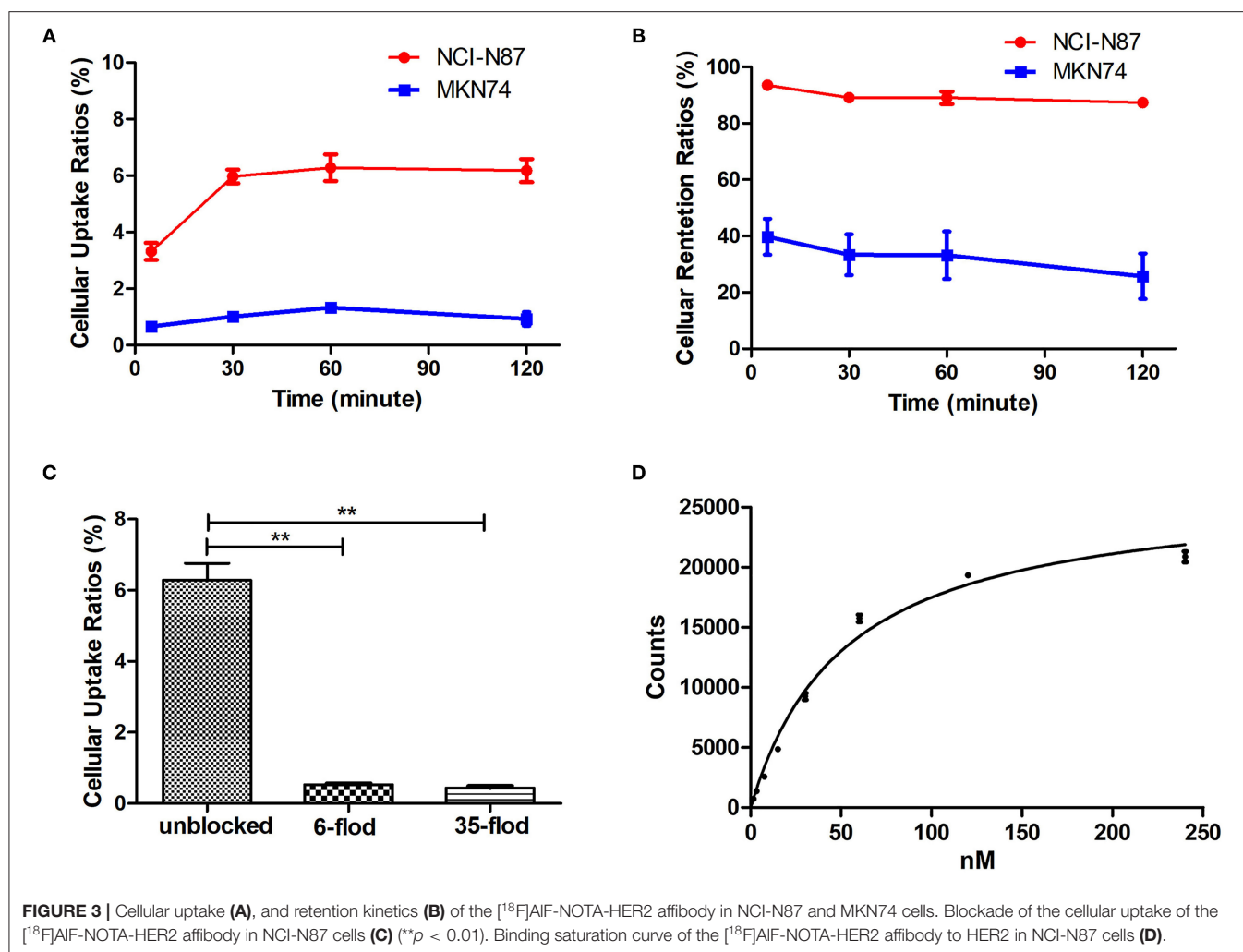
The [¹⁸F]AIF-NOTA-HER2 affibody was efficiently accumulated in HER2-expressing tumors. HER2+ tumor uptake of the radiolabeled agent was 1.27 ± 0.54% ID/g, 1.46 ± 0.65% ID/g, and 1.35 ± 0.07% ID/g at 30, 60, and 120 min p.i., respectively (Table 1). The [¹⁸F]AIF-NOTA-HER2 affibody showed a significantly higher concentration in HER2+ tumors than in HER2- tumors at each time point ($p = 0.003, 0.016,$

and 0.010, respectively; Figure 4), which was consistent with the tumor/muscle ratio (T/M) ($p = 0.046, 0.046,$ and 0.002, respectively). The kidney showed the highest uptake of the radiotracer, suggesting that the urinary system is the main route of excretion.

The [¹⁸F]AIF-NOTA-HER2 affibody concentration in the blood was decreased from 0.38 ± 0.14% ID/g at 30 min p.i. to 0.11 ± 0.05% ID/g at 120 min p.i. (Table 2). The radiolabeled affibody molecules showed rapid clearance from the blood and normal organs, causing a high tumor-to-background ratio.

PET Imaging

3D-rendered digital Vereos PET/CT images of mice-bearing NCI-N87 and MKN74 tumors at 30, 60, and 120 min p.i. are displayed in Figure 5. As early as 30 min after injection, a considerably higher signal intensity was observed in HER2+ tumors and was consistently sustained at subsequent time points. HER2+ tumors, kidneys, and bladder were clearly visualized, while HER2- tumors were almost invisible, consistent with the biodistribution studies. The differences in T/M between NCI-N87 tumor-bearing mice and MKN74 tumor-bearing mice were



statistically significant throughout the whole imaging process ($p = 0.001, 0.004, \text{ and } 0.004$). The detection ability of Vereos PET/CT is comparable to that of micro-PET/CT in HER2+ tumors. In terms of image quality, the image resolution of [¹⁸F]AIF-NOTA-HER2 affibody is higher than that of ⁶⁸Ga-NOTA-HER2 affibody (Figure 6).

The accumulation in NCI-N87 tumors was blocked by a coinjection of excess cold HER2 affibody at 30, 60, and 120 min after injection (Figure 5C). The quantitative analysis of T/M acquired from PET imaging data displayed a significant decrease in the blocked group compared to the non-blocked group ($p = 0.003, 0.016, \text{ and } 0.010$).

DISCUSSION

The specific expression of HER2 in tumor biopsy samples is crucial in tumor diagnosis and the selection of the appropriate therapy. This approach may not be reliable for gastric tumors, which display high HER2 heterogeneity. Molecular imaging has great potential to characterize important specific targets in malignancies, such as HER2. Moreover, ⁶⁸Ga-labeled affibody

TABLE 1 | Biodistribution of the [¹⁸F]AIF-NOTA-HER2 affibody in mice-bearing NCI-N87 tumors.

Organ (Mean ± SD, %ID/g)	30 min	60 min	120 min
Blood	0.38 ± 0.14	0.24 ± 0.05	0.11 ± 0.05
Heart	0.17 ± 0.08	0.12 ± 0.03	0.10 ± 0.03
Lung	0.37 ± 0.31	0.22 ± 0.12	0.14 ± 0.05
Liver	0.21 ± 0.12	0.21 ± 0.11	0.17 ± 0.08
Spleen	0.15 ± 0.11	0.14 ± 0.06	0.15 ± 0.11
Kidney	15.48 ± 1.60	17.11 ± 2.17	18.97 ± 4.82
Stomach	0.09 ± 0.06	0.05 ± 0.02	0.05 ± 0.01
Small intestine	0.12 ± 0.10	0.07 ± 0.03	0.07 ± 0.02
Large intestine	0.07 ± 0.04	0.05 ± 0.03	0.19 ± 0.12
Muscle	0.11 ± 0.04	0.09 ± 0.04	0.09 ± 0.02
Bone	0.51 ± 0.22	0.63 ± 0.40	0.48 ± 0.23
Brain	0.03 ± 0.01	0.04 ± 0.03	0.03 ± 0.01
Tumor	1.27 ± 0.54	1.46 ± 0.65	1.35 ± 0.07

probes have been reported to be successful in many preclinical investigations and a first-in-human study in HER2+ tumor imaging (26, 27). However, applications of the ⁶⁸Ga labeling

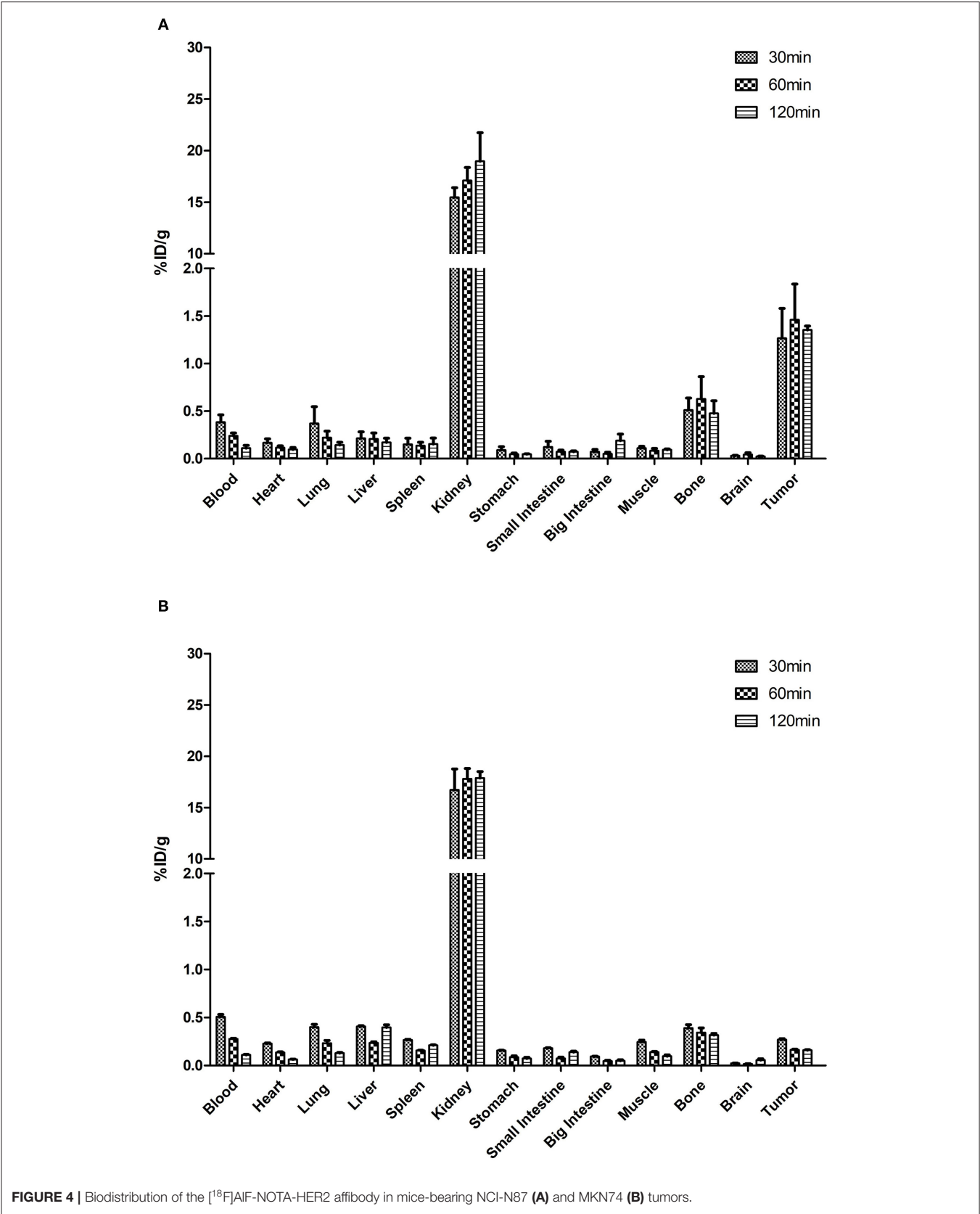


TABLE 2 | Biodistribution of the [¹⁸F]AIF-NOTA-HER2 affibody in mice-bearing MKN74 tumors.

Organ (Mean ± SD, %ID/g)	30 min	60 min	120 min
Blood	0.51 ± 0.04	0.28 ± 0.01	0.11 ± 0.01
Heart	0.23 ± 0.01	0.14 ± 0.01	0.07 ± 0.01
Lung	0.40 ± 0.05	0.24 ± 0.05	0.13 ± 0.01
Liver	0.41 ± 0.02	0.24 ± 0.02	0.40 ± 0.04
Spleen	0.27 ± 0.01	0.16 ± 0.01	0.21 ± 0.01
Kidney	16.72 ± 3.53	17.80 ± 1.75	17.88 ± 1.10
Stomach	0.15 ± 0.01	0.09 ± 0.03	0.07 ± 0.02
Small intestine	0.18 ± 0.01	0.07 ± 0.02	0.14 ± 0.02
Big intestine	0.09 ± 0.01	0.05 ± 0.02	0.05 ± 0.01
Muscle	0.25 ± 0.03	0.14 ± 0.01	0.10 ± 0.03
Bone	0.39 ± 0.06	0.34 ± 0.09	0.32 ± 0.04
Brain	0.03 ± 0.01	0.01 ± 0.01	0.06 ± 0.02
Tumor	0.27 ± 0.02	0.16 ± 0.01	0.16 ± 0.01

method are limited due to the relatively short half-life (67.7 min) of ⁶⁸Ga compared with ¹⁸F. ¹⁸F-labeled affibody molecules that meet the requirements for clinical use with a single good manufacturing practice production and a longer time window for image acquisition. The positron energy of ¹⁸F is lower than ⁶⁸Ga ($E_{\text{mean}} = 0.25$ MeV vs. 0.83 MeV), resulting in a shorter positron range than ⁶⁸Ga (0.6 vs. 3.5 mm), which leads to a higher spatial resolution in PET/CT imaging (28). The high image resolution of ¹⁸F and easy formation of [¹⁸F]AIF chelates make [¹⁸F]AIF molecular probes an engaging approach (29–32). Inspired by the emergence of [¹⁸F]AIF labeling strategy and the fact that [¹⁸F]AIF-NOTA-Octreotide is developed as a clinical substitute for ⁶⁸Ga labeled somatostatin analog, we constructed a promising HER2-targeting tracer, the [¹⁸F]AIF-NOTA-HER2 affibody, and evaluated the biodistribution characteristics and preliminary HER2-targeted imaging efficacy in animal models. Meanwhile, we compared the image quality between [¹⁸F]AIF-NOTA-HER2 affibody and ⁶⁸Ga-NOTA-HER2 affibody.

The preparation of [¹⁸F]AIF-NOTA-Z_{HER2:342} and PET imaging study have already been reported previously (24). However, compared with previous studies, the labeling rate of [¹⁸F]AIF-NOTA-HER2 affibody in our study has been greatly improved. Using KHP as the reaction buffer, which was different from sodium acetate buffer, the volume of the reaction system was reduced, and the labeling rate was increased to a certain extent compared to sodium acetate buffer in the previous study (23, 29, 30), which allows a lower concentration of ¹⁸F to be used in radiosynthesis. Moreover, KHP with non-volatile characteristics is suitable for the preparation and automatic production of kits, which lays the foundation for clinical translation in the future.

The [¹⁸F]AIF-NOTA-HER2 affibody with a K_d value of 52.25 ± 3.68 nM showed good uptake in the HER2+ tumor cell, and the *in vitro* uptake was blocked by excess cold HER2 affibody, indicating that the probe had high target-binding affinity and specificity in HER2+ cells. The high uptake of [¹⁸F]AIF-NOTA-HER2 affibody by HER2+ cells led to an obvious increase in

the brightness of HER2+ xenografts on PET images. NCI-N87 xenografts were clearly distinguished from the surrounding normal organs at 30–120 min p.i. Quantification of PET imaging showed that high T/M ratios (12.19 ± 4.71) persisted at 120 min after injection, consistent with distribution study. Meanwhile, the coinjection of excess HER2 affibody noticeably decreased NCI-N87 tumor accumulation. These results confirmed the excellent HER2 targeting specificity *in vivo*. Moreover, the suitable half-life of ¹⁸F allows a longer time window for [¹⁸F]AIF-NOTA-HER2 affibody imaging acquisition, which is more practical in clinical situations. In order to clarify the advantage to use [¹⁸F]AIF, we contrasted PET images between [¹⁸F]AIF-NOTA-HER2 affibody and ⁶⁸Ga-NOTA-HER2 affibody. The results demonstrated that [¹⁸F]AIF-NOTA-HER2 affibody PET can provide higher image resolution than that of ⁶⁸Ga-NOTA-HER2 affibody. Digital Vereos PET/CT can provide high-quality images and the tumor detection ability of it is comparable to that of micro-PET/CT, which will widen the road for the development of preclinical experimental in some institutions without micro-PET/CT.

The biodistribution results were consistent with the quantitative analysis of PET data, and the [¹⁸F]AIF-NOTA-HER2 affibody was rapidly localized in NCI-N87 xenografts and was quickly cleared from the blood. As an improved structure of Z_{HER2:342}, the HER2 affibody used in this study contains the amino acid sequence AEN- at the N-terminus, which might be associated with low hepatic uptake. The probe was removed from blood circulation predominantly by urinary excretion resulting in optimized contrast and improved imaging sensitivity and accuracy.

No free ¹⁸F[−] or other dissociated products were detected in the stability study, indicating that the [¹⁸F]AIF-NOTA-HER2 affibody was highly stable *in vitro* and *in vivo*. Although the biodistribution results showed that the radioactive accumulation was slightly higher in bone than in most non-target organs, the low radioactive uptake of bone observed in PET images did not affect tumor detection. PET imaging revealed high HER2+ tumor-to-bone contrast, indicating that [¹⁸F]AIF was stably complexed to the HER2 affibody by NOTA. Nonetheless, it should be considered that bone accumulation of the free ¹⁸F[−] might hamper visualization of small lesions or lesions with low HER2 expression in the clinical setting. Whether minor interference originating from ¹⁸F[−] accumulation in the bone affects the detection of bone metastases remains to be verified in the next clinical trials.

The combination therapy of chemotherapy and trastuzumab was approved as the first-line treatment for HER2-positive AGC by the FDA in 2010 (16). Many studies have shown that radiolabeled trastuzumab can efficiently detect HER2. The trastuzumab-based probe has some disadvantages in monitoring changes in HER2 expression during trastuzumab treatment because the therapeutic antibody might compete with the probe for the same epitope on HER2 (27, 33). So we deduced that ongoing HER2-targeted therapy did not interfere with [¹⁸F]AIF-NOTA-HER2 affibody imaging, because the affibody and trastuzumab bind to different HER2 domains. Whether the [¹⁸F]AIF-NOTA-HER2 affibody can be used to monitor the initial response to treatment with trastuzumab and to re-evaluate

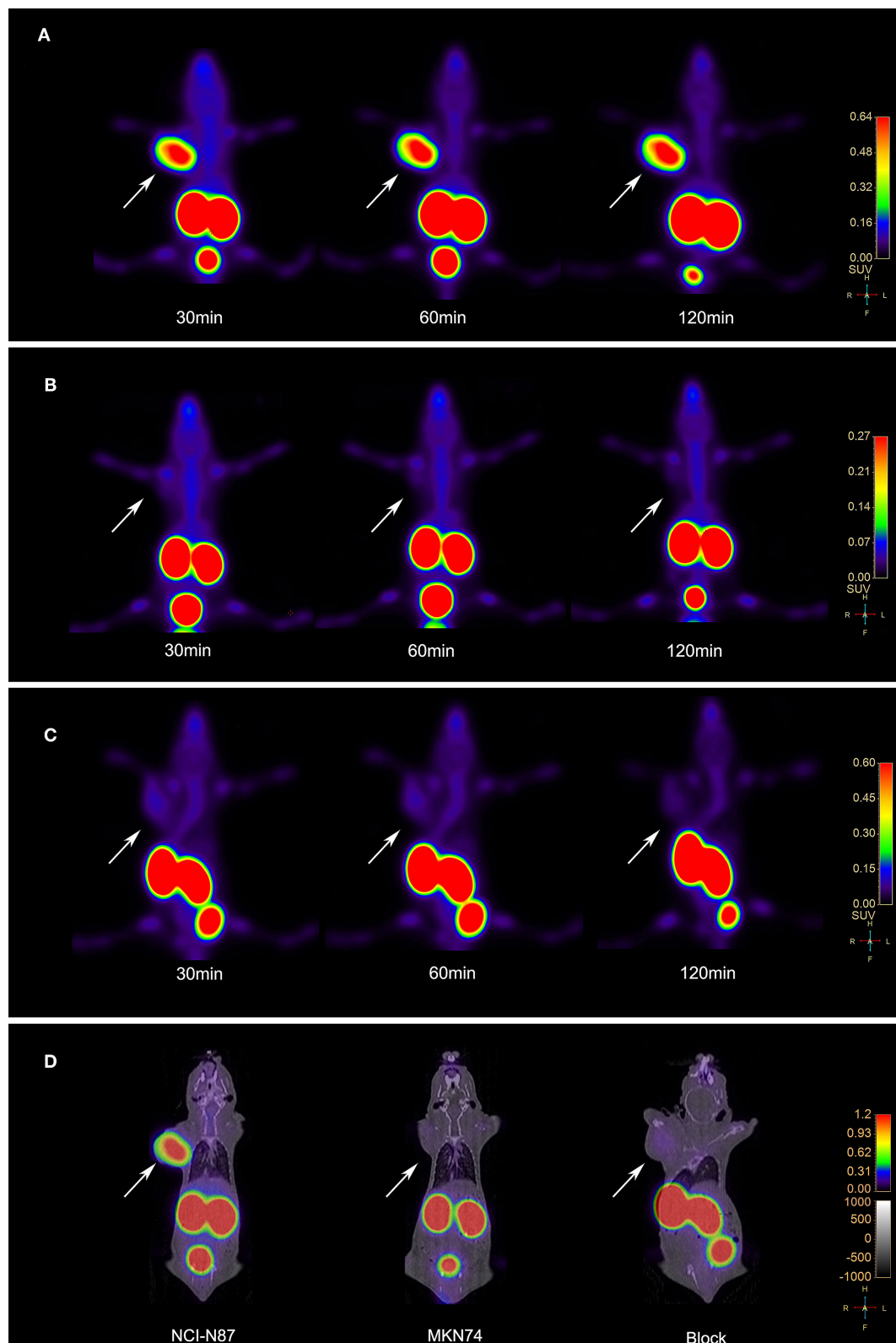


FIGURE 5 | (A) Vereos PET images of the [¹⁸F]AIF-NOTA-HER2 affibody in tumor-bearing mice NCI-N87 xenografts. **(B)** Vereos PET images of the [¹⁸F]AIF-NOTA-HER2 affibody in tumor-bearing mice MKN74 xenografts. **(C)** Blocking study after a coinjection with excess cold NOTA-HER2 affibody in mice-bearing NCI-N87 tumors. **(D)** Fusion images of mouse model at 60 min post-injection by Vereos PET/CT. White arrows indicate xenografts.

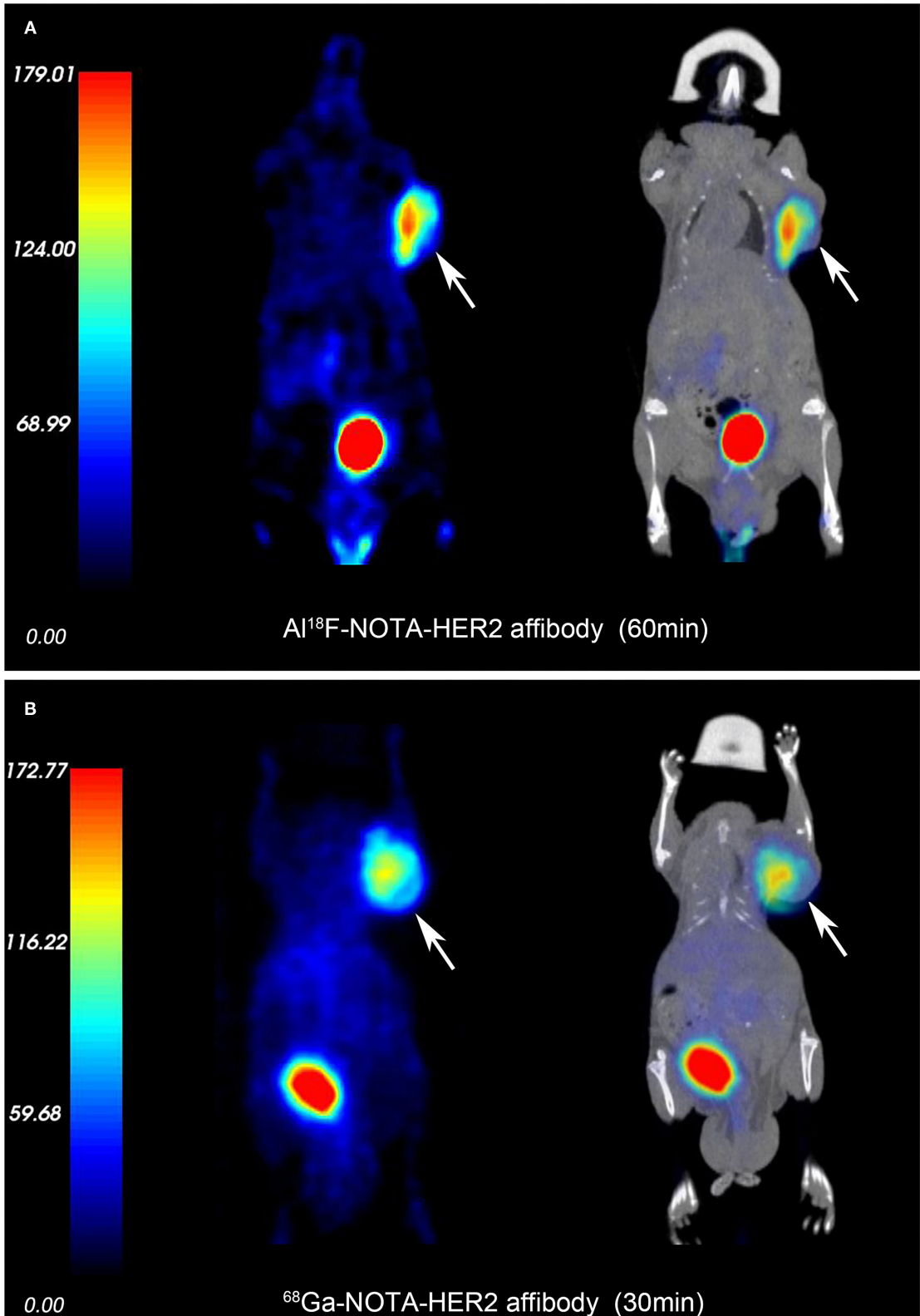


FIGURE 6 | PET and fusion images of the ^{18}F AlF-NOTA-HER2 affibody (A) and ^{68}Ga -NOTA-HER2 affibody (B) in mice-bearing NCI-N87 by micro-PET/CT. White arrows indicate xenografts.

the systemic HER2 status during trastuzumab treatment need further research.

This research also has some limitations. The radiation-absorbed doses of the kidney are high, renal protection could be performed by the use of positively charged amino acids, albumin fragments, or gelofusine. Moreover, the labeling rate needs to be further improved to minimize radiation exposure for technicians by subtly adjusting the ratio of HER2 affibody to AlCl₃·6H₂O solution or the pH value of the reaction system.

CONCLUSIONS

The [¹⁸F]AIF-NOTA-HER2 affibody can be produced in high yields and with high radiochemical purity in a one-step procedure within 30 min. This new radiolabeled tracer can visualize HER2+ tumors with high specific tumor uptake and rapid blood clearance. [¹⁸F]AIF-NOTA-HER2 affibody may serve as a novel PET molecular probe with tremendous clinical potential for the non-invasive, real-time, and whole-body detection of the HER2 status in GC with good image contrast and resolution. This method could provide an *in vivo* understanding of GC biology that will ultimately guide the accurate diagnosis and treatment of GC. It is worth the clinical transformation.

DATA AVAILABILITY STATEMENT

The raw data supporting the conclusions of this article will be made available by the authors, without undue reservation.

REFERENCES

- Bray F, Ferlay J, Soerjomataram I, Siegel RL, Torre LA, Jemal A. Global cancer statistics 2018: GLOBOCAN estimates of incidence and mortality worldwide for 36 cancers in 185 countries. *CA Cancer J Clin.* (2018) 68:394–424. doi: 10.3322/caac.21492
- Shen L, Shan YS, Hu HM, Price TJ, Sirohi B, Yeh KH, et al. Management of gastric cancer in Asia: resource-stratified guidelines. *Lancet Oncol.* (2013) 14:e535–47. doi: 10.1016/S1470-2045(13)70436-4
- Palle J, Rochand A, Pernot S, Gallois C, Taïeb J, Zaanane A, et al. Human epidermal growth factor receptor 2 (her2) in Advanced Gastric Cancer: Current Knowledge and Future Perspectives. *Drugs* (2020) 80:401–15. doi: 10.1007/s40265-020-01272-5
- Smyth EC, Nilsson M, Grabsch HI, van Grieken NC, Lordick F. Gastric cancer. *Lancet.* (2020) 396:635–48. doi: 10.1016/S0140-6736(20)31288-5
- Wu Y, Li L, Wang Z, Shi J, Hu Z, Gao S, et al. Imaging and monitoring HER2 expression in breast cancer during trastuzumab therapy with a peptide probe ^{99m}Tc-HYNIC-H10F. *Nur J Nucl Med Mol Imaging.* (2020) 47:2613–23. doi: 10.1007/s00259-020-04754-6
- Park SR, Park YS, Ryu MH, Ryoo BY, Woo CG, Jung HY, et al. Extra-gain of HER2-positive cases through HER2 reassessment in primary and metastatic sites in advanced gastric cancer with initially HER2-negative primary tumours: results of GASTric cancer HER2 reassessment study 1 (GASTHER1). *Eur J Cancer.* (2016) 53:42–50. doi: 10.1016/j.ejca.2015.09.018
- Bang YJ, Van Cutsem E, Feyereislova A, Chung HC, Shen L, Sawaket A, et al. Trastuzumab in combination with chemotherapy versus chemotherapy alone for treatment of HER2-positive advanced gastric or gastro-oesophageal junction cancer (ToGA): a phase 3, open-label, randomised controlled trial. *Lancet.* (2010) 376:687–97. doi: 10.1016/S0140-6736(10)61121-X
- Niikura N, Liu J, Hayashi N, Mittendorf EA, Gong Y, Pallaet SL, et al. Loss of human epidermal growth factor receptor 2 (HER2) expression in metastatic sites of HER2-overexpressing primary breast tumors. *J Clin Oncol.* (2012) 30:593–9. doi: 10.1200/JCO.2010.33.8889
- Altundag K. Role of endocrine therapy in weak estrogen/progesterone receptor expression in HER2 negative breast cancer. *Eur J Surg Oncol.* (2018) 44:539. doi: 10.1016/j.ejso.2017.08.021
- Altundag K. Digital breast tomosynthesis findings may be different in HER2 positive breast cancer patients according to hormone receptor status. *Br J Radiol.* (2018) 91:20170730. doi: 10.1259/bjr.20170730
- Di Leo A, Johnston S, Lee KS, Ciruelos E, Lønning PE, Janni W, et al. Buparlisib plus fulvestrant in postmenopausal women with hormone-receptor-positive, HER2-negative, advanced breast cancer progressing on or after mTOR inhibition (BELLE-3): a randomised, double-blind, placebo-controlled, phase 3 trial. *Lancet Oncol.* (2018) 19:87–100. doi: 10.1016/S1470-2045(17)30688-5
- Kim KM, Bilous M, Chu KM, Kim BS, Kim WH, Park YS, et al. Human epidermal growth factor receptor 2 testing in gastric cancer: recommendations of an Asia-Pacific task force. *Asia Pac J Clin Oncol.* (2014) 10:297–307. doi: 10.1111/ajco.12263
- Soda N, Rehm BHA, Sonar P, Shiddiky MJA. Advanced liquid biopsy technologies for circulating biomarker detection. *J Mater Chem B.* (2019) 7:6670–704. doi: 10.1039/C9TB01490J
- Lopes C, Piairo P, Chicharo A, Diéguez L, Pires LR, Corredeira P, et al. HER2 expression in circulating tumour cells isolated from metastatic

ETHICS STATEMENT

The animal study was reviewed and approved by the Principles of Ethical Committee of the Fourth Hospital Hebei Medical University (2018MEC123).

AUTHOR CONTRIBUTIONS

JH, YC, YZ, XZ, JZ, JW, and ZZ contributed to the study conception and design. Material preparation, data collection, and analysis were performed by JH and YC. The first draft of the manuscript was written by JH. The manuscript was reviewed by XZ. All authors commented on previous versions of the manuscript, contributed to the article, and approved the submitted version.

FUNDING

This work was financially supported by grants from the National Natural Science Foundation of China (NSFC) project (Grant No. 82071959) and Hebei Provincial Natural Science Foundation, Jing-Jin-Ji special projects for basic research cooperation (Grant No. H2018206600).

ACKNOWLEDGMENTS

The authors thank all the technicians from the Department of Nuclear Medicine, The Fourth Hospital of Hebei Medical University for their contributions to PET imaging. The authors thank the chemists from the Department of Nuclear Medicine, Peking University Cancer Hospital, and General Hospital of the Chinese People's Liberation Army for providing technical assistance.

- breast cancer patients using a size-based microfluidic device. *Cancers*. (2021) 13:4446. doi: 10.3390/cancers13174446
15. O'Donoghue JA, Lewis JS, Pandit-Taskar N, Fleming SE, Schöder H, Larson SM, et al. Pharmacokinetics, biodistribution, and radiation dosimetry for (89)Zr-trastuzumab in patients with esophagogastric cancer. *J Nucl Med*. (2018) 59:61–6. doi: 10.2967/jnumed.117.194555
 16. Guo X, Zhou N, Chen Z, Liu T, Xu X, Lei X, et al. Construction of ¹²⁴I-trastuzumab for noninvasive PET imaging of HER2 expression: from patient-derived xenograft models to gastric cancer patients. *Gastric Cancer*. (2020) 23:614–26. doi: 10.1007/s10120-019-01035-6
 17. Guo X, Zhu H, Zhou N, Chen Z, Liu T, Liu F, et al. Noninvasive detection of HER2 expression in gastric cancer by ⁶⁴Cu-NOTA-trastuzumab in PDX mouse model and in patients. *Mol Pharm*. (2018) 15:5174–82. doi: 10.1021/acs.molpharmaceut.8b00673
 18. Paudyal P, Paudyal B, Hanaoka H, Oriuchi N, Iida Y, Yoshioka H, et al. Imaging and biodistribution of Her2/neu expression in non-small cell lung cancer xenografts with Cu-labeled trastuzumab PET. *Cancer Sci*. (2010) 101:1045–50. doi: 10.1111/j.1349-7006.2010.01480.x
 19. Orlova A, Wällberg H, Stone-Elander S, Tolmachev V. On the selection of a tracer for PET imaging of HER2-expressing tumors: direct comparison of a ¹²⁴I-labeled affibody molecule and trastuzumab in a murine xenograft model. *J Nucl Med*. (2009) 50:417–25. doi: 10.2967/jnumed.108.057919
 20. Sörensen J, Velikyan I, Sandberg D, Wennborg A, Feldwisch J, Tolmachev V, et al. Measuring HER2-receptor expression in metastatic breast cancer using [⁶⁸Ga] ABY-025 affibody PET/ CT. *Theranostics*. (2016) 6:262–71. doi: 10.7150/thno.13502
 21. Fersing C, Bouhrel A, Cantelli C, Guillet B, Lisowski V, Guillet B. A comprehensive review of non-covalent radiofluorination approaches using aluminum [¹⁸F]fluoride: will [¹⁸F]AIF replace ⁶⁸Ga for metal chelate labeling? *Molecules*. (2019) 24:2866. doi: 10.3390/molecules24162866
 22. McBride WJ, Sharkey RM, Karacay H, D'Souza CA, Rossi EA, Laverman P, et al. A novel method of ¹⁸F radiolabeling for PET. *J Nucl Med*. (2009) 50:991–8. doi: 10.2967/jnumed.108.060418
 23. Laverman P, McBride WJ, Sharkey RM, Eek A, Joosten L, Oyen WJG, et al. A novel facile method of labeling octreotide with ¹⁸F-fluorine. *J Nucl Med*. (2010) 51:454–61. doi: 10.2967/jnumed.109.066902
 24. Xu Y, Bai Z, Huang Q, Pan Y, Pan D, Wang L, et al. PET of HER2 expression with a novel ¹⁸F-labeled affibody. *J Cancer*. (2017) 8:1170–8. doi: 10.7150/jca.18070
 25. Wällberg H, Orlova A, Altai M, Hosseinimehr SJ, Widström C, Malmberg J, et al. Molecular design and optimization of ^{99m}Tc-labeled recombinant affibody molecules improves their biodistribution and imaging properties. *J Nucl Med*. (2011) 52:461–9. doi: 10.2967/jnumed.110.083592
 26. Glaser M, Iveson P, Hoppmann S, Indrevoll B, Wilson A, Arukwe J, et al. Three methods for ¹⁸F labeling of the HER2-binding affibody molecule Z_{HER2}: 2891 including preclinical assessment. *J Nucl Med*. (2013) 54:1981–8. doi: 10.2967/jnumed.113.122465
 27. Zhou N, Liu C, Guo X, Xu Y, Gong J, Qi C, et al. Impact of ⁶⁸Ga-NOTA-MAL-MZHER2 PET imaging in advanced gastric cancer patients and therapeutic response monitoring. *Eur J Nucl Med Mol Imaging*. (2021) 48:161–75. doi: 10.1007/s00259-020-04898-5
 28. Wang S, Zhou X, Xu X, Ding J, Liu S, Hou X, et al. Clinical translational evaluation of Al¹⁸F-NOTA-FAPI for fibroblast activation protein-targeted tumour imaging. *Eur J Nucl Med Mol Imaging*. (2021) 48:4259–71. doi: 10.1007/s00259-021-05470-5
 29. Machulla HJ, Al-Momani E. PSMA ligands for imaging prostate cancer: alternative labeling by complex formation with Al¹⁸F²⁺. *J Nucl Med*. (2017) 58:2040–1. doi: 10.2967/jnumed.117.197996
 30. Liu T, Liu C, Xu X, Liu F, Guo X, Li N, et al. Preclinical evaluation and pilot clinical study of Al¹⁸F-PSMA-BCH for prostate cancer PET imaging. *J Nucl Med*. (2019) 60:1284–92. doi: 10.2967/jnumed.118.221671
 31. Jiang X, Wang X, Shen T, Yao Y, Chen M, Li Z, et al. FAPI-04 PET/CT using [¹⁸F]AIF labeling strategy: automatic synthesis, quality control, and *in vivo* assessment in patient. *Front Oncol*. (2021) 11:649148. doi: 10.3389/fonc.2021.649148
 32. Lu J, Zhang C, Yang X, Yao X, Zhang Q, Sun X. Synthesis and preliminary evaluation of a novel ¹⁸F-labeled 2-nitroimidazole derivative for hypoxia imaging. *Front Oncol*. (2020) 10:572097. doi: 10.3389/fonc.2020.572097
 33. Sandberg D, Tolmachev V, Velikyan I, Olofsson H, Wennborg A, Feldwisch J, et al. Intra-image referencing for simplified assessment of HER2-expression in breast cancer metastases using the affibody molecule ABY-025 with PET and SPECT. *Eur J Nucl Med Mol Imaging*. (2017) 44:1337–46. doi: 10.1007/s00259-017-3650-3

Conflict of Interest: The authors declare that the research was conducted in the absence of any commercial or financial relationships that could be construed as a potential conflict of interest.

Publisher's Note: All claims expressed in this article are solely those of the authors and do not necessarily represent those of their affiliated organizations, or those of the publisher, the editors and the reviewers. Any product that may be evaluated in this article, or claim that may be made by its manufacturer, is not guaranteed or endorsed by the publisher.

Copyright © 2022 Han, Chen, Zhao, Zhao, Zhang, Wang and Zhang. This is an open-access article distributed under the terms of the Creative Commons Attribution License (CC BY). The use, distribution or reproduction in other forums is permitted, provided the original author(s) and the copyright owner(s) are credited and that the original publication in this journal is cited, in accordance with accepted academic practice. No use, distribution or reproduction is permitted which does not comply with these terms.



The Impact of Total Variation Regularized Expectation Maximization Reconstruction on ^{68}Ga -DOTA-TATE PET/CT Images in Patients With Neuroendocrine Tumor

Lin Liu^{1,2,3†}, Hanxiang Liu^{1,2,3†}, Shijie Xu⁴, Shumao Zhang^{1,2,3}, Yi Tao^{1,2,3}, Greta S. P. Mok⁵ and Yue Chen^{1,2,3*}

¹ Department of Nuclear Medicine, The Affiliated Hospital of Southwest Medical University, Luzhou, China, ² Nuclear Medicine and Molecular Imaging Key Laboratory of Sichuan Province, Luzhou, China, ³ Academician (Expert) Workstation of Sichuan Province, Luzhou, China, ⁴ United Imaging Healthcare, Shanghai, China, ⁵ Biomedical Imaging Laboratory (BIG), Department of Electrical and Computer Engineering, Faculty of Science and Technology, University of Macau, Taipa, Macao SAR, China

OPEN ACCESS

Edited by:

Philipp Lohmann,
Institute of Neuroscience and
Medicine, Germany

Reviewed by:

Ismini C. Mainta,
Geneva University Hospitals
(HUG), Switzerland
Virginia Liberini,
University of Turin, Italy

*Correspondence:

Yue Chen
chenyue5523@126.com

[†]These authors have contributed
equally to this work

Specialty section:

This article was submitted to
Nuclear Medicine,
a section of the journal
Frontiers in Medicine

Received: 30 December 2021

Accepted: 16 February 2022

Published: 11 March 2022

Citation:

Liu L, Liu H, Xu S, Zhang S, Tao Y,
Mok GSP and Chen Y (2022) The
Impact of Total Variation Regularized
Expectation Maximization
Reconstruction on ^{68}Ga -DOTA-TATE
PET/CT Images in Patients With
Neuroendocrine Tumor.
Front. Med. 9:845806.
doi: 10.3389/fmed.2022.845806

Objective: The aim of this study was to investigate the effects of the total variation regularized expectation maximization (TVREM) reconstruction on improving ^{68}Ga -DOTA-TATE PET/CT images compared to the ordered subset expectation maximization (OSEM) reconstruction.

Method: A total of 17 patients with neuroendocrine tumors who underwent clinical ^{68}Ga -DOTA-TATE PET/CT were involved in this study retrospectively. The PET images were acquired with either 3 min-per-bed (min/bed) acquisition time and reconstructed with OSEM (2 iterations, 20 subsets, and a 3.2-mm Gaussian filter) and TVREM (seven penalization factors = 0.01, 0.07, 0.14, 0.21, 0.28, 0.35, and 0.42) for 2 and 3 min-per-bed (min/bed) acquisition time using list-mode. The SUV_{mean} of the liver, background variability (BV), signal-to-noise ratios (SNR), SUV_{max} of the lesions and tumor-to-background ratios (TBR) were measured. The mean percentage difference in the SNR and TBR between TVREM with difference penalization factors and OSEM was calculated. Qualitative image quality was evaluated by two experienced radiologists using a 5-point score scale (5-excellent, 1-poor).

Results: In total, 63 lesions were analyzed in this study. The SUV_{mean} of the liver did not differ significantly between TVREM and OSEM. The BV of all TVREM groups was lower than OSEM groups (all $p < 0.05$), and the BV of TVREM 2 min/bed group with penalization factor of 0.21 was considered comparable to OSEM 3 min/bed group ($p = 0.010$ and 0.006). The SNR, SUV_{max} and TBR were higher for all TVREM groups compared to OSEM groups (all $p < 0.05$). The mean percentage difference in the SNR and TBR was larger for small lesions ($< 10\text{mm}$) than that for medium ($\geq 10\text{mm}$ but $< 20\text{mm}$) and large lesions ($\geq 20\text{mm}$). The highest image quality score was given to TVREM 2 min/bed group with penalization factor of 0.21 (3.77 ± 0.26) and TVREM 3 min/bed group with penalization factor of 0.35 (3.77 ± 0.26).

Conclusion: TVREM could reduce image noise, improve the SNR, SUV_{max} and TBR of the lesions, and has the potential to preserve the image quality with shorter acquisition time.

Keywords: PET/CT, ^{68}Ga -DOTA-TATE, TVREM, OSEM, image quality

INTRODUCTION

Neuroendocrine tumors (NETs) are a heterogeneous group of cancers derived from the diffuse neuroendocrine system. Neuroendocrine cells are distributed in every organ, the primary NET may occur in any part of the human body, and therefore early diagnosis of NET is very important for treatment (1). NET's early diagnosis methods include multiple CT, MRI, and endoscopic ultrasound. However, the specificity and sensitivity of these methods to NET are not high. One of the characteristics of neuroendocrine tumors is the high expression of somatostatin receptors (SSTR) (2). SSTR-expression tends to correlate inversely with tumor grade and differentiation, and consequently, the role of SRI is more limited in high grade and particularly in poorly differentiated carcinomas (3). Different types of tumors, primary tumors at different locations, and tumors in different differentiation grades have different somatostatin receptors over-expressed. There are 5 somatostatin receptors (SSTR 1-5) widely expressed in both normal tissues and tumors. In most tumors, SSTR2 and 5 are usually over-expressed (4, 5). This expression enables imaging with high sensitivity using PET with radioactively labeled somatostatin analogs such as ^{68}Ga -DOTA-TATE. PET with ^{68}Ga -labeled somatostatin ligands is well-established as a tool for localizing the primary tumor in metastatic NET (6, 7).

The radionuclide, the performance of the equipment, and the reconstruction algorithm are important factors that affect the precise positioning of the lesion. Ordered subsets expectation maximization (OSEM) is the clinical standard reconstruction method. However, due to the special requirements for noise and reconstruction time in clinical applications, the iteration of OSEM must be stopped before converging. This always leads to underestimation of radio-tracer uptake and low contrast of the lesion. Bayesian penalized likelihood reconstruction (BPL) can reduce image noise and increase lesion contrast compared to OSEM reconstruction (8–10). Total variation regularized expectation maximization (TVREM), a new BPL algorithm, was introduced recently (HYPER Iterative, United Imaging Healthcare). Related studies have shown that TVREM algorithm in ^{68}Ga -PSMA imaging can ensure image quality while shortening the acquisition time (11). Therefore, as a BPL algorithm, TVREM has the potential to further increase the detection rate of lesions, shorten the acquisition time or reduce the dose (reduce administered dose) for ^{68}Ga -DOTA-TATE PET imaging.

The purpose of this research is to explore the effect of TVREM algorithm on ^{68}Ga -DOTA-TATE PET/CT image quality, and the possibility of shortening the acquisition time and reducing the radiation burden.

METHODS AND MATERIALS

Study Population

Between March 1st, 2021 and May 30th, 2021, 17 patients with neuroendocrine tumors undergoing ^{68}Ga -DOTA-TATE PET/CT were enrolled in this study retrospectively. The study was approved by the ethics committee of the Affiliated Hospital of Southwest Medical University and was in accordance with the 1964 Helsinki declaration and its later amendments. The informed consent of this retrospective study was waived.

Preparation of ^{68}Ga -DOTA-TATE

^{68}Ga stock solution was made by rinsing the ^{68}Ga generator using 4 mL of 0.05 mol/L hydrochloric acid. The pH value was adjusted to 3.5–4.0 with sodium acetate (0.25 mol/L). Twenty μg of DOTA-TATE (ABX, Germany) was added to the solution and mixed, which was then heated at 95°C for 10 min. The solution was first purified by a Sep-Pak C18 column, and then was filtered using a sterile filter to obtain ^{68}Ga -DOTA-TATE injection after washing the column with 50% ethanol solution and saline solution. The radiochemical purity was $>99\%$ analyzed by a radioactive high performance liquid chromatography (Radio-HPLC).

Image Acquisition

For ^{68}Ga -DOTA-TATE PET/CT imaging, the activity of intravenously injected according to the patients' weight ($2.04 \pm 0.19 \text{ MBq/kg}$). PET/CT images were acquired after 50–70 min of intravenous administration using a digital PET/CT scanner (uMI780, United Imaging Healthcare). A non-enhanced CT was used for attenuation correction of PET and anatomic localization. The CT parameters were as follows: 120 kV, 100 mAs, rotation of 0.8 s, and 3-mm slice thickness. After CT scanning, a whole-body PET scan was performed with 5–6 bed positions and 3 min/bed.

Attenuation corrected images were reconstructed with OSEM and TVREM. All images were reconstructed with time of flight (TOF), point spread function model (PSF), 600 mm field of view (FOV), 128×128 matrix, and slice thickness 3.0 mm. The OSEM reconstruction was performed with 2 iterations, 20 subsets and 3.2 mm of full width at half maximum (FWHM). Reconstruction with TVREM was performed with seven penalization factors: 0.01, 0.07, 0.14, 0.21, 0.28, 0.35, and 0.42. List-mode data were re-binned using the first 2 min/bed of the data and reconstructed with the same parameters.

In total, there were 16 groups of PET images in the final evaluation. We named these groups as OSEM_2 and OSEM_3 for OSEM with 2 and 3 min/bed; R201, R207, R214, R221, R228, R235, R242 for TVREM with different factors (0.01–0.42 for 2

min/bed) and R301-R342 for TVREM with factors (0.01–0.42 for 3 min/bed).

Clinical Studies Analysis

All the images were evaluated by an experienced nuclear medicine doctor with HERMES (HERMES, Stockholm, Sweden), and the regions of interest (ROI) were drawn on transaxial images around the tumor lesions to perform a semiquantitative analysis. A spherical (approximated 3 cm in diameter) in the right liver lobe was used as the activity background for each patient. The mean standardized uptake value (SUV_{mean}) and the standard deviation (SD) of liver were recorded. Background variability (BV) was used as parameter to evaluate the image noise level and calculated as follow:

$$BV = SD/\text{SUV}_{\text{mean}} \quad (1)$$

Maximum SUV (SUV_{max}) values of lesions were recorded. Signal-to-noise ratios (SNR) and tumor-to-background ratios (TBR) were calculated as follows:

$$\text{SNR} = (\text{SUV}_{\text{max}} \text{ of lesion})/BV \quad (2)$$

$$\text{TBR} = (\text{SUV}_{\text{max}} \text{ of lesion})/(\text{SUV}_{\text{mean}} \text{ of liver}) \quad (3)$$

Lesions were also divided and compared according to their size (diameter < 10 mm, ≥ 10 mm but < 20 mm, and ≥ 20 mm). The diameter of lesions were calculated as follows:

$$\text{diameter}_{\text{lesion}} = \sqrt[3]{(\text{Volume}_{\text{lesion}}/4\pi) \times 3 \times 2} \quad (4)$$

where the volume of lesions was measured on PET images.

Clinical Evaluation

Two experienced nuclear physicians evaluated the image quality of ^{68}Ga -DOTA-TATE PET images reconstructed using OSEM and TVREM independently on a commercial workstation (uWS-MI R004, United Imaging Healthcare). The nuclear physicians evaluated the images using a 5-point scale without knowing the reconstruction parameters (Table 1). The image of 5-point was with excellent image quality, almost free of noise, ideal contrast and sharp border. The image of 4-point was with good image quality, and its noise did not affect the identification and diagnosis of the lesion at all. The image of 3-point was with moderate image quality, obvious noise, and sufficient lesion delineation to make a diagnosis. The image of 2-point was barely acceptable, and the noise was large, which affected the diagnosis. The image of 1-point had the worst image quality and could not be used for diagnosis at all.

Statistical Analysis

SPSS 22.0 statistical analysis software (IBM, Armonk, NY, USA) was used for statistical analysis, and Graphpad8.0 was used for graphing. The data were presented as mean \pm SD. The SUV of OSEM_3 was served as the reference for the comparison between different reconstruction groups. Shapiro-Wilk test were used to test the normal distribution of data. Paired samples were

TABLE 1 | The 5-point scale of image quality.

Scores	Descriptions
5	Excellent image quality, almost free of noise, ideal contrast and sharp border
4	Good image quality, and its noise did not affect the identification and diagnosis of the lesion at all
3	Moderate image quality, obvious noise, and sufficient lesion delineation to make a diagnosis
2	Barely acceptable, and the noise was large, which affected the diagnosis
1	The worst image quality and could not be used for diagnosis at all

compared using the Wilcoxon signed-rank test and paired *t*-test. The inter-evaluator agreement was measured by Cohen's κ . A *p* < 0.05 was considered significant.

RESULTS

A total of 17 patients (7 women and 10 men; mean age \pm SD, 48 \pm 17 years) with suspicion and diagnosis of NET were enrolled and the presence of lesions was confirmed by CT, MRI, ^{18}F -FDG PET and biochemical evidence of NETs. The characteristics of the study population were summarized in Table 2.

Lesion Analysis

In total, 63 lesions were identified in both reconstructions. The lesions' diameter ranged from 7.0 to 60.0 mm. The mean values of SUV_{mean} were not significant different between TVREM and OSEM (all *p* > 0.80). The mean values of BV in OSEM_2 and OSEM_3 were $8.2 \pm 1.9\%$ and $7.2 \pm 1.9\%$, the BV in TVREM groups decreased with the increase of penalization factors and the BV of R221 group was considered comparable to OSEM_3. The SUV_{max} , SNR, and TBR were higher in all TVREM groups than OSEM (all *p* < 0.05). The SNR increased with the increase of penalization factor. Moreover, the SUV_{max} and TBR of the lesions decreased as the penalization factors increased (Table 3).

Figure 1 shows the results of lesions SNR and TBR. When lesions were divided into different groups according to their sizes, the SNR of small lesions (<10 mm) in most TVREM groups for 2 min/bed were higher than OSEM_3 significantly (all *p* < 0.05) except for R201 (*p* = 0.25), and the TBR of small lesions (<10 mm) in all TVREM groups were higher than OSEM significantly (all *p* < 0.05).

For medium lesions (≥ 10 mm but < 20 mm), there were not significant differences in the SNR between most TVREM groups and OSEM_3 except for R235 (*p* = 0.02) and R242 (*p* = 0.01), and the SNR of R214 was considered comparable to OSEM_3. The TBR of lesions in TVREM were higher than OSEM_3 significantly (all *p* < 0.05) except for R228 (*p* = 0.05), R235 (*p* = 0.06), and R242 (*p* = 0.07).

TABLE 2 | Characteristics of study population.

Patient number	Age (years)	Gender	Tumor location	Ki-67	NET grade	The number of lesions
1	47	F	Pancreas NET	3%	G2	7
2	44	F	Adrenal pheochromocytoma	20%	G2	7
3	38	M	Adrenal pheochromocytoma	8%	G2	5
4	57	M	Pancreas NET	5%	G2	7
5	38	F	CBT	3%	G2	7
6	31	F	Pancreas NET	10%	G2	3
7	34	M	Pancreas NET	10%	G2	1
8	48	M	Pancreas NET	6%	G2	3
9	27	F	Pancreas NET	2%	G2	2
10	30	M	Pelvic NET	8%	G2	7
11	64	F	Pancreas NET	1%	G1	2
12	15	F	Hypophysoma	10%	G2	1
13	63	M	Pheochromocytoma	12%	G2	1
14	67	M	Highly differentiated neuroendocrine tumor of the left laryngeal wall	10%	G2	1
15	73	M	Mediastinal NET	80–90%	G3	2
16	66	M	Small cell NET of the left neck	40%	G3	4
17	75	M	Left groin NET	20%	G2	3

NET, neuroendocrine tumor; CBT, carotid body tumor.

TABLE 3 | SUV_{mean} , background variability, SUV_{max} , SNR and TBR of the clinical study.

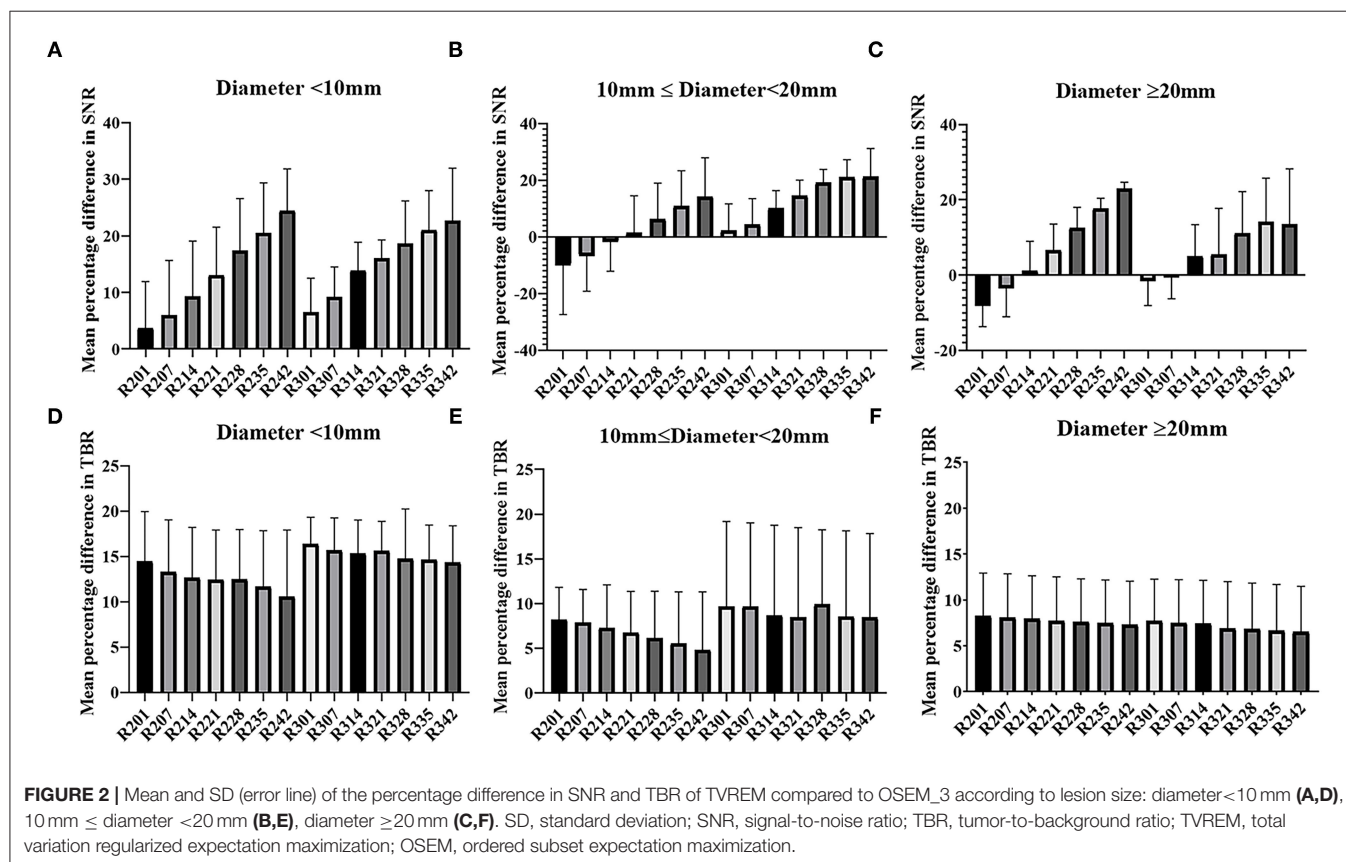
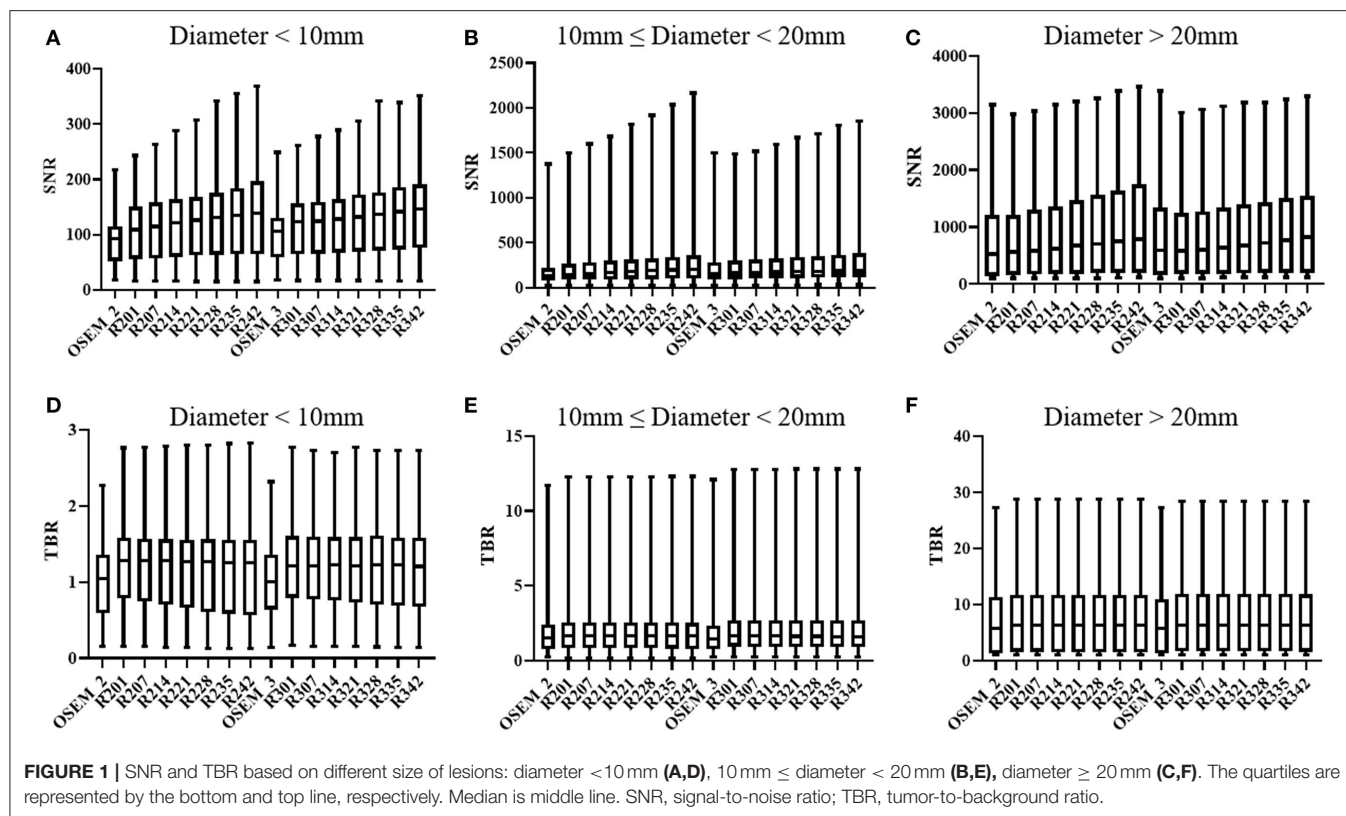
	Background SUV_{mean}	Background variability %	SUV_{max}	SNR	TBR
OSEM_2	7.62	8%	19.06	268.20	2.62
R201	7.56	8%	20.82	281.92	2.88
R207	7.56	8%	20.78	294.46	2.87
R214	7.57	8%	20.73	309.71	2.86
R221	7.57	7%	20.68	325.63	2.85
R228	7.60	7%	20.63	341.02	2.85
R235	7.60	7%	20.57	357.25	2.84
R242	7.60	6%	20.53	373.98	2.83
OSEM_3	7.56	7%	18.94	297.89	2.61
R301	7.61	8%	20.98	299.67	2.89
R307	7.61	8%	20.95	305.71	2.89
R314	7.58	7%	20.92	317.58	2.88
R321	7.58	7%	20.89	329.07	2.88
R328	7.62	7%	20.90	339.40	2.88
R335	7.61	7%	20.85	352.69	2.88
R342	7.61	6%	20.81	364.06	2.87

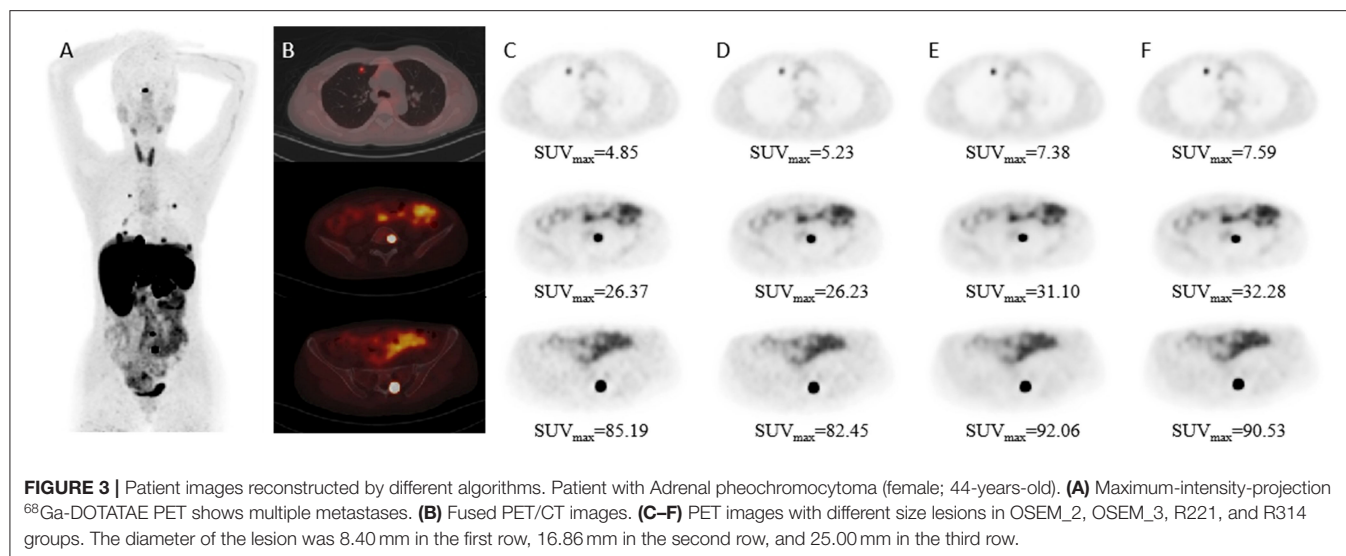
SUV, standardized uptake value; SNR, signal-to-noise ratio; TBR, tumor-to-background ratio.

For large lesions (≥ 20 mm), there were not significantly differences in the SNR and TBR between TVREM groups and OSEM_3 (all $p > 0.05$).

The mean percentage difference in the SNR and TBR between TVREM with difference penalization factors and OSEM_3 were shown in **Figure 2**. The mean percentage

difference in the SNR of R242 was $19.25 \pm 22.76\%$ for small lesions, $12.79 \pm 18.40\%$ for medium lesions, and $18.13\% \pm 9.80\%$ for large lesions compared to OSEM_3. The mean percentage difference in the TBR of R201 was $14.31 \pm 9.66\%$ for small lesions, $8.06 \pm 8.65\%$ for medium lesions, and $8.88 \pm 7.41\%$ for large lesions compared to OSEM_3. A





representative case for lesions with different sizes is shown in **Figure 3**.

The results of subject evaluation for image quality were shown in **Figure 4**. The image quality scores of all the TVREM groups were higher than OSEM groups. R221 and R228 had higher image quality scores compared to OSEM_3 ($p = 0.010$ and 0.006), and the image quality scores of R328, R335, and R342 were significantly higher than OSEM_3 ($p = 0.019$, 0.004 and 0.029). The highest score was given to R221 (3.77 ± 0.26) in 2 min/bed groups and R335 (3.77 ± 0.26) in 3 min/bed groups. In all reconstruction series, the Kappa value of 0.45 indicated moderate reliability.

DISCUSSION

In our study, we evaluated the impact of TVREM on the image quality of ^{68}Ga -DOTA-TATE. There was no significant difference in the liver SUV_{mean} between TVREM and OSEM, and TVREM showed a significant improvement of SNR and TBR compared to OSEM, especially for small lesions with diameter <10 mm. Moreover, we found that SUV_{max} values in TVREM were higher than that in OSEM significantly. TVREM with a penalization factor of 0.14 and 2 min/bed acquisition time could provide equivalent image quality compared to OSEM with 3 min/bed acquisition time.

It has been shown that BPL provided better image quality without affecting the background liver uptake and improved the lesions conspicuity (12, 13). Yoshie et al. showed that BPL reconstruction significantly improved the detection of small inconspicuous malignant tumors (diameter <10 mm) in the lung and improved the diagnostic performance of PET/CT (14). In our study, the results showed that the SNR and TBR of small lesions (diameter <10 mm) increased more than 3 and 6% in all TVREM groups compared to OSEM 3 min/bed. Those results were partly consistent with a previous study by

Ewa et al. in which showed that BPL SUVs and TBR tend to be higher for small lesions (9). In addition, the SUV_{max} of lesions in our study decreased with the increase of penalization factor, which was consistent with a previous study using ^{18}F -FDG PET/CT (15).

The capability of BPL algorithm of shortening acquisition time was reported in several studies (16, 17). A phantom and clinical study by Yang et al. showed that TVREM could improve the lesion contrast and lower image noise of ^{68}Ga -PSMA-11 PET/CT compared to OSEM and enable a fast acquisition with 2 min/bed with preserved image quality (10). Similarly, the results in our study showed that a penalization factor between 0.21 and 0.42 for TVREM with 2 min/bed acquisition time could attain equivalent or lower noise compared to OSEM with 3 min/bed acquisition time.

New image reconstruction methods could help in clinical practice by reducing acquisition times while maintaining accuracy (18), getting better image quality in obese patients (19), improving accurately identify of very small lesions (20), and underpinning the use of further new tools such as data driven gating which can help to differentiate malignant lesions from benign structures and injuries (21). And the most accurate reconstruction factor were likely depending on the count statistics and uptake pattern vary between the radionuclide and radiopharmaceutical (22). In our subjective evaluation, the image quality was assessed using a 5-grade scale by two radiologists. Our results showed that the higher quality score was given to TVREM groups with the penalization factor ranged from 0.14 to 0.35 for 2 and 3 min/bed acquisition. In our study, the image noise and TBR decreased with the increase of penalization factor. Although the increase of the penalization factor could reduce more noise, it could also reduce the contrast of the lesion, which was reflected in the lower image quality scores of the high-level penalization factor groups.

Our study has some limitations. First, the patient population was relatively small; a larger and multicenter study should

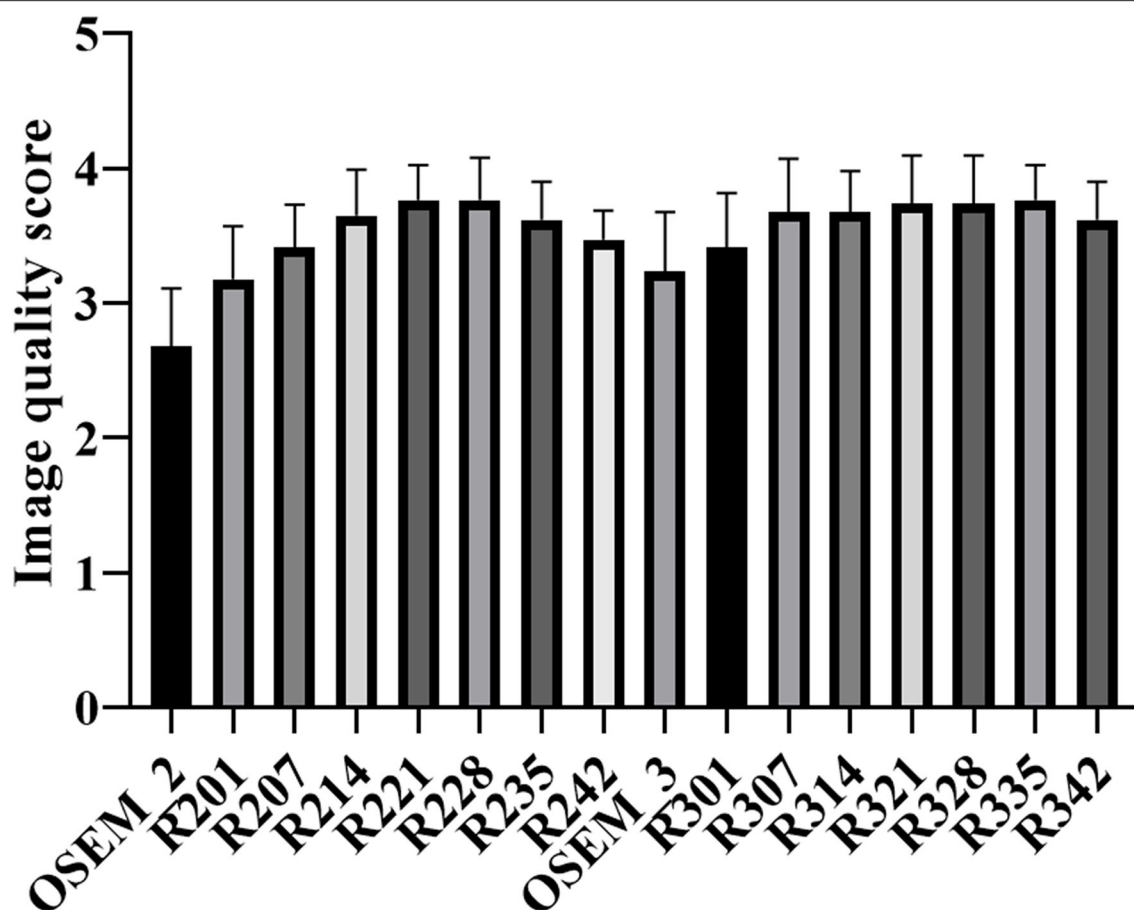


FIGURE 4 | The mean and standard deviation (error bar) of the image quality score for TVREM and OSEM groups. The highest score was given to R221 and R335 for 2 and 3 min/bed acquisition. TVREM, total variation regularized expectation maximization; OSEM, ordered subset expectation maximization.

be involved in the future. Second, the experience of two radiologists who evaluated the images were different, and the agreement was not very high. Furthermore, there was no pathologic confirmation of most lesions. The biopsy results should be used to investigate whether the TVREM could improve the detection rate of lesion in further studies.

CONCLUSION

TVREM reconstruction algorithm can improve the SUV_{max} , SNR and TBR and lower image noise of ^{68}Ga -DOTA-TATE compared to OSEM, especially for small lesions <10 mm in diameter. TVREM has the potential to preserve image quality in short acquisition time with penalization factors ranged from 0.14 to 0.35.

DATA AVAILABILITY STATEMENT

The raw data supporting the conclusions of this article will be made available by the authors, without undue reservation.

ETHICS STATEMENT

The studies involving human participants were reviewed and approved by the Affiliated Hospital of Southwest Medical University. The patients/participants provided their written informed consent to participate in this study.

AUTHOR CONTRIBUTIONS

LL conducted statistical analyses. LL and HL drafted the manuscript. SX, SZ, and YT collected cases. GM and YC provided critical review of the manuscript for key intellectual content. YC is the guarantor and as such, had full access to the data, and takes responsibility for its integrity and accuracy. All authors conceived and designed the study, interpreted the findings, and approved the final manuscript.

ACKNOWLEDGMENTS

We are grateful to all the nuclear medicine professionals in the Affiliated Hospital of Southwest Medical University who helped with this research.

REFERENCES

- Caplin ME, Buscombe JR, Hilson AJ, Jones AL, Watkinson AF, Burroughs AK. Carcinoid tumour. *Lancet*. (1998) 352:799–805. doi: 10.1016/S0140-6736(98)02286-7
- Pelosi G, Volante M, Papotti M, Sonzogni A, Masullo M, Viale G. Peptide receptors in neuroendocrine tumors of the lung as potential tools for radionuclide diagnosis and therapy. *Q J Nucl Med Mol Imaging*. (2006) 50:272–87.
- Haider M, Al-Toubah T, El-Haddad G, Strosberg J. Molecular imaging and radionuclide therapy of neuroendocrine tumors. *Curr Opin Endocrinol Diabetes Obes*. (2020) 27:16–21. doi: 10.1097/MED.0000000000000519
- Reubi JC, Schär JC, Waser B, Wenger S, Heppeler A, Schmitt JS, et al. Affinity profiles for human somatostatin receptor subtypes SST1–SST5 of somatostatin radiotracers selected for scintigraphic and radiotherapeutic use. *Eur J Nucl Med*. (2000) 27:273–82. doi: 10.1007/s002590050034
- Hoyer D, Bell GL, Berelowitz M, et al. Classification and nomenclature of somatostatin receptors. *Trends Pharmacol Sci*. (1995) 16:86–8. doi: 10.1016/S0165-6147(00)88988-9
- Breeman W, Blois ED, Chan HS, Epelbaum J, Feniuk W, Humphrey PPA, et al. 68Ga-labeled DOTA-peptides and 68Ga-labeled radiopharmaceuticals for positron emission tomography: current status of research, clinical applications, and future perspectives. *Semin Nucl Med*. (2011) 41:314–21. doi: 10.1053/j.semnuclmed.2011.02.001
- Haug AR, Cindea-Drimus R, Auernhammer CJ, Reincke M, Wängler B, Uebleis C, et al. The role of 68Ga-DOTATATE PET/CT in suspected neuroendocrine tumors. *J Nucl Med*. (2012) 53:1686–92. doi: 10.2967/jnumed.111.101675
- Teoh EJ, McGowan DR, Macpherson RE, Bradley KM, Gleeson FV. Phantom and clinical evaluation of the Bayesian penalized likelihood reconstruction algorithm Q. Clear on an LYSO PET/CT system. *J Nucl Med*. (2015) 56:1447–522. doi: 10.2967/jnumed.115.159301
- Spasic E, Jehanno N, Gomes SB, Huchet V, Luporsi M, Mounat TC. Phantom and clinical evaluation for new PET/CT reconstruction algorithm: Bayesian penalized likelihood reconstruction algorithm Q. Clear. *J Nucl Med Radiat Ther*. (2018) 9:371. doi: 10.4172/2155-9619.1000371
- Witkowska-Patena E, Budzyńska A, Gizewska A, Dziuk M, Walecka-Mazur A. Ordered subset expectation maximization vs Bayesian penalised likelihood reconstruction algorithm in 18F-PSMA-1007 PET/CT. *Ann Nucl Med*. (2020) 34:192–9. doi: 10.1007/s12149-019-01433-x
- Yang FJ, Ai SY, Wu R, Lv Y, Xie HF, Dong Y, et al. Impact of total variation regularized expectation maximization reconstruction on the image quality of 68Ga-PSMA PET: a phantom and patient study. *Br J Radiol*. (2021) 94:20201356. doi: 10.1259/bjr.20201356
- Ahn S, Ross SG, Asma E, Miao J, Jin X, Cheng L, et al. Quantitative comparison of OSEM and penalized likelihood image reconstruction using relative difference penalties for clinical PET. *Phys Med Biol*. (2015) 60:5733–51. doi: 10.1088/0031-9155/60/15/5733
- Rogasch JM, Suleiman S, Hofheinz F, Bluemel S, Lukas M, Amthauer H, et al. Reconstructed spatial resolution and contrast recovery with Bayesian penalized likelihood reconstruction (QClear) for FDG-PET compared to time-of-flight (TOF) with point spread function (PSF). *EJNMMI Phys*. (2020) 7:2. doi: 10.1186/s40658-020-0270-y
- Kurita Y, Ichikawa Y, Nakanishi T, Tomita Y, Hasegawa D, Murashima S, et al. The value of Bayesian penalized likelihood reconstruction for improving lesion conspicuity of malignant lung tumors on 18F-FDG PET/CT: comparison with ordered subset expectation maximization reconstruction incorporating time-of-flight model and point spread function correction. *Ann Nucl Med*. (2020) 34:272–9. doi: 10.1007/s12149-020-01446-x
- Ter Voert EEGW, Muehlematter UJ, Delso G, Pizzuto DA, Müller J, Nagel HW, et al. Quantitative performance and optimal regularization parameter in block sequential regularized expectation maximization reconstructions in clinical 68Ga-PSMA PET/MR. *EJNMMI Res*. (2018) 8:70. doi: 10.1186/s13550-018-0414-4
- Lindstrom E, Sundin A, Trampal C, Lindsjö L, Ilan E, Danfors T, et al. Evaluation of penalized-likelihood estimation reconstruction on a digital time-of-flight PET/CT scanner for 18F-FDG whole-body examinations. *J Nucl Med*. (2018) 59:1152–8. doi: 10.2967/jnumed.117.200790
- Yoshii T, Miwa K, Yamaguchi M, Shimada K, Wagatsuma K, Yamao T, et al. Optimization of a Bayesian penalized likelihood algorithm (QClear) for 18F-NaF bone PET/CT images acquired over shorter durations using a custom-designed phantom. *EJNMMI Phys*. (2020) 7:56. doi: 10.1186/s40658-020-00325-8
- Chicheportiche A, Goshen E, Godefroy J, Grozinsky-Glasberg S, Oleinikov K, Meirovitz A, et al. Can a penalized-likelihood estimation algorithm be used to reduce the injected dose or the acquisition time in 68Ga-DOTATATE PET/CT studies? *EJNMMI Phys*. (2021) 8:13. doi: 10.1186/s40658-021-00359-6
- Zanoni L, Argalia G, Fortunati E, Malizia C, Allegri V, Calabrò D, et al. Can Q. clear reconstruction be used to improve [68 Ga]Ga-DOTANOC PET/CT image quality in overweight NEN patients? *Eur J Nucl Med Mol Imaging*. (2021). doi: 10.1007/s00259-021-05592-w. [In press].
- Liberini V, Messerli M, Husmann L, Kudura K, Grünig H, Maurer A, et al. Improved detection of in-transit metastases of malignant melanoma with BSREM reconstruction in digital [18F]FDG PET/CT. *Eur Radiol*. (2021) 31:8011–20. doi: 10.1007/s00330-021-07852-7
- Liberini V, Kotasidis F, Treyer V, Messerli M, Orita E, Engel-Bicik I, et al. Impact of PET data driven respiratory motion correction and BSREM reconstruction of 68Ga-DOTATATE PET/CT for differentiating neuroendocrine tumors (NET) and intrapancreatic accessory spleens (IPAS). *Sci Rep*. (2021) 11:2273. doi: 10.1038/s41598-020-80855-4
- Lindström E, Lindsjö L, Sundin A, Sörensen J, Lubberink M. Evaluation of block-sequential regularized expectation maximization reconstruction of 68Ga-DOTATOC, 18F-fluoride, and 11C-acetate whole-body examinations acquired on a digital time-of-flight PET/CT scanner. *EJNMMI Phys*. (2020) 7:40. doi: 10.1186/s40658-020-00310-1

Conflict of Interest: SX is employed by Shanghai United Imaging Healthcare Co., Ltd.

The remaining authors declare that the research was conducted in the absence of any commercial or financial relationships that could be construed as a potential conflict of interest.

Publisher's Note: All claims expressed in this article are solely those of the authors and do not necessarily represent those of their affiliated organizations, or those of the publisher, the editors and the reviewers. Any product that may be evaluated in this article, or claim that may be made by its manufacturer, is not guaranteed or endorsed by the publisher.

Copyright © 2022 Liu, Liu, Xu, Zhang, Tao, Mok and Chen. This is an open-access article distributed under the terms of the Creative Commons Attribution License (CC BY). The use, distribution or reproduction in other forums is permitted, provided the original author(s) and the copyright owner(s) are credited and that the original publication in this journal is cited, in accordance with accepted academic practice. No use, distribution or reproduction is permitted which does not comply with these terms.



Differentiation Between Malignant and Benign Pulmonary Nodules by Using Automated Three-Dimensional High-Resolution Representation Learning With Fluorodeoxyglucose Positron Emission Tomography-Computed Tomography

OPEN ACCESS

Edited by:

Yiyang Liu,

University of Louisville, United States

Reviewed by:

Luca Camoni,

University of Brescia, Italy

Giorgio Treglia,

Ente Ospedaliero Cantonale (EOC),

Switzerland

Salvatore Annunziata,

Fondazione Policlinico Universitario A.

Gemelli IRCCS, Italy

*Correspondence:

Chia-Hung Kao

D10040@mail.cmuh.org.tw;

dr.kaochiahung@gmail.com

† These authors have contributed
equally to this work

Specialty section:

This article was submitted to

Nuclear Medicine,

a section of the journal

Frontiers in Medicine

Received: 09 September 2021

Accepted: 14 February 2022

Published: 18 March 2022

Citation:

Lai Y-C, Wu K-C, Tseng N-C,

Chen Y-J, Chang C-J, Yen K-Y and

Kao C-H (2022) Differentiation

Between Malignant and Benign

Pulmonary Nodules by Using

Automated Three-Dimensional

High-Resolution Representation

Learning With Fluorodeoxyglucose

Positron Emission

Tomography-Computed Tomography.

Front. Med. 9:773041.

doi: 10.3389/fmed.2022.773041

Yung-Chi Lai^{1†}, Kuo-Chen Wu^{2,3}, Neng-Chuan Tseng^{4†}, Yi-Jin Chen³, Chao-Jen Chang³,
Kuo-Yang Yen^{1,5} and Chia-Hung Kao^{1,3,6,7*}

¹ Department of Nuclear Medicine, PET Center, China Medical University Hospital, Taichung, Taiwan, ² Graduate Institute of Biomedical Electronics and Bioinformatics, National Taiwan University, Taipei, Taiwan, ³ Center of Augmented Intelligence in Healthcare, China Medical University Hospital, Taichung, Taiwan, ⁴ Division of Nuclear Medicine, Tungs' Taichung MetroHarbor Hospital, Taichung, Taiwan, ⁵ Department of Biomedical Imaging and Radiological Science, School of Medicine, College of Medicine, China Medical University, Taichung, Taiwan, ⁶ Graduate Institute of Biomedical Sciences, College of Medicine, China Medical University, Taichung, Taiwan, ⁷ Department of Bioinformatics and Medical Engineering, Asia University, Taichung, Taiwan

Background: The investigation of incidental pulmonary nodules has rapidly become one of the main indications for 18F-fluorodeoxyglucose (FDG) positron emission tomography (PET), currently combined with computed tomography (PET-CT). There is also a growing trend to use artificial Intelligence for optimization and interpretation of PET-CT Images. Therefore, we proposed a novel deep learning model that aided in the automatic differentiation between malignant and benign pulmonary nodules on FDG PET-CT.

Methods: In total, 112 participants with pulmonary nodules who underwent FDG PET-CT before surgery were enrolled retrospectively. We designed a novel deep learning three-dimensional (3D) high-resolution representation learning (HRRL) model for the automated classification of pulmonary nodules based on FDG PET-CT images without manual annotation by experts. For the images to be localized more precisely, we defined the territories of the lungs through a novel artificial intelligence-driven image-processing algorithm, instead of the conventional segmentation method, without the aid of an expert; this algorithm is based on deep HRRL, which is used to perform high-resolution classification. In addition, the 2D model was converted to a 3D model.

Results: All pulmonary lesions were confirmed through pathological studies (79 malignant and 33 benign). We evaluated its diagnostic performance in the differentiation of malignant and benign nodules. The area under the receiver operating characteristic

curve (AUC) of the deep learning model was used to indicate classification performance in an evaluation using fivefold cross-validation. The nodule-based prediction performance of the model had an AUC, sensitivity, specificity, and accuracy of 78.1, 89.9, 54.5, and 79.4%, respectively.

Conclusion: Our results suggest that a deep learning algorithm using HRRL without manual annotation from experts might aid in the classification of pulmonary nodules discovered through clinical FDG PET-CT images.

Keywords: pulmonary nodules, 3D high-resolution representation learning, fluorodeoxyglucose (FDG), positron emission tomography-computed tomography (PET-CT), operating characteristic curve (AUC), artificial intelligence, deep learning

INTRODUCTION

Lung cancers usually present as either abnormal lung masses or small pulmonary nodules on chest computed tomography (CT) images and are the leading cause of cancer deaths worldwide, including in Taiwan. Several guidelines have stipulated that patients at high risk must undergo annual screening with low-dose CT scanning for pulmonary nodules to be more easily discovered (1–6). These incidentally detected pulmonary nodules could be benign or malignant (7), and differentiating between them is challenging for clinical physicians. Understanding the nature of these pulmonary nodules is crucial because it has vital implications in both therapeutic and prognostic areas. Fluorodeoxyglucose-positron emission tomography (FDG PET) has played a crucial role in the diagnosis of indeterminate pulmonary nodules with CT imaging. FDG PET detects malignancy based on the high FDG uptake, which reflects the increased glucose metabolic activity of cancer cells. Traditionally, a standardized uptake value of 2.5 has been used as a threshold to differentiate between malignant and benign nodules (8, 9). There is evidence showing that dual time point (18)F-FDG PET imaging is an important non-invasive method for the differentiation of malignant and non-malignant lesions (10–13). For instance, the sequential dual-time-point [18F]FDG PET-CT examinations may increase the sensitivity and the specificity of the PET-CT method in differential palatine tonsils diagnosis according to Pietrzak et al. (11). In addition, PET is typically used as an adjunct to CT in the evaluation of suggestive nodules (11, 14–16). However, FDG PET has several intrinsic limitations in differentiating lesions with extreme metabolic rate, leading to false positives or false negatives (17). In addition, many researchers reported that ground-glass nodules with minor metabolic activities and lower SUVmax might have a high malignancy potential (18).

Artificial intelligence (AI) algorithms based on convolutional neural networks have been increasingly applied in cross-domain image translation (19). According to previous studies, machine learning (ML) models can help in detection, differentiation from benign lesions, segmentation, staging, response assessment, and prognosis determination. More specifically, researchers have found that FDG-PET-CT metrics and radiomics features had a significant role in predicting the final diagnosis of solitary pulmonary nodules (20–22).

Conventional radiographic findings that are suggestive of benignity or malignancy include size, density, stability over time, margin appearance, wall thickness, and the presence of cavitation and calcification. According to several previous studies, uptake parameters from FDG PET have shown good diagnostic performance (accuracy between 65 and 91%) (23–28) with potential improvements coming from the characterization of uptake heterogeneity. However, a meta-analysis (29) suggested that FDG PET-CT showed insufficient sensitivity and specificity for diagnosing malignant solitary pulmonary nodules; it cannot replace the “gold standard” pathology by either resection or percutaneous biopsy. Therefore, we planned not to use traditional imaging features to differentiate benign from malignant pulmonary nodules in this study. Instead, we hoped to utilize deep learning methods that learn these features directly from data, without the need of hand-engineered feature extraction from inputs (20–22, 30).

Some of the most remarkable results of AI algorithms have been produced by systems that aid in medical image diagnoses. Several state-of-the-art AI models, such as Visual Geometry Group (VGG) and ResNet, are widely used in nuclear medical imaging (31). These algorithms take advantage of stride and pooling to downsize the feature maps, which are done prior to input from a classifier. However, the aforementioned methods result in the loss of intrinsic high-resolution information of medical images. This study aimed to use high-resolution representation learning (HRRL) as the AI algorithm to retain the high-resolution imaging features, without any stride or pooling, to reserve the size of the images (32). Therefore, we implemented automated HRRL without manual annotation by an expert as the deep learning approach to aid in the differential diagnoses of FDG PET-CT scanning for pulmonary nodules.

MATERIALS AND METHODS

Patients

A total of 112 consecutive cases of eligible patients (age range 29–85 years; mean age 62.28) with pulmonary nodules (PN) were enrolled in this retrospective study from 30 December 2008 through 30 July 2010 at China Medical University Hospital. Patients were selected for this study according to the following criteria: (a) underwent integrated FDG PET-CT and (b) had

definitive diagnosis determined by surgical pathology (**Figure 1**). The final study group of 112 patients comprised 60 men and 52 women. Overall, pulmonary nodules detected by CT of the chest were divided into two groups (i.e., benign and malignant) as diagnosed by surgical pathology (**Table 1**). The first group comprised 33 benign nodules (mean diameter: 24.88 ± 16.49 mm), 4 of them were ground-glass nodules (GGN) and the other 29 were solid nodules. The second group comprised 79 malignant nodules (mean diameter: 29.86 ± 18.99 mm), 12 of them were GGN and the other 67 were solid nodules. The imaging and clinical data of these patients were reviewed and analyzed retrospectively. This study was approved by the Ethics Committee of our hospital [DMR99-IRB-010-(CR-12)].

Fluorodeoxyglucose Positron Emission Tomography-Computed Tomography Imaging Protocol

All patients were asked to fast for at least 4 h before FDG PET-CT imaging. Imaging was performed with a PET-CT scanner (Discovery STE, GE Medical Systems, Milwaukee, WI, United States). Whole-body FDG PET-CT images were acquired approximately 45 min after intravenous injection of 370 MBq (10 mCi) of FDG. Delayed FDG PET-CT images were obtained approximately 70 min after FDG injection (33–35). In this study, however, we only adopted the delayed FDG PET-CT images for further preprocessing and input to the deep learning models. PET emission images were acquired after CT scans at 2 min per field of view in the three-dimensional acquisition mode. The CT images were reconstructed onto a 512×512 matrix with a section thickness of 3.75 mm, reconstructed onto a 128×128 matrix, and converted into 511 keV equivalent attenuation factors for attenuation correction of the corresponding PET emission images. The maximum SUVmax of lung nodules on early and delayed FDG PET-CT images were measured.

Preprocessing for Automated Models

We defined each patient's lung territories by using the mediastinal window on the CT images. The CT mediastinal window level (WL) was 40, and the window width (WW) was 400. Therefore, values less than -160 were rendered entirely black, and values >240 were rendered entirely white (**Figure 2A**). Under this setting, the tracheal lumen and lung parenchyma appeared to be almost black. Such an image preprocessing can help the program automatically determine which trans-axial slice of image is the upper edge of the lung parenchyma. The lungs were indicated by the presence of air.

In order to accurately determine the contour of bilateral lung regions, the body block must be found first. This study used the Python Open Source Computer Vision Library (OpenCV) package. It comes free with a cross-platform program and can execute a few functions, such as finding contours. The contour function can perform threshold calculations for grayscale images or customize the threshold of the cutting block to optimize the contour finding function. In this study, we used the contour function of the OpenCV package to identify all the contours on the CT images (**Figure 2B**).

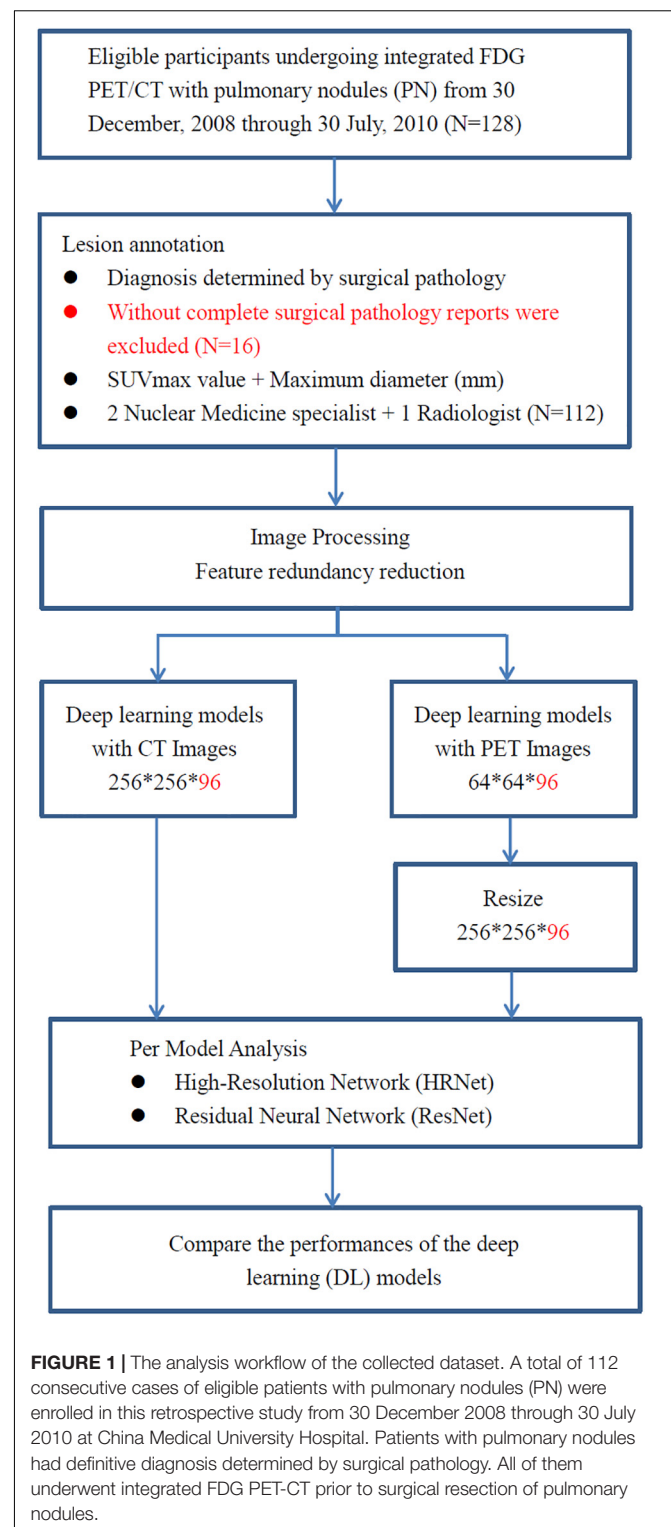


FIGURE 1 | The analysis workflow of the collected dataset. A total of 112 consecutive cases of eligible patients with pulmonary nodules (PN) were enrolled in this retrospective study from 30 December 2008 through 30 July 2010 at China Medical University Hospital. Patients with pulmonary nodules had definitive diagnosis determined by surgical pathology. All of them underwent integrated FDG PET-CT prior to surgical resection of pulmonary nodules.

When identifying the contour block of CT images in OpenCV, determining the contour block of the body is essential. The contour area of the body can be determined according to the center of gravity and the size of the contour area (**Figure 2C**). A contour area with its center of gravity biased toward

TABLE 1 | Patient characteristics.

Patient	Benign	Malignant	P-value
Sex			
Male	21	39	0.120
Female	12	40	
Age			
Age, mean (years) ^b	58.55 ± 13.31	63.84 ± 11.60	0.038*
Age, range (years)	29–85	39–82	
Pathology of pulmonary nodules (PNs)			
Diameter, means (mm) ^b	24.88 ± 16.49	29.86 ± 18.99	0.192
Early maximum SUV ^b	2.97 ± 3.30	5.20 ± 3.80	0.004*
Delayed maximum SUV ^b	3.45 ± 3.82	6.13 ± 4.56	0.002*
Solid/GGN ^a	29/4	67/12	0.775
Total	33 (29.46)	79 (70.54)	

PNs, pulmonary nodules; Excluded, without surgical pathology reports; GGN, ground-glass nodules.

^aChi-square (χ^2) test.

^bStudent's t-test.

*The p-value of <0.05 was considered statistically.

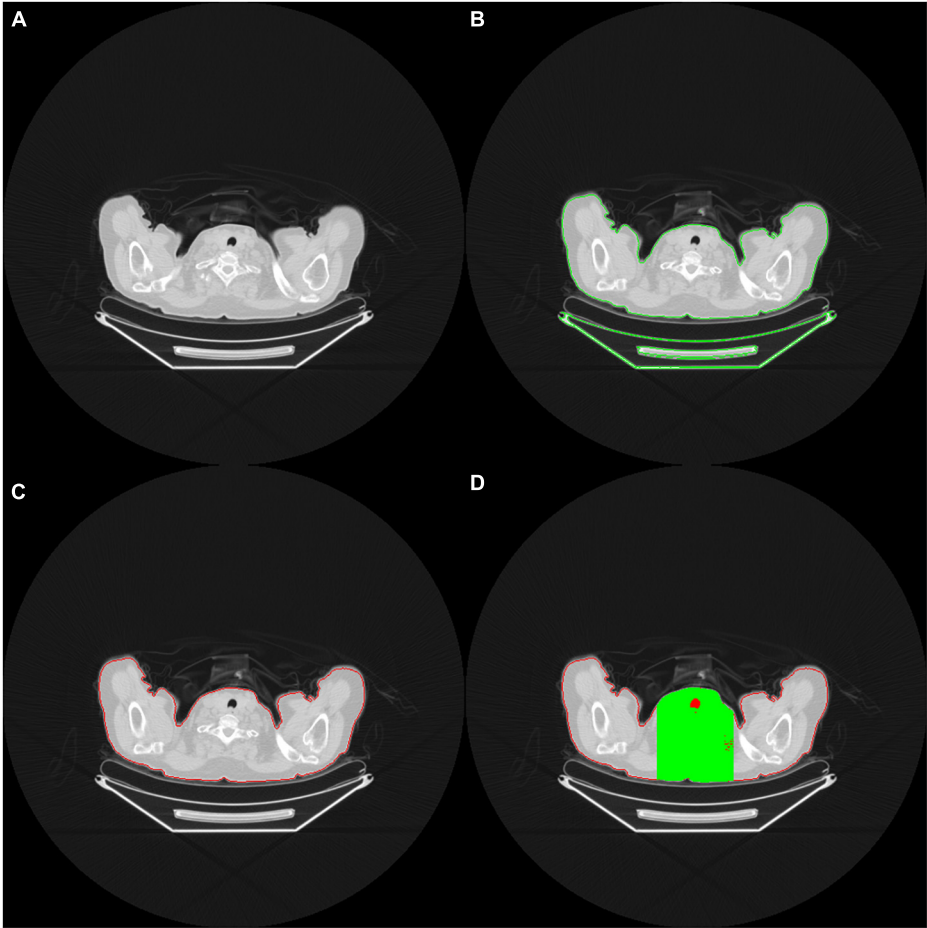


FIGURE 2 | (A) The red contour delineates the air (black area) within the tracheal lumen, which helps the program determine the upper edge of the lungs (B) OpenCV identifies the contour area of the body on the CT images (C) Body contour block (red contour block) (D) Green area indicates the limited calculation area. Only the black area in the green range is included in the calculation of the ratio.

the edge area or with an overly small size is generally not the main body area.

After identifying the body contour area, we determined the upper edge of the lung parenchyma within the body area. As we viewed the consecutive trans-axial slices of the CT images from the top to the bottom, the lung parenchyma usually begins at the level where the air (i.e., black area) does. When the black area of the uppermost lung air exceeds a certain percentage (e.g., 5%) of the body block area, the block is adopted as the starting level of the lungs. However, in this circumstance, the presence of some unusual, poor quality CT images results in the presence of many hollow black areas in the body contour block, which may cause errors in the capture. Therefore, to determine the area of the body block accurately, we took the center of the images as the starting point and extended to the left and right of it until the framed area was 33% of the body block area. The derived region (marked in green on **Figure 2D**) was then defined as the calculation region of interest, and only the black area (i.e., air) within that region (marked in red on **Figure 2D**) was subsequently adopted for further calculation. When the proportion of air exceeded a particular proportion (e.g., 5% of the body block area), the trans-axial slice of that image was regarded as depicting the upper edge of the lung parenchyma, and the image was ready to be captured for training.

To obtain accurate three-dimensional (3D) CT images and to improve training efficiency, the body contour area was obtained from the determined uppermost level trans-axial image slice of the lung parenchyma. The center of gravity of the body contour area was identified. Subsequently, we retrieved 256-pixel wide images that extended outward based on the center of gravity of the body contour block, followed by obtaining the counterpart PET images. From the uppermost level trans-axial image slice of the lung parenchyma, 96 consecutive trans-axial image slices were captured downward from both CT and PET images.

The 96 images retrieved from CT and PET, respectively, were of the same thickness and size and could cover the entire bilateral lung regions. Finally, both CT and PET 3D images from 112 patients were obtained for subsequent input to the deep learning models. The 3D image data were unified into $256 \times 256 \times 96$ and $64 \times 64 \times 96$ for the CT and PET images, respectively (**Figure 3**).

Preprocessing by Manual Annotation

An experienced nuclear physician carried out conventional manual annotation by determining the representative image slices that contain the maximum diameters (i.e., tumor coordinates) of pulmonary nodules. A total of 16 consecutive image slices (adjacent to the aforementioned representative image slices) were then retrieved. We cropped out CT images of $64 \times 64 \times 16$ and PET images of $16 \times 16 \times 16$, followed by resizing the PET images to the same size as the CT images.

Input to Deep Learning Models

Under the lung window setting (WL: -400 and WW: $1,500$), we normalized the input image data by converting the data to a value from 0 to 1. For PET images, the maximum value in the image range was normalized. Furthermore, PET image data

were converted into values ranging from 0 to 1 to enhance the convergence efficiency of the model.

Conventional convolutional neural network such as VGG and ResNet models pass through the stride and pooling layers to continuously reduce the sizes of the feature maps and finally enter the classifiers (**Figure 4**). However, reducing the sizes of the features leads to the loss of resolution. Therefore, we proposed a High-Resolution Network (HRNet) architecture with a view to preserving high-resolution features. The top layer of HRNet does not pass through any of the stride and pooling layers so that the features were able to retain their sizes.

Statistical Analyses

The statistical analysis was performed using SPSS 26 statistical software (IBM, Armonk, NY, United States) and MedCalc statistical software¹. Fisher's exact or Chi-square (χ^2) test was used to compare categorical variables. Student's *t*-test was used to compare continuous variables between groups as appropriate. The *p*-value of <0.05 was considered statistically significant. MedCalc statistical software was used to perform ROC curve analysis, the value of the models was predicted based on the ROC curve analysis and corresponding 95% confidence intervals (CIs) were calculated. ROC analysis for the models prediction with benign and malignant lesion revealed an area under the ROC curve (AUC) of 0.781 (95% CI = 0.755–0.834), 0.789 (95% CI = 0.761–0.906), 0.652 (95% CI = 0.582–0.737), and 0.743 (95% CI = 0.680–0.842) for High-Resolution Network (HRNet)-automated, High-Resolution Network (HRNet)-manual, Residual Network (ResNet)-automated, and Residual Network (ResNet)-manual models, respectively (**Figure 5**).

Deep learning often uses heat maps to differentiate regions with characteristic features (**Figure 6**). The lungs are adjacent to other internal organs and tissues, such as the heart, liver, and lymph nodes. If these organs also exhibit high FDG uptake, they may disrupt the focus of the deep learning model and affect the accuracy (ACC) of the analysis. Therefore, the heat map is based on the feature map in the last layer of the proposed model and is concentrated on the area of pulmonary nodules.

RESULTS

The effects of the two groups of PET-CT images on the differentiation between benign and malignant pulmonary nodules were evaluated. First, when applied only to automatically detected pulmonary nodules on the PET-CT images, the HRNet model [sensitivity (SEN): 0.899; specificity (SPE): 0.545; ACC: 0.795] performed significantly better than the ResNet model (SEN: 0.785; SPE: 0.394, ACC: 0.670) did. Compared with the ResNet model, the HRNet performed better in terms of SEN and ACC. HRNet and ResNet models performed comparably when applied only to the PET-CT images of pulmonary nodules. The ACC of the ResNet model was only slightly better than that of the HRNet model. In summary, HRNet is suitable for two

¹www.medcalc.org

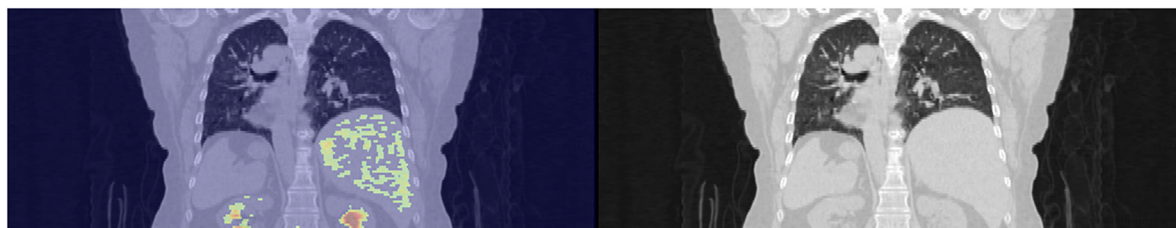


FIGURE 3 | Extraction of the 3D images of the lungs with a thickness of 96 slices of trans-axial CT images.

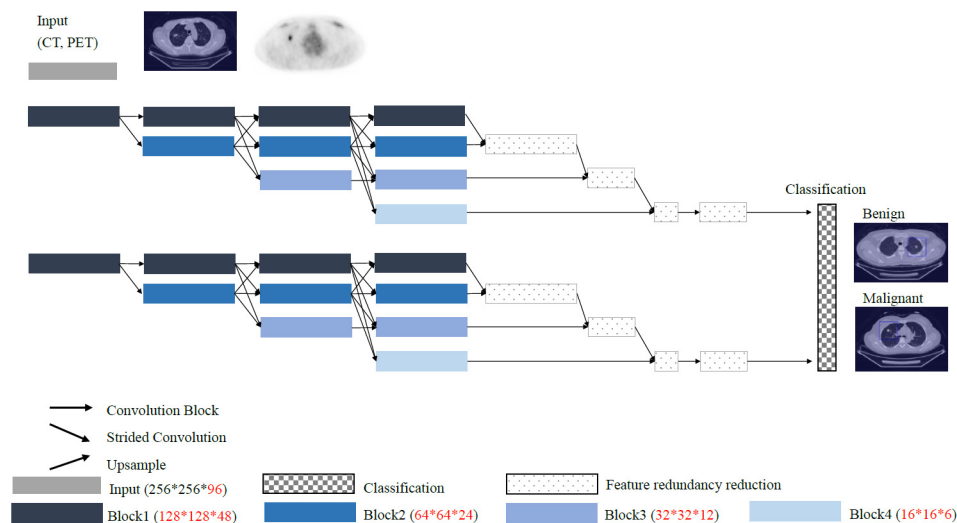


FIGURE 4 | Overall structure of the proposed deep learning model (i.e., HRNet).

types of PET-CT datasets, and its performance is more stable than that of ResNet.

Model Comparison

Compared with the traditional model, the HRNet-automated model used in this study performed significantly better than the ResNet-automated models. When models which automatically detected pulmonary nodules were compared with each other, HRNet performed significantly better than ResNet (significance level: 0.0036) did. The performance for the HRNet-automated versus that for the ResNet-manual (significance level: 0.3343) did not significantly differ, indicating that this study's method, which functions without manual expert annotation, yield comparable predictions as traditional labeling models that require expert annotation (Table 2).

The results of manual and automated detection show that the prediction performance of ResNet is low in automated detection ($AUC = 0.652$), and the prediction effect must be improved by manually labeling detection ($AUC = 0.743$). The results of HRNet manual ($AUC = 0.789$) and automated detection ($AUC = 0.781$) have comparable prediction performances.

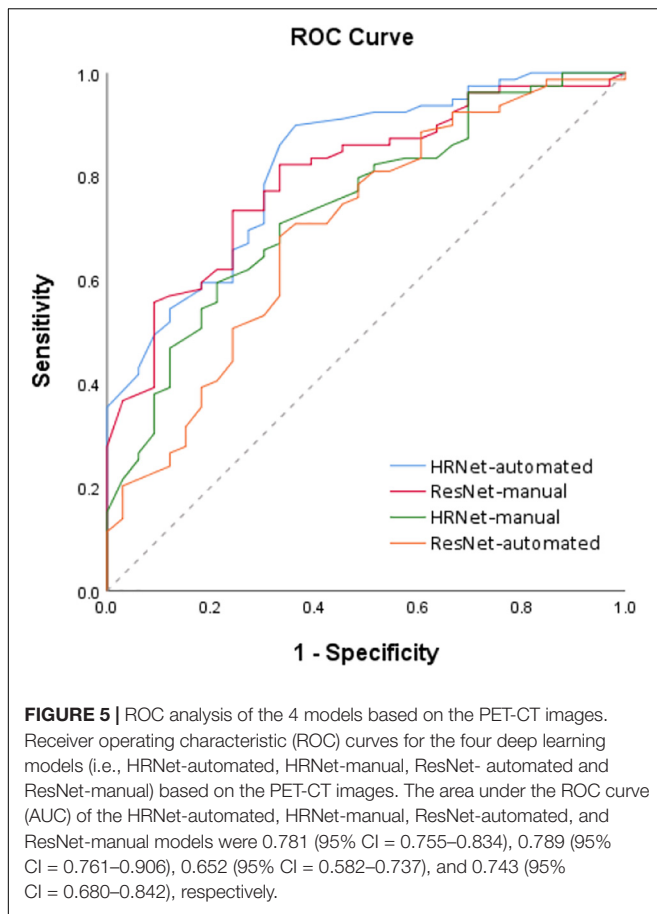
According to the ROC curves based on image data from automated detection, the prediction performance of HRNet using PET-CT ($AUC = 0.781$) is moderately better than that of only

using CT ($AUC = 0.725$); and the performance of ResNet utilizing PET-CT ($AUC = 0.652$) is also better than that of utilizing only CT ($AUC = 0.566$).

The sensitivity (0.899) and AUC of HRNet-PET-CT-automated are moderately better than those of HRNet-CT-automated (p -value = 0.742). Although the specificity of HRNet-PET-CT-automated (0.545) is slightly lower than that of HRNet-CT-automated, it does not markedly affect the overall prediction performance, as evidenced by the satisfactory precision (0.795) of HRNet-PET-CT-automated. Therefore, the HRNet-PET-CT-automated model is quite effective in predicting malignant pulmonary nodules, which is also one of the most prominent findings in this research.

DISCUSSION

With the advancement of chest CT and plain radiographs, the detection rate of pulmonary nodules has drastically improved (36, 37). The assessment of pulmonary nodules is crucial because they may be the first indications of early lung neoplasm. Approximately 35% of single pulmonary nodules are primary malignancies (38). Differentiating small nodules into malignant and benign nodules is challenging because of their small size and



lack of specific morphological features (39). A study reported that approximately half of lung cancer patients missed the optimal time for surgical treatment, resulting in a decrease in the 5-year survival rate by 10–15% (40). Therefore, the accurate diagnosis of patients with pulmonary nodules helps to improve the ACC of the

initial cancer staging and prognosis of patients with malignant nodules (23).

Nevertheless, pulmonary nodules are not all malignant lesions. Pulmonary nodules, except in lung cancer, can be inflammatory or infectious lesions and can have other relatively rare benign etiologies. The prevalence of lung cancer in pulmonary nodules is high, and the early detection of malignant nodules might improve the chances of successful treatment. Transbronchial needle aspiration biopsy, percutaneous transthoracic biopsy, or video-assisted thoracoscopic surgery can yield histopathological information. However, they have variable ACC in diagnosing lung cancer because these are invasive procedures dependent on the diameter and position of the nodule and whose execution is dependent on skill.

FDG-PET-CT is commonly used in the diagnosis of pulmonary nodules. It can be used to detect malignancy through high FDG accumulation, which indicates the presence of metabolically active cancer cells by quantifying the rate of cellular glucose metabolism. Malignant nodules generally have increased glucose transporter expression and metabolic activity, which is evidenced by a high FDG uptake (41). However, benign lesions also occasionally exhibit increased metabolic activity, such as infections, tuberculosis, and granulomatous disease (29, 42–44). Conversely, malignant lung lesions with false-negative findings on PET scan may be relevant tumors with low glycolytic activity (such as adenocarcinomas, bronchioloalveolar carcinomas, carcinoid tumors, and low-grade lymphomas), small-sized tumors (partial volume effect), or metastasized tumors with a mucinous component (relative low cellularity) (45). In pooled results from a meta-analysis, FDG-PET-CT had a diagnostic SEN of 0.89 [95% confidence interval (CI), 0.87–0.91] and an SPE of 0.70 (95% CI, 0.66–0.73) in the diagnosis of malignant solitary pulmonary nodules (29). Thus, at present, the evidence in the literature indicates only moderate ACC for FDG-PET-CT in differentiating malignant from benign pulmonary nodules. Further research is required to improve its reliability.

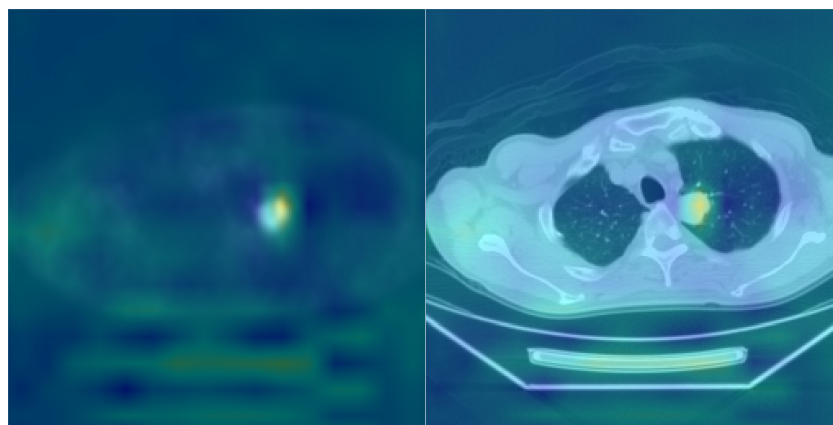


FIGURE 6 | Heatmap visualization of the HRNet-automated model. The highlighted (e.g., red) area on the heat map were used to indicate the portions/pixels of an image that have the greatest contribution to the output of the model. The heated area matched quite well with the actual locations of pulmonary nodules on the DICOM PET-CT images and the clinical records, which potentially serves as a beneficial clinical tool for patient treatment planning.

TABLE 2 | Model comparison.

Model comparison	Significance level, p^*
HRNet-automated vs. HRNet-manual	0.6526
HRNet-automated vs. ResNet-automated	0.0036*
HRNet-automated vs. ResNet-manual	0.3343
HRNet-manual vs. ResNet-automated	0.0039*
HRNet-manual vs. ResNet-manual	0.6398
ResNet-automated vs. ResNet-manual	0.0014*
ResNet-PET-CT vs. ResNet-CT	0.0749
HRNet-PET-CT vs. HRNet-CT	0.7422

*The p -value of <0.05 was considered statistically.

Recently, several studies have applied deep learning or machine learning approaches to conventional CT and FDG-PET-CT images to diagnose lung cancer (20–22). A study evaluated the performance of a deep learning system for the differential diagnosis of lung cancer with conventional CT and FDG-PET-CT by using transfer learning and metadata (46). The introduction of metadata and data on SUVmax and lesion size derived from PET-CT into baseline CT models improved diagnostic performance for models applied to CT images derived from PET-CT [area under the receiver operating characteristic curve (AUC) = 0.837 vs. 0.762] or conventional CT images (AUC = 0.877 vs. 0.817) models.

In our study, we sought to assess whether deep learning may be helpful in the differentiation of pulmonary nodules in FDG PET-CT imaging. In total, 112 patients with pulmonary nodules who underwent FDG PET-CT before surgery were enrolled retrospectively. The images of the lungs were automatically extracted through deep HRRL without the aid of an expert. The deep convolutional networks were trained within a HRNet framework, which executes high-resolution classification instead of using the conventional segmentation method to provide more precise localization of image data.

The performance of two-dimensional (2D) and 3D networks were evaluated. According to a recently published study, the additional spatial dimension of the 3D network substantially improved the quality of the inference because the additional dimension allowed an equivalent 3D network to produce volumes with higher fidelity across all spatial dimensions. Therefore, we implemented the 3D model instead of the conventional 2D model. The lung images obtained were then fed to the HRRL algorithm to automatically classify the detected pulmonary nodules into malignant and benign ones, followed by an assessment of ACC. To our knowledge, our study is the first to determine the value of deep learning for the automated classification of pulmonary nodules on FDG-PET-CT images.

Conventional deep learning model architectures generally use a classification task model as the primary framework. When the image is being extended, its size is gradually compressed, which compromises its high-resolution representations. Therefore, we applied the conventional deep learning algorithm for the overall 3D image classification, which led to decreased diagnostic ACC and loss of features.

The proposed HRNet retains the high-resolution features. However, it is challenging to solve multiscale problems effectively by using only high-resolution representations. Therefore, we implement the proposed architecture to preserve high-resolution features. The network solves multiscale problems through continuous reduction, followed by multiscale fusions, to maintain the resolution of various scales. Therefore, in this study, HRNet used for lung image recognition did not lead to the loss of pulmonary nodule characteristics (47, 48).

With regard to the overall 3D image classification target processed in this study, the aforementioned reduced size feature causes the loss of regional lung features and decreases ACC.

High-Resolution Network maintains high-resolution features, but it is not easy to extract deep textural features using only high-resolution features. Therefore, the proposed architecture preserves high-resolution features. It aims to solve the multiscale problem through continuous shrinking. The architecture of HRNet is similar to that of ICLR18-MSDNet, which works through multiscale fusion and preserves high resolution.

The main architecture of HRNet acts to integrate each branch of the feature map. The resolution of each feature map is different, and the actual operation involves the use of upsampling and downsampling to achieve integration. Although the resolution of each branch is different, the features are fused through the multiscale fusion method to extract meaningful information for overall 3D image classification.

Furthermore, we used 3D HRRL and compared the ACC values of two types of model input: The CT component of PET-CT input, and the combined PET-CT input based on FDG PET-CT imaging. Although most previous studies assessing the ACC of AI algorithm in differentiating malignant from benign lesions have taken advantage of a combination of different tests as the reference standard, such as clinical follow-up with additional imaging for some study participants and histopathology for others, surgical pathology was the sole definitive reference standard used for all individuals in this study.

The significant findings of our study are detailed as follows: First, deep learning might be a promising technique for the detection and differentiation of pulmonary nodules on FDG PET-CT images. Although our study only consisted of 112 patients, the AI algorithm generally gave accurate and reliable results. Second, the lung images could be extracted automatically through HRRL in the absence of any manual delineation. Third, the deep HRNet kept the high resolution of the images intact, unlike in other well-known AI models, such as VGG and ResNet, which compromised their resolution at each round of k -fold cross-validation (46). Fourth, the performance metrics of the combined PET-CT model were generally better than those of the model derived from the CT component solely.

CONCLUSION

This retrospective study indicates that automated 3D HRRL with FDG-PET-CT has promising performance in distinguishing

between malignant and benign pulmonary nodules. One of the most significant strengths of the proposed deep learning algorithm is that it can potentially automatically detect and classify pulmonary nodules without any time-consuming manual annotation. However, this study had a limited number of participants, and an extensive multicenter study with external validation is required for further verification of the results.

DATA AVAILABILITY STATEMENT

The original contributions presented in the study are included in the article/supplementary material, further inquiries can be directed to the corresponding author/s.

ETHICS STATEMENT

This study was approved by the Ethics Committee of our hospital [DMR99-IRB-010-(CR-11)]. Written informed consent

for participation was not required for this study in accordance with the National Legislation and the Institutional Requirements.

AUTHOR CONTRIBUTIONS

Y-CL, K-CW, and C-HK: conception and design. C-HK: administrative support. All authors: significant contributions, agreement with the content of the manuscript, collection and assembly of data, data analysis and interpretation, manuscript writing, and final approval of manuscript.

FUNDING

This study was supported in part by the China Medical University Hospital (DMR-110-089, DMR-111-090, and DMR-111-091). The funders had no role in the study design, data collection and analysis, the decision to publish, or preparation of the manuscript.

REFERENCES

- Moyer VA, U.S. Preventive Services Task Force. Screening for lung cancer: U.S. preventive services task force recommendation statement. *Ann Intern Med.* (2014) 160:330–8.
- Rivera MP, Mehta AC, Wahidi MM. Establishing the diagnosis of lung cancer: diagnosis and management of lung cancer, 3rd ed: American college of chest physicians evidence-based clinical practice guidelines. *Chest.* (2013) 143:e142S–e165S. doi: 10.1378/chest.12-2353
- Detterbeck FC, Mazzone PJ, Naidich DP, Bach PB. Screening for lung cancer: diagnosis and management of lung cancer, 3rd ed: American college of chest physicians evidence-based clinical practice guidelines. *Chest.* (2013) 143:e78S–e92S. doi: 10.1378/chest.12-2350
- Wender R, Fontham ET, Barrera E Jr., Colditz GA, Church TR, Ettinger DS, et al. American cancer society lung cancer screening guidelines. *CA Cancer J Clin.* (2013) 63:107–17.
- Roberts H, Walker-Dilks C, Sivjee K, Ung Y, Yasufuku K, Hey A, et al. Screening high-risk populations for lung cancer: guideline recommendations. *J Thorac Oncol.* (2013) 8:1232–7. doi: 10.1097/JTO.0b013e31829fd3d5
- Jacobson FL, Austin JH, Field JK, Jett JR, Keshavjee S, MacMahon H, et al. Development of the american association for thoracic surgery guidelines for low-dose computed tomography scans to screen for lung cancer in North America: recommendations of the American association for thoracic surgery task force for lung cancer screening and surveillance. *J Thorac Cardiovasc Surg.* (2012) 144:25–32. doi: 10.1016/j.jtcvs.2012.05.059
- Wahidi MM, Govert JA, Goudar RK, Gould MK, McCrory DC, American College of Chest Physicians. Evidence for the treatment of patients with pulmonary nodules: when is it lung cancer?: ACCP evidence-based clinical practice guidelines (2nd edition). *Chest.* (2007) 132:94S–107S. doi: 10.1378/chest.07-1352
- Patz EF Jr., Lowe VJ, Hoffman JM, Paine SS, Burrowes P, Coleman RE, et al. Focal pulmonary abnormalities: evaluation with F-18 fluorodeoxyglucose PET scanning. *Radiology.* (1993) 188:487–90. doi: 10.1148/radiology.188.2.8327702
- Knight SB, Delbeke D, Stewart JR, Sandler MP. Evaluation of pulmonary lesions with FDG-PET. Comparison of findings in patients with and without a history of prior malignancy. *Chest.* (1996) 109:982–8. doi: 10.1378/chest.109.4.982
- Houshmand S, Salavati A, Segtnan EA, Grupe P, Høilund-Carlson PF, Alavi A. Dual-time-point imaging and delayed-time-point fluorodeoxyglucose-PET/computed tomography imaging in various clinical settings. *PET Clin.* (2016) 11:65–84. doi: 10.1016/j.cpet.2015.07.003
- Pietrzak AK, Kazmierska J, Marszałek A, Cholewinski W. Evaluation of physiologic and abnormal glucose uptake in palatine tonsils: differential diagnostics with sequential dual-time-point 2-deoxy-2-[18F]FDG PET/CT. *Q J Nucl Med Mol Imaging.* (2020) 64:299–306. doi: 10.23736/S1824-4785.18.03065-0
- Shimizu K, Okita R, Saisho S, Yukawa T, Maeda A, Nojima Y, et al. Clinical significance of dual-time-point 18F-FDG PET imaging in resectable non-small cell lung cancer. *Ann Nucl Med.* (2015) 29:854–60. doi: 10.1007/s12149-015-1013-3
- Pietrzak A, Marszałek A, Paterska M, Golusinski P, Narozna J, Cholewinski W. Initial and delayed metabolic activity of palatine tonsils measured with the PET/CT-dedicated parameters. *Diagnostics (Basel).* (2020) 10:836. doi: 10.3390/diagnostics10100836
- Sanz-Viedma S, Torigian DA, Parsons M, Basu S, Alavi A. Potential clinical utility of dual time point FDG-PET for distinguishing benign from malignant lesions: implications for oncological imaging. *Rev Esp Med Nucl.* (2009) 28:159–66. doi: 10.1016/s1578-200x(09)90000-6
- Koppenol WH, Bounds PL, Dang CV. Otto Warburg's contributions to current concepts of cancer metabolism. *Nat Rev Cancer.* (2011) 11:325–37. doi: 10.1038/nrc3038
- Beyer T, Townsend DW, Brun T, Kinahan PE, Charron M, Roddy R, et al. A combined PET/CT scanner for clinical oncology. *J Nucl Med.* (2000) 41:1369–79.
- Pauwels EK, Ribeiro MJ, Stoot JH, McCready VR, Bourguignon M, Mazière B. FDG accumulation and tumor biology. *Nucl Med Biol.* (1998) 25:317–22. doi: 10.1016/s0969-8051(97)00226-6
- Goudarzi B, Jacene HA, Wahl RL. Diagnosis and differentiation of bronchioloalveolar carcinoma from adenocarcinoma with bronchioloalveolar components with metabolic and anatomic characteristics using PET/CT. *J Nucl Med.* (2008) 49:1585–92. doi: 10.2967/jnumed.108.052712
- Schaefferkoetter J, Yan J, Moon S, Chan R, Ortega C, Metser U, et al. Deep learning for whole-body medical image generation. *Eur J Nucl Med Mol Imaging.* (2021) 48:3817–26. doi: 10.1007/s00259-021-05413-0
- Zaharchuk G, Davidzon G. Artificial Intelligence for optimization and interpretation of PET/CT and PET/MR images. *Semin Nucl Med.* (2021) 51:134–42. doi: 10.1053/j.semnuclmed.2020.10.001
- Sadaghiani MS, Rowe SP, Sheikhbahaei S. Applications of artificial intelligence in oncologic 18F-FDG PET/CT imaging: a systematic review. *Ann Transl Med.* (2021) 9:823. doi: 10.21037/atm-20-6162
- Albano D, Gatta R, Marini M, Rodella C, Camoni L, Dondi F, et al. Role of 18F-FDG PET/CT radiomics features in the differential diagnosis of solitary pulmonary nodules: diagnostic accuracy and comparison between

- two different PET/CT scanners. *J Clin Med.* (2021) 10:5064. doi: 10.3390/jcm10215064
23. Tang K, Wang L, Lin J, Zheng X, Wu Y. The value of 18F-FDG PET/CT in the diagnosis of different size of solitary pulmonary nodules. *Medicine (Baltimore).* (2019) 98:e14813. doi: 10.1097/MD.00000000000014813
 24. Evangelista L, Cuocolo A, Pace L, Mansi L, Vecchio SD, Mileto P, et al. Performance of FDG-PET/CT in solitary pulmonary nodule based on pre-test likelihood of malignancy: results from the Italian retrospective multicenter trial. *Eur J Nucl Med Mol Imaging.* (2018) 45:1898–907. doi: 10.1007/s00259-018-4016-1
 25. Wang L, Chen Y, Tang K, Lin J, Zhang H. The value of 18F-FDG PET/CT mathematical prediction model in diagnosis of solitary pulmonary nodules. *Biomed Res Int.* (2018) 2018:9453967. doi: 10.1155/2018/9453967
 26. Chen S, Harmon S, Perk T, Li X, Chen M, Li Y, et al. Using neighborhood gray tone difference matrix texture features on dual time point PET/CT images to differentiate malignant from benign FDG-avid solitary pulmonary nodules. *Cancer Imaging.* (2019) 19:56. doi: 10.1186/s40644-019-0243-3
 27. Taralli S, Scolozzi V, Foti M, Ricciardi S, Forcione AR, Cardillo G, et al. 18F-FDG PET/CT diagnostic performance in solitary and multiple pulmonary nodules detected in patients with previous cancer history: reports of 182 nodules. *Eur J Nucl Med Mol Imaging.* (2019) 46:429–36. doi: 10.1007/s00259-018-4226-6
 28. Karyagar S, Koç Z, Karyagar S, Bekar Y. Diagnostic performance of 18F-FDG PET/CT in solitary pulmonary nodules of non-smokers. *Turk J Thorac Cardiovasc Surg.* (2017) 25:235–41.
 29. Li ZZ, Huang YL, Song HJ, Wang YJ, Huang Y. The value of 18F-FDG-PET/CT in the diagnosis of solitary pulmonary nodules: a meta-analysis. *Medicine (Baltimore).* (2018) 97:e0130. doi: 10.1097/MD.00000000000010130
 30. Chartrand G, Cheng PM, Vorontsov E, Drozdal M, Turcotte S, Pal CJ, et al. Deep learning: a primer for radiologists. *Radiographics.* (2017) 37:2113–31. doi: 10.1148/rg.2017170077
 31. Puttagunta M, Ravi S. Medical image analysis based on deep learning approach. *Multimed Tools Appl.* (2021) 80:24365–98. doi: 10.1007/s11042-021-10707-4
 32. Wang J, Sun K, Cheng T, Jiang B, Deng C, Zhao Y, et al. Deep high-resolution representation learning for visual recognition. *IEEE Trans Pattern Anal Mach Intell.* (2020) 43:3349–64. doi: 10.1109/TPAMI.2020.2983686
 33. Conrad GR, Sinha P. Narrow time-window dual-point 18F-FDG PET for the diagnosis of thoracic malignancy. *Nucl Med Commun.* (2003) 24:1129–37. doi: 10.1097/00006231-200311000-00002
 34. Schillaci O, Travascio L, Bolacchi F, Calabria F, Bruni C, Ciccio C, et al. Accuracy of early and delayed FDG PET-CT and of contrast-enhanced CT in the evaluation of lung nodules: a preliminary study on 30 patients. *Radiol Med.* (2009) 114:890–906. doi: 10.1007/s11547-009-0400-z
 35. Chen YM, Huang G, Sun XG, Liu JJ, Chen T, Shi YP, et al. Optimizing delayed scan time for FDG PET: comparison of the early and late delayed scan. *Nucl Med Commun.* (2008) 29:425–30. doi: 10.1097/MNM.0b013e3282f4d389
 36. Leef JL III, Klein JS. The solitary pulmonary nodule. *Radiol Clin North Am.* (2002) 40:123–43.
 37. Seemann MD, Seemann O, Luboldt W, Bonel H, Sittek H, Dienemann H, et al. Differentiation of malignant from benign solitary pulmonary lesions using chest radiography, spiral CT and HRCT. *Lung Cancer.* (2000) 29:105–24. doi: 10.1016/s0169-5002(00)00104-5
 38. Jemal A, Thomas A, Murray T, Thun M. Cancer statistics, 2002. *CA Cancer J Clin.* (2002) 52:23–47.
 39. Swensen SJ. CT screening for lung cancer. *AJR Am J Roentgenol.* (2002) 179:833–6.
 40. Fletcher JW, Kymes SM, Gould M, Alazraki N, Coleman RE, Lowe VJ, et al. A comparison of the diagnostic accuracy of 18F-FDG PET and CT in the characterization of solitary pulmonary nodules. *J Nucl Med.* (2008) 49:179–85. doi: 10.2967/jnumed.107.044990
 41. Mochizuki T, Tsukamoto E, Kuge Y, Kanegae K, Zhao S, Hikosaka K, et al. FDG uptake and glucose transporter subtype expressions in experimental tumor and inflammation models. *J Nucl Med.* (2001) 42:1551–5.
 42. Ost D, Fein AM, Feinsilver SH. Clinical practice. The solitary pulmonary nodule. *N Eng J Med.* (2003) 348:2535–42.
 43. Chen CJ, Lee BF, Yao WJ, Cheng L, Wu PS, Chu CL, et al. Dual-phase 18F-FDG PET in the diagnosis of pulmonary nodules with an initial standard uptake value less than 2.5. *AJR Am J Roentgenol.* (2008) 191:475–9. doi: 10.2214/AJR.07.3457
 44. Huang YE, Lu HI, Liu FY, Huang YJ, Lin MC, Chen CF, et al. Solitary pulmonary nodules differentiated by dynamic F-18 FDG PET in a region with high prevalence of granulomatous disease. *J Radiat Res.* (2012) 53:306–12. doi: 10.1269/jrr.11089
 45. Chang JM, Lee HJ, Goo JM, Lee HY, Lee JJ, Chung JK, et al. False positive and false negative FDG-PET scans in various thoracic diseases. *Korean J Radiol.* (2006) 7:57–69. doi: 10.3348/kjr.2006.7.1.57
 46. Park YJ, Choi D, Choi JY, Hyun SH. Performance evaluation of a deep learning system for differential diagnosis of lung cancer with conventional CT and FDG PET/CT using transfer learning and metadata. *Clin Nucl Med.* (2021) 46:635–40. doi: 10.1097/RLU.0000000000003661
 47. He K, Zhang X, Ren S, Sun J. Deep residual learning for image recognition. *arXiv.* (2015) [Preprint]. 1512.03385 [cs.CV].
 48. Sun K, Xiao B, Liu D, Wang J. Deep high-resolution representation learning for human pose estimation. *arXiv.* (2019) [Preprint]. 1902.09212 [cs.CV].

Conflict of Interest: The authors declare that the research was conducted in the absence of any commercial or financial relationships that could be construed as a potential conflict of interest.

Publisher's Note: All claims expressed in this article are solely those of the authors and do not necessarily represent those of their affiliated organizations, or those of the publisher, the editors and the reviewers. Any product that may be evaluated in this article, or claim that may be made by its manufacturer, is not guaranteed or endorsed by the publisher.

Copyright © 2022 Lai, Wu, Tseng, Chen, Chang, Yen and Kao. This is an open-access article distributed under the terms of the Creative Commons Attribution License (CC BY). The use, distribution or reproduction in other forums is permitted, provided the original author(s) and the copyright owner(s) are credited and that the original publication in this journal is cited, in accordance with accepted academic practice. No use, distribution or reproduction is permitted which does not comply with these terms.



Prognostic Significance of PD-L1 Expression and Standardized Uptake Values in the Primary Lesions of Stage IV Adenocarcinoma Lung Cancer

OPEN ACCESS

Edited by:

Domenico Albano,
University of Brescia, Italy

Reviewed by:

Francesco Dondi,
Università degli Studi di Brescia, Italy
Sang Van Nguyen,
Thai Nguyen Pharmacy and Medical
University, Vietnam

*Correspondence:

Pham-Van Thai
phamvanthai@hmu.edu.vn
Nguyen Minh Duc
bsnguyenminhduc@pnt.edu.vn

[†]These authors have contributed
equally to this work and share first
authorship

Specialty section:

This article was submitted to
Nuclear Medicine,
a section of the journal
Frontiers in Medicine

Received: 13 March 2022

Accepted: 19 April 2022

Published: 13 May 2022

Citation:

Tien Cong B, Cam Phuong P,
Thai P-V, Thuong V-L, Quang Hung N,
Hang D-T, Anh Tuan H, Minh Khuy D,
Tuyen P-V and Minh Duc N (2022)
Prognostic Significance of PD-L1
Expression and Standardized Uptake
Values in the Primary Lesions of Stage
IV Adenocarcinoma Lung Cancer.
Front. Med. 9:895401.
doi: 10.3389/fmed.2022.895401

Bui Tien Cong^{1,2†}, Pham Cam Phuong^{1,2†}, Pham-Van Thai^{1,2*}, Vu-Le Thuong^{1,2},
Nguyen Quang Hung², Dong-Thi Hang³, Hoang Anh Tuan⁴, Doan Minh Khuy⁴,
Pham-Van Tuyen⁴ and Nguyen Minh Duc^{5*}

¹ Department of Nuclear Medicine, Ha Noi Medical University, Hanoi, Vietnam, ² Nuclear Medicine and Oncology Center, Bach Mai Hospital, Hanoi, Vietnam, ³ Department of Examination, Bach Mai Hospital, Hanoi, Vietnam, ⁴ Pathology and Cytology Center, Bach Mai Hospital, Hanoi, Vietnam, ⁵ Department of Radiology, Pham Ngoc Thach University of Medicine, Ho Chi Minh City, Vietnam

Background: This study evaluated the prognostic ability of ¹⁸F-fluorodeoxyglucose (¹⁸F-FDG) positron emission tomography (PET)/computed tomography (CT) in patients with stage IV adenocarcinoma lung cancer to detect protein death-ligand 1 (PD-L1) expression levels.

Methods: In total, 86 patients with stage IV adenocarcinoma lung cancer underwent ¹⁸F-FDG PET/CT imaging and PD-L1 expression evaluation before treatment from February 2019 to November 2020 at Bach Mai Hospital, Hanoi, Vietnam. The assessed patient characteristics in this study included sex, age, smoking status, epidermal growth factor receptor (*EGFR*) mutation, PD-L1 expression level, survival status, tumor, node, and metastasis (TNM) stage, and metastasis locations.

Results: The average age was 62.23 ± 9.51 years, and men and women represented 67.4% and 32.6% of the population, respectively. The *EGFR* mutation rate was 36%. PD-L1 expression was negative (detected in <1% of the tumor) in 40.7% of cases and positive in 59.3% of cases (detected in 1–49% of the tumor in 32.6%; detected in $\geq 50\%$ of the tumor in 26.7%). The mean maximum standardized uptake value (SUV_{max}) was 11.09 ± 3.94 . SUV_{max} was significantly higher in PD-L1-positive tumors than in PD-L1-negative tumors (12.24 ± 4.01 and 9.43 ± 3.22 , respectively; $p = 0.001$). Receiver operating characteristic curve analysis revealed an area under the curve of SUV_{max} was 0.681 (95% confidence interval 0.570–0.793, $p = 0.004$). Compared with PD-L1-negative cases, SUV_{max} was significantly different in all PD-L1-positive cases ($p = 0.001$), weakly PD-L1-positive cases (1–49%, $p = 0.005$), and strongly PD-L1-positive

cases ($\geq 50\%$, $p = 0.003$). PD-L1 expression levels were significantly associated with SUV_{max} ($p = 0.001$), tumor size ($p = 0.022$), and *EGFR* mutation status ($p = 0.045$).

Conclusions: SUV_{max} in the primary lesions was able to predict PD-L1 expression and may play a role in predicting PD-L1 immunotherapy efficacy in patients with stage IV lung adenocarcinoma.

Keywords: lung cancer, adenocarcinoma, stage IV, FDG PET/CT, PD-L1, prediction, SUV_{max}

INTRODUCTION

Lung cancer is associated with high morbidity and mortality rates. According to GLOBOCAN 2020, lung cancer is the second-most frequent cancer type worldwide (11.4%), accounting for over 2.3 million new cases each year. Lung cancer is estimated to be the leading cause of cancer-related death in both sexes (1) and is the leading cause of cancer-related death in most developed countries (2).

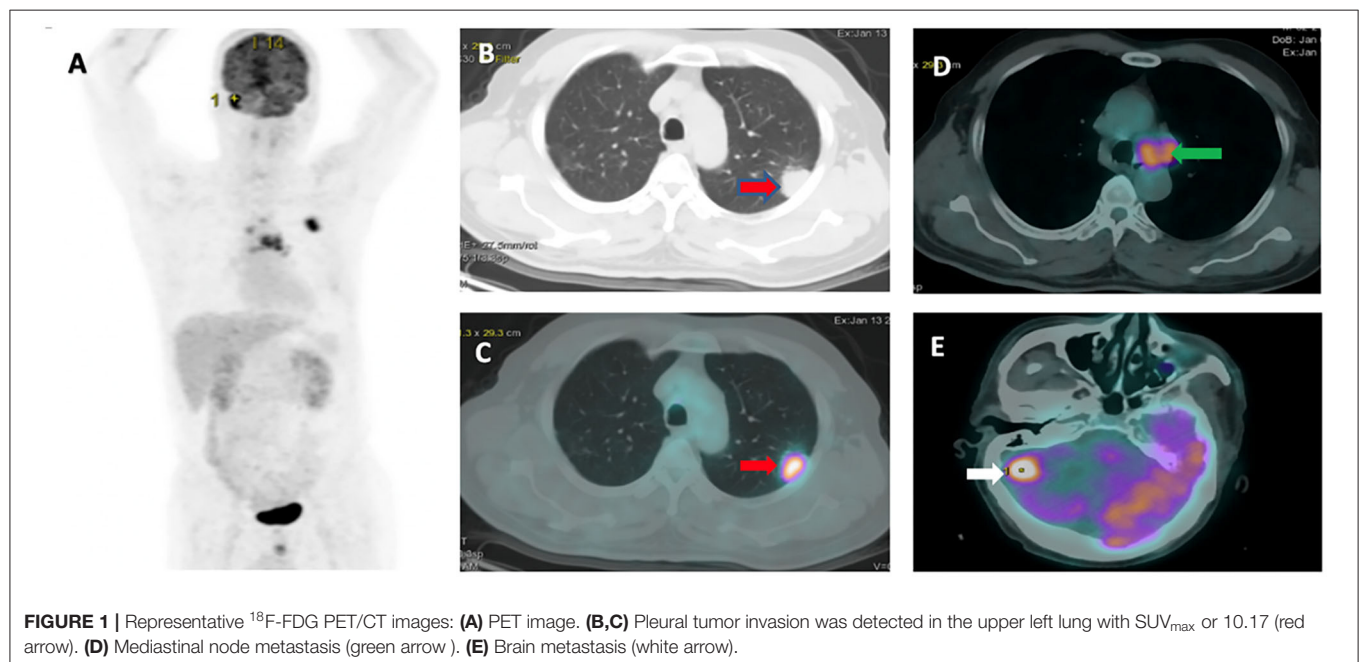
Lung cancer is highly aggressive, rapidly developing, and has poor prognosis, with a 5-year survival rate of only 15% for both sexes (2). However, the majority of individuals are diagnosed at stage III, and late-stage diagnosis (stage IV) is particularly common in developing countries. In recent years, immunotherapy have become increasingly popular treatment options for late stage lung cancer. Testing for programmed death-ligand 1 (PD-L1) expression level should be routinely performed routinely to choose the most suitable treatment approach for patients with non-small cell lung cancer (NSCLC) (3).

Positron emission tomography (PET)/computed tomography (CT) is a nuclear medicine diagnostic tool that enables

early detection, provides comprehensive information regarding disease stage, and has prognostic value in patients with NSCLC. Monoclonal antibodies have been developed that target PD-L1, a critical immune system checkpoint. The binding of programmed cell death protein 1 (PD-1) with PD-L1 induces T-lymphocyte depletion or death. The inhibition of this signaling pathway has been shown to increase T cell activity, boost antitumor immunity, and prevent tumor cells from evading host immune responses, representing a viable technique for successful tumor immunotherapy (4).

Numerous studies have been conducted worldwide to ascertain the relationship between the maximum standard uptake value (SUV_{max}) and PD-L1 expression. Our published research has not established any relationships between PD-L1 expression levels and SUV_{max} in patients with NSCLC. PD-L1 expression is higher in solid tumors, such as lung cancer, breast cancer, colorectal cancer, and liver cancer, than in other tumor types (5–9).

Limited data is available for late-stage NSCLC, especially stage IV. Additionally, little research has been conducted in Vietnam examining PD-L1 expression in NSCLC patients, and no existing studies in Vietnam have demonstrated a



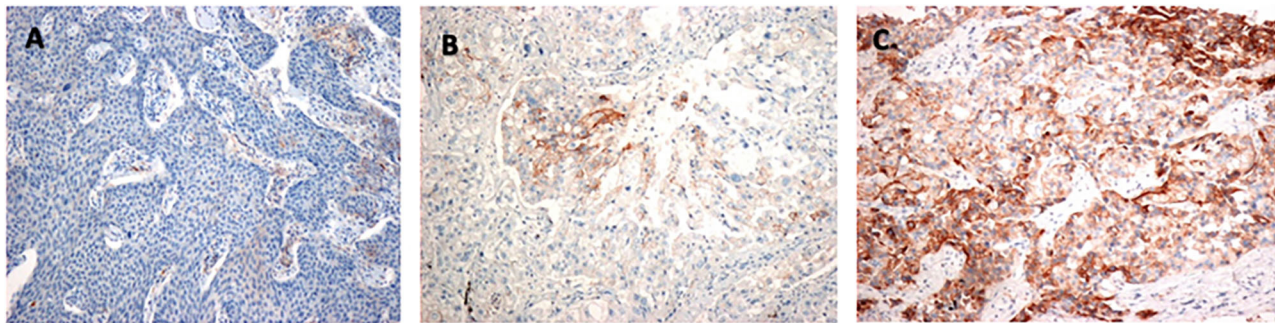


FIGURE 2 | Identification of PD-L1-positive tumor cells: (A) Negative staining (TPS < 1%). (B) Weakly positive staining (TPS 1–49%). (C) Highly positive staining (TPS ≥ 50%). PD-L1, programmed death-ligand 1; TPS, tumor proportion score.

relationship between PET/CT values and PD-L1 expression levels. Therefore, this study evaluated the prognostic significance of ^{18}F -fluorodeoxyglucose (^{18}F -FDG) PET/CT values to predict different PD-L1 expression levels in patients with stage IV adenocarcinoma lung cancer.

MATERIALS AND METHODS

This cross-sectional study was conducted in patients with stage IV adenocarcinoma lung cancer treated at the Nuclear Medicine and Oncology Center and Pathology and Cytology Center, Bach Mai Hospital, from February 2019 to November 2020.

This study was approved by the Ethics Committee of Hanoi Medical University (accession No. NCS02/HMU-IRB), and written informed consent was obtained from all included patients. We included all patients with stage IV NSCLC with an adenocarcinoma histologic subtype treated at our hospital during the study period. Before treatment, patients underwent ^{18}F -FDG PET/CT and were tested for PD-L1 expression and *EGFR* mutations. The normal functions of the liver, kidney, and bone marrow were recorded. All patients who agreed to participate in this study provided a complete medical record for study use. Exclusion criteria included lung cancer types and stages other than stage IV adenocarcinoma, no histologic sample from the primary tumor, or lack of *EGFR* mutation or PD-L1 testing. Patients whose primary tumors were not defined on ^{18}F -FDG PET/CT were also excluded.

The patient characteristics assessed in this study included sex, age, smoking status, *EGFR* mutation, PD-L1 expression level, CEA level, Cyfra 21-1 level, survival status, tumor, node, and metastasis (TNM) stage, and metastasis locations. Patients were asked to fast for 4 h prior to intravenous administration of 0.15 mCi/kg bodyweight ^{18}F -FDG. PET testing was performed 45 min after ^{18}F -FDG administration. ^{18}F -FDG PET/CT was performed using an ECAT ACCEL (Siemens). Image slices were obtained and analyzed by Syngo Via software from the skull to midthigh vertex. The following variables were assessed using the PET/CT results: primary tumor size, TNM stage, and tumor characteristics. A region of interest (ROI) was manually placed on the lung lesion detected in PET/CT images, and SUV_{max} was

TABLE 1 | General patient characteristics ($n = 86$).

Characteristics		n	Percentage (%)
Sex	Male	58	67.4
	Female	28	32.6
Age, years	<65	55	64.0
	>65	31	36.0
Smoking	Yes	38	44.2
	No	48	55.8
<i>EGFR</i> mutation	No	55	64.0
	Yes	31	36.0
PD-L1 expression level	Negative	35	40.7
	1–49%	28	32.6
	≥50%	23	26.7
SUV_{max}	Mean ± SD	11.09 ± 3.94	
Survival	Yes	78	90.7
	No	8	9.3
T stage	T1	9	10.5
	T2	9	10.5
	T3	29	33.7
	T4	39	45.3
N stage	N0	5	5.8
	N1	3	3.5
	N2	33	38.4
	N3	45	52.3
Pleural metastasis	Yes	34	39.5
	No	52	60.5
Lymph metastasis	Yes	16	18.6
	No	70	81.4
Brain metastasis	Yes	7	8.1
	No	79	91.9
Liver metastasis	Yes	9	10.5
	No	77	89.5
Adrenal metastasis	Yes	7	8.1
	No	79	91.9
Bone metastasis	Yes	43	50.0
	No	43	50.0
Other lung metastasis	Yes	39	45.3
	No	47	54.7

EGFR, epidermal growth factor receptor; PD-L1, programmed death-ligand 1; SUV_{max} , maximum standard uptake value; T, tumor; N, node; SD, standard deviation.

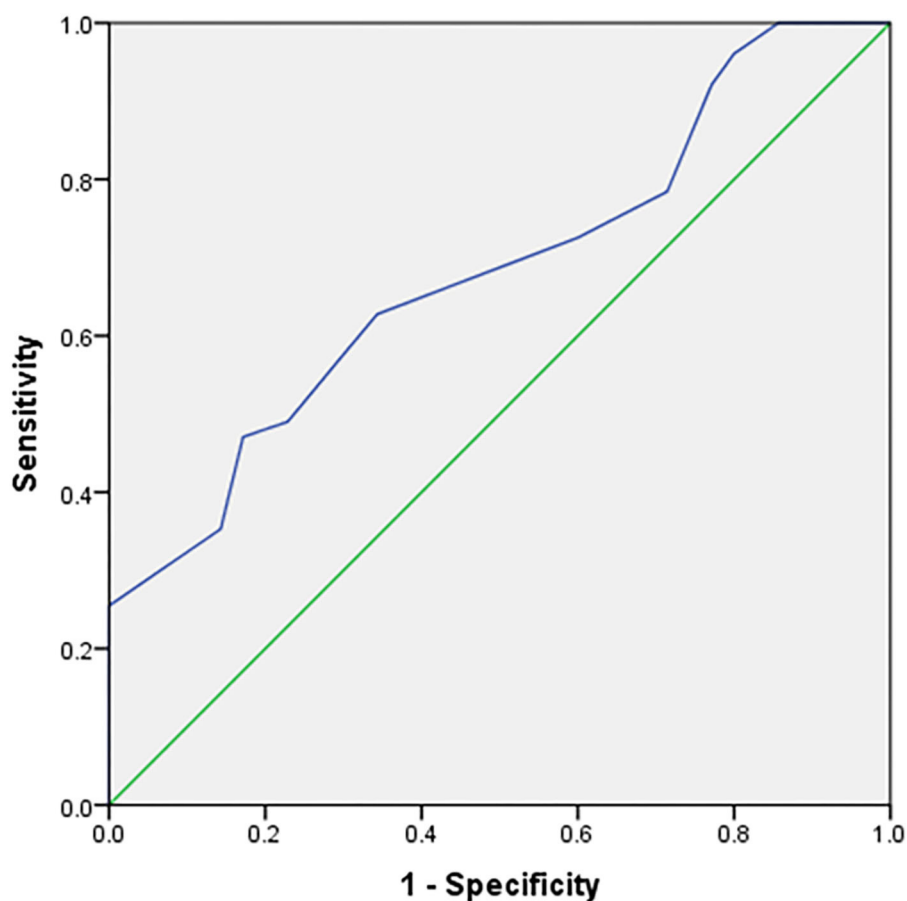


FIGURE 3 | The ability of SUV_{max} to predict PD-L1 expression.

obtained. **Figure 1** shows one representative patient in our study with TNM staging according to PET/CT.

PD-L1 testing was performed at our institution by an expert pathologist. Samples were obtained from the primary tumor.

PD-L1 Expression

We followed the instructions provided in the “PD-L1 Immunohistochemistry Testing in Lung Cancer” manual distributed by the International Association for the Study of Lung Cancer (IASLC). Briefly, pathologists counted PD-L1-positive tumor cells, defined as complete circumferential or partial cell membrane staining. Cytoplasmic staining and tumor-associated immune cells, such as macrophages, were excluded from scoring. The tumor proportion score (TPS) was calculated as follows:

$TPS (\%) = (\text{PD-L1-positive tumor cells} / \text{Total number of tumor cells}) \times 100$. (https://www.accessdata.fda.gov/cdrh_docs/pdf16/p160046c.pdf).

The TPS was used to categorize PD-L1 expression status as follows: <1% (negative staining), 1%–49% (weakly positive staining), and $\geq 50\%$ (highly positive staining). All tumors with

TABLE 2 | The association between SUV_{max} and PD-L1 expression.

	n	Mean \pm SD	P-value
SUV_{max} in PD-L1-negative	35	9.43 \pm 3.22	0.005 (*)
SUV_{max} in PD-L1 positive (1–49%)	28	12.18 \pm 4.23	
SUV_{max} in PD-L1 negative	35	9.43 \pm 3.22	0.003 (*)
SUV_{max} in PD-L1 positive ($\geq 50\%$)	23	12.30 \pm 3.81	
SUV_{max} in PD-L1 positive (1%–49%)	28	12.18 \pm 4.23	0.913
SUV_{max} in PD-L1 positive ($\geq 50\%$)	23	12.30 \pm 3.81	
SUV_{max} in PD-L1 negative	35	9.43 \pm 3.22	0.001 (*)
SUV_{max} in PD-L1 positive (total)	51	12.24 \pm 4.01	

(*) Significant according to t-test.

SUV_{max} , maximum standard uptake value; PD-L1, programmed death-ligand 1; SD, standard deviation.

$TPS \geq 1\%$ were considered PD-L1-positive. **Figure 2** shows representative images of the three PD-L1 categories.

Statistical Analysis

Statistical analyses were performed using SPSS, version 20.0 (SPSS Inc., Chicago, IL, USA). Data are presented as the number

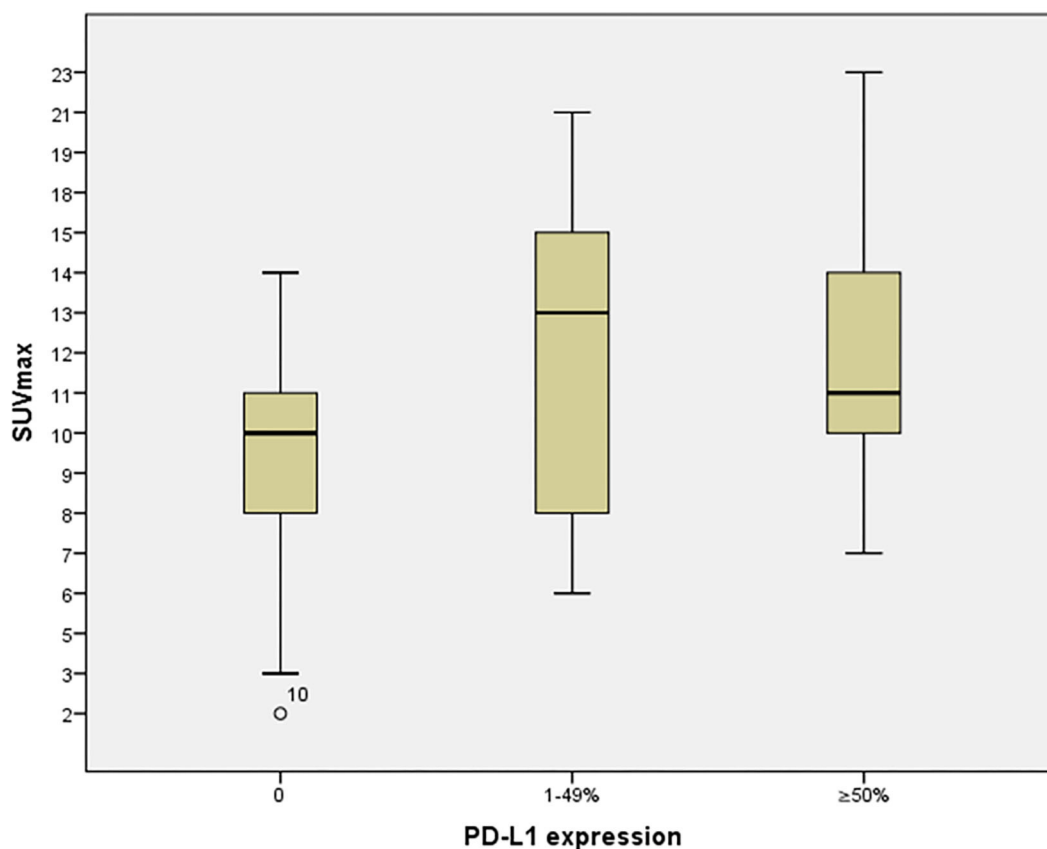


FIGURE 4 | The relationships between SUV_{max} and PD-L1 expression.

and frequency or the mean \pm standard deviation (SD). The association between two continuous variables was analyzed by the Mann–Whitney U test or *t*-test. The association between two categorical variables was evaluated by the Chi-square test. Significance was established at $p < 0.05$.

RESULTS

Patient Population

The general characteristics of the study population are shown in **Table 1**. The average age was 62.23 ± 9.51 years, and 64% of patients were younger than 65 years. Men represented 67.4% of the study population. Smoking was reported by 44.2% of patients. *EGFR* mutations were detected in 36% of the study population. PD-L1 expression was negative in 40.7% of cases and positive in 59.3% of cases, including 32.6% with weak PD-L1 expression (1–49% of cells) and 26.7% with strong PD-L1 expression ($\geq 50\%$ of cells). The mean SUV_{max} was 11.09 ± 3.94 . Other characteristics are summarized in **Table 1**.

The expression of PD-L1 was evaluated in 86 tumor samples by immunohistochemical analysis. A positive association was identified between SUV_{max} from ^{18}F -FDG PET/CT imaging and PD-L1 expression. SUV_{max} was significantly higher in PD-L1-positive tumors than in PD-L1-negative tumors ($12.24 \pm$

4.01 vs. 9.43 ± 3.22 , respectively; $p = 0.001$). The ability of SUV_{max} to predict PD-L1 expression was determined (**Figure 3**) by performing receiver operating characteristic curve analysis, which showed revealed an area under the curve (AUC) of 0.681 (95% confidence interval [95% CI] = 0.570–0.793, $p = 0.004$).

Table 2 shows the relationship between SUV_{max} and PD-L1 expression. Significance differences were identified between SUV_{max} in PD-L1-negative and SUV_{max} for all PD-L1-positive cases ($p = 0.001$), weakly PD-L1-positive cases (1–49%, $p = 0.005$), and strongly PD-L1-positive cases ($\geq 50\%$, $p = 0.003$). These relationships are displayed graphically in **Figure 4**.

Table 3 shows all the associations between patient characteristics and PD-L1 expression status. PD-L1 expression was significantly associated with SUV_{max} ($p = 0.001$), tumor size ($p = 0.022$), and *EGFR* mutation status. However, we found no associations with age, sex, carcinoembryonic antigen (CEA) level, cytokeratin 19 fragment (CYFRA 21-1) level, smoking, survival status, T stage, N stage, or any metastasis location (pleural, lymph, brain, liver, adrenal, bone, or other lung).

DISCUSSION

^{18}F -FDG PET/CT can reveal disease at the molecular level prior to the occurrence of anatomical structural alterations, detected

TABLE 3 | Comparisons between patient characteristics and PD-L1 expression.

Characteristics		PD-L1-Positive	PD-L1-Negative	p-value
Age, years (mean \pm SD)		61.67 \pm 9.42	63.06 \pm 9.73	0.509
CEA level		60.94 \pm 108.23	88.40 \pm 209.04	0.415
CYRFR 21-1 level		10.38 \pm 14.82	9.95 \pm 12.43	0.898
Size of tumor		4.98 \pm 2.26	3.91 \pm 1.77	0.022 (*)
SUV _{max}		12.24 \pm 4.01	9.43 \pm 3.29	0.001 (*)
Sex	Male	35	23	0.777
	Female	16	12	
Age, years	<65	34	21	0.527
	>65	17	14	
Smoking	Yes	20	18	0.263
	No	31	17	
Survival	No	5	3	0.847
	Yes	46	32	
T stage	T1	4	5	0.550
	T2	4	5	
	T3	18	11	
	T4	25	14	
N stage	0	4	1	0.286
	1	3	0	
	2	17	16	
	3	27	18	
EGFR mutation	Negative	37	18	0.045 (**)
	Positive	14	17	
Pleural metastasis	Yes	18	16	0.332
	No	33	19	
Lymph metastasis	Yes	12	4	0.157
	No	39	31	
Brain metastasis	Yes	5	2	0.496
	No	46	33	
Liver metastasis	Yes	6	3	0.635
	No	45	32	
Adrenal metastasis	Yes	3	4	0.355
	No	48	31	
Bone metastasis	Yes	26	17	0.826
	No	25	18	
Other lung metastasis	Yes	25	14	0.426
	No	25	20	

(*) Significance determined by t-test.

(**) Significance determined by Chi-square test.

PD-L1, programmed death-ligand 1; CEA, carcinoembryonic antigen; CYRFR 21-1, cytokeratin 19 fragment; SUV_{max}, maximum standard uptake value; T, tumor; N, node; EGFR, epidermal growth factor receptor; SD, standard deviation.

via observing changes in metabolism. SUV_{max} measured by ¹⁸F-FDG PET/CT has excellent reproducibility and is widely available; therefore, this measurement is often used to establish precise diagnoses, perform TNM staging, plan radiation therapy, and monitor therapeutic effects for lung cancers in comparison with other imaging modalities such as computed tomography, magnetic resonance imaging, and scintigraphy (10–12).

Takada et al. demonstrated that the metabolic features of lung cancers expressing PD-L1 on ¹⁸F-FDG PET/CT were associated

with other parameters, such as smoking status, pleural invasion, and SUV_{max} (13). In our study, we discovered no relationships between PD-L1 and smoking status, pleural invasion, or any other invasion type.

In our investigation, ¹⁸F-FDG PET/CT measurements were able to predict PD-L1 expression status in stage IV adenocarcinoma lung cancer patients, with an AUC of 0.681. This outcome differs slightly from results reported by Cui Y et al., who studied 73 patients with adenocarcinoma lung cancer and

found an AUC of 0.855 for the prediction of PD-L1 expression using SUV_{max} (14). This difference could be due to differences in the patient populations between these two studies.

SUV_{max} has been found to be a prognostic indicator for both early and advanced NSCLC (15). A meta-analysis revealed that a high SUV_{max} is associated with poor OS in patients with NSCLC (16). Although we obtained survival data from the stage IV patients in our study, the OS rate is still being evaluated. Preoperative SUV_{max} at the primary lesion is a more accurate indicator of nodal metastases when a cutoff of 3 is used (17). Almost all patients in our study had an $SUV_{max} > 3$ because they were all in stage IV with metastases. Increased PD-L1 expression is associated with worse prognosis in patients with NSCLC (18), supporting the concept that enhanced PD-L1 expression in tumor cells facilitates the evasion of host immune monitoring, promoting disease progression (19). However, Kerr et al. demonstrated that increased PD-L1 expression was associated with better OS in patients with resected NSCLC (20). Thus, high PD-L1 expression has been associated with both favorable and adverse prognoses (20). PD-L1 expression was associated with poorer OS prognosis in a study examining the relationships between PD-L1 expression and various clinicopathologic factors in 90 resected NSCLC patients, including various adenocarcinoma subtypes (21). The preoperative SUV_{max} at the primary lesion measured during ^{18}F -FDG PET/CT is a more efficient index of nodal metastasis than tumor size, and SUV_{max} can predict regional lymph node metastases (22).

In patients with early-stage lung cancer who are suitable for resection, preoperative SUV_{max} is associated with PD-L1 expression in NSCLC patients (22), as demonstrated in another study (13). An SUV_{max} of 8.6 is associated with PD-L1 expression (TPS 11%) and is an independent prognostic factor for OS in lung squamous cell carcinoma (23). Additionally, elevated PD-L1 expression and a high SUV_{max} (>11.2) are both independently associated with poor OS in surgical lung squamous cell carcinoma (24). A significant difference in OS was identified between individuals with lung adenocarcinoma with SUV_{max} of 2.9 (25).

Although clinical research studies examining the association between SUV_{max} and PD-L1 are limited, the findings remain controversial. Determining the relationship between PD-L1 expression and SUV_{max} can determine optimal treatment selection. Previous clinical trials have demonstrated that the expression of immune checkpoints, such as PD-L1, in various patient populations can predict treatment efficacy, including pembrolizumab vs. chemotherapy, pembrolizumab vs. platinum-based chemotherapy for advanced NSCLC (26–28). SUV_{max} is considerably higher in patients with positive PD-L1 expression than in those with negative PD-L1 expression (13). This finding suggests that combining the evaluation of PD-L1 expression and SUV_{max} in the primary tumor may help predict stage IV adenocarcinoma lung cancer prognosis.

Immuno-PET imaging may become a routine clinical assessment tool in this field in the near future. By defining

tumors using TKI-PET and immuno-PET, we can tailor NSCLC therapy (29). Whole-body PD-L1 PET can also be conducted on NSCLC (30). We could obtain more detailed information on PD-L1 expression by using immune-PET because immune-PET delays the resolution of unresolved issues. Immune-PET can provide more precise information regarding PD-L1 expression while also consistently collecting the SUV_{max} of the primary site. This study may gain increased significance in the future as this imaging method becomes more regularly used.

Several limitations existed in this study. First, this is a cross-sectional study, which did not allow us to evaluate the response to treatment PD-L1-targeted treatment. Additional studies with larger, externally validated cohorts remain needed to elucidate the value of PD-L1 and SUV_{max} for evaluating treatment and prognosis. Second, glutamine transporters (GLUT1) and hexokinase II should be included in future investigations. Further studies are also essential to evaluate the value of FDG PET/CT in predicting immunotherapy response.

CONCLUSION

The SUV measured in the primary lesion was valuable for predicting PD-L1 expression status in stage IV adenocarcinoma lung cancer patients. Therefore, SUV_{max} may play a role in predicting the efficacy of PD-L1 immunotherapy in patients with stage IV lung adenocarcinoma.

DATA AVAILABILITY STATEMENT

The original contributions presented in the study are included in the article/supplementary material, further inquiries can be directed to the corresponding authors.

ETHICS STATEMENT

This study was approved by the Ethics Committee of Hanoi Medical University (accession no. NCS02/HMU-IRB). The patients/participants provided their written informed consent to participate in this study.

AUTHOR CONTRIBUTIONS

BTC and PCP gave a substantial contribution in acquisition, analysis, and data interpretation. BTC, P-VT, and NMD prepared, drafted, and revised manuscript critically for important intellectual content. All authors gave the final approval of the version to be published and agreed to be accountable for all aspects of the work, ensuring that questions related to the accuracy or integrity of any part of the work are appropriately investigated and resolved.

REFERENCES

- Sung H, Ferlay J, Siegel RL, Laversanne M, Soerjomataram I, Jemal A, et al. Global cancer statistics 2020: GLOBOCAN estimates of incidence and mortality worldwide for 36 cancers in 185 countries. *CA Cancer J Clin.* (2021) 71:209–49. doi: 10.3322/caac.21660
- Siegel RL, Miller KD, Jemal A. Cancer statistics, 2018. *CA Cancer J Clin.* (2018) 68:7–30. doi: 10.3322/caac.21442
- Mielgo-Rubio X, Uribe-Larrea EA, Cortés LQ, Moyano MS. Immunotherapy in non-small cell lung cancer: update and new insights. *J Clin Transl Res.* (2021) 7:1–21.
- Iwai Y, Ishida M, Tanaka Y, Okazaki T, Honjo T, Minato N. Involvement of PD-L1 on tumor cells in the escape from host immune system and tumor immunotherapy by PD-L1 blockade. *Proc Natl Acad Sci U S A.* (2002) 99:12293–7. doi: 10.1073/pnas.192461099
- Zou W, Wolchok JD, Chen L. PD-L1 (B7-H1) and PD-1 pathway blockade for cancer therapy: Mechanisms, response biomarkers, and combinations. *Sci Transl Med.* (2016) 8:328rv4. doi: 10.1126/scitranslmed.aad7118
- Scheel AH, Ansén S, Schultheis AM, Scheffler M, Fischer RN, Michels S, et al. PD-L1 expression in non-small cell lung cancer: correlations with genetic alterations. *Oncoimmunology.* (2016) 5:e1131379. doi: 10.1080/2162402X.2015.1131379
- Li Z, Dong P, Ren M, Song Y, Qian X, Yang Y, et al. PD-L1 expression is associated with tumor FOXP3(+) regulatory T-cell infiltration of breast cancer and poor prognosis of patient. *J Cancer.* (2016) 7:784–93. doi: 10.7150/jca.14549
- Li Y, Liang L, Dai W, Cai G, Xu Y, Li X, et al. Prognostic impact of programmed cell death-1 (PD-1) and PD-ligand 1 (PD-L1) expression in cancer cells and tumor infiltrating lymphocytes in colorectal cancer. *Mol Cancer.* (2016) 15:55. doi: 10.1186/s12943-016-0539-x
- Calderaro J, Rousseau B, Amadeo G, Mercey M, Charpy C, Costentin C, et al. Programmed death ligand 1 expression in hepatocellular carcinoma: relationship with clinical and pathological features. *Hepatology.* (2016) 64:2038–46. doi: 10.1002/hep.28710
- Chao F, Zhang H. PET/CT in the staging of the non-small-cell lung cancer. *J Biomed Biotechnol.* (2012) 2012:783739. doi: 10.1155/2012/783739
- Gould MK, Kuschner WG, Rydzak CE, Maclean CC, Demas AN, Shigemitsu H, et al. Test performance of positron emission tomography and computed tomography for mediastinal staging in patients with non-small-cell lung cancer: a meta-analysis. *Ann Intern Med.* (2003) 139:879–92. doi: 10.7326/0003-4819-139-11-200311180-00013
- Li J, Xu W, Kong F, Sun X, Zuo X. Meta-analysis: accuracy of 18FDG PET-CT for distant metastasis staging in lung cancer patients. *Surg Oncol.* (2013) 22:151–5. doi: 10.1016/j.suronc.2013.04.001
- Takada K, Toyokawa G, Okamoto T, Baba S, Kozuma Y, Matsubara T, et al. Metabolic characteristics of programmed cell death-ligand 1-expressing lung cancer on ¹⁸F-fluorodeoxyglucose positron emission tomography/computed tomography. *Cancer Med.* (2017) 6:2552–61. doi: 10.1002/cam4.1215
- Cui Y, Li X, Du B, Diao Y, Li Y. PD-L1 in lung adenocarcinoma: insights into the role of ¹⁸F-FDG PET/CT. *Cancer Manag Res.* (2020) 12:6385–95. doi: 10.2147/CMARS.256871
- Billè A, Okiror L, Skanjeti A, Errico L, Arena V, Penna D, et al. The prognostic significance of maximum standardized uptake value of primary tumor in surgically treated non-small-cell lung cancer patients: analysis of 413 cases. *Clin Lung Cancer.* (2013) 14:149–56. doi: 10.1016/j.clcc.2012.04.007
- Liu J, Dong M, Sun X, Li W, Xing L, Yu J. Prognostic value of 18F-FDG PET/CT in surgical non-small cell lung cancer: a meta-analysis. *PLoS ONE.* (2016) 11:e0146195. doi: 10.1371/journal.pone.0146195
- Nakamura H, Saji H, Marushima H, Kimura H, Tagaya R, Kurimoto N, et al. Standardized uptake values in the primary lesions of non-small-cell lung cancer in FDG-PET/CT can predict regional lymph node metastases. *Ann Surg Oncol.* (2015) 22 Suppl 3:S1388–93. doi: 10.1245/s10434-015-4564-6
- Kim H, Kwon HJ, Park SY, Park Y, Park E, Chung JH. Clinicopathological analysis and prognostic significance of programmed cell death-ligand 1 protein and mRNA expression in non-small cell lung cancer. *PLoS One.* (2018) 13:e0198634. doi: 10.1371/journal.pone.0198634
- Wang J, Yuan R, Song W, Sun J, Liu D, Li Z. PD-1, PD-L1 (B7-H1) and tumor-site immune modulation therapy: the historical perspective. *J Hematol Oncol.* (2017) 10:34. doi: 10.1186/s13045-017-0403-5
- Kerr KM, Thunnissen E, Dafni U, Finn SP, Bubendorf L, Soltermann A, et al. A retrospective cohort study of PD-L1 prevalence, molecular associations and clinical outcomes in patients with NSCLC: results from the European Thoracic Oncology Platform (ETOP) lungscape project. *Lung Cancer.* (2019) 131:95–103. doi: 10.1016/j.lungcan.2019.03.012
- Miyazawa T, Marushima H, Saji H, Kojima K, Hoshikawa M, Takagi M, et al. PD-L1 expression in non-small-cell lung cancer including various adenocarcinoma subtypes. *Ann Thorac Cardiovasc Surg.* (2019) 25:1–9. doi: 10.5761/atcs.0a.18-00163
- Kudo Y, Shimada Y, Saji H, Kato Y, Yoshida K, Matsubayashi J, et al. Prognostic factors for survival after recurrence in patients with completely resected lung adenocarcinoma: important roles of epidermal growth factor receptor mutation status and the current staging system. *Clin Lung Cancer.* (2015) 16:e213–21. doi: 10.1016/j.clcc.2015.04.005
- Kasahara N, Kaira K, Bao P, Higuchi T, Arisaka Y, Erkhem-Ochir B, et al. Correlation of tumor-related immunity with 18F-FDG-PET in pulmonary squamous-cell carcinoma. *Lung Cancer.* (2018) 119:71–7. doi: 10.1016/j.lungcan.2018.03.001
- Zhang M, Wang D, Sun Q, Pu H, Wang Y, Zhao S, et al. Prognostic significance of PD-L1 expression and ¹⁸F-FDG PET/CT in surgical pulmonary squamous cell carcinoma. *Oncotarget.* (2017) 8:51630–40. doi: 10.18632/oncotarget.18257
- Kaira K, Shimizu K, Kitahara S, Yajima T, Atsumi J, Kosaka T, et al. 2-Deoxy-2-[fluorine-18] fluoro-d-glucose uptake on positron emission tomography is associated with programmed death ligand-1 expression in patients with pulmonary adenocarcinoma. *Eur J Cancer.* (2018) 101:181–90. doi: 10.1016/j.ejca.2018.06.022
- Reck M, Rodríguez-Abreu D, Robinson AG, Hui R, Csoszi T, Fülöp A, et al. Pembrolizumab versus chemotherapy for PD-L1-positive non-small-cell lung cancer. *N Engl J Med.* (2016) 375:1823–33. doi: 10.1056/NEJMoa1606774
- Reck M, Rodríguez-Abreu D, Robinson AG, Hui R, Csoszi T, Fülöp A, et al. Updated analysis of KEYNOTE-024: pembrolizumab versus platinum-based chemotherapy for advanced non-small-cell lung cancer with PD-L1 tumor proportion score of 50% or greater. *J Clin Oncol.* (2019) 37:537–46. doi: 10.1200/JCO.18.00149
- Mok TSK, Wu YL, Kudaba I, Kowalski DM, Cho BC, Turna HZ, et al. Pembrolizumab versus chemotherapy for previously untreated, PD-L1-expressing, locally advanced or metastatic non-small-cell lung cancer (KEYNOTE-042): a randomised, open-label, controlled, phase 3 trial. *Lancet.* (2019) 393:1819–30. doi: 10.1016/S0140-6736(18)32409-7
- Bahce I, Yaqub M, Smit EF, Lammertsma AA, van Dongen GA, Hendrikse NH. Personalizing NSCLC therapy by characterizing tumors using TKI-PET and immuno-PET. *Lung Cancer.* (2017) 107:1–13. doi: 10.1016/j.lungcan.2016.05.025
- Niemeijer AN, Leung D, Huisman MC, Bahce I, Hoekstra OS, van Dongen GAMS, et al. Whole body PD-1 and PD-L1 positron emission tomography in patients with non-small-cell lung cancer. *Nat Commun.* (2018) 9:4664. doi: 10.1038/s41467-018-07131-y

Conflict of Interest: The authors declare that the research was conducted in the absence of any commercial or financial relationships that could be construed as a potential conflict of interest.

Publisher's Note: All claims expressed in this article are solely those of the authors and do not necessarily represent those of their affiliated organizations, or those of the publisher, the editors and the reviewers. Any product that may be evaluated in this article, or claim that may be made by its manufacturer, is not guaranteed or endorsed by the publisher.

Copyright © 2022 Tien Cong, Cam Phuong, Thai, Thuong, Quang Hung, Hang, Anh Tuan, Minh Khuy, Tuyen and Minh Duc. This is an open-access article distributed under the terms of the Creative Commons Attribution License (CC BY). The use, distribution or reproduction in other forums is permitted, provided the original author(s) and the copyright owner(s) are credited and that the original publication in this journal is cited, in accordance with accepted academic practice. No use, distribution or reproduction is permitted which does not comply with these terms.



18F-FDG /18F-Choline Dual-Tracer PET Behavior and Tumor Differentiation in HepatoCellular Carcinoma. A Systematic Review

Jérôme Ghidaglia^{1*}, Nicolas Golse^{2,3}, Alina Pascale², Mylène Sebah⁴ and Florent L. Besson^{1,5,6}

¹ Department of Biophysics and Nuclear Medicine-Molecular Imaging, Hôpitaux Universitaires Paris-Saclay, Assistance Publique-Hôpitaux de Paris, Le Kremlin-Bicêtre, France, ² Centre Hépatobiliaire, Hôpitaux Universitaires Paris-Saclay, Assistance Publique-Hôpitaux de Paris, Villejuif, France, ³ Université Paris-Saclay, INSERM, Physiopathogénèse et Traitement des Maladies du Foie, UMR-S 1193, Gif-sur-Yvette, France, ⁴ Department of Pathology, Hôpitaux Universitaires Paris-Saclay, Assistance Publique-Hôpitaux de Paris, Le Kremlin-Bicêtre, France, ⁵ Université Paris-Saclay, School of Medicine, Le Kremlin-Bicêtre, France, ⁶ Université Paris-Saclay, CEA, CNRS, Inserm, BioMaps, Orsay, France

OPEN ACCESS

Edited by:

Francesco Cicone,
Magna Graecia University, Italy

Reviewed by:

Giorgio Treglia,
Ente Ospedaliero Cantonale (EOC),
Switzerland
Lucia Baratto,
Stanford University, United States

*Correspondence:

Jérôme Ghidaglia
jerome.ghidaglia@gmail.com

Specialty section:

This article was submitted to
Nuclear Medicine,
a section of the journal
Frontiers in Medicine

Received: 20 April 2022

Accepted: 07 June 2022

Published: 07 July 2022

Citation:

Ghidaglia J, Golse N, Pascale A,
Sebah M and Besson FL (2022)
18F-FDG /18F-Choline Dual-Tracer
PET Behavior and Tumor
Differentiation in HepatoCellular
Carcinoma. A Systematic Review.
Front. Med. 9:924824.
doi: 10.3389/fmed.2022.924824

Background: Post-operative recurrence remains the strongest prognostic factor of resected hepatocellular carcinoma (HCC), making the accurate selection of patients with curable HCC a crucial issue. PET imaging combining both 18F-FDG and fatty acid synthase (FAS) radiotracers—such as Choline—has shown its interest for the initial staging and therapeutic management of patients with HCC, but its use is still not consensual. Importantly, the very first dual-tracer PET studies suggested 18F-FDG/FAS PET behavior be linked to the degree of differentiation of HCC, a major predictive factor of post-operative recurrence. Although this key molecular imaging concept may impact how dual-tracer PET will be used in early-stage HCC, its level of evidence remains largely unexplored. In this study, we conducted a systematic review of the available evidence-based data to clarify the relevance of dual 18F-FDG/18F-Choline PET in characterizing the degree of differentiation of HCC tumors.

Methods: A systematic search of the PubMed/Medline and Embase databases was performed up to November 2021. A systematic review of the dual-tracer 18F-FDG/18F-Choline PET behavior of histology-proven HCC according to their degree of differentiation was conducted. The overall quality of the included studies was critically assessed based on the STROBE guidelines. Information on study date, design, patient cohort characteristics, grade of differentiation of HCC tumors, and the dual-tracer PET behavior per HCC was independently extracted and summarized.

Results: From 440 records initially available, 6 full-text articles (99 histology-proven HCC) provided dual-tracer 18F-FDG/18F-Choline PET behavior per HCC tumor grade were included in the systematic review. Based on our analysis, 43/99 HCCs were

reported to be well-differentiated, and 56/99 HCCs were reported to be less-differentiated tumors. In the well-differentiated subgroup, more than half were exclusively positive for 18F-Choline (51%), whereas 39% were positive for both 18F-FDG and 18F-Choline. In the less-differentiated subgroup, 37% of HCC patients were positive exclusively for FDG, 36% were positive for both 18F-FDG and 18F-Choline, and 25% were positive exclusively for 18F-Choline.

Conclusion: The 18F-FDG/18F-Choline dual-tracer PET behavior of uptake shows high overlap between well- and less differentiated HCC, making the characterization of tumors challenging based on such PET combination alone. Given our growing knowledge of the molecular complexity of HCC, further studies are necessary to refine our understanding of radiotracers' behavior in this field and improve the usefulness of PET imaging in the clinical decision process of HCC.

Keywords: HCC, PET, FDG, choline, molecular imaging

INTRODUCTION

Hepatocellular carcinoma (HCC), the most common primary liver cancer and the third leading cause of cancer death worldwide, represents a major health challenge (1). Chronic liver disease—cirrhosis—which can be related to alcohol, NASH, HBV or HCV infection, or less frequently primary biliary cholangitis, hemochromatosis, or α 1-antitrypsin deficiency, is the strongest risk factor of HCC development, concerning more than 90% of the cases. The treatment strategy is currently mainly driven by the Barcelona Clinic Liver Cancer staging system (BCLC), a five-stage classification scale integrating the characteristics of the primary tumor (size, number of nodules), the disease extent (portal invasion, N+ and M+ status), the liver function (Child-Pugh), and the performance status (ECOG). Very early and early-stage HCC patients may benefit from various curative options (resection, ablation or liver transplantation), whereas more advanced stages are candidate to chemoembolization, systemic therapies including immunotherapy, or best supportive care. In early-stage HCC, post-operative recurrence remains the strongest survival prognostic factor (2) making the accurate selection of patients with curable HCC a crucial issue. Tumor differentiation is a major predictive factor of post-operative recurrence in HCC (3, 4). However, the histological analysis of tumor differentiation, which remains the gold standard, is currently carried out only in atypical cases. Conventional imaging is essential for the management of HCC patients (5–8), but its limited value in such atypical cases and the need for non-invasive biomarkers of tumor differentiation have progressively motivated the use of PET imaging in this field (9), while this functional imaging is still not consensually recommended. Because 18F-fluorodeoxyglucose (18F-FDG) shows mitigated performance to detect HCC (10, 11) but excellent specificity for HCC metastases (9), PET radiotracers of fatty acid synthase (FAS) have been proposed as complements,

such radiolabeled choline, the most widely used FAS-targeted radiotracer in clinical practice (12, 13). Although 18F-FDG and FAS PET radiotracers have shown their complementarity for the initial staging and treatment management of HCC patients (14–17) their combined use is still not consensual, making dedicated recommendations challenging (18).

The very first dual 18F-FDG/18F-Choline PET studies suggested 18F-FDG/FAS PET behavior be linked to the degree of differentiation of HCC tumors (19, 20). Although this key concept could impact the rational for using dual-tracer PET in HCC, its level of evidence remains largely unexplored. In this study, we conducted a systematic review of the available evidence-based data, to clarify whether ^{18}F -FDG/ ^{18}F -Choline dual-tracer PET behavior is a relevant imaging biomarker of tumor differentiation in HCC.

METHODS

This methodological study was conducted according to the PRISMA 2020 statement for systematic review reports (21).

Search Strategy

Two authors (JG and FLB) independently performed a comprehensive search of PubMed/Medline and Embase databases to find studies using 18F-FDG and 18F-Choline dual PET tracers for HCC purposes. The search strategy combined the following keywords: “HCC + PET” or “HCC + FDG” AND “HCC + Choline.” No starting date was used, and the search procedure was updated until 10 November 2021. Moreover, references of the retrieved articles were also screened for additional studies. The inclusion criteria were as follows: (i) articles exclusively in English; (ii) the combined use of 18F-FDG and 18F/11C-Choline dual PET tracers for each HCC tumor, in order to assess the dual-tracer PET behavior without a priori; (iii) histology-confirmed HCC diagnosis; and (iv) available description of HCC differentiation for each patient. All the articles not fulfilling the inclusion criteria mentioned above, together with review articles, editorials, letters, comments, or case reports, were excluded from

Abbreviations: PET, Positron emission tomography; HCC, Hepatocellular carcinoma; 18F-FDG, 18F-Fluorodeoxyglucose; FAS, Fatty acid synthase; BCLC, Barcelona Clinic Liver Cancer staging system; NASH, Non-Alcoholic SteatoHepatitis; HBV, Hepatitis B Virus; HCV, Hepatitis C Virus; SUV, Standard Uptake Value.

the analysis. For each eligible study, the following information was independently extracted: study date; design; patient cohort characteristics, including sample size, number of patients with HCC, and number of HCC lesions per patient confirmed by histology (either by surgery or biopsy); delay time between the 18F-FDG and 18F-Choline PET acquisitions; histological differentiation of HCC; and dual PET radiotracer behavior of HCC patients per histological subtype. For all included studies, the same predefined definition of PET positivity was considered: any focal uptake superior to the locoregional background was considered positive, whereas iso or hypometabolic lesions were considered negative for the radiotracer of interest.

Quality Assessment of the Studies

The overall quality of each included study was critically assessed by two authors (JG and FLB) based on the “STROBE guidelines” (22). Because the dual PET tracer behavior according to the level of differentiation of HCC was never considered the primary outcome, a general standardized checklist of 22 items covering the overall quality statements of non-interventional studies (22) was independently applied by the two readers as follows: each item was quoted “yes” if present, “no” if absent, or “unclear” if the statement was equivocal. All disagreements between the two readers were resolved by consensus.

Ethics and Data

The need for ethical approval was waived due to the nature of the study (review article).

RESULTS

Literature Search

The PRISMA flow diagram of the literature search is provided in **Figure 1**. The comprehensive literature search from PubMed/MEDLINE and Embase identified the following records: 440 records using the “HCC + PET CT” keywords; 353 records using the “HCC + FDG” keywords; 192 records using the “HCC + Choline” keywords; and 19 records using the “HCC + FDG + Choline” keywords. Among the 19 articles, 12 were discarded due to study type (reviews $n = 4$), analysis of metastatic disease ($n = 1$), cholangiocarcinoma study ($n = 1$), use of Choline only in 18F-FDG-negative patients ($n = 1$), and preclinical studies ($n = 2$). At the end of the screening process, 7 full-text articles were retrieved. Among them, one article was discarded because no explicit HCC differentiation status per patient was provided (23), and two studies presented patient data overlap (20, 24). Of the two studies with patient data overlap, we discarded the second study (24). Finally, 6 full-text articles over the last 15 years (2006–2021) were included in the systematic review (14, 16, 19, 20, 25, 26).

Methodological Quality of the Included Studies

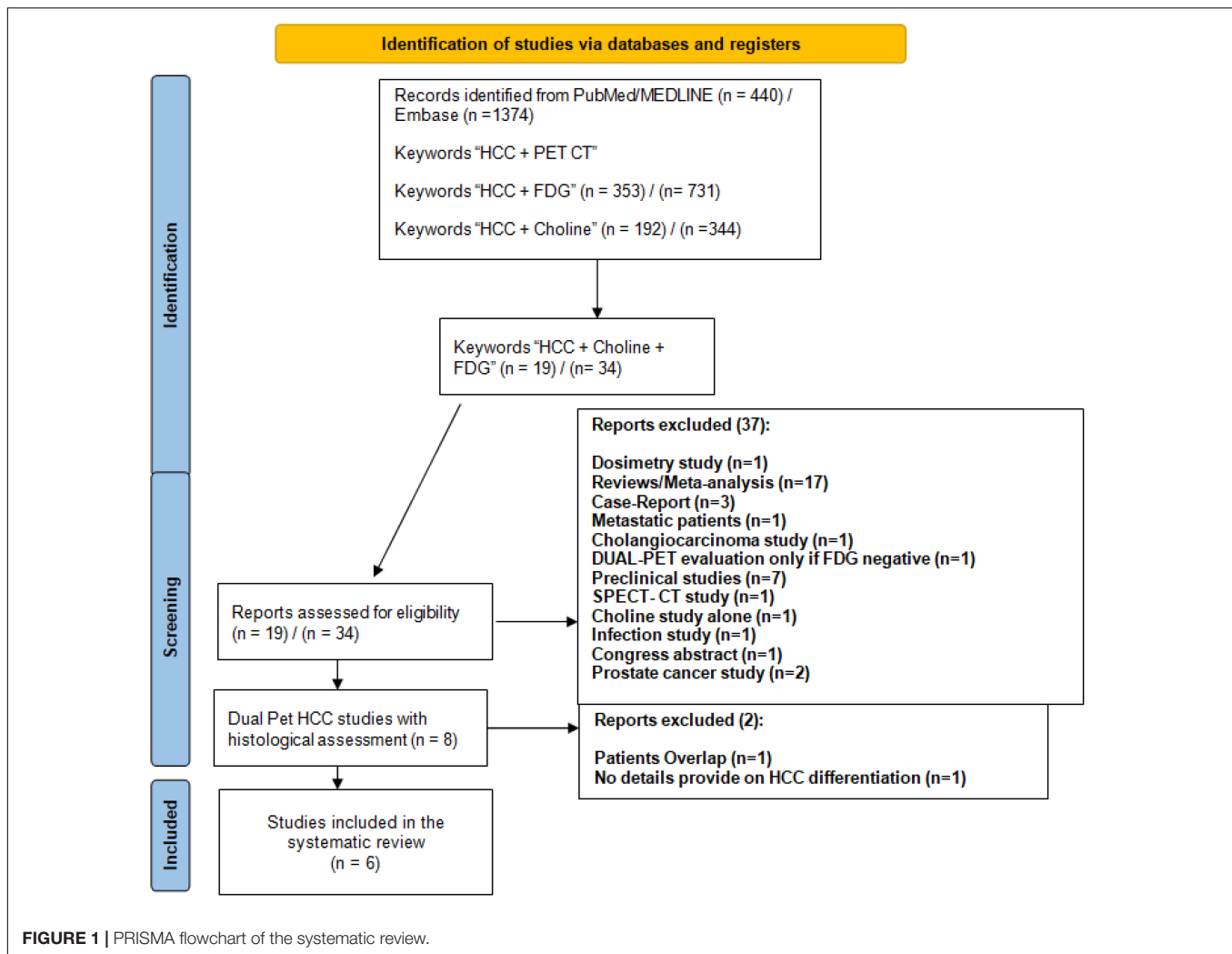
The overall quality assessment of the 6 included studies is shown in **Figure 2**. The studies were of limited quality with 12

items (55%) considered present (range = 9–16), 3 items (14%) considered absent (range = 0–6) and 6 items (27%) considered unclear after a double blinded reading (range = 5–11). In particular, only two studies provided a majority of unequivocal item statements for the results section (19, 26), and one study provided unclear or no information for the majority of the STROBE statements of the discussion section (25). Considering these statements, the level of evidence for the dedicated use of dual 18F-FDG/18F-Choline PET tracer for the characterization of HCC differentiation was considered a level 4–5 (grade C-D of recommendation) according to the Oxford Centre for Evidence-Based Medicine.

Qualitative Analysis (Systematic Review)

The main characteristics of the 6 included studies are provided in **Table 1**. The primary outcomes were as follows: the detection rate of 18F-FDG and 18F-Choline PET tracers for HCC tumors (16, 19); the diagnostic performance of 18F-FDG and 18F-Choline PET tracers for detecting and staging HCC in patients with chronic liver disease (14, 20); and the assessment of dual 18F-FDG and 18F-Choline PET with perfusion CT behaviors of HCC tumors (25). The dual radiotracer PET data of 99 biopsy-proven HCC patients were reanalyzed. The study samples were mainly limited with only two prospective studies reaching more than 20 histologically proven HCC samples (14, 20). Talbot et al. (20) included a case mix of 34 HCC patients (27 biopsy proven), 2 hepato-cholangiocarcinoma patients, 10 patients with other malignancies, and 8 patients with benign conditions. Castilla-Lièvre et al. (14) included 38 HCC patients (22 biopsy proven) with 4 cholangiocarcinoma patients and one adenoma patient. The other 4 studies exclusively focused on HCC patients. Among the pooled 99 HCC tumors, 43 were considered well-differentiated tumors, and 56 were considered moderate to poorly differentiated tumors. The classification used for tumor differentiation (Edmonson Steiner or WHO) was mentioned for only 57% of the HCC tumors as follows: biopsy for 14 HCC tumors (14, 16) surgery for 37 HCC tumors (14, 19), and a case mix of biopsy/surgery for the rest of the dataset without any information concerning the ratio. Additionally, 50 HCC patients were explicitly qualified as having unifocal HCC tumors (14, 16, 19), and 25 HCC patients were explicitly qualified as having multifocal HCC tumors (14, 16, 19, 25). In all studies, PET positivity was defined visually as non-physiological focal liver radiotracer uptake in four studies (14, 16, 19, 25), whereas one study also proposed a “photopenic” pattern for Choline PET positivity (20).

The 18F-FDG and 18F-Choline PET tumor behaviors according to the differentiation of the tumors are shown in **Table 2**. In the well-differentiated subgroup, 51% were exclusively positive for 18F-Choline, 39% were positive for both 18F-FDG and 18F-Choline, and only 5% were exclusively positive for FDG. Two patients were negative for the two PET radiotracers (20, 26). In the poorly differentiated subgroup, 37% of HCC patients were exclusively positive for 18F-FDG, 36% were positive for both 18F-FDG and 18F-Choline, and 25% were exclusively positive for Choline. One patient was considered negative for both radiotracers (20).



Five studies also performed SUV-based semiquantitative analyses (14, 16, 19, 25, 26) with discrepant results. In one study, no significant difference was observed between the 18F-FDG or 18F-Choline signal-to-noise ratio irrespective of the HCC level of differentiation (16). Yamamoto et al. found no significant difference in radiotracer uptake between the histological subgroups (19). Tulin et al. reported a significant difference in radiotracer uptake according to the liver areas (well-differentiated HCC, poorly differentiated HCC, or normal parenchyma) (25). Chotipanich et al. found a significant difference between well- and poorly differentiated HCC only for ^{18}F -FDG (26). The last study did not perform any comparative analyses (14).

DISCUSSION

Based on our analysis of the literature data, well-differentiated HCC patients were positive for ^{18}F -FDG in approximately 44% of the reported cases and positive for 18F-Choline in 90% of the reported cases. For the less-differentiated HCC tumors (moderate

to poorly differentiated HCC), 73% of reported HCC cases were 18F-FDG-positive, and 61% of reported HCC cases were ^{18}F -Choline-positive. Among the 56 less differentiated tumors considered in the present study, 16 were explicitly mentioned as poorly differentiated HCC, of which 100% were 18F-FDG-positive and 31% were 18F-Choline-positive. However, the 8 poorly differentiated tumors all considered 18F-FDG-positive and 18F-Choline-negative in one study had no information regarding the motivation of their inclusion criteria (25). Focusing on the 8 remaining poorly differentiated HCC patients (16, 19, 26), 100% were reported to be positive for 18F-FDG, of whom 63% were also positive for 18F-Choline. Moreover, more than one-third of patients showed dual PET tracer positivity regardless of the degree of HCC differentiation.

A trend toward an inverse gradient of dual-PET HCC tumor behavior has been previously suggested (16, 20), but our systematic review showed that a strong mirrored dual-PET tumor behavior according to HCC differentiation should be considered with caution. First, the lack of standardized histological grading of HCC remains a major issue. Although Edmonson Steiner and WHO classifications share similarities (4-level grades and

	Talbot 2006	Yamamoto 2008	Talbot 2010	Lièvre-Castilla 2015	Chotipanich 2016	Tulin 2017
Title & abstract						
Introduction						
Background						
Objectives						
Methods						
Study design						
Setting						
Participants						
Variables						
Data source / measurements						
Bias						
Study size						
Quantitative variables						
Statistical methods						
Results						
Participants						
Descriptive data						
Outcome data						
Main results						
Other analyses						
Discussion						
Key results						
Limitations						
Interpretation						
Generalizability						
Other Information						
Funding						



 Yes
 No
 Unclear

FIGURE 2 | STROBE quality assessment.

structural/cellular features), the respective definitions for well- and less differentiated grades are not fully concordant with a related impact on subgroup outcomes (27). In our systematic review, only two of the six included studies explicitly mentioned either Edmonson Steiner (19) or WHO (14) classifications (39% of the included HCC). As 61% of the biopsy-proven reported HCC cases were potentially a blinded case mix of ES/WHO definitions, any generalizability of 18F-FDG/18F-Choline dual PET tracer behavior according to HCC grading would be

ambiguous. Second, a significant association between glucose metabolism assessed by FDG PET and microvascular invasion (MVI), another strong prognostic factor in HCC (28, 29), has been widely reported (23, 30–32). Surprisingly, Kornberg et al. reported that 14 of the 16 HCC patients who were positive for 18F-FDG PET had MVI (87.5%), of whom only 1/3 were poorly differentiated (5 patients) (30). Although an extensive review by Gouw et al. showed that high-grade tumors but also tumor size and number of nodules to be predictive of MVI (33), MVI has also

TABLE 1 | Characteristics of the included studies with dual PET tracer.

References	Country	Design	HCC patients	Histology proven HCC	Delay time between the two PETs
Talbot et al. (16)	France	prospective	9	7	1 Week
Yamamoto et al. (19)	Japan	retrospective	12	16	2 Weeks
Talbot et al. (20)	France	prospective	34	27	1–4 Weeks
Castilla-Lièvre et al. (14)	France	prospective	38	22	0–2.5 Weeks
Chotipanich et al. (26)	Thailand	prospective	12	9	Unknown
Tulin et al. (25)	Russia	retrospective	18	18	Unknown
Total			111	99	

Patients who underwent dual PET tracers exclusively. Histology was confirmed by either surgery or tumor biopsy.

TABLE 2 | Dual PET radiotracer behaviors function of HCC level of differentiation.

References	HCC	Grade of tumor differentiation							
		Well differentiated				Moderate-poorly differentiated			
		Ch+/FDG–	Ch–/FDG+	Ch+/FDG+	Ch–/FDG–	Ch+/FDG–	Ch–/FDG+	Ch+/FDG+	Ch–/FDG–
Talbot et al. (16)	7	3/4	0/4	1/4	0/4	0/3	0/3	3/3	0/3
Yamamoto et al. (19)	16	0/0	0/0	0/0	0/0	8/16	6/16	2/16	0/16
Talbot* et al. (20)	27	6/11	1/11	4/11	0/11	2/16	4/16	9/16	1/16
Castilla-Lièvre et al. (14)	22	11/16	1/16	3/16	1/16	4/6	2/6	0/6	0/6
Chotipanich et al. (26)	9	2/6	0/6	3/6	1/6	0/3	1/3	2/3	0/3
Tulin* et al. (25)	18	0/6	0/6	6/6	0/6	0/12	8/12	4/12	0/12
Total	99	22/43 (51%)	2/43 (5%)	17/43 (39%)	2/43 (5%)	14/56 (25%)	21/56 (37%)	20/56 (36%)	1/56 (2%)

*Because its biological significance is currently unknown, photopenic lesions on Choline were not considered positive here.

#In this study, the tumor to liver ratio was assessed based on the quantitative data provided. A ratio > 1 was considered positive.

been reported in 29% of HCCs with a size ranging from 2 to 5 cm (34). Sabaté-Llobera et al. reported that the ratios of well- to less differentiated tumors ranged from 1.3 in the 18F-FDG-positive group to 5.7 in the 18F-FDG-negative group (31). However, nearly 50% of 18F-FDG-positive cases in the present study were well-differentiated HCC. Consequently, ¹⁸F-FDG PET positivity may reflect both MVI and tumor differentiation, which are two prognostic factors that are not highly interlinked. Third, studies by Okazumi, Torizuka, and Trojan (35–37) have suggested that a loss of FDG 6-phosphatase activity in undifferentiated tumor cells explains the higher 18F-FDG avidity of poorly differentiated HCC. Importantly, the studies by Okazumi and Torizuka were mainly dynamic PET studies (35, 36). The tissue behavior of advanced PET kinetic parameters, especially k3 or k4 microparameters, cannot be directly extrapolated to static PET metrics, such as SUV, a surrogate of the glucose retention index in cells. Trojan et al. reported that the 18F-FDG uptake (SUV) was more efficient not only in poorly differentiated tumors but also in large tumors and elevated AFP (37). In particular, the vast majority of the reported FDG-positive tumors also showed multiple nodules, all being predictive factors of MVI (38).

Evidence-based analysis of the literature over the past 20 years suggests complex interlinks between tumor grade and MVI, and the related FDG PET behaviors in HCC patients. In contrast, 18F-Choline appears not as informative as 18F-FDG to characterize tumor aggressiveness in HCC patients. In 29 HCC patients, Mulé et al. showed a higher 18F-FDG uptake for MVI-positive HCC

cases compared to MVI-negative HCC cases (SUVr 2.65 vs. 1, $p = 0.003$) without any significant difference in 18F-Choline uptake (39). This lack of prognostic significance of 18F-Choline was also reported by Castilla-Lièvre et al. (14). Notably, a combined photopenic 18F-Choline with a positive 18F-FDG-PET pattern has been suggested to be a pejorative prognostic factor of HCC recurrence (24). In light of this methodological review, the question of the leading prognostic value of 18F-FDG PET arises. The biological significance of glucose- and Choline-based PET tracer behaviors in HCC patients remains poorly understood.

Recently, a better understanding of biological pathways of HCC tumors has led to the emergence of a new molecular-based classification of HCC, dichotomizing the tumors into proliferation and non-proliferation classes based on their multidimensional molecular pattern (40–45). While the proliferative class is characterized by poorly differentiated tumors, high vascular invasion, and elevated AFP, the non-proliferative class corresponds to well to moderately differentiated tumors, less vascular invasion, and lower level of AFP. In both groups, the characteristics of T-cell infiltrates further define four immune-related subclasses (46). Because the characterization of tumor heterogeneity at the molecular level is emerging in HCC (47, 48), the powerful capabilities of vectorized PET molecular imaging in this field would gain in relevance. Although several 18F-FDG/FAS studies emphasize the clinical usefulness of PET to manage HCC patients (17, 49), future

multitracer PET studies are mandatory to better understand the deep biological meaning of multitracer PET behavior in this field.

Our systematic review had several limitations. The limited number of dual 18F-FDG/18F-Choline PET articles with available per patient-based HCC tumor differentiation hampered any quantitative analysis. However, our pooled semiquantitative analysis revealed the high overlap of 18F-FDG/18F-Choline PET behavior between well- and less differentiated HCC. Additionally, we did not include acetate PET studies in this systematic review (11, 50–52). Initially, evaluated in cardiac (53) and urological oncology settings (54, 55), acetate shows a biodistribution quite similar to that of Choline. Although both substrates are fed into fatty acid synthesis, also known as the Kennedy pathway (56–58), Choline and acetate have various other biological functions (59, 60), making them not strictly comparable. Additionally, ¹⁸F-Choline is currently the most widely used FAS-targeted PET tracer of HCC in clinical practice, which is why we focused on this PET radiotracer in this study.

REFERENCES

- Sung H, Ferlay J, Siegel RL, Laversanne M, Soerjomataram I, Jemal A, et al. Global cancer statistics 2020: GLOBOCAN estimates of incidence and mortality worldwide for 36 cancers in 185 countries. *CA Cancer J Clin.* (2021) 71:209–49. doi: 10.3322/caac.21660
- Colecchia A. Prognostic factors for hepatocellular carcinoma recurrence. *World J Gastroenterol.* (2014) 20:5935.
- Imamura H, Matsuyama Y, Tanaka E, Ohkubo T, Hasegawa K, Miyagawa S, et al. Risk factors contributing to early and late phase intrahepatic recurrence of hepatocellular carcinoma after hepatectomy. *J Hepatol.* (2003) 38:200–7. doi: 10.1016/s0168-8278(02)00360-4
- Cucchetti A, Piscaglia F, Caturelli E, Benvegnù L, Vivarelli M, Ercolani G, et al. Comparison of recurrence of hepatocellular carcinoma after resection in patients with cirrhosis to its occurrence in a surveilled cirrhotic population. *Ann Surg Oncol.* (2009) 16:413–22. doi: 10.1245/s10434-008-0232-4
- Chernyak V, Fowler KJ, Kamaya A, Kielar AZ, Elsayes KM, Bashir MR, et al. Liver imaging reporting and data system (LI-RADS) version 2018: imaging of hepatocellular carcinoma in at-risk patients. *Radiology.* (2018) 289:816–30. doi: 10.1148/radiol.2018181494
- van der Pol CB, Lim CS, Sirlin CB, McGrath TA, Salameh JP, Bashir MR, et al. Accuracy of the liver imaging reporting and data system in computed tomography and magnetic resonance image analysis of hepatocellular carcinoma or overall malignancy—a systematic review. *Gastroenterology.* (2019) 156:976–86. doi: 10.1053/j.gastro.2018.11.020
- Llovet JM, Lencioni R. mRECIST for HCC: performance and novel refinements. *J Hepatol.* (2020) 72:288–306. doi: 10.1016/j.jhep.2019.09.026
- Llovet JM, Villanueva A, Marrero JA, Schwartz M, Meyer T, Galle PR, et al. Trial design and endpoints in hepatocellular carcinoma: AASLD consensus conference. *Hepatology.* (2021) 73:158–91. doi: 10.1002/hep.31327
- Sharma B, Martin A, Zerizer I. Positron emission tomography-computed tomography in liver imaging. *Semin Ultrasound CT MR.* (2013) 34:66–80.
- Khan MA, Combs CS, Brunt EM, Lowe VJ, Wolverson MK, Solomon H, et al. Positron emission tomography scanning in the evaluation of hepatocellular carcinoma. *J Hepatol.* (2000) 32:792–7. doi: 10.1016/s0168-8278(00)80248-2
- Park JW, Kim JH, Kim SK, Kang KW, Park KW, Choi JI, et al. A prospective evaluation of 18F-FDG and 11C-acetate PET/CT for detection of primary and metastatic hepatocellular carcinoma. *J Nucl Med.* (2008) 49:1912–21. doi: 10.2967/jnumed.108.055087
- Bertagna F, Bertoli M, Bosio G, Biasiotto G, Sadeghi R, Giubbini R, et al. Diagnostic role of radiolabelled choline PET or PET/CT in hepatocellular carcinoma: a systematic review and meta-analysis. *Hepatol Int.* (2014) 8:493–500. doi: 10.1007/s12072-014-9566-0
- Signore G, Nicod-Lalonde M, Prior JO, Bertagna F, Muoio B, Giovannella L, et al. Detection rate of radiolabelled choline PET or PET/CT in hepatocellular

CONCLUSION

The 18F-FDG/18F-Choline dual-tracer PET behavior of uptake shows high overlap between well- and less differentiated HCC, making the characterization of tumors challenging based on such PET combination alone. Given our growing knowledge of the molecular complexity of HCC, further studies are necessary to refine our understanding of radiotracers' behavior in this field and improve the usefulness of PET imaging in the clinical decision process of HCC.

AUTHOR CONTRIBUTIONS

All authors: design, acquisition analysis, revising for intellectual content, final approval, and agreement to be accountable for all aspects of this work (accuracy and integrity of any part of the work).

- carcinoma: an updated systematic review and meta-analysis. *Clin Transl Imaging.* (2019) 7:237–53.
- Castilla-Lièvre MA, Franco D, Gervais P, Kuhnast B, Agostini H, Marthey L, et al. Diagnostic value of combining ¹¹C-choline and ¹⁸F-FDG PET/CT in hepatocellular carcinoma. *Eur J Nucl Med Mol Imaging.* (2016) 43:852–9. doi: 10.1007/s00259-015-3241-0
- Wu HB, Wang QS, Li BY, Li HS, Zhou WL, Wang QY. F-18 FDG in conjunction with 11C-choline PET/CT in the diagnosis of hepatocellular carcinoma. *Clin Nucl Med.* (2011) 36:1092–7. doi: 10.1097/RLU.0b013e3182335df4
- Talbot JN, Gutman F, Fartoux L, Grange JD, Ganne N, Kerrou K, et al. PET/CT in patients with hepatocellular carcinoma using [(18)F]fluorocholine: preliminary comparison with [(18)F]FDG PET/CT. *Eur J Nucl Med Mol Imaging.* (2006) 33:1285–9. doi: 10.1007/s00259-006-0164-9
- Chalaye J, Costentin CE, Luciani A, Amaddeo G, Ganne-Carrié N, Baranes L, et al. Positron emission tomography/computed tomography with 18F-fluorocholine improve tumor staging and treatment allocation in patients with hepatocellular carcinoma. *J Hepatol.* (2018) 69:336–44. doi: 10.1016/j.jhep.2018.02.018
- European Association for the Study of the Liver. EASL clinical practice guidelines: management of hepatocellular carcinoma. *J Hepatol.* (2018) 69:182–236.
- Yamamoto Y, Nishiyama Y, Kameyama R, Okano K, Kashiwagi H, Deguchi A, et al. Detection of hepatocellular carcinoma using 11C-choline PET: comparison with 18F-FDG PET. *J Nucl Med.* (2008) 49:1245–8. doi: 10.2967/jnumed.108.052639
- Talbot JN, Fartoux L, Balogova S, Nataf V, Kerrou K, Gutman F, et al. Detection of hepatocellular carcinoma with PET/CT: a prospective comparison of 18F-fluorocholine and 18F-FDG in patients with cirrhosis or chronic liver disease. *J Nucl Med.* (2010) 51:1699–706. doi: 10.2967/jnumed.110.075507
- Page MJ, McKenzie JE, Bossuyt PM, Boutron I, Hoffmann TC, Mulrow CD, et al. The PRISMA 2020 statement: an updated guideline for reporting systematic reviews. *BMJ.* (2021) 372:n71. doi: 10.1136/bmj.n71
- Vandenbroucke JP, von Elm E, Altman DG, Gøtzsche PC, Mulrow CD, Pocock SJ, et al. Strengthening the reporting of observational studies in epidemiology (STROBE): explanation and elaboration. *Ann Intern Med.* (2007) 147:W163–94.
- Mulé S, Chalaye J, Legou F, Tenenhaus A, Calderaro J, Galletto Pregliasco A, et al. Hepatobiliary MR contrast agent uptake as a predictive biomarker of aggressive features on pathology and reduced recurrence-free survival in resectable hepatocellular carcinoma: comparison with dual-tracer 18F-FDG and 18F-FCH PET/CT. *Eur Radiol.* (2020) 30:5348–57. doi: 10.1007/s00330-020-06923-5
- Fartoux L, Balogova S, Nataf V, Kerrou K, Huchet V, Rosmorduc O, et al. A pilot comparison of 18F-fluorodeoxyglucose and 18F-fluorocholine

- PET/CT to predict early recurrence of unifocal hepatocellular carcinoma after surgical resection. *Nucl Med Commun.* (2012) 33:757–65. doi: 10.1097/MNM.0b013e328350fb9f
25. Tulin PE, Dolgushin MB, Odzharova AA, Mikhaylov AI, Medvedeva BM, Shiryaev SV, et al. Perfusion CT and PET with 18F-FDG and 18F-FCh in the complex diagnosis of hepatocellular carcinoma. *Eur J Hybrid Imaging.* (2017) 1:13. doi: 10.1186/s41824-017-0018-7
 26. Chotipanich C, Kunawudhi A, Promteangtrong C, Tungsuppawattanakit P, Sricharunrat T, Wongs P. Diagnosis of hepatocellular carcinoma using C11 choline PET/CT: comparison with F18 FDG, contrastenhanced MRI and MDCT. *Asian Pac J Cancer Prev.* (2016) 17:3569–73.
 27. Martins-Filho SN, Paiva C, Azevedo RS, Alves VAF. Histological grading of hepatocellular carcinoma—a systematic review of literature. *Front Med.* (2017) 4:193. doi: 10.3389/fmed.2017.00193
 28. Rodríguez-Perálvarez M, Luong TV, Andreana L, Meyer T, Dhillon AP, Burroughs AK. A systematic review of microvascular invasion in hepatocellular carcinoma: diagnostic and prognostic variability. *Ann Surg Oncol.* (2013) 20:325–39. doi: 10.1245/s10434-012-2513-1
 29. Sumie S, Nakashima O, Okuda K, Kuromatsu R, Kawaguchi A, Nakano M, et al. The significance of classifying microvascular invasion in patients with hepatocellular carcinoma. *Ann Surg Oncol.* (2014) 21:1002–9. doi: 10.1245/s10434-013-3376-9
 30. Kornberg A, Freesmeyer M, Bärthel E, Jandt K, Katenkamp K, Steenbeck J, et al. 18F-FDG-uptake of hepatocellular carcinoma on PET predicts microvascular tumor invasion in liver transplant patients. *Am J Transplant.* (2009) 9:592–600. doi: 10.1111/j.1600-6143.2008.02516.x
 31. Sabaté-Llobera A, Mestres-Martí J, Reynés-Llompart G, Lladó L, Mils K, Serrano T, et al. 2-[18F]FDG PET/CT as a predictor of microvascular invasion and high histological grade in patients with hepatocellular carcinoma. *Cancers.* (2021) 13:2554. doi: 10.3390/cancers13112554
 32. Cuccurullo V, Di Stasio GD, Mazzarella G, Cascini GL. Microvascular invasion in HCC: the molecular imaging perspective. *Contrast Media Mol Imaging.* (2018) 2018:9487938. doi: 10.1155/2018/9487938
 33. Gouw ASH, Balabaud C, Kusano H, Todo S, Ichida T, Kojiro M. Markers for microvascular invasion in hepatocellular carcinoma: where do we stand? *Liver Transplant.* (2011) 17(Suppl. 2):S72–80. doi: 10.1002/lt.22368
 34. Yamashita Y, Tsujita E, Takeishi K, Fujiwara M, Kira S, Mori M, et al. Predictors for microinvasion of small hepatocellular carcinoma ≤ 2 cm. *Ann Surg Oncol.* (2012) 19:2027–34. doi: 10.1245/s10434-011-2195-0
 35. Okazumi S, Isono K, Enomoto K, Kikuchi T, Ozaki M, Yamamoto H, et al. Evaluation of liver tumors using fluorine-18-fluorodeoxyglucose PET: characterization of tumor and assessment of effect of treatment. *J Nucl Med.* (1992) 33:333–9.
 36. Torizuka T, Tamaki N, Inokuma T, Magata Y, Sasayama S, Yonekura Y, et al. In vivo assessment of glucose metabolism in hepatocellular carcinoma with FDG-PET. *J Nucl Med.* (1995) 36:1811–7.
 37. Trojan J, Schroeder O, Raedle J, Baum RP, Herrmann G, Jacobi V, et al. Fluorine-18 FDG positron emission tomography for imaging of hepatocellular carcinoma. *Am J Gastroenterol.* (1999) 94:3314–9.
 38. Zhao WC, Fan LF, Yang N, Zhang HB, Chen BD, Yang GS. Preoperative predictors of microvascular invasion in multinodular hepatocellular carcinoma. *Eur J Surg Oncol.* (2013) 39:858–64. doi: 10.1016/j.ejso.2013.04.003
 39. Mulé S, Pigneur F, Quelever R, Tenenhaus A, Baranes L, Richard P, et al. Can dual-energy CT replace perfusion CT for the functional evaluation of advanced hepatocellular carcinoma? *Eur Radiol.* (2018) 28:1977–85. doi: 10.1007/s00330-017-5151-y
 40. Lee JS, Heo J, Libbrecht L, Chu IS, Kaposi-Novak P, Calvisi DF, et al. A novel prognostic subtype of human hepatocellular carcinoma derived from hepatic progenitor cells. *Nat Med.* (2006) 12:410–6. doi: 10.1038/nm1377
 41. Boyault S, Rickman DS, de Reyniès A, Balabaud C, Rebouissou S, Jeannot E, et al. Transcriptome classification of HCC is related to gene alterations and to new therapeutic targets. *Hepatology.* (2007) 45:42–52. doi: 10.1002/hep.21467
 42. Chiang DY, Villanueva A, Hoshida Y, Peix J, Newell P, Minguez B, et al. Focal gains of VEGFA and molecular classification of hepatocellular carcinoma. *Cancer Res.* (2008) 68:6779–88. doi: 10.1158/0008-5472.CAN-08-0742
 43. Hoshida Y, Nijman SMB, Kobayashi M, Chan JA, Brunet JP, Chiang DY, et al. Integrative transcriptome analysis reveals common molecular subclasses of human hepatocellular carcinoma. *Cancer Res.* (2009) 69:7385–92. doi: 10.1158/0008-5472.CAN-09-1089
 44. Cancer Genome Atlas Research Network. Comprehensive and integrative genomic characterization of hepatocellular carcinoma. *Cell.* (2017) 169:1327–41.e23. doi: 10.1016/j.cell.2017.05.046
 45. Llovet JM, Kelley RK, Villanueva A, Singal AG, Pikarsky E, Roayaie S, et al. Hepatocellular carcinoma. *Nat Rev Dis Primer.* (2021) 7:6.
 46. Sia D, Jiao Y, Martinez-Quetglas I, Kuchuk O, Villacorta-Martin C, Castro de Moura M, et al. Identification of an immune-specific class of hepatocellular carcinoma, based on molecular features. *Gastroenterology.* (2017) 153:812–26. doi: 10.1053/j.gastro.2017.06.007
 47. Ding X, He M, Chan AWH, Song QX, Sze SC, Chen H, et al. Genomic and epigenomic features of primary and recurrent hepatocellular carcinomas. *Gastroenterology.* (2019) 157:1630–45.e6.
 48. Zhang Q, Lou Y, Bai XL, Liang TB. Intratumoral heterogeneity of hepatocellular carcinoma: from single-cell to population-based studies. *World J Gastroenterol.* (2020) 26:3720–36. doi: 10.3748/wjg.v26.i26.3720
 49. Cheung TT, Ho CL, Chen S, Chan SC, Poon RTP, Fan ST, et al. Reply: underestimated role of 18F-FDG PET for HCC evaluation and promise of 18F-FDG PET/MR imaging in this setting. *J Nucl Med.* (2013) 54:1511–2. doi: 10.2967/jnumed.113.126185
 50. Ho CL, Yu SCH, Yeung DWC. 11C-acetate PET imaging in hepatocellular carcinoma and other liver masses. *J Nucl Med.* (2003) 44:213–21.
 51. Hwang KH, Choi DJ, Lee SY, Lee MK, Choe W. Evaluation of patients with hepatocellular carcinomas using [(11)C]acetate and [(18)F]FDG PET/CT: a preliminary study. *Appl Radiat Isot.* (2009) 67:1195–8. doi: 10.1016/j.apradiso.2009.02.011
 52. Au KP, Dai WC, Chi-Yan Chan A, Cheung TT, Lo CM, Chok KSH. Performance of dual-tracer PET-CT for staging post-liver transplant hepatocellular carcinoma recurrence. *Transplant Direct.* (2021) 7:e769. doi: 10.1097/TXD.0000000000001213
 53. Brown M, Marshall DR, Sobel BE, Bergmann SR. Delineation of myocardial oxygen utilization with carbon-11-labeled acetate. *Circulation.* (1987) 76:687–96. doi: 10.1161/01.cir.76.3.687
 54. Shreve P, Chiao PC, Humes HD, Schwaiger M, Gross MD. Carbon-11-acetate PET imaging in renal disease. *J Nucl Med.* (1995) 36:1595–601.
 55. Oyama N, Akino H, Kanamaru H, Suzuki Y, Muramoto S, Yonekura Y, et al. 11C-acetate PET imaging of prostate cancer. *J Nucl Med.* (2002) 43:181–6.
 56. Podo F. Tumour phospholipid metabolism. *NMR Biomed.* (1999) 12:413–39. doi: 10.1002/(sici)1099-1492(199911)12:7<413::aid-nbm587>3.0.co;2-u
 57. Gibellini F, Smith TK. The Kennedy pathway—de novo synthesis of phosphatidylethanolamine and phosphatidylcholine. *IUBMB Life.* (2010) 62:414–28. doi: 10.1002/iub.337
 58. Deford-Watts LM, Mintz A, Kridel SJ. The potential of ¹¹C-acetate PET for monitoring the fatty acid synthesis pathway in tumors. *Curr Pharm Biotechnol.* (2013) 14:300–12. doi: 10.2174/1389201011314030006
 59. Wellen KE, Hatzivassiliou G, Sachdeva UM, Bui TV, Cross JR, Thompson CB. ATP-citrate lyase links cellular metabolism to histone acetylation. *Science.* (2009) 324:1076–80. doi: 10.1126/science.1164097
 60. Moffett JR, Puthillathu N, Vengilote R, Jaworski DM, Namboodiri AM. Acetate revisited: a key biomolecule at the nexus of metabolism, epigenetics and oncogenesis—part 1: acetyl-CoA, acetogenesis and acyl-CoA short-chain synthetases. *Front Physiol.* (2020) 11:580167. doi: 10.3389/fphys.2020.580167

Conflict of Interest: The authors declare that the research was conducted in the absence of any commercial or financial relationships that could be construed as a potential conflict of interest.

Publisher's Note: All claims expressed in this article are solely those of the authors and do not necessarily represent those of their affiliated organizations, or those of the publisher, the editors and the reviewers. Any product that may be evaluated in this article, or claim that may be made by its manufacturer, is not guaranteed or endorsed by the publisher.

Copyright © 2022 Ghidaglia, Golse, Pascale, Sebah and Besson. This is an open-access article distributed under the terms of the Creative Commons Attribution License (CC BY). The use, distribution or reproduction in other forums is permitted, provided the original author(s) and the copyright owner(s) are credited and that the original publication in this journal is cited, in accordance with accepted academic practice. No use, distribution or reproduction is permitted which does not comply with these terms.

Advantages of publishing in Frontiers



OPEN ACCESS

Articles are free to read
for greatest visibility
and readership



FAST PUBLICATION

Around 90 days
from submission
to decision



HIGH QUALITY PEER-REVIEW

Rigorous, collaborative,
and constructive
peer-review



TRANSPARENT PEER-REVIEW

Editors and reviewers
acknowledged by name
on published articles

Frontiers

Avenue du Tribunal-Fédéral 34
1005 Lausanne | Switzerland

Visit us: www.frontiersin.org

Contact us: frontiersin.org/about/contact



REPRODUCIBILITY OF RESEARCH

Support open data
and methods to enhance
research reproducibility



DIGITAL PUBLISHING

Articles designed
for optimal readership
across devices



FOLLOW US

@frontiersin



IMPACT METRICS

Advanced article metrics
track visibility across
digital media



EXTENSIVE PROMOTION

Marketing
and promotion
of impactful research



LOOP RESEARCH NETWORK

Our network
increases your
article's readership